



School of Mechanical and Manufacturing Engineering  
Faculty of Engineering

---

**Calibration of empirical, semi-empirical, and physics-based material models for  
the prediction of creep and tensile behaviour of Alloy 617**

---

A thesis in fulfilment of the requirements for the degree of  
Doctor of Philosophy

BY

**Janzen Hing Ho Choi**

December 2025

## Abstract

Material models are powerful analytical tools for predicting material behaviour under various loading conditions. These models vary in complexity, progressing from **empirical models** that rely solely on fitting experimental data, to **semi-empirical** models that incorporate simplified physical concepts, and finally to **physics-based** models that explicitly represent the underlying deformation and degradation processes. Typically, as material models become more sophisticated, they provide improved predictive accuracy, broader applicability, and richer mechanistic insight. However, this added sophistication often introduces larger and more interdependent parameter spaces, higher computational demands, and greater calibration difficulty.

This thesis explores the development and calibration of various empirical, semi-empirical, and physics-based material models to capture the creep and tensile behaviour of Alloy 617. The thesis is organised into three studies. The first study focuses on calibrating twelve empirical models and on symbolic regression-based model discovery to capture elevated-temperature creep behaviour. The second study presents the calibration of three semi-empirical elastic-viscoplastic (EVP) models using a multi-objective three-stage calibration workflow to capture elevated-temperature creep and tensile behaviour. In the third study, three physics-based crystal plasticity finite element method (CPFEM) models are calibrated using a multi-objective surrogate-assisted calibration workflow to capture multiscale tensile behaviour. The results from these studies are then synthesised to assess the predictive accuracy, robustness, generalisability, interpretability, and calibration difficulty of the different material modelling frameworks.

## Acknowledgements

The author wishes to express sincere gratitude to their supervisors, Ondrej Muránsky, Mark Messner, and Jay Kružic, for their invaluable guidance, patience, and encouragement throughout the candidature. They are truly bastions of intellect and wisdom, and it has been a privilege for the author to learn from their expertise and develop under their mentorship. The author also thanks their parents, Miliawati Tanadi and Joffrey Choi, as well as friends and family, for their unwavering support throughout the course of these studies.

The author acknowledges the University of New South Wales (UNSW), Australian Nuclear Science and Technology Organisation (ANSTO), and Argonne National Laboratory (ANL) for access to facilities and technical support. The author also acknowledges the support of the Australian Government Research Training Program (RTP) Scholarship, Engineering Top up Award (ETA), Tyree Scholarship, Future Now Scholarship Program, as well as the UNSW Development and Research Training Grant (DRTG) for providing the funding and resources that made this research possible.

Portions of the dissertation include material from articles published by the author, which were produced in collaboration with Ondrej Muránsky, Mark Messner, Jay Kružic, Tao Wei, Tianchen Hu, Zhiyang Wang, and Michael McMurtrey. The author thanks the co-authors for their contributions to the conceptualisation, experimental work, data analysis, software development, and manuscript preparation. The text, figures, and data from these publications are reproduced here with permission and have been incorporated into the relevant chapters with appropriate attribution.

## Publications

### *List of journal papers*

- J. Choi, O. Muránsky, M.C. Messner, J.J. Kruzic, M.D. McMurtrey, *Multi-objective Calibration of Elastic-Viscoplastic Models to Capture the Elevated-Temperature Creep and Tensile Behaviour of Alloy 617*, International Journal of Pressure Vessels and Piping 218 (2025) 105566
- J. Choi, O. Muránsky, M.C. Messner, T. Wei, T. Hu, J.J. Kruzic, M.D. McMurtrey, *Multi-Objective Surrogate-Assisted Calibration of CPFEM Models Using Macroscopic Response and In Situ EBSD Measurements of Grain Reorientation Trajectories*, Acta Materialia (2026) 121809

### *List of conference presentations*

- J. Choi, O. Muránsky, M.C. Messner, J.J. Kruzic, M.D. McMurtrey, *Genetic Algorithm based Calibration of Elastic-Viscoplastic Models for Predicting the Elevated-Temperature Behaviour of Alloy 617*, 8th Conference of the Combined Australian Materials Societies (CAMS2024)
- J. Choi, M.C. Messner, Z. Wang, T. Wei, T. Hu, J.J. Kruzic, O. Muránsky, *Surrogate-Model-Assisted Multi-Objective Calibration of Crystal Plasticity Finite Element Method (CPFEM) Models*, Structural Integrity and Failure Conference (SIF2025)
- J. Choi, M.C. Messner, Z. Wang, T. Wei, T. Hu, J.J. Kruzic, O. Muránsky, *Surrogate-Model-Assisted Multi-Objective Calibration of Crystal Plasticity Finite Element Method (CPFEM) Models*, 8th World Congress on Integrated Computational Materials Engineering (ICME2025)

## Table of contents

Abstract .....	i
Acknowledgements.....	ii
Publications .....	iii
Table of contents .....	iv
List of symbols .....	ix
List of figures.....	xiv
List of tables.....	xxiii
List of abbreviations.....	xxiv
Chapter 1 Introduction.....	1
Chapter 2 Literature review .....	3
2.1.    Structure of metals.....	3
2.1.1.    Structural hierarchy .....	3
2.1.2.    Microstructural features .....	4
2.1.3.    Alloy 617.....	4
2.2.    Material deformation .....	6
2.2.1.    Elastic and plastic deformation .....	6
2.2.2.    Plastic deformation of single crystals .....	7
2.2.3.    Latent hardening of FCC crystals .....	9
2.2.4.    Plastic deformation of polycrystals .....	10
2.2.5.    Texture evolution .....	10
2.3.    Experimental testing .....	12
2.3.1.    Tensile testing.....	12
2.3.2.    Creep testing .....	13
2.3.3.    Electron backscatter diffraction .....	15
2.4.    Material models .....	17
2.4.1.    Empirical material models .....	17
2.4.2.    Semi-empirical material models.....	18
2.4.3.    Physics-based material models .....	19
2.5.    Material model calibration .....	21
2.5.1.    Optimisation algorithms .....	22

2.5.2. Genetic algorithm .....	23
2.5.3. Multi-objective genetic algorithm .....	24
2.5.4. Improving calibration efficiency .....	26
2.6. Surrogate modelling .....	27
2.6.1. Training process .....	28
2.6.2. Modelling techniques .....	29
2.6.3. Artificial neural network .....	29
2.7. Symbolic regression .....	30
2.7.1. Classical material models .....	31
2.7.2. Automated model discovery .....	31
2.7.3. Applications in material modelling .....	32
2.8. Conclusion .....	34
2.8.1. Review summary .....	34
2.8.2. Research gaps .....	35
Chapter 3 Research objectives .....	37
3.1. Empirical and symbolic regression models .....	37
3.2. Semi-empirical elastic-viscoplastic models .....	38
3.3. Physics-based crystal plasticity finite element method models .....	38
Chapter 4 Calibration of empirical and symbolic regression models for the elevated-temperature creep behaviour of Alloy 617 .....	40
4.1. Introduction .....	40
4.2. Experimental data .....	41
4.3. Empirical creep models .....	42
4.3.1. Minimum creep rate models .....	43
4.3.2. Time-to-failure models .....	43
4.3.3. Strain-to-failure models .....	44
4.3.4. Strain–time models .....	44
4.4. Calibration methodology .....	45
4.4.1. Data preparation .....	46
4.4.2. Parameter optimisation using genetic algorithm .....	46
4.4.3. Model discovery using symbolic regression .....	48
4.5. Results and discussion .....	48

4.5.1.	Minimum creep rate predictions.....	49
4.5.2.	Time-to-failure predictions .....	51
4.5.3.	Strain-to-failure predictions.....	53
4.5.4.	Regular strain–time predictions .....	55
4.5.5.	Mechanism-shifted strain–time predictions.....	58
4.5.6.	Comparison of empirical and symbolic regression models .....	60
4.6.	Conclusion.....	62
Chapter 5 Calibration of semi-empirical elastic-viscoplastic models for the elevated-temperature creep and tensile behaviour of Alloy 617.....		64
5.1.	Introduction .....	64
5.2.	Experimental data .....	65
5.3.	Elastic viscoplastic material models .....	66
5.3.1.	Definition of elastic-viscoplastic model .....	67
5.3.2.	Coupling with a classical creep damage model.....	68
5.3.3.	Coupling with a work damage model .....	69
5.4.	Calibration methodology .....	69
5.4.1.	Splitting the experimental datasets .....	70
5.4.2.	Multi-objective genetic algorithm optimisation .....	70
5.4.3.	Multi-objective three-stage calibration workflow .....	72
5.5.	Results and discussion .....	73
5.5.1.	Calibration of elastic-viscoplastic creep damage model .....	73
5.5.2.	Calibration of elastic-viscoplastic work damage model .....	75
5.5.3.	Assessment of calibration process .....	77
5.5.4.	Performance of calibrated models.....	78
5.5.5.	Computational costs .....	80
5.6.	Conclusion.....	80
Chapter 6 Calibration of physics-based crystal plasticity finite element method models for the multiscale deformation behaviour of Alloy 617 .....		82
6.1.	Introduction .....	82
6.2.	Experimental data .....	84
6.2.1.	Material.....	84
6.2.2.	Data acquisition during tensile loading .....	84

6.2.3.	Grain reorientation trajectories .....	86
6.2.4.	Finite element model generation.....	87
6.3.	Microstructure-informed material models .....	88
6.3.1.	Crystal plasticity formulation .....	88
6.3.2.	Voce hardening formulation .....	89
6.3.3.	Two-coefficient latent hardening formulation .....	89
6.3.4.	Six-coefficient latent hardening formulation.....	90
6.4.	Calibration methodology .....	90
6.4.1.	Multi-objective genetic algorithm optimisation .....	90
6.4.2.	Deep neural network surrogate modelling.....	91
6.4.3.	Multi-objective surrogate-assisted calibration workflow .....	92
6.5.	Results and discussion .....	94
6.5.1.	Performance of trained surrogate models .....	94
6.5.2.	Performance of calibrated models.....	96
6.5.3.	Robustness of calibration workflow .....	100
6.5.4.	Impact of mesoscale constraints on model calibration.....	103
6.5.5.	Transferability across microstructural fidelities.....	105
6.6.	Conclusion.....	108
Chapter 7 Discussion.....		110
7.1.	Research overview .....	110
7.2.	Addressing research objectives .....	111
7.2.1.	Application of symbolic regression for mechanism-shifted creep behaviour .....	111
7.2.2.	Comparison of empirical and symbolic regression models .....	112
7.2.3.	Development of multi-objective multi-stage calibration workflow.....	113
7.2.4.	Comparison of creep and work damage models .....	114
7.2.5.	Development of multi-objective surrogate-assisted calibration workflow.....	115
7.2.6.	Comparison of crystal plasticity hardening models .....	115
7.2.7.	Evaluation of parameter transferability across fidelities .....	116
7.3.	Comparison of modelling frameworks .....	117
7.3.1.	Comparison of model generalisability.....	117
7.3.2.	Comparison of model interpretability .....	118

7.3.3. Comparison of model practicality .....	119
7.4. Remaining gaps and future work .....	120
7.4.1. Future work for empirical and symbolic regression models .....	120
7.4.2. Future work for semi-empirical elastic-viscoplastic models.....	120
7.4.3. Future work for physics-based crystal plasticity finite element method models.....	121
Chapter 8 Conclusion .....	122
References .....	124
Appendix A     Supplementary materials for Chapter 4 .....	138
Appendix A.1. Material parameters of empirical models .....	138
Appendix A.2. Alternate symbolic regression approaches .....	139
Appendix A.3. Regular strain–time predictions from empirical models.....	140
Appendix A.4. Mechanism-shifted strain–time predictions from empirical models .....	142
Appendix B     Supplementary materials for Chapter 5 .....	144
Appendix B.1. Material parameter of elastic-viscoplastic models.....	144
Appendix B.2. Functions for work density and damage exponent .....	144
Appendix B.3. Calibration results at 900°C and 1000°C .....	146
Appendix B.4. Optimised material parameter values .....	149
Appendix C     Supplementary materials for Chapter 6 .....	150
Appendix C.1. Experimental and simulated deformation of Alloy 617 specimen .....	150
Appendix C.2. Grain tracking across electron backscatter diffraction maps.....	151
Appendix C.3. Sensitivity study for mesh resolution.....	154
Appendix C.4. Material parameters of crystal plasticity hardening models .....	156
Appendix C.5. Knee-point identification method .....	156
Appendix C.6. Sensitivity study for initial training dataset size .....	157
Appendix C.7. Computational costs of crystal plasticity finite element method models .....	158
Appendix C.8. Calibration of Voce hardening formulation with swapped grain trajectories .....	159

## List of symbols

### *Material deformation*

$C$	=	Isotropic elasticity tensor
$E$	=	Elastic modulus
$G$	=	Shear modulus
$I$	=	Identity tensor
$L^p$	=	Plasticity velocity gradient
$q$	=	Quaternion
$t$	=	Time
$t_f$	=	Creep time-to-failure
$t_{f,o}$	=	Oxidation-affected creep time-to-failure
$T$	=	Temperature
$T_m$	=	Melting temperature
$\dot{\gamma}$	=	Slip rate of a slip system
$\lambda_\alpha$	=	Angle between stress direction and slip direction
$\nu$	=	Poisson's ratio
$\varepsilon$	=	Strain
$\varepsilon_{area}$	=	Total creep deformation (area under creep curve)
$\varepsilon_d$	=	Strain-at-ductility
$\varepsilon_e$	=	Elastic strain tensor
$\varepsilon_f$	=	Creep strain-to-failure
$\varepsilon_{f,o}$	=	Oxidation-affected creep strain-to-failure
$\dot{\varepsilon}_m$	=	Minimum creep rate
$\varepsilon_{UTS}$	=	Strain at ultimate tensile stress
$\varepsilon_{vp}$	=	Viscoplastic strain tensor
$\varepsilon_y$	=	Strain at tensile yield stress
$\sigma$	=	Stress
$\sigma$	=	Stress tensor
$\sigma_{area}$	=	Toughness (area under tensile curve)
$\sigma_d$	=	Stress-at-ductility
$\sigma_M$	=	Maximum true stress
$\sigma_{UTS}$	=	Ultimate tensile stress
$\sigma_y$	=	Yield stress
$\tau_\alpha$	=	Resolved shear stress
$\tau_\alpha^*$	=	Critical resolved shear stress
$\phi_\alpha$	=	Angle between stress direction and slip normal

### *Empirical material models*

#### Norton power law parameters

$A_{No}$  = Stress prefactor  
 $n_{No}$  = Stress sensitivity

#### Norton-Arrhenius parameters

$A_{NA}$  = Pre-exponential factor  
 $n_{NA}$  = Stress sensitivity  
 $Q_{NA}$  = Activation energy

#### Altenbach-Arrhenius parameters

$A_{AA}$  = Pre-exponential factor  
 $B_{AA}$  = Stress scale prefactor  
 $n_{AA}$  = Stress sensitivity  
 $Q_{AA}$  = Activation energy

#### Garafalo-Arrhenius parameters

$A_{GA}$  = Pre-exponential factor  
 $\beta_{GA}$  = Stress scale prefactor  
 $n_{GA}$  = Stress sensitivity  
 $Q_{GA}$  = Activation energy

#### Monkman-Grant parameters

$c_{MG}$  = Material constant  
 $m_{MG}$  = Creep rate exponent

#### Dorn-Shepherd parameters

$D_{DS}$  = Pre-exponential factor  
 $n_{DS}$  = Stress sensitivity  
 $Q_{DS}$  = Activation energy

#### Larson-Miller parameters

$a_{LM}$  = Log-stress coefficient  
 $b_{LM}$  = Linear-stress coefficient  
 $c_{LM}$  = Intercept coefficient  
 $C_{LM}$  = Larson-Miller constant

#### Dobes parameters

$c_{Do}$  = Material constant  
 $m_{Do}$  = Creep rate exponent

Evan parameters

$a_{Ev}$	=	Intercept coefficient
$b_{Ev}$	=	Stress coefficient
$c_{Ev}$	=	Temperature coefficient
$d_{Ev}$	=	Stress-temperature coefficient

Soares parameters

$a_{So}$	=	Intercept coefficient
$b_{So}$	=	Temperature coefficient
$c_{So}$	=	Stress-temperature coefficient
$d_{So}$	=	Log-temperature coefficient
$e_{So}$	=	Stress coefficient

Omega parameters

$\Omega_{1,Om}$	=	Primary accelerator
$\Omega_{2,Om}$	=	Primary decay
$\Omega_{3,Om}$	=	Tertiary accelerator
$\Omega_{4,Om}$	=	Tertiary decay
$A_{i,Om}$	=	Pre-exponential factor
$n_{i,Om}$	=	Stress sensitivity
$Q_{i,Om}$	=	Activation energy

Phi parameters

$\phi_{1,Ph}$	=	Primary scale
$\phi_{2,Ph}$	=	Primary exponent
$\phi_{3,Ph}$	=	Tertiary scale
$\phi_{4,Ph}$	=	Tertiary exponent
$A_{i,Ph}$	=	Pre-exponential factor
$n_{i,Ph}$	=	Stress sensitivity
$Q_{i,Ph}$	=	Activation energy

Theta-projection parameters

$\theta_{1,TP}$	=	Primary amplitude
$\theta_{2,TP}$	=	Primary rate sensitivity
$\theta_{3,TP}$	=	Tertiary amplitude
$\theta_{4,TP}$	=	Tertiary rate sensitivity
$a_{i,TP}$	=	Intercept coefficient
$b_{i,TP}$	=	Stress coefficient
$c_{i,TP}$	=	Temperature coefficient

$d_{i,TP}$  = Stress-temperature coefficient

### *Semi-empirical material models*

#### Creep damage (CD) model parameters

$A_{CD}$  = Stress prefactor  
 $\xi_{CD}$  = Stress power law exponent  
 $\phi_{CD}$  = Damage power law exponent

#### Elastic-viscoplastic ( EVP) model parameters

$d_{VIH}$  = Isotropic hardening rate  
 $n_{PF}$  = Flow surface exponent  
 $R_{VIH}$  = Isotropic hardening modulus  
 $\eta_{PF}$  = Viscoplastic fluidity parameter  
 $\sigma_{y,0}$  = Initial yield stress

#### Work damage model parameters

$a_{WD}$  = Creep critical work density intercept  
 $A_{WD}$  = Creep critical work density gradient  
 $b_{WD}$  = Tensile critical work density intercept  
 $B_{WD}$  = Tensile critical work density gradient  
 $\alpha_{WD}$  = Creep damage exponent  
 $\beta_{WD}$  = Tensile damage exponent

#### Miscellaneous parameters

$f_{PF}$  = Perzyna yield function  
 $J_2$  = Deviatoric stress invariant  
 $n_d$  = Damage exponent  
 $W$  = Plastic work density  
 $W_{crit}$  = Critical plastic work density  
 $\lambda_1$  = Work density rate threshold for decay  
 $\lambda_2$  = Work density rate threshold for transition  
 $\sigma_h$  = Hardening stress  
 $\omega$  = Damage state variable

### *Physics-based material models*

#### Crystal plasticity (CP) hardening model parameters

$n$  = Strain rate sensitivity parameter  
 $\tau_0$  = Static slip system strength

Voce hardening (VH) formulation parameters

$b$	=	Saturation rate parameter
$\tau_s$	=	Saturation slip system strength

Latent hardening (LH) formulation parameters

$h_{\alpha\alpha}$	=	Self-hardening coefficient
$h_{\alpha\beta}$	=	Latent hardening coefficient
$h_1$	=	Coplanar interaction coefficient
$h_2$	=	Hirth interaction coefficient
$h_3$	=	Collinear interaction coefficient
$h_4$	=	Glissile interaction coefficient
$h_5$	=	Lomer interaction coefficient

Miscellaneous parameters

$H_2$	=	Two-coefficient interaction matrix
$H_6$	=	Six-coefficient interaction matrix
$M$	=	Taylor factor
$\dot{\gamma}_0$	=	Reference slip rate
$\tau'$	=	Dynamic slip system strength

*Objective functions*Creep predictions

$E_{tf}$	=	Objective function for time-to-failure
$E_\varepsilon$	=	Objective function for strain values
$E_{\varepsilon_f}$	=	Objective function for strain-to-failure
$E_{\dot{\varepsilon}_m}$	=	Objective function for minimum creep rate
$E_p$	=	Objective function for parameter functions

Tensile predictions

$E_{\varepsilon_d}$	=	Objective function for strain-at-ductility
$E_\sigma$	=	Objective function for stress values
$E_{\sigma_M}$	=	Objective function for maximum true stress
$E_{\sigma_y}$	=	Objective function for yield stress
$E_\phi$	=	Objective function for reorientation trajectories

## List of figures

Figure 2.1. Schematics of common crystal structures of metals, namely a) body-centred cubic (BCC), b) face-centred cubic (FCC), and c) hexagonal close-packed (HCP).....	3
Figure 2.2. Optical micrograph of a typical Alloy 617 microstructure, adapted from Haribabu <i>et al.</i> [46] by permission of Springer Nature. ....	5
Figure 2.3. Deformation mechanism map of Alloy 617 reproduced from H.-J. Penkalla, H.-H. Over, and F. Schubert, <i>Constitutive equations for the description of creep and creep rupture behavior of metallic materials at temperatures above 800°C</i> , Nuclear Technology [52], © 2017. Image reprinted by permission of Informa UK Limited, trading as Taylor & Francis Group, <a href="https://www.tandfonline.com">https://www.tandfonline.com</a> .....	7
Figure 2.4. Illustrations of a) an undeformed lattice, b) lattice distortion produced by slip, and c) lattice reorientation produced by twinning. The dashed arrows indicate the directions of slip and twinning. ....	7
Figure 2.5. Schematic showing three {111}110 slip systems in a face centred cubic (FCC) crystal structure, where the constituent atoms are shown in blue, the slip plane is shown in green, and the slip directions are shown in red.....	8
Figure 2.6. Annotated schematic of a typical stress–strain curve of a metal single crystal.....	8
Figure 2.7. Microstructure of a CoCrNi specimen at a) $\varepsilon = 0\%$ , b) $\varepsilon = 10\%$ , and c) $\varepsilon = 20\%$ , shown as inverse pole figure (IPF) colour maps in the $x$ direction. Panels are adapted from Huang <i>et al.</i> [69] by permission of Elsevier.....	11
Figure 2.8. Schematics of a) a pole figure (PF) diagram containing common directions and b) an inverse pole figure (IPF) diagram of the standard triangle containing directions with positive indices in descending order. 11	11
Figure 2.9. Uniaxial tensile test specimen and machine. Panel a) shows the undeformed and ruptured aluminium alloy specimen, panel b) shows the dimensions of the specimen (in mm), and panel c) shows the INSTRON tensile testing machine. Panels are adapted from Talebi-Ghadikolaei <i>et al.</i> [74] by permission of Springer Nature. ....	12
Figure 2.10. Annotated schematic of a typical tensile curve for a polycrystalline metal alloy. ....	13
Figure 2.11. Creep test specimens and machine. Panel a) shows undeformed aluminium-silicon alloy specimens, panel b) shows the dimensions of the specimens (in mm), and panel c) shows the SCT-30 SANTAM creep testing machine. Panels are adapted from Golshan <i>et al.</i> [82] by permission of Springer Nature. ....	14
Figure 2.12. Annotated schematic of a typical creep curve for a polycrystalline metal alloy. ....	14
Figure 2.13. Annotated schematics of a) transmission electron microscopy (TEM) and b) scanning electron microscopy (SEM), adapted from Son <i>et al.</i> [91] by permission of Oxford University Press. ....	16
Figure 2.14. Typical diffraction patterns from a face-centred cubic (FCC) material obtained through electron backscatter diffraction (EBSD), reproduced from Randle [98] by permission of Elsevier.....	16
Figure 2.15. 3D finite element (FE) models generated using the representative volume element (RVE) approach, containing a) 98, b) 140, and c) 243 grains. Panels are adapted from Zhang <i>et al.</i> [136] by permission of IOP Publishing.....	20
Figure 2.16. Generation of a 2.5D finite element (FE) model using the projection approach. Panel a) shows an electron backscatter diffraction (EBSD) map coloured with respect to IPF- $x$ , while panels b) and c) show the resulting 2.5D FE model in top and angled views, respectively. Panels are adapted from Abdolvand [124] by permission of Elsevier.....	21

Figure 2.17. Flowchart of the genetic algorithm workflow.....	24
Figure 2.18. Illustration and example of the utopia-point approach. Panel a) shows an illustration adapted from Gu <i>et al.</i> [155] by permission of Springer Nature, while panel b) shows an example adapted from Muránsky <i>et al.</i> [156] by permission of Elsevier. ....	26
Figure 2.19. Examples of stationary sampling strategies for two parameters: a) two-level factorial design, b) three-level factorial design, c) central composite design, and d) Latin hypercube sampling. ....	28
Figure 2.20. Annotated schematic of a) a neuron and b) a simple neural network. ....	30
Figure 2.21. Illustration of a unary-binary expression tree that encodes $fx = x_1x_2 - 2x_3$ , adapted from Makke <i>et al.</i> [192] by permission of Springer Nature. ....	32
Figure 2.22. Illustrations of the a) crossover and b) mutation operations on exemplary expression trees, adapted from Makke <i>et al.</i> [192] by permission of Springer Nature. ....	32
Figure 2.23. Comparison of contributions related to machine learning machine learning and symbolic regression (SR) from different research fields to scientific journals from 1998 to 2018, reproduced from Wang <i>et al.</i> [193] by permission of Springer Nature.....	33
Figure 2.24. Plots of the true creep rate and true stress at a) 600°C, b) 650°C, and c) 700°C, showing the predictions by the symbolic regression (SR) model (lines) and logistic model (ovals). Panels are adapted with permission from D. Baraldi, S. Holmström, K.-F. Nilsson. M. Bruchhausen, and I. Simonovski, <i>316L(N) Creep Modeling with Phenomenological Approach and Artificial Intelligence Based Methods</i> [194]; published by MDPI, 2021. ....	33
Figure 4.1. Annotated plots of the experimental creep data of Alloy 617 from the Idaho National Laboratory at a) 800°C, b) 900°C, and c) 1000°C. The typical and atypical portions of the creep responses are shown in dark grey and light grey, respectively. ....	41
Figure 4.2. Calibration and validation results for the Norton-Arrhenius, Altenbach-Arrhenius, Garofalo-Arrhenius, and symbolic regression (SR) models in predicting the minimum creep rate across five independent runs. Plots a), c), e), and g) compare the experimental and simulated minimum creep rate values for the calibration (green) and validation (red) datasets, with the dashed lines representing the line of best fit (LOBF) corresponding to the run that achieved the lowest objective value. Panels b), d), and f) show the parameter distributions for the empirical models, with the mean (black line), standard deviation (box), range (whiskers), bounds (limits), and best-performing values (green circle and number). Panel h) shows the SR-derived constitutive expressions with the best-performing expression highlighted in green. ....	49
Figure 4.3. Comparison of empirical and symbolic regression (SR) models in reproducing the minimum creep rate from the calibration (green) and validation (red) datasets. Plot a) compares the average relative errors (RE) while plot b) compares the average coefficient of variation (CV). ....	50
Figure 4.4. Experimental correlations between a) $\ln(\varepsilon m)$ and $\ln(\sigma)$ and b) $\ln(\varepsilon m)$ and $1/T$ for Alloy 617 at 800°C, 900°C, and 1000°C, showing calibration (green) and validation (red) datasets with dashed lines indicating the lines of best fit (LOBF). ....	51
Figure 4.5. Calibration and validation results for the Monkman-Grant, Dorn-Shepherd, Larson-Miller, and symbolic regression (SR) models in predicting the time-to-failure across five independent runs. Plots a), c), e), and g) compare the experimental and simulated time-to-failure values for the calibration (green) and validation (red) datasets, with the dashed lines representing the line of best fit (LOBF) corresponding to the run that	

achieved the lowest objective value. Panels b), d), and f) show the parameter distributions for the empirical models, with the mean (black line), standard deviation (box), range (whiskers), bounds (limits), and best-performing values (green circle and number). Panel h) shows the SR-derived constitutive expressions with the best-performing expression highlighted in green..... 52

Figure 4.6. Comparison of empirical and symbolic regression (SR) models in reproducing the time-to-failure from the calibration (green) and validation (red) datasets. Plot a) compares the average relative errors (RE) while plot b) compares the average coefficient of variation (CV)..... 52

Figure 4.7. Experimental correlations between a)  $\ln(tf)$  and  $\ln(\varepsilon m)$ , b)  $\ln(tf)$  and  $\ln(\sigma)$ , and c)  $\ln(tf)$  and  $1/T$  for Alloy 617 at 800°C, 900°C, and 1000°C, showing calibration (green) and validation (red) datasets with dashed lines indicating the lines of best fit (LOBF). ..... 53

Figure 4.8. Calibration and validation results for the Dobes, Evans, Soares, and symbolic regression (SR) models in predicting the strain-to-failure across five independent runs. Plots a), c), e), and g) compare the experimental and simulated strain-to-failure values for the calibration (green) and validation (red) datasets, with the dashed lines representing the line of best fit (LOBF) corresponding to the run that achieved the lowest objective value. Panels b), d), and f) show the parameter distributions for the empirical models, with the mean (black line), standard deviation (box), range (whiskers), bounds (limits), and best-performing values (green circle and number). Panel h) shows the SR-derived constitutive expressions with the best-performing expression highlighted in green..... 54

Figure 4.9. Comparison of empirical and symbolic regression (SR) models in reproducing the strain-to-failure from the calibration (green) and validation (red) datasets. Plot a) compares the average relative errors (RE) while plot b) compares the average coefficient of variation (CV)..... 54

Figure 4.10. Experimental correlations between  $\varepsilon m \cdot tf$  and  $\varepsilon f$  for Alloy 617 at 800°C, 900°C, and 1000°C, showing calibration (green) and validation (red) datasets with dashed lines indicating the lines of best fit (LOBF). ..... 55

Figure 4.11. Calibration and validation results for the omega model in predicting the regular strain–time response across five independent runs. Plots a), b), and c) compare the experimental and simulated strain–time curves at 800°C, 900°C, and 1000°C, respectively, for the calibration (green) and validation (red) datasets. Panels d), e), and f) show the model’s parameter distributions, with the mean (black line), standard deviation (box), range (whiskers), bounds (limits), and best-performing values (green circle and number). ..... 56

Figure 4.12. Calibration and validation results for the symbolic regression (SR) model in predicting the regular strain–time response across five independent runs. Plots a), b), and c) compare the experimental and simulated strain–time curves at 800°C, 900°C, and 1000°C, respectively, for the calibration (green) and validation (red) datasets. Panel d) shows the SR-derived constitutive expressions with the best-performing expression highlighted in green..... 56

Figure 4.13. Comparison of empirical and symbolic regression (SR) models in reproducing the regular strain–time responses from the calibration (green) and validation (red) datasets. Plot a) compares the average relative errors (RE) while plot b) compares the average coefficient of variation (CV)..... 57

Figure 4.14. Calibration and validation results for the omega model in predicting the mechanism-shifted strain–time response across five independent runs. Plots a), b), and c) compare the experimental and simulated strain–time curves at 800°C, 900°C, and 1000°C, respectively, for the calibration (green) and validation (red)

datasets. Panels d), e), and f) show the model's parameter distributions, with the mean (black line), standard deviation (box), range (whiskers), bounds (limits), and best-performing values (green circle and number)..... 58

Figure 4.15. Calibration and validation results for the symbolic regression (SR) model in predicting the mechanism-shifted strain–time response across five independent runs. Plots a), b), and c) compare the experimental and simulated strain–time curves at 800°C, 900°C, and 1000°C, respectively, for the calibration (green) and validation (red) datasets. Panel d) shows the SR-derived constitutive expressions with the best-performing expression highlighted in green..... 59

Figure 4.16. Comparison of empirical and symbolic regression (SR) models in reproducing the mechanism-shifted strain–time responses from the calibration (green) and validation (red) datasets. Plot a) compares the average relative errors (RE) while plot b) compares the average coefficient of variation (CV)..... 59

Figure 4.17. Supplementary calibration and validation results for the symbolic regression (SR) model in predicting the mechanism-shifted strain–time response across five independent runs using renormalised time values. Plots a), b), and c) compare the experimental and simulated strain–time curves at 800°C, 900°C, and 1000°C, respectively, for the calibration (green) and validation (red) datasets. Panel d) shows the SR-derived constitutive expressions with the best-performing expression highlighted in green. .... 60

Figure 4.18. Comparison of the computational requirements for the calibration of the empirical models (in blue) and symbolic regression (SR) models (in orange), averaged across five independent runs. The costs were calculated for the predictions of the minimum creep rate, time-to-failure, strain-to-failure, regular strain–time response, and mechanism-shifted strain–time response. .... 62

Figure 5.1. Annotated plots of the experimental tensile data of Alloy 617 from the Idaho National Laboratory at a) 800°C, b) 900°C, and c) 1000°C. ..... 66

Figure 5.2. Flowchart of multi-objective three-stage calibration workflow. .... 70

Figure 5.3. Schematics of an experimentally observed and simulated a) creep curve and b) tensile curve, annotated with the discrepancies that the implemented objective functions aim to minimise. .... 71

Figure 5.4. Calibration results for the EVP-CD model at 800°C, calibrated with short-term creep curves (70MPa and 80MPa) and tensile curve, and validated with longer-term creep curves (60MPa and 65MPa). The top row of plots (a, c, e) shows the creep results while the bottom row of plots (b, d, and f) shows the tensile results after stages 1, 2, and 3. The experimental datasets are in grey, the simulated curves used for calibration are in green, and the simulated curves used for validation are in red. The boxplots (g) show the distribution of the found parameters, where  $x^*$  represents the optimal parameter value, the vertical line represents the mean, the boxes represent the standard deviations, and the whiskers represent the ranges. .... 74

Figure 5.5. Calibration results for the EVP-WD model at 800°C, calibrated with short-term creep curves (70MPa and 80MPa) and tensile curve, and validated with longer-term creep curves (60MPa and 65MPa). The top row of plots (a, c, e) shows the creep results while the bottom row of plots (b, d, and f) shows the tensile results after stages 1, 2, and 3. The experimental datasets are in grey, the simulated curves used for calibration are in green, and the simulated curves used for validation are in red. The boxplots (g) show the distribution of the found parameters, where  $x^*$  represents the optimal parameter value, the vertical line represents the mean, the boxes represent the standard deviations, and the whiskers represent the ranges. .... 76

Figure 5.6. Assessment of simulated material properties by the EVP-CD model (orange) and EVP-WD model (blue) at 800°C, 900°C, and 1000°C. The plots in a), b), c), and d) compare the total creep deformation, minimum

creep rate, time-to-failure, and strain-to-failure of the experimental and simulated creep curves. The plots in e), f), g), and h) compare the toughness, yield stress, maximum tensile stress, and strain-at-ductility of the experimental and simulated tensile curves.....	79
Figure 6.1. Images of the experimental data acquisition — a) dimensioned drawing of the specimen, b) photograph of the specimen in the loading stage, c) SEM micrograph of the specimen in the loading stage, and d) initial EBSD map shown as IPF- $x$ coloured map.....	85
Figure 6.2. Comparison of the recorded true stress–strain curves obtained during the in-situ EBSD experiment on the miniaturised tensile specimen (Figure 6.1) and on a standard tensile specimen [77]. Dashed blue lines indicate the stress–strain positions at which the EBSD datasets were collected (Figure C.1).....	85
Figure 6.3. Selected grains ( $g1..16$ ) on the a) initial EBSD map ( $\varepsilon = 0.0\%$ ) and b) final EBSD map ( $\varepsilon = 29.0\%$ ) shown as IPF- $x$ coloured maps.....	86
Figure 6.4. Inverse pole figures (IPFs) of the raw and SLERP-smoothened reorientation trajectories of grains a) $g1..8$ and b) $g9..16$ in the $x$ -direction.....	87
Figure 6.5. IPF- $x$ coloured maps of a) the low-fidelity mesh (top and side view), b) the high-fidelity mesh (top and side view), and c) the low-fidelity mesh (angled view). .....	87
Figure 6.6. Flow chart of the multi-objective surrogate-assisted calibration workflow. ....	93
Figure 6.7. Discrepancies between the surrogate model approximations and the low-fidelity VH simulations across five calibration runs using an initial dataset size of 8. Plot a) shows the discrepancies in the stress–strain response (%) while plot b) shows the discrepancies in the reorientation trajectories (°). Each plot shows the discrepancies (black line), accuracy threshold (blue dashed line), and the termination cycle (red circle) for each calibration run. ....	95
Figure 6.8. Comparison of the surrogate model approximations and the low-fidelity VH simulations, with the experimental data in grey, the approximations in black, and the VH responses in red. These plots compare the a) stress–strain responses and b) reorientation trajectories of $g1..8$ , including the corresponding objective values ( $E\sigma$ and $E\Phi$ from Eqs. (41) and (51)).....	96
Figure 6.9. Calibration and validation results for the VH formulation after five runs, comparing the experimental data in grey with the simulated responses in green (all runs) and red (best run). The plots in the top row compare the a) stress–strain responses (calibration), b) reorientation trajectories of $g1..8$ (calibration), and c) reorientation trajectories of $g9..16$ (validation), including the corresponding objective values ( $E\sigma$ and $E\Phi$ from Eqs. (41) and (51)). The plots in the bottom row compare the overall texture evolution (validation) using d) contoured 111 pole figures at $\varepsilon = 0.0\%, 10.6\%,$ and $29.0\%$ , and e) texture indexes over $0.0\%$ to $29.0\%$ .....	97
Figure 6.10. Calibration and validation results for the LH2 formulation after five runs, comparing the experimental data in grey with the simulated responses in green (all runs) and red (best run). The plots in the top row compare the a) stress–strain responses (calibration), b) reorientation trajectories of $g1..8$ (calibration), and c) reorientation trajectories of $g9..16$ (validation), including the corresponding objective values ( $E\sigma$ and $E\Phi$ from Eqs. (41) and (51)). The plots in the bottom row compare the overall texture evolution (validation) using d) contoured 111 pole figures at $\varepsilon = 0.0\%, 10.6\%,$ and $29.0\%$ , and e) texture indexes over $0.0\%$ to $29.0\%$ .....	97

Figure 6.11. Calibration and validation results for the LH6 formulation after five runs, comparing the experimental data in grey with the simulated responses in green (all runs) and red (best run). The plots in the top row compare the a) stress-strain responses (calibration), b) reorientation trajectories of  $g1..8$  (calibration), and c) reorientation trajectories of  $g9..16$  (validation), including the corresponding objective values ( $E\sigma$  and  $E\Phi$  from Eqs. (41) and (51)). The plots in the bottom row compare the overall texture evolution (validation) using d) contoured 111 pole figures at  $\varepsilon = 0.0\%$ ,  $10.6\%$ , and  $29.0\%$ , and e) texture indexes over  $0.0\%$  to  $29.0\%$ ..... 98

Figure 6.12. Comparison of the low-fidelity responses of the three CPFEM models, with the experimental data in grey, the VH responses in cyan, the LH2 responses in orange, and the LH6 responses in purple. The plots in the top row compare the a) stress-strain responses (calibration), b) reorientation trajectories of  $g1..8$  (calibration), and c) reorientation trajectories of  $g9..16$  (validation), including the corresponding objective values ( $E\sigma$  and  $E\Phi$  from Eqs. (41) and (51)). The plots in the bottom row compare the overall texture evolution (validation) using d) contoured 111 pole figures at  $\varepsilon = 0.0\%$ ,  $10.6\%$ , and  $29.0\%$ , and e) texture indexes over  $0.0\%$  to  $29.0\%$ ..... 100

Figure 6.13. Boxplots of the optimised parameters for the a) VH formulation, b) LH2 formulation, and c) LH6 formulation across five calibration runs, showing the mean (black horizontal line), standard deviation (box), range (whiskers), and bounds (limits). The knee-point values are overlaid as red circles, with their exact values annotated on the right..... 101

Figure 6.14. Supplementary calibration and validation results for the VH formulation after five single-objective runs, comparing the experimental data in grey with the simulated responses in green (all runs) and red (best run). The plots in the top row compare the a) stress-strain responses (calibration), b) reorientation trajectories of  $g1..8$  (validation), and c) reorientation trajectories of  $g9..16$  (validation), including the corresponding objective values ( $E\sigma$  and  $E\Phi$  from Eqs. (41) and (51)). The plots in the bottom row compare the overall texture evolution (validation) using d) contoured 111 pole figures at  $\varepsilon = 0.0\%$ ,  $10.6\%$ , and  $29.0\%$ , and e) texture indexes over  $0.0\%$  to  $29.0\%$ ..... 103

Figure 6.15. Supplementary boxplots of the optimised parameters for the VH formulation across five single-objective calibration runs, showing the mean (black horizontal line), standard deviation (box), range (whiskers), and bounds (limits). The knee-point values are overlaid as red circles, with their exact values annotated on the right..... 104

Figure 6.16. Comparison of the low- and high-fidelity responses from the VH formulation, with the experimental data in grey, the low-fidelity responses in red, and the high-fidelity responses in blue. The plots in the top row compare the a) stress-strain responses (calibration), b) reorientation trajectories of  $g1..8$  (calibration), and c) reorientation trajectories of  $g9..16$  (validation), including the corresponding objective values ( $E\sigma$  and  $E\Phi$  from Eqs. (41) and (51)). The plots in the bottom row compare the overall texture evolution (validation) using d) contoured 111 pole figures at  $\varepsilon = 0.0\%$ ,  $10.6\%$ , and  $29.0\%$ , and e) texture indexes over  $0.0\%$  to  $29.0\%$ ..... 105

Figure 6.17. Comparison of the low- and high-fidelity responses from the LH2 formulation, with the experimental data in grey, the low-fidelity responses in red, and the high-fidelity responses in blue. The plots in the top row compare the a) stress-strain responses (calibration), b) reorientation trajectories of  $g1..8$  (calibration), and c) reorientation trajectories of  $g9..16$  (validation), including the corresponding objective

values ( $E\sigma$  and  $E\Phi$  from Eqs. (41) and (51)). The plots in the bottom row compare the overall texture evolution (validation) using d) contoured 111 pole figures at  $\varepsilon = 0.0\%$ , 10.6%, and 29.0%, and e) texture indexes over 0.0% to 29.0%..... 106

Figure 6.18. Comparison of the low- and high-fidelity responses from the LH6 formulation, with the experimental data in grey, the low-fidelity responses in red, and the high-fidelity responses in blue. The plots in the top row compare the a) stress-strain responses (calibration), b) reorientation trajectories of  $g1..8$  (calibration), and c) reorientation trajectories of  $g9..16$  (validation), including the corresponding objective values ( $E\sigma$  and  $E\Phi$  from Eqs. (41) and (51)). The plots in the bottom row compare the overall texture evolution (validation) using d) contoured 111 pole figures at  $\varepsilon = 0.0\%$ , 10.6%, and 29.0%, and e) texture indexes over 0.0% to 29.0%..... 106

Figure A.1. Supplementary calibration and validation results for the symbolic regression (SR) models in predicting the minimum creep rate, time-to-failure, and log-transformed strain-to-failure across five independent runs. Plots a), c), and e) compare the experimental and simulated values for the calibration (green) and validation (red) datasets, with the dashed lines representing the line of best fit (LOBF) corresponding to the run that achieved the lowest objective value. Panels b), d), and f) show the SR-derived constitutive expressions with the best-performing expression highlighted in green..... 140

Figure A.2. Calibration and validation results for the phi model in predicting the regular strain–time response across five independent runs. Plots a), b), and c) compare the experimental and simulated strain–time curves at 800°C, 900°C, and 1000°C, respectively, for the calibration (green) and validation (red) datasets. Panels d), e), and f) show the model’s parameter distributions, with the mean (black line), standard deviation (box), range (whiskers), bounds (limits), and best-performing values (green circle and number)..... 141

Figure A.3. Calibration and validation results for the theta projection model in predicting the regular strain–time response across five independent runs. Plots a), b), and c) compare the experimental and simulated strain–time curves at 800°C, 900°C, and 1000°C, respectively, for the calibration (green) and validation (red) datasets. Panels d), e), and f) show the model’s parameter distributions, with the mean (black line), standard deviation (box), range (whiskers), bounds (limits), and best-performing values (green circle and number)..... 141

Figure A.4. Calibration and validation results for the phi model in predicting the mechanism-shifted strain–time response across five independent runs. Plots a), b), and c) compare the experimental and simulated strain–time curves at 800°C, 900°C, and 1000°C, respectively, for the calibration (green) and validation (red) datasets. Panels d), e), and f) show the model’s parameter distributions, with the mean (black line), standard deviation (box), range (whiskers), bounds (limits), and best-performing values (green circle and number)..... 142

Figure A.5. Calibration and validation results for the theta projection model in predicting the mechanism-shifted strain–time response across five independent runs. Plots a), b), and c) compare the experimental and simulated strain–time curves at 800°C, 900°C, and 1000°C, respectively, for the calibration (green) and validation (red) datasets. Panels d), e), and f) show the model’s parameter distributions, with the mean (black line), standard deviation (box), range (whiskers), bounds (limits), and best-performing values (green circle and number)..... 143

Figure B.1. Critical plastic work density and logarithmic average plastic work density rate of experimental creep and tensile data of Alloy 617; the creep and tensile relationships are represented in green and red, respectively..... 145

Figure B.2. Schematics of a) critical plastic work density and the b) damage exponent the piecewise functions.	146
Figure B.3. Calibration results for the EVP-CD model at 900°C, calibrated with short-term creep curves (36MPa and 31MPa) and tensile curve, and validated with longer-term creep curves (28MPa and 26MPa). The top row of plots (a, c, e) shows the creep results while the bottom row of plots (b, d, and f) shows the tensile results after stages 1, 2, and 3. The experimental datasets are in grey, the simulated curves used for calibration are in green, and the simulated curves used for validation are in red. The boxplots (g) show the distribution of the found parameters, where $x^*$ represents the optimal parameter value, the vertical line represents the mean, the boxes represent the standard deviations, and the whiskers represent the ranges. ....	147
Figure B.4. Calibration results for the EVP-CD model at 1000°C, calibrated with short-term creep curves (16MPa and 13MPa) and tensile curve, and validated with longer-term creep curves (12MPa and 11MPa). The top row of plots (a, c, e) shows the creep results while the bottom row of plots (b, d, and f) shows the tensile results after stages 1, 2, and 3. The experimental datasets are in grey, the simulated curves used for calibration are in green, and the simulated curves used for validation are in red. The boxplots (g) show the distribution of the found parameters, where $x^*$ represents the optimal parameter value, the vertical line represents the mean, the boxes represent the standard deviations, and the whiskers represent the ranges. ....	148
Figure B.5. Calibration results for the EVP-WD model at 900°C, calibrated with short-term creep curves (36MPa and 31MPa) and tensile curve, and validated with longer-term creep curves (28MPa and 26MPa). The top row of plots (a, c, e) shows the creep results while the bottom row of plots (b, d, and f) shows the tensile results after stages 1, 2, and 3. The experimental datasets are in grey, the simulated curves used for calibration are in green, and the simulated curves used for validation are in red. The boxplots (g) show the distribution of the found parameters, where $x^*$ represents the optimal parameter value, the vertical line represents the mean, the boxes represent the standard deviations, and the whiskers represent the ranges. ....	148
Figure B.6. Calibration results for the EVP-WD model at 1000°C, calibrated with short-term creep curves (16MPa and 13MPa) and tensile curve, and validated with longer-term creep curves (12MPa and 11MPa). The top row of plots (a, c, e) shows the creep results while the bottom row of plots (b, d, and f) shows the tensile results after stages 1, 2, and 3. The experimental datasets are in grey, the simulated curves used for calibration are in green, and the simulated curves used for validation are in red. The boxplots (g) show the distribution of the found parameters, where $x^*$ represents the optimal parameter value, the vertical line represents the mean, the boxes represent the standard deviations, and the whiskers represent the ranges. ....	149
Figure C.1. Electron backscatter diffraction (EBSD) maps of the Alloy 617 specimen shown as IPF- $\bar{x}$ coloured maps.....	150
Figure C.2. Simulated deformation of the high-fidelity finite element mesh using the Voce hardening (VH) model shown as IPF- $\bar{x}$ coloured maps.....	151
Figure C.3. Pseudocode for the grain tracking algorithm. ....	152
Figure C.4. Evolution of the grains selected for calibration ( $g1..8$ ) and validation ( $g9..16$ ) at $\varepsilon = 0.0\%, 5.2\%, 10.6\%, 20.8\%$ , and $29.0\%$ . ....	153
Figure C.5. Plots of the changes in the morphology of the FE models across different resolutions (5 $\mu m$ to 45 $\mu m$ ). Plot a) shows the number of grains in FE models, while plots b) and c) show the lognormal	

distributions of the equivalent radius and circularity of the grains, respectively. The mean and standard deviation of the lognormal distributions are indicated in the legend.....	154
Figure C.6. Plots of the changes in the VH simulation results of the FE models across different resolutions (10 $\mu m$ to 45 $\mu m$ ). Plot a) shows the $E\sigma$ (%) distribution in the stress-strain response while plot b) shows the $E\phi$ ( $^{\circ}$ ) distribution in the reorientation trajectories compared to the 5 $\mu m$ reference FE model, where the vertical lines represent the means, the boxes represent the standard deviations, and the whiskers represent the ranges. Plot c) shows the average evaluation time at each resolution.....	155
Figure C.7. Plots of the discrepancies between the low- and high-fidelity VH-simulated responses with the discrepancies between the low-fidelity VH-simulated responses and experimental data. The discrepancies were calculated for a) the stress-strain response using $E\sigma$ (%) and b) the reorientation trajectories using $E\phi$ ( $^{\circ}$ ) ..	156
Figure C.8. Results from the Pareto front of the final population of a MOGA optimisation performed on the surrogate model for the VH formulation. Panel a) presents the normalised objective values ( $E\sigma$ and $E\phi$ ), showing the Pareto-dominated solutions (grey), Pareto-efficient solutions (green), and knee point solution (red). Panels b) and c) present the stress-strain response and reorientation trajectories of g1..8 predicted by the surrogate model, comparing the experimental data (grey), Pareto-efficient solutions (green), and knee point solution (red). ....	157
Figure C.9. Plot of the total number of evaluations to calibrate the Voce hardening (VH) model with the adaptive surrogate-assisted calibration workflow using various initial dataset sizes. ....	158
Figure C.10. Comparison of the computational requirements for the calibration of the VH formulation (in cyan), LH2 formulation (in orange), and LH6 formulation (in purple). The average costs for the initial evaluations are represented by single-hashed bars while the costs for the additional evaluations are represented by plain bars. ....	159
Figure C.11. Supplementary calibration and validation results for the VH formulation after five runs, comparing the experimental data in grey with the simulated responses in green (all runs) and red (best run). The plots in the top row compare the a) stress-strain responses (calibration), b) reorientation trajectories of g1..8 (validation), and c) reorientation trajectories of g9..16 (calibration), including the corresponding objective values ( $E\sigma$ and $E\Phi$ from Eqs. (41) and (51)). The plots in the bottom row compare the overall texture evolution (validation) using d) contoured 111 pole figures at $\varepsilon = 0.0\%$ , 10.6%, and 29.0%, and e) texture indexes over 0.0% to 29.0%. ....	160

## List of tables

Table 2.1. Summary of latent hardening interactions in the single-crystal deformation of face-centred cubic (FCC) materials. ....	9
Table 2.2. Summary of research gaps in the literature.....	35
Table 3.1. Summary of research objectives for the thesis.....	37
Table 4.1. Chemical composition of solution-annealed plate of Alloy 617 Heat 314626 in weight percent [85]. .....	41
Table 4.2. Summary of experimental creep data of Alloy 617 from Idaho National Laboratory. ....	42
Table 5.1. Summary of experimental tensile data of Alloy 617 from Idaho National Laboratory. ....	66
Table A.1. Summary of adjustable constitutive parameters for empirical creep models. ....	138
Table B.1. Summary of material parameters for EVP, EVP-CD, and EVP-WD models.....	144
Table B.2. Material parameters from the best calibration run for the EVP-CD model at 800°C, 900°C, and 1000°C. ....	149
Table B.3. Material parameters from the best calibration run for the EVP-WD model at 800°C, 900°C, and 1000°C. ....	149
Table C.1. Summary of constitutive parameters for the Voce hardening (VH), two-coefficient latent hardening (LH2), and six-coefficient latent hardening (LH6) formulations. ....	156

## List of abbreviations

ANN	=	Artificial neural network
ASME	=	American society of mechanical engineers
ASTM	=	American Society for Testing and Materials
BCC	=	Body-centred cubic
BPVC	=	Boiler pressure vessel code
BSE	=	Backscatter electron
CD	=	Creep damage
CNN	=	Convolutional neural network
CP	=	Crystal plasticity
CPFEM	=	Crystal plasticity finite element method
CRSS	=	Critical resolved shear stress
CV	=	Coefficient of variation
EBSD	=	Electron backscatter diffraction
EVP	=	Elastic viscoplastic
FCC	=	Face-centred cubic
FE	=	Finite element
FEM	=	Finite element method
FFNN	=	Feed-forward neural network
GA	=	Genetic algorithm
HCP	=	Hexagonal close-packed
HEM	=	Homogeneous equivalent medium
HTGR	=	High-temperature gas-cooled reactor
INL	=	Idaho National Laboratory
IPF	=	Inverse pole figure
KR	=	Kachanov-Rabotnov
LHS	=	Latin hypercube sampling
LH2	=	Two-coefficient latent hardening
LH6	=	Six-coefficient latent hardening
LOBF	=	Line of best fit
MOGA	=	Multi-objective genetic algorithm
MOO	=	Multi-objective optimisation
MOOSE	=	Multi-physics object-oriented simulation environment
ND	=	Normal direction
NEML	=	Nuclear engineering material model library
NRMSE	=	Normalised root mean square error
NSGA	=	Non-dominated sorting genetic algorithm-II
PF	=	Pole figure
RBF	=	Radial basis function
RD	=	Rolling direction

RE	=	Relative error
RNN	=	Recurrent neural network
ROM	=	Reduced order model
RSS	=	Resolved shear stress
RVE	=	Representative volume element
SD	=	Standard deviation
SE	=	Secondary electron
SEM	=	Scanning electron microscope
SLERP	=	Spherical linear interpolation
SR	=	Symbolic regression
TD	=	Transverse direction
TEM	=	Transmission electron microscopy
UTS	=	Ultimate tensile stress
VDM	=	Vereinigte Deutsch Metallwerke
VH	=	Voce hardening
VHTR	=	Very high temperature reactor
WD	=	Work damage

# Chapter 1

## Introduction

Alloy 617 is a solid solution strengthened Ni-Cr-Co alloy used in applications across various industries [1]. The alloy offers an exceptional combination of thermal, mechanical, physical, and corrosion-resistant properties that make it a desirable choice for many engineering applications. It maintains high strength and excellent creep resistance at elevated temperatures. In addition, its corrosion resistance supports applications in chemical processing environments [2, 3], while its high ductility and toughness at lower temperatures allow for use in certain cryogenic systems [4]. These properties allow Alloy 617 to perform reliably across a broad temperature range, expanding its versatility in critical engineering applications. In particular, the nuclear industry is pursuing the alloy as structural material for intermediate heat exchangers in the next generation (Gen IV) of nuclear reactor systems [5], which are expected to operate at significantly higher temperatures (750°C) [1, 6, 7] than the current fleet of nuclear reactor systems (300°C). The aerospace industry also employs Alloy 617 in the combustion chambers and exhaust systems of gas turbines due to the alloy's ability to withstand thermal and mechanical stresses [8-10]. As such, the ability to predict the behaviour of Alloy 617 is of technological importance for ensuring the safe and reliable operation of these crucial systems.

Over the years, many material models have been developed to predict the deformation behaviour of alloys in operational, in-service conditions. Empirical material models like Norton's power law [11], the theta projection model [12, 13], and Hollomon's equation [14] use simplified mathematical equations to establish relationships between measurable material responses. These models are widely used due to their simple definitions and low-computational loads [15]. However, these models neglect the material's underlying mechanisms, limiting their ability to precisely describe the ongoing deformation and degradation of materials under operating in-service conditions. Furthermore, these simple models are prone to over-conservatism and require a large number of experimental data [15, 16]. Semi-empirical material models improve upon empirical models by connecting deformation behaviour to physical phenomena that take place within the material. Well-established examples include the Kachanov-Rabotnov model [17, 18], ductility exhaustion models [19-21], and elastic-viscoplastic (EVP) models [22-25]. These models can consider the entire deformation life of the material, capture multiple loading modes, and require less experimental data to calibrate. However, semi-empirical models are still heavily influenced by the trends in the experimental data, which can result in over-conservatism and the poor capturing of mechanism shifts [15, 26]. Physics-based models, such as crystal plasticity finite element method (CPFEM) models, aim to address these issues by considering microstructural heterogeneities and grain-to-grain interactions to account for complex deformation and accumulation mechanisms. By integrating detailed microstructural information, these physics-based models can potentially provide enhanced accuracy and richer mechanistic insight [16]. However, they are significantly more complex and computationally expensive, posing challenges for their use in practical engineering applications [16, 27].

Material models require calibration against experimental data to ensure that their simulated responses accurately reflect the observed material behaviour. This calibration process involves the numerical identification of the constitutive material parameters that govern the material's behaviour. Traditionally, manual trial-and-

error methods were employed to calibrate material models. However, these methods are often subjective, time-consuming, and heavily dependent on prior knowledge of the constitutive parameters. This is especially true for semi-empirical and physics-based models with complex theoretical frameworks and expansive parameter spaces [16, 27, 28]. To address these issues, various optimisation algorithms have been employed to automate and streamline the calibration process. These optimisation algorithms vary in search scope, with local algorithms focusing on a limited region of the parameter space and global algorithms exploring the entire space. These algorithms also vary in navigation strategy, with gradient-based algorithms relying on derivatives to find optimal parameter values and direct-search algorithms relying on alternative derivative-free strategies [15, 29]. The choice of optimisation algorithms is crucial in the calibration of semi-empirical and physics-based models, since these models typically have complex, high-dimensional parameter spaces with interdependent constitutive parameters that reflect physical phenomena [30-33]. Due to this complexity, global optimisation algorithms are better equipped to explore the parameter space and capture the intricate relationships between the parameters. In addition, direct-search algorithms can provide a more robust exploration approach that does not rely on gradient information, since noise in the experimental data will likely deteriorate convergence behaviour [27]. A notable example of a global, direct-search optimisation algorithms is the genetic algorithm (GA), which has been used extensively to identify the constitutive parameter in various crystal plasticity constitutive laws [27, 33, 34]. However, a major limitation inherent in optimisation algorithms is that they require a substantial number of evaluations to achieve convergence, which can be prohibitive for complex models with high computational cost. As such, the calibration of semi-empirical and physics-based material models requires specialised optimisation techniques to remain computationally feasible for engineering applications.

This thesis is composed of three research studies focusing on the development and calibration of material models to capture the creep and tensile behaviour of Alloy 617. In the first study, twelve established empirical material models were calibrated to predict key creep characteristics and the overall strain–time response. In parallel, symbolic regression (SR) was applied to automatically discover constitutive expressions to predict the same target responses, enabling a direct comparison between the empirical and SR models. In the second study, two semi-empirical models were calibrated using a multi-objective three-stage calibration workflow to capture the elevated-temperature creep and tensile behaviour of Alloy 617. The two semi-empirical models employed a temperature-dependent EVP constitutive model that was coupled with either a classical creep damage (CD) or work-based damage (WD) model to capture the failure response. In the third study, three physics-based models were calibrated using a multi-objective surrogate-assisted calibration workflow to capture the multiscale behaviour of Alloy 617. The physics-based models employed the CPFEM framework using three different hardening models, namely a Voce hardening (VH) model, a two-coefficient latent hardening (LH2) model, and a six-coefficient latent hardening (LH6) model. The results of the three studies were then compared to assess the predictive accuracy, robustness, generalisability, interpretability, and calibration difficulty of the different material modelling frameworks.

# Chapter 2

## Literature review

To provide the necessary context for the present work, a comprehensive literature review was conducted. This review begins by examining the structure (Section 2.1), deformation behaviour (Section 2.2), and experimental testing methods (Section 2.3) of metallic materials, with particular emphasis on Alloy 617. It then presents an overview of empirical, semi-empirical, and physics-based material models used to predict material behaviour (Section 2.4), and outlines their calibration using optimisation algorithms (Section 2.5). The review continues by introducing surrogate modelling techniques for reducing the computational cost of calibrating complex material models (Section 2.6), as well as symbolic regression for the automated discovery of constitutive expressions (Section 2.7). Finally, the review concludes by summarising the key insights and existing gaps in the literature to frame the motivation of the presented research (Section 2.8).

### 2.1. Structure of metals

The behaviour and performance of metals are fundamentally governed by their crystalline structure and microstructural features. These characteristics determine key properties such as strength, ductility, thermal stability, and corrosion resistance, which are critical for a wide range of demanding engineering applications. As such, the following section first examines the hierarchical structure of crystalline materials (Section 2.1.1) and explores relevant microstructural features, such as phases, solid solutions, and precipitates (Section 2.1.2). The section then provides an overview of Alloy 617, highlighting its composition, microstructure, and properties that enable its role across diverse applications (Section 2.1.3).

#### 2.1.1. Structural hierarchy

The structural hierarchy of crystalline materials begins with the unit cell, which describes the structural arrangement of constituent particles (i.e., atoms, molecules, or ions) in the material. In metals, the most common structural arrangements (i.e., crystal structures) include body-centred cubic (BCC), face-centred cubic (FCC), and hexagonal close-packed (HCP). Schematics of these crystal structures are shown in Figure 2.1, with the nodes representing the constituents and the edges representing the dimensions of the unit cell.

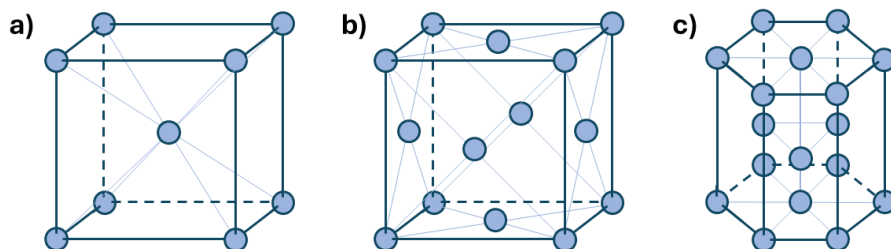


Figure 2.1. Schematics of common crystal structures of metals, namely a) body-centred cubic (BCC), b) face-centred cubic (FCC), and c) hexagonal close-packed (HCP).

These unit cells repeat in a regular, highly ordered, three-dimensional pattern to form a crystal lattice. Most engineering materials are polycrystalline, meaning that the lattice is not continuous throughout the material.

Instead, the lattice is divided into individual crystalline regions, known as grains (or crystals), each with a distinct orientation (i.e., crystallographic orientation). The interfaces between the grains are known as grain boundaries, where the crystallographic orientations change abruptly. The size, shape, and distribution of the grains (i.e., grain morphology) can influence the mechanical properties of the material, such as strength, toughness, and ductility. The distribution of crystallographic orientations (i.e., crystallographic texture) can also influence properties such as thermal conductivity, magnetism, void growth, and hardness [35, 36].

### 2.1.2. Microstructural features

The microstructure of a metal describes the size, shape, and distribution of its internal constituents at the microscopic scale. These constituents often organise into distinct phases, which are regions with specific crystal structures, atomic arrangements, and chemical compositions [37, 38]. The primary phase is the dominant phase, which constitutes the bulk of the metal and typically has a homogeneous composition with uniform properties. Secondary phases are additional phases that form within the metal through processes such as alloying, heat treatment, and solidification. Intermediate phases exist between the primary and secondary phases, resulting from partial reactions, phase transformations, and alloying effects. When a metal is subjected to temperature changes (e.g., heating or cooling), it can undergo phase transformations, often altering the material's mechanical behaviour and stability.

Within these phases, metals can form solid solutions, in which solute atoms are incorporated into the crystal lattice of the solvent to create a single-phase crystalline structure [38, 39]. Solid solutions can be substitutional, where the comparably sized solute atoms replace solvent atoms, or interstitial, where smaller solute atoms occupy spaces between the solvent atoms [37]. These solute atoms distort the lattice and create local stress fields, affecting properties such as hardness, strength, and thermal stability [37]. Solid solutions can also be ordered, where solute atoms uniformly occupy well-defined lattice sites, or disordered, where solute atoms are randomly distributed. Ordered structures typically exhibit precise, anisotropic behaviour, while disordered structures generally exhibit enhanced ductility, processability, and toughness. The structural order of metals can change when undergoing processes such as deformation, phase transformations, or heat treatments.

When the solubility of solute atoms in a solid solution exceeds the equilibrium limit, the undissolved solute particles cluster together and attract more solute atoms [37]. The aggregation of these particles forms precipitates, which are solid second-phase particles that consist predominantly of the solute atoms. Precipitates can be promoted to strengthen the alloy through heat treatment processes such as ageing and annealing. The coherency of a precipitate describes the degree to which the precipitate matches the surrounding solvent lattice [40]. Coherent precipitates generally have similar crystal structures and lattice parameters as the solvent, which creates a smooth and continuous interface. Smaller precipitates usually have coherent interfaces with the solvent lattice, resulting in minimal distortion at the interface that allows for more efficient stress transfer during deformation.

### 2.1.3. Alloy 617

Alloy 617 is a nickel-based alloy (Ni-22Cr-10Co-9Mo) that consists of two major phases, namely the  $\gamma$  and  $\gamma'$  phases [41]. The  $\gamma$  phase is a solid solution phase composed mainly of nickel, chromium, cobalt, and molybdenum, with a disordered FCC crystal structure. The  $\gamma'$  phase is a precipitating phase primarily comprising

nickel and aluminium, with an ordered FCC structure. Alloy 617 is predominantly strengthened through the solid-solution strengthening of the  $\gamma$  phase by cobalt and molybdenum [42]. The slight differences in atomic size and electronegativity (i.e., ability to attract shared electrons) distort the crystal lattice, which hinders the movement of dislocations (i.e., irregularities in the lattice) and strengthens the alloy. Alloy 617 is also precipitation strengthened by the presence of second-phase particles such as  $\gamma'$  precipitates and carbides, which obstruct dislocation motion in the narrow  $\gamma$  channels due to anti-phase boundary shearing and Orowan looping [41-43]. Notably, the  $\gamma'$  phase tends to dissolve into the  $\gamma$  phase at temperatures above 900°C [42, 44, 45], reducing its contribution to precipitation strengthening under elevated-temperature conditions. Figure 2.2 presents an optical micrograph of a typical Alloy 617 microstructure, reproduced from Haribabu *et al.* [46].

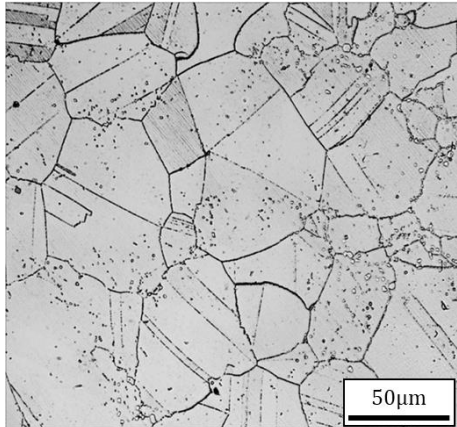


Figure 2.2. Optical micrograph of a typical Alloy 617 microstructure, adapted from Haribabu *et al.* [46] by permission of Springer Nature.

Alloy 617 offers an exceptional combination of thermal, mechanical, and corrosion-resistant properties that make it a desirable choice for many engineering applications. In particular, the nuclear industry is pursuing Alloy 617 as a structural material for intermediate heat exchangers in the next generation (Gen IV) of nuclear reactor systems [5], such as the high-temperature gas-cooled reactor (HTGR) and very high-temperature reactor (VHTR) systems. These advanced reactor systems are designed to cogenerate electricity and industrial heat for the decarbonisation of heavy industries, such as steel, cement, and fertiliser production [47-49]. As a result, they are expected to operate at significantly higher temperatures (750°C) [1, 6, 7] than the current fleet of nuclear reactor systems (300°C). Under Section III Division 5 of the American Society of Mechanical Engineers (ASME) Boiler Pressure Vessel Code (BPVC), Alloy 617 is approved for use in nuclear power applications at temperatures of up to 954°C with a service time limit of 100,000 hours (~11.4 years) [50]. However, nuclear reactors are expected to operate for decades [51], necessitating further investigation into the long-term behaviour of Alloy 617 under extreme conditions, to build upon the current design framework.

The exceptional properties of Alloy 617 extend beyond nuclear power applications. The aerospace industry also employs Alloy 617 in the combustion chambers and exhaust systems of gas turbines due to the alloy's ability to withstand thermal and mechanical stresses [8-10]. Additionally, the alloy's corrosion resistance supports applications in chemical processing environments [2, 3], while its ductility and toughness at lower temperatures allow for use in certain cryogenic systems [4]. In many of these applications, components are subjected to significant temperature gradients which cause different regions of the material to experience distinct thermal

conditions. As such, the ability to predict the deformation and degradation behaviour of Alloy 617 across a broad temperature range is essential for the safe and reliable operation of these crucial systems.

## 2.2. Material deformation

Understanding the deformation behaviour of materials under operational, in-service conditions is essential for ensuring the safety, reliability, and longevity of crucial engineering systems. Accordingly, the following section begins with an overview of elastic and plastic deformation (Section 2.2.1). The section then examines plastic deformation mechanisms in single crystals (Section 2.2.2), as well as the latent hardening mechanisms that govern strength and strain hardening in FCC crystals (Section 2.2.3). The section concludes with an overview of plastic deformation in polycrystals (Section 2.2.4) and the development of texture during deformation (Section 2.2.5).

### 2.2.1. Elastic and plastic deformation

When a stress is applied to a material, it can undergo elastic and plastic deformation. Elastic deformation refers to the temporary change in the shape and size of a material's crystal lattice. When the applied stress is removed, the lattice returns to its original form, which resides in a lower energy state. For most metals, elastic deformation is governed by Hooke's law, which defines a linear relationship between stress and strain. The simplest form of Hooke's law is presented in Eq. (1), where  $\sigma$  is the applied stress,  $\varepsilon$  is the resulting strain, and  $E$  is the elastic modulus. This expression applies to isotropic materials, such as randomly oriented polycrystals, under uniaxial loading conditions.

$$\sigma = E \cdot \varepsilon \quad (1)$$

The generalised form of Hooke's law is expressed in Voigt notation in Eq. (2), where  $\sigma_{ij}$  and  $\varepsilon_{ij}$  represent components of the stress and strain tensors, respectively, and  $C_{ij}$  represents material-dependent elastic constants. This expression is applicable for anisotropic materials, such as single crystals or textured polycrystals, under multiaxial loading.

$$\begin{bmatrix} \sigma_{xx} \\ \sigma_{yy} \\ \sigma_{zz} \\ \sigma_{yz} \\ \sigma_{xz} \\ \sigma_{xy} \end{bmatrix} = \begin{bmatrix} C_{11} & C_{12} & C_{13} & C_{14} & C_{15} & C_{16} \\ C_{21} & C_{22} & C_{23} & C_{24} & C_{25} & C_{26} \\ C_{31} & C_{32} & C_{33} & C_{34} & C_{35} & C_{36} \\ C_{41} & C_{42} & C_{43} & C_{44} & C_{45} & C_{46} \\ C_{51} & C_{52} & C_{53} & C_{54} & C_{55} & C_{56} \\ C_{61} & C_{62} & C_{63} & C_{64} & C_{65} & C_{66} \end{bmatrix} \cdot \begin{bmatrix} \varepsilon_{xx} \\ \varepsilon_{yy} \\ \varepsilon_{zz} \\ \varepsilon_{yz} \\ \varepsilon_{xz} \\ \varepsilon_{xy} \end{bmatrix} \quad (2)$$

Plastic deformation refers to permanent change in the material's form, whereby the crystal lattice does not revert to its original form when the applied force is removed. In crystalline materials, plastic deformation can occur through various mechanisms, such as slip, twinning, and grain boundary sliding. The dominant deformation mechanism depends on several factors such as crystal structure, temperature, strain rate, and grain size. Deformation mechanism maps are commonly used to identify the dominant mechanism under a given stress ( $\sigma$ ) and temperature ( $T$ ). Figure 2.3 presents a mechanism map for Alloy 617 reproduced from Penkalla *et al.* [52], where the stresses are normalised by the shear modulus ( $G$ ) and the temperatures by the melting

point ( $T_m$ ). In this figure, the broken curve represents the range of service conditions encountered in high-temperature gas-cooled reactor (HTGR) systems (Generation IV).

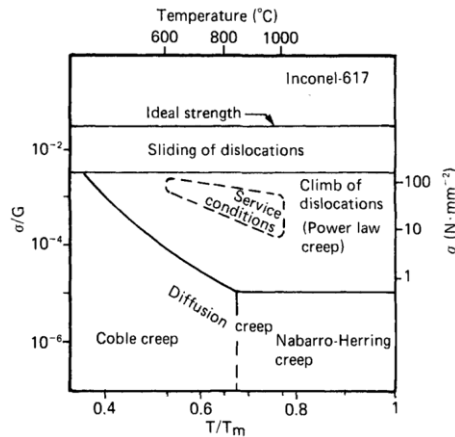


Figure 2.3. Deformation mechanism map of Alloy 617 reproduced from H.-J. Penkalla, H.-H. Over, and F. Schubert, *Constitutive equations for the description of creep and creep rupture behavior of metallic materials at temperatures above 800°C*, Nuclear Technology [52], © 2017. Image reprinted by permission of Informa UK Limited, trading as Taylor & Francis Group, <https://www.tandfonline.com>.

## 2.2.2. Plastic deformation of single crystals

The plastic deformation of single crystals occurs primarily through slip, in which planes of atoms slide past each other under shear stress [53] (Figure 2.4b). Twinning can also occur, in which a portion of the lattice reorients into a mirror-image configuration across a specific plane (Figure 2.4c). However, twinning is generally considered a secondary mechanism, occurring only when slip cannot fully accommodate the applied deformation. In FCC crystals, slip is the dominant mechanism under most conditions, though twinning may occur at high strain rates or low temperatures.

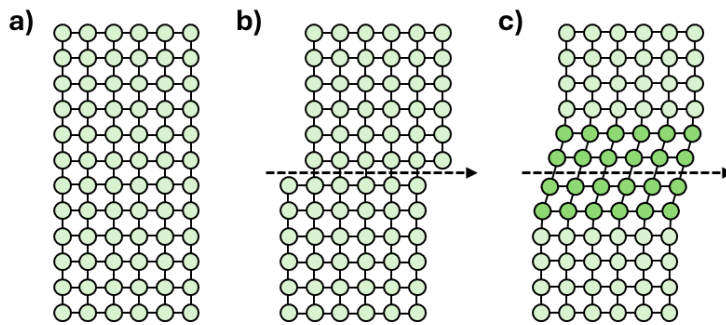


Figure 2.4. Illustrations of a) an undeformed lattice, b) lattice distortion produced by slip, and c) lattice reorientation produced by twinning. The dashed arrows indicate the directions of slip and twinning.

Plastic deformation by slip occurs through the movement of dislocations [54, 55], which are irregularities that disrupt the arrangement of atoms in the crystal lattice. When a shear force is imparted on a crystal lattice that contains dislocations, the dislocations will move through the lattice, continually breaking and reestablishing bonds between the atoms [56]. Dislocation movement causes planes of atoms to slide along each other in a process known as dislocation slip, which permanently deforms the material's crystal lattice [57]. Slip occurs on

specific planes (i.e., slip planes) along specific directions (i.e., slip directions). A slip system is a combination of a slip plane and slip direction [55]. In FCC structures, slip occurs on close-packed planes and directions [55]. Close-packed planes are the planes with the most atoms per unit area, while close-packed directions are the directions with the most atoms per unit length. Since the close-packed planes in FCC structures are of type {111}, FCC structures have four {111} slip planes with six {110} slip directions in each plane. With each slip direction being common to two planes, FCC materials have a total of 12 independent slip systems [55]. An example showing three of the FCC slip systems is presented in Figure 2.5.

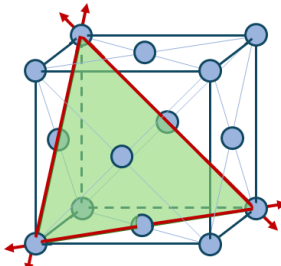


Figure 2.5. Schematic showing three {111}(110) slip systems in a face centred cubic (FCC) crystal structure, where the constituent atoms are shown in blue, the slip plane is shown in green, and the slip directions are shown in red.

In single crystals, slip behaviour is governed by the resolved shear stress (RSS) acting on its slip systems, where the RSS of a given slip system represents the component of the applied stress resolved along its slip plane and direction. Under uniaxial loading conditions, this relationship is described by Schmid's law [58], as shown in Eq. (3), where  $\tau_\alpha$  represents the RSS of the slip system,  $\sigma$  represents the applied stress,  $\phi_\alpha$  represents the angle between the stress direction and the normal of the slip plane, and  $\lambda_\alpha$  represents the angle between the stress direction and slip direction. In this expression, the  $\cos(\phi_\alpha) \cos(\lambda_\alpha)$  term represents the Schmid factor, which determines how effectively the slip system resolves the applied stress.

$$\tau_\alpha = \sigma \cos(\phi_\alpha) \cos(\lambda_\alpha) \quad (3)$$

When a load is applied to a single crystal, the RSS of each slip system will increase until one of them reaches the critical resolved shear stress (CRSS) [59], thereby activating that slip system. This activation initiates plastic deformation, as shown in the annotated schematic in Figure 2.6.

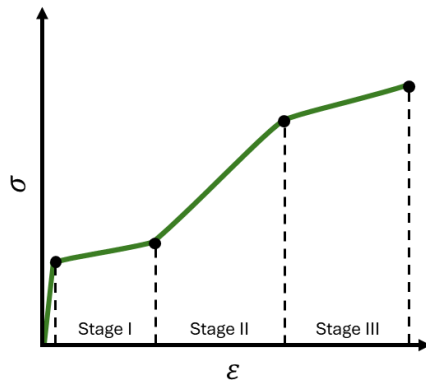


Figure 2.6. Annotated schematic of a typical stress–strain curve of a metal single crystal.

The plastic deformation of an FCC single crystal typically progresses through three distinct stages [60-62]. In the first stage (i.e., easy glide stage), dislocations begin to move along the initially activated (i.e., primary) slip system. During this stage, the crystal is primarily hardened through self-hardening, in which dislocations accumulate and interact within the primary slip system. However, the self-hardening interactions are generally limited, resulting in a low hardening rate. The second stage (i.e., linear hardening stage) begins when additional (i.e., secondary) slip systems are activated. In this stage, self-hardening continues to occur through the accumulation of dislocations within the activated primary and secondary systems. However, the crystal is also hardened through latent hardening, where mobile dislocations from active systems interact with immobile dislocations in inactive systems (i.e., forest dislocations). The combined effects of self- and latent hardening result in an approximately linear hardening rate. The final stage (i.e., saturation stage) occurs at larger strains, in which the dislocation density reaches a critical threshold. In this stage, the crystal undergoes dynamic recovery, whereby dislocations annihilate each other and rearrange themselves into lower-energy configurations. The dynamic recovery mechanisms weaken the self- and latent hardening effects, resulting in a reduced hardening rate.

### 2.2.3. Latent hardening of FCC crystals

The latent hardening effects of FCC crystal structures, such as those in Alloy 617, can be categorised based on the relative orientation of the interacting dislocations, following Franciosi *et al.* [62]. These categories include coplanar, Hirth lock, collinear, glissile, and sessile interactions, as summarised in Table 2.1.

Table 2.1. Summary of latent hardening interactions in the single-crystal deformation of face-centred cubic (FCC) materials.

Interaction	Slip System Relationship	Interaction type	Relative Strength
Coplanar	Coplanar	Non-contact	Weak
Hirth lock	Non-coplanar with normal slip directions	Contact	Moderate
Collinear	Non-coplanar with collinear slip directions	Non-contact	Strong
Glissile junction	Non-coplanar	Contact	Strong
Sessile junction	Non-coplanar	Contact	Strong

Coplanar interactions occur between coplanar slip systems with parallel slip planes and different slip directions. These are considered non-contact interactions, in which the dislocations interact with each other through their long-range stress fields [63]. Since these interactions do not form physical dislocation locks, they contribute minimally to strain hardening [64]. Hirth lock interactions occur between non-coplanar slip systems with normal slip directions. Dislocations from these systems meet at an orthogonal angle, forming weak junctions where dislocations temporarily pin each other, known as Hirth locks [64]. Collinear interactions occur between non-coplanar slip systems with collinear slip directions. Similar to coplanar interactions, collinear interactions are also considered non-contact and do not result in physical dislocation locks. However, the collinearity of the dislocations results in strong, mutually repulsive stress fields. As such, collinear interactions are considered one of the strongest latent hardening mechanisms [63-65]. In contrast, glissile interactions occur due to the formation of glissile junctions, which are temporary semi-mobile structures, created when dislocations from non-coplanar slip systems intersect. These structures can readily glide along the slip plane

while acting as an obstacle for other dislocations. Lastly, sessile interactions occur due to the formation of sessile junctions, which are permanent immobile structures, created when dislocations from non-coplanar slip systems intersect. These interactions are considered stronger than Hirth lock interactions, but similar in strength to glissile junction interactions [64].

#### 2.2.4. Plastic deformation of polycrystals

The deformation of polycrystals is a complex process based on the collective behaviour of many single crystals (i.e., grains) and their interactions. As discussed in Section 2.2.2, plastic deformation in individual grains occurs primarily through slip on specific planes along specific directions. Since grains generally have different crystallographic orientations, their slip systems are not aligned the same way relative to a common external load. As a result, each grain experiences a different RSS on its available slip systems, causing grains to deform at different rates [66]. Because adjacent grains must maintain geometric continuity during loading, the mismatch in deformation behaviour between adjacent grains leads to the development of internal stresses within the microstructure [67]. Over time, these internal stresses contribute to strain hardening, texture evolution, as well as the formation of microcracks.

During deformation, the interface between adjacent grains (i.e., grain boundaries) can also act as barriers to dislocation motion [67]. Dislocations approaching a boundary must reorient their slip direction to accommodate the difference in orientation between adjacent grains, with the difficulty of this reorientation increasing with the misorientation angle [53]. Grain boundaries with small misorientations (i.e., small-angle boundaries) allow some degree of slip transmission, while grain boundaries with high misorientations (i.e., high-angle boundaries) strongly impede dislocation motion and may cause dislocations to pile up at the boundaries. These pile-ups introduce local stress concentrations that can generate new dislocations, trigger localised slip, or initiate microcracks in adjacent grains [67]. In addition to impeding dislocation motion, grain boundaries can also accommodate plastic deformation through mechanisms such as grain boundary sliding [53], which occurs at low strain rates and elevated stress–temperature conditions, enabling adjacent grains to shift relative to one another. While grain boundary sliding can relieve local stress concentrations, it can also contribute to cavitation and void formation along the boundaries.

#### 2.2.5. Texture evolution

During plastic deformation, grains in a polycrystalline material may rotate to align their orientations more favourably with the applied stress, facilitating slip along the most active slip systems. The collective effect of these rotations alters the overall distribution of orientations, leading to texture evolution [68]. Before the material is deformed, it can exhibit random textures, whereby the crystallographic orientations of their grains are uniformly distributed [68]. With no dominant orientation, the material exhibits isotropic properties, such that its behaviour is consistent in all directions. After plastic deformation occurs, the grains can rotate to non-random (i.e., preferred) orientations that are characteristic of the applied deformation. As a result, the material can exhibit anisotropic properties, such that its behaviour varies in different directions. An example of texture evolution in a Co-Cr-Ni specimen is presented in Figure 2.7, as adapted from Huang *et al.* [69]. The colours assigned to the grains correspond to their orientations, with the progression of colours from 0% to 20% strain reflecting the rotation of the grains as the polycrystal is deformed.

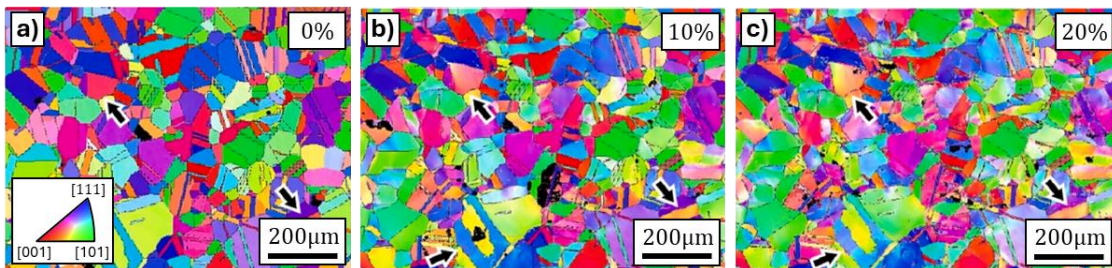


Figure 2.7. Microstructure of a CoCrNi specimen at a)  $\varepsilon = 0\%$ , b)  $\varepsilon = 10\%$ , and c)  $\varepsilon = 20\%$ , shown as inverse pole figure (IPF) colour maps in the  $x$  direction. Panels are adapted from Huang *et al.* [69] by permission of Elsevier.

The crystallographic texture of a crystalline material can be visualised using pole figures (PFs) and inverse pole figures (IPFs). A PF visualises the texture of a material on a stereogram with axes defined by the sample reference frame, namely the sample's normal direction (ND), rolling direction (RD), and transverse direction (TD) [39]. PFs represent each crystallographic orientation as three poles (i.e., normals to the planes) and stereographically project the poles onto a two-dimensional polar plot [70]. PFs are constructed for a chosen plane — for cubic structures, PFs are generally constructed for the (100), (110), and (111) planes. PFs are useful for visualising how the texture evolves based on the accumulation of poles about specific sample directions (i.e., ND, RD, or TD). A schematic of a PF with stereographic projections of common crystal directions is shown in Figure 2.8a. The projection region of the PF diagram is separated into 24 curvilinear triangles.

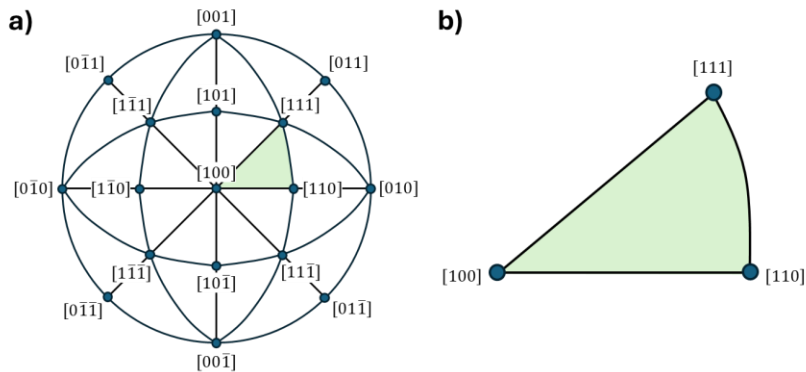


Figure 2.8. Schematics of a) a pole figure (PF) diagram containing common directions and b) an inverse pole figure (IPF) diagram of the standard triangle containing directions with positive indices in descending order.

IPFs differ by visualising the crystallographic orientations with axes defined by the crystal reference frame instead of the sample reference frame. IPFs represent each orientation as a single pole on a two-dimensional stereographic triangle [70], and are constructed for a chosen sample direction (i.e., ND, RD, or TD). While IPFs can be used to visualise texture evolution, they are particularly useful for visualising the changes in orientation of individual grains (i.e., reorientation trajectories). A schematic of an IPF of the standard triangle is shown in Figure 2.8b. The standard triangle is one of the 24 curvilinear triangles, as highlighted in the PF diagram in Figure 2.8a. The standard triangle is distinct in that it captures the stereographic projections of all the crystal directions with positive indices in descending order, namely the [100], [110], and [111] directions. IPFs are conventionally presented using the standard triangle, in which all crystallographic orientations can be easily manipulated so that their projections lie in the standard triangle.

## 2.3. Experimental testing

Experimental tests are conducted on materials to understand how they respond to different loading conditions. A broad suite of testing methods exists to probe different aspects of material performance, such as hardness, fatigue, and fracture-toughness testing. This review focuses on experimental techniques relevant to the discussed studies. As such, the following section begins with an overview of tensile testing (Section 2.3.1), which evaluates deformation under controlled uniaxial tension. The section then explores creep testing (Section 2.3.2), which evaluates long-term deformation under sustained high stress–temperature conditions. The section concludes by discussing electron backscatter diffraction (EBSD; Section 2.3.3), which evaluates crystallographic orientation and grain-scale features.

### 2.3.1. Tensile testing

Tensile testing is an experimental method to characterise the mechanical behaviour of materials under controlled uniaxial tension, usually until failure [71]. Specimens are typically designed with a reduced cross-sectional area in the central portion, often in a dog-bone shape, to ensure that deformation and fracture occur within this region [72]. During testing, a specimen is mounted in a tensile testing machine, which applies a gradually increasing uniaxial tensile load while simultaneously measuring the resulting elongation. These measurements are used to produce a stress–strain curve, from which critical mechanical properties can be extracted, such as the yield strength, ultimate tensile stress (UTS), elastic modulus ( $E$ ), and Poisson’s ratio ( $\nu$ ). Tensile tests are conducted in accordance with established standards, such as ASTM E8-11 [73], which specify the specimen geometry, testing procedure, and measurement criteria to ensure the reproducibility and comparability of the results across different materials and testing conditions. Figure 2.9 presents an example of a tensile test specimen machined from an aluminium sheet as well as a tensile testing machine, reproduced from Talebi-Ghadikolaee *et al.* [74].

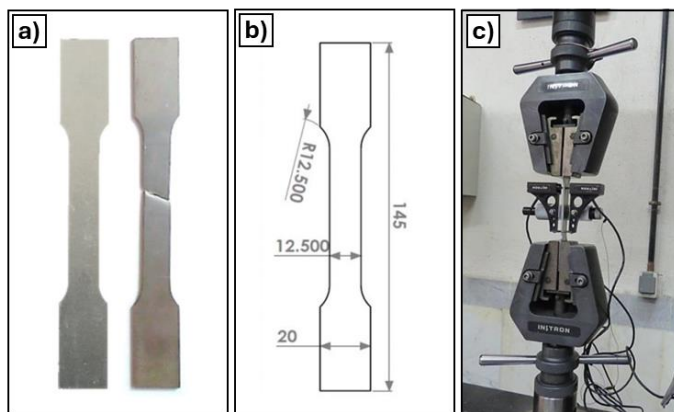


Figure 2.9. Uniaxial tensile test specimen and machine. Panel a) shows the undeformed and ruptured aluminium alloy specimen, panel b) shows the dimensions of the specimen (in mm), and panel c) shows the INSTRON tensile testing machine. Panels are adapted from Talebi-Ghadikolaee *et al.* [74] by permission of Springer Nature.

In tensile deformation, the specimen initially undergoes elastic deformation, where stress and strain are proportional, until it reaches the yield point. The specimen then enters the strain hardening phase, where plastic deformation occurs as dislocation motion strengthens the metal and allows it to sustain increasing stress. This continues until the specimen reaches the UTS and enters the necking phase, which is characterised by a rapid

loss in strength due to the localised reduction in the cross-sectional area of the specimen gauge [71]. The necking phase continues until the specimen can no longer withstand the applied stresses, which causes the specimen to fracture. Note that some metals (e.g., steel) will experience a sudden decrease in strength after the yield point (i.e., yield drop) due to the formation of Lüders bands [75]. The schematic in Figure 2.10 shows a typical tensile curve for a polycrystalline metal alloy plotted in terms of engineering stress and strain, where  $\sigma_y$  represents the yield stress / strength,  $\sigma_{UTS}$  represents the ultimate tensile stress, and  $\sigma_d$  represents the stress-at-ductility. Additionally,  $\varepsilon_y$  represents the yield strain,  $\varepsilon_{UTS}$  represents the ultimate tensile strain, and  $\varepsilon_d$  represents the strain-at-ductility. The material's toughness is quantified by the area under the tensile curve, while the material's ductility can be quantified by the amount of elongation at fracture.

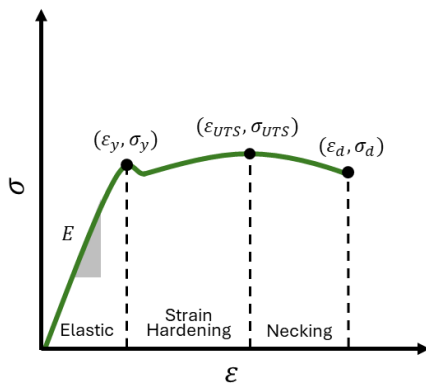


Figure 2.10. Annotated schematic of a typical tensile curve for a polycrystalline metal alloy.

Tensile behaviour is strongly influenced by the loading condition, with temperature and strain rate serving as primary factors controlling key mechanical properties as well as the overall stress-strain response [76-78]. For most alloys, the yield strength and ultimate tensile strength (UTS) gradually decrease from room temperature as temperature rises, often dropping sharply at higher temperatures. The yield strength can exhibit a slight increase over an intermediate temperature range for ordered alloys or those containing ordered precipitates, such as with Alloy 617 [77, 78]. Both the yield strength and UTS are often relatively insensitive to strain rate at lower temperatures but tend to decrease with slower strain rates at higher temperature [76-78]. These temperature and strain-rate dependencies are also reflected in the overall shape of the stress-strain response. For instance, the strain-hardening region is pronounced at lower temperatures but progressively diminishes with increasing temperature due to softening mechanisms. At higher temperatures softening becomes the dominant behaviour, with its influence increasing at slower strain rates (e.g.,  $10^{-4}\text{s}^{-1}$ ) [78].

### 2.3.2. Creep testing

Creep testing is a method for characterising the time-dependent deformation of materials under a sustained tensile or compressive load at elevated temperatures. The specimens used for creep testing under tensile loads are similar to those employed in simple tensile tests [79], as discussed in Section 2.3.1. During a creep test, the specimen is subjected to a constant uniaxial stress below the material's yield strength and a constant temperature below its melting point, typically exceeding around one-third of the melting point [80]. The resulting elongation is recorded throughout the duration of the test to produce a strain-time curve, from which properties such as the minimum creep rate, time-to-failure, and strain-to-failure are obtained. Creep tests are

similarly performed in accordance with established standards, with ASTM E139-11 [81] being one of the most widely used for metals. Figure 2.11 presents an example of creep test specimens cast from an aluminium-silicon alloy as well as a creep testing machine, reproduced from Golshan et al. [82].

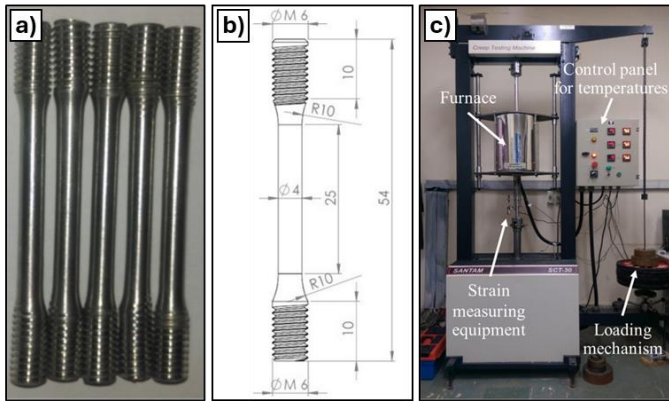


Figure 2.11. Creep test specimens and machine. Panel a) shows undeformed aluminium-silicon alloy specimens, panel b) shows the dimensions of the specimens (in mm), and panel c) shows the SCT-30 SANTAM creep testing machine. Panels are adapted from Golshan et al. [82] by permission of Springer Nature.

The creep behaviour of metals is typically defined by three distinct stages, namely the primary, secondary, and tertiary stages. The metal begins in the primary (or transient) stage, where it deforms with an initially high strain rate that gradually reduces due to strain hardening. During the secondary (steady-state) stage, the metal experiences recovery, where the dislocations are annihilated, rearranged, or reorganised through thermally activated processes. The effects of recovery balance the ongoing strain hardening, with this equilibrium causing the metal to exhibit a constant, minimum creep rate. Finally, when the metal reaches the tertiary stage, it experiences necking and small cavities within the metal begin expanding. This results in the metal's strength rapidly deteriorating, which accelerates the creep rate, and ultimately leads to the fracture of the metal [80]. The schematic in Figure 2.12 shows a typical creep (strain–time) curve, where  $t_f$  represents the time-to-failure,  $\varepsilon_f$  represents the strain-to-failure, and  $\dot{\varepsilon}_m$  represents the minimum creep rate.

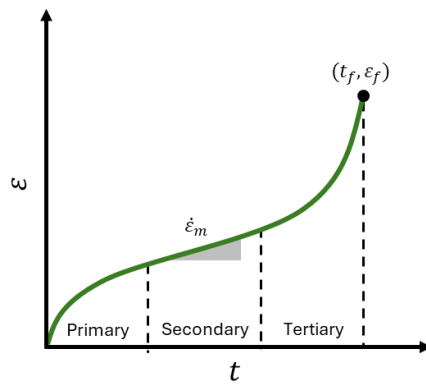


Figure 2.12. Annotated schematic of a typical creep curve for a polycrystalline metal alloy.

Creep behaviour is strongly influenced by the applied stress and temperature, governing its key characteristics and overall time–strain response [83-85]. In general, higher temperatures and stresses lead to a higher overall creep rate, and therefore a shorter time-to-failure due to the acceleration of damage

accumulation [83]. In contrast, the strain-to-failure may increase at moderate temperatures due to enhanced ductility but decrease under elevated temperatures or stresses [85]. However, the exact response may vary depending on the combined effects of temperature, stress, and material microstructure, making strain-to-failure predictions less certain under complex conditions.

### 2.3.3. Electron backscatter diffraction

Diffraction techniques can be employed to provide insight into the microstructure of crystalline materials. These techniques involve directing a beam of particles towards the sample material, where they are scattered by the arrangement of atoms in the sample's crystal lattice. This scattering produces a pattern of interference known as a diffraction pattern, whose angles and intensities can be analysed to obtain crystallographic information within the material [86]. The wavelength of particles used in diffraction must be similar in magnitude to the atomic spacings in the crystal structure such that noticeable diffraction effects can be observed [87]. As such, x-rays, electrons, and neutrons are commonly used in diffraction studies, with each interacting with the sample in different ways. When targeted towards the sample, x-rays interact primarily with the electron cloud of atoms in the sample [86]. In contrast, neutrons interact directly with the atomic nuclei as well as magnetic fields, due to their non-zero magnetic moments [88]. Finally, due to the negative charge, electrons interact with the positively charged atomic core as well as the negatively charged electron cloud [89]. The choice of diffraction technique depends heavily on the application. X-ray and neutron diffraction have higher penetrative depth and are well-suited for bulk analyses of materials to obtain averaged information over larger volumes [86]. Neutron diffraction are also useful for investigating light elements (e.g., hydrogen) and magnetic materials (e.g., superconductors) [87, 88]. In contrast, electron diffraction offers higher spatial resolutions due to significantly smaller interaction volume [89]. This allows for detailed mapping of crystallographic orientations and other microstructural features at the individual grain level [89].

Electron diffraction can be acquired through various microscopy techniques, most commonly transmission electron microscopy (TEM) and scanning electron microscopy (SEM) [90]. Annotated schematics of TEM and SEM are presented in Figure 2.13, as adapted from Son *et al.* [91]. Both techniques rely on a beam of electrons impacting the sample inside a vacuum chamber, with the primary difference being that TEM is used to examine internal structures whereas SEM is used to examine material surfaces [92]. In TEM, a broad beam of electrons is transmitted over a defined area through the sample [92]. The transmitted electrons are scattered and collected at the other end of the sample for analysis [93]. This technique provides high-resolution images of the sample's internal structure. However, due to the increased complexity of the technique, the process is substantially slower, more costly, and requires nanometre-thin samples (< 100nm), necessitating rigorous sample preparation [94]. In SEM, a focused beam of electrons scans the surface of the sample in a rectangular raster pattern [92]. The interactions between the electron beam and sample surface generate secondary electrons (SEs), backscattered electrons (BSEs), and x-rays, which are collected and analysed to create an image of the topography of the sample's surface [95]. While this technique is simpler and quicker than TEM, it provides lower-resolution images without information about the sample's internal structure. That said, SEM is sufficient for analysing the surface crystallography of micrometre-sized grains [96].

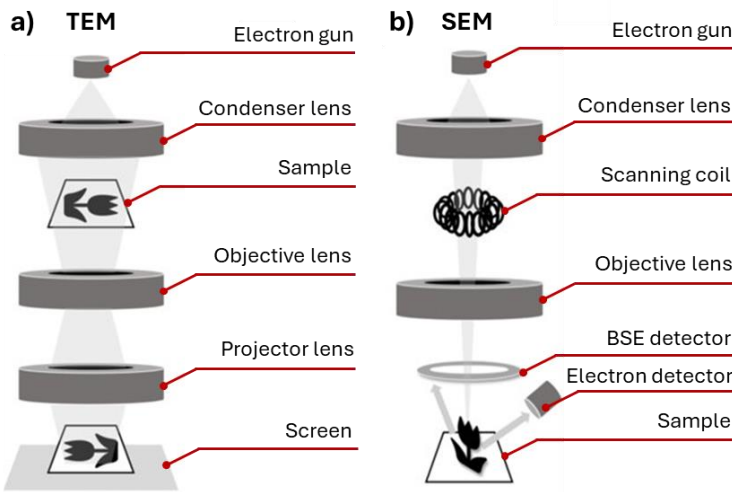


Figure 2.13. Annotated schematics of a) transmission electron microscopy (TEM) and b) scanning electron microscopy (SEM), adapted from Son *et al.* [91] by permission of Oxford University Press.

Electron backscatter diffraction (EBSD) is an SEM technique that analyses the elastically scattered BSEs that undergo coherent Bragg scattering as they leave the sample surface [92]. In EBSD, the BSEs are collected on a phosphor screen, which create diffraction patterns made up of Kikuchi bands [97], examples of which are shown in Figure 2.14 [98]. These diffraction patterns are captured by a digital camera and analysed to quantify the orientations, sizes, and morphology of individual grains in the sample [92]. During analysis, the sample is titled by  $70^\circ$  to the electron beam, allowing access to a wider range of crystallographic orientations and enhancing the clarity and intensity of diffraction spots to resolve phase and grain boundaries more accurately [92, 99]. EBSD has been widely used over the years to study the surface crystallography in polycrystalline materials [76, 96, 99]. Notably, a 2013 study [96] used EBSD to analyse the texture development and twinning generation in individual grains of Alloy 617 under elevated-temperature conditions. Another 2023 study [76] used *in situ* EBSD to simulate local stress–strain development in Alloy 617, by performing EBSD measurements at various strain intervals as the sample was deformed. These studies are crucial in improving the understanding of how the properties of polycrystalline materials change as they deform under extreme stress–temperature conditions.

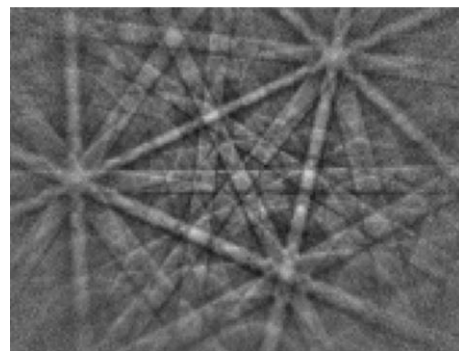


Figure 2.14. Typical diffraction patterns from a face-centred cubic (FCC) material obtained through electron backscatter diffraction (EBSD), reproduced from Randle [98] by permission of Elsevier.

## 2.4. Material models

Performing experimental tests under all possible service conditions is often impractical due to the substantial time, cost, and resource requirements, particularly for elevated stress–temperature applications. As such, material models serve as powerful complementary tools for predicting material behaviour across a wide range of loading conditions without the need for exhaustive experimental testing. Material models can reproduce key material characteristics (e.g., time-to-failure, strain-to-failure, yield strength) as well as complete deformation responses (e.g., creep strain–time and tensile stress–strain curves). These models are typically governed by a set of constitutive parameters that can be adjusted to reproduce observable material behaviour through calibration, as discussed in Section 2.5.

Broadly, material models can be classified as empirical, semi-empirical, or physics based, with each category offering distinct balances between simplicity, accuracy, and complexity. Empirical material models rely on simplified mathematical expressions to establish relationships between observable material responses in the experimental data. These models are popular due to their simplicity and low computational costs, but they often require extensive experimental data and exhibit limited generalisability [15, 16]. To address these issues, semi-empirical material models connect empirical relationships to underlying principles, often incorporating parameters with partial physical meaning. These models are slightly more complex and computationally demanding than purely empirical models but offer improved predictive accuracy and better generalisability. However, semi-empirical models are still influenced by trends in the experimental data, resulting in over-conservatism and poor capturing of mechanism shifts [15, 26]. Physics-based models extend semi-empirical models by explicitly representing fundamental deformation mechanisms, such as dislocation motion [16]. As a result, these models offer higher fidelity, greater reliability when extrapolating beyond experimental conditions, and more direct interpretability of material behaviour. However, physics-based models are significantly more complex and computationally expensive, posing challenges for their use in practical engineering applications [16, 27]. To contextualise these different material modelling approaches, the following section provides an overview of empirical (Section 2.4.1), semi-empirical (Section 2.4.2), and physics-based material models (Section 2.4.3), highlighting their principles, strengths, and limitations.

### 2.4.1. Empirical material models

Among conventional material models, empirical models operate at the highest level of abstraction, focusing on capturing observable trends in the experimental data without considering the underlying physical mechanisms. These are usually expressed as simple mathematical equations that include polynomials, power laws, and exponential functions. For creep behaviour, a notable example is Norton's power law [11], which describes the minimum creep rate ( $\dot{\varepsilon}_m$ ) as a function of stress ( $\sigma$ ) and two material parameters ( $A_{No}$  and  $n_{No}$ ), as shown in Eq. (4). The values of these parameters are typically obtained by applying regression techniques (see Section 2.5) to fit  $\ln(\dot{\varepsilon}_m)$  against  $\ln(\sigma)$ . Since these parameters have no direct physical interpretation, they rely solely on the assumed linear relationship between the logarithmic quantities.

$$\dot{\varepsilon}_m = A_{No} \cdot \sigma^{n_{No}} \quad (4)$$

Other well-established empirical creep models include the Larson-Miller method [100], the Manson-Haferd method [101], and the theta projection model [102], which are often used for long-term life predictions. For

tensile responses, Hollomon's equation [14], Ludwik's law [103], and Voce law [104] are frequently used. Beyond their standard forms, these classical empirical models can be coupled to provide a more comprehensive description of material behaviour. For instance, minimum creep rate models can be used as an input for life prediction methods like the Monkman-Grant relation [105]. Additionally, strain-time models that capture individual creep regimes can be additively coupled to provide a single unified expression to capture multiple creep regimes. Notable examples of these include the theta projection model [12, 13], phi model [106, 107], and omega model [108, 109]. Empirical tensile models can also be additively or piecewise coupled to capture both early hardening and eventual saturation behaviour observed in many engineering alloys [110-112], such as with the Hollomon-Voce model [14, 104].

The main challenge with empirical modelling is extending their predictive capability across multiple loading conditions. For creep models, this involves different stresses and temperatures, whereas for tensile models, it concerns varying strain rates and temperatures. A common approach is to treat these loading variables as explicit inputs by incorporating them directly into the model's functional form, such as in Arrhenius' law [113] and the Johnson-Cook model [114]. However, this approach may reduce predictive accuracy outside the training range and can limit flexibility when capturing complex, multi-stage creep behaviour or non-linear hardening in tensile responses [108]. Another widely used strategy involves defining the model's constitutive parameters as explicit functions of the loading variables [102, 115]. For instance, the Larson-Miller parameter [100] can be expressed as a function of applied stress, while the parameters of the theta projection model can be defined by a multilinear expression of stress and temperature [102]. While this strategy can enhance the flexibility and generalisability of empirical models, it introduces additional parameters that can complicate the calibration of the models and reduce their physical interpretability [102, 115].

Overall, empirical material models are widely employed due to their simplicity, flexibility, low computational costs, and minimal number of constitutive parameters [15]. In particular, they are commonly incorporated into design codes to provide safe and practical guidelines for engineering applications [116]. However, they often require extensive experimental data, which restricts their predictive capability beyond the training domain and makes long-term or high-accuracy predictions challenging [15, 16]. Consequently, empirical material models are rarely used in isolation for comprehensive material analyses. Instead, they are typically integrated into broader frameworks — such as semi-empirical or physics-based models — where they provide a practical foundation for capturing general trends while more mechanistic components account for complex deformation mechanisms [17, 18, 26, 117].

#### 2.4.2. Semi-empirical material models

Empirical models rely heavily on experimental observations to define their constitutive relationships. In contrast, semi-empirical models integrate physical principles with experimental data, where their constitutive parameters are intrinsically linked to fundamental material behaviour rather than serving merely as fitting parameters. This integration allows semi-empirical models to achieve enhanced predictive capabilities over a wider range of conditions [16]. By incorporating these physical principles, semi-empirical models can generalise beyond their training domain, making it suitable for long-term predictions, such as with creep. However, compared to empirical models, semi-empirical models are typically more complex to implement and require

greater computational resources to evaluate, reflecting the additional mechanistic detail incorporated into their formulation.

One of the most widely used semi-empirical models is the Kachanov-Rabotnov (KR) isotropic creep damage model [17, 18]. This model has been adapted extensively for different applications, such as in a 2012 study by Stewart and Gordan [118], where Norton's power law was integrated into the KR model [17, 18] to capture the secondary and tertiary creep behaviour of a nickel alloy. While the KR model has been shown to produce reasonable creep predictions [15, 80, 118], the predictions are inherently limited to creep behaviour. To address this limitation, the elastic-viscoplastic (EVP) model [22-25] can be employed to capture a broader scope of material deformation. In this model, the elastic behaviour is typically described by a form of Hooke's law, such as in Eq. (1). The EVP model describes plastic behaviour through viscoplasticity, which accounts for time-dependent deformation resulting from diffusion, dislocation motion, cavity formation, and grain boundary sliding [119]. Importantly, the EVP model can capture the deformation behaviour of materials under various loading conditions, such as creep and tensile behaviour. While the EVP model is unable to capture damage by itself, it can be readily coupled with a damage model to capture the entire service life of a material.

While semi-empirical models are more computationally demanding than empirical models, they offer improved predictive accuracy and generalisability. However, these models still operate at a relatively high level of abstraction, relying heavily on simplified approximations and trends in the experimental data. As a result, these models are prone to over-conservative predictions and may struggle to capture mechanism shifts [15, 26]. Physics-based models aim to address these limitations by directly accounting for the underlying mechanisms that govern deformation behaviour.

#### 2.4.3. Physics-based material models

Physics-based material models incorporate fundamental physical principles to describe the deformation and degradation behaviour of materials. These models aim to simulate the intrinsic behaviour of materials by considering the underlying mechanisms, instead of relying on experimentally observed trends. Various physics-based modelling approaches have been developed to capture specific aspects of material behaviour across various length and time scales. A notable approach is dislocation dynamics, which captures plastic deformation at the microscale based on the motion and interaction of individual dislocations within the crystal lattice [63]. These models have been used to investigate a range of behaviours, from latent hardening effects [63] to dislocation-particle interactions [120]. Another popular approach is phase-field modelling, which describes microstructural evolution through continuous field variables [121, 122]. Since phase-field models do not explicitly track interfaces (e.g., grain boundaries), they can study evolution phenomena over larger length and time scales than other methods [122]. Among these physics-based modelling approaches, crystal plasticity (CP) stands out for its ability to capture the influence of microstructural mechanisms on macroscopic deformation behaviour [123, 124], integrating multiple length scales. CP models describe plastic deformation based on the collective motion of dislocations across multiple slip systems, allowing them to capture the anisotropic deformation behaviour of crystalline materials with direct account of crystallographic texture, slip system activation, and dislocation interactions [124-128]. The inherent multiscale capability of CP models is particularly useful for accurately predicting deformation behaviour under complex loading conditions, such as those

encountered in nuclear reactor systems. That said, these capabilities come with substantially increased model complexity and computational cost, which can limit their practical application in large-scale simulations.

CP models can be incorporated into various frameworks to capture the deformation behaviour of polycrystalline materials [22]. One of the earliest CP modelling approaches involved the mean-field framework [129], where grain behaviour is approximated based on averaged field quantities (e.g., stress, strain). Another popular approach is the self-consistent framework, where the material is represented as a homogeneous equivalent medium (HEM) that has uniform properties reflecting the average grain characteristics [130]. Each grain interacts with the HEM rather than with each other, thereby avoiding direct grain-to-grain interactions. Both these frameworks approximate material behaviour through averaged properties, leading to substantially reduced computational costs. While these frameworks are suitable for larger-scale simulations, their oversimplification of grain interactions limit their ability to accurately capture local behaviour, such as strain localisation, grain boundary effects, and the reorientation trajectories of individual grains [131]. To address these limitations, the finite element method (FEM) can be employed to provide a high fidelity, spatially resolved representation of a polycrystalline material by discretising its continuous structure into a mesh of smaller finite elements [132, 133]. CP models can be integrated into the FEM framework (CPFEM) to govern the internal deformation mechanisms of individual elements. The responses of each element are then assembled to describe the overall mechanical response of the material. The CPFEM framework explicitly accounts for microstructural features such as grain morphology and texture, as well as microstructural interactions between grains, boundaries, and dislocations [132-134]. This allows CPFEM models to capture the inherent heterogeneity and anisotropy of polycrystalline materials [132-134], providing more accurate representations of local behaviour.

A key consideration in the development of CPFEM models is the construction of the finite element models. Various approaches have been employed to represent the internal, three-dimensional architecture of polycrystalline materials. One of the most common techniques involves generating a 3D representative volume element (RVE) model based on the geometric statistics of the grains, ensuring that the model is statistically equivalent to the investigated microstructure [16, 134, 135]. RVEs were used with the CPFEM framework in a 2016 study by Zhang *et al.* [136] to investigate the high-temperature behaviour of Alloy 617 under cyclic loading, as presented in Figure 2.15. In their study, the RVEs were generated using 3D tetrahedral elements from experimentally observed bi-modal grain size distributions.

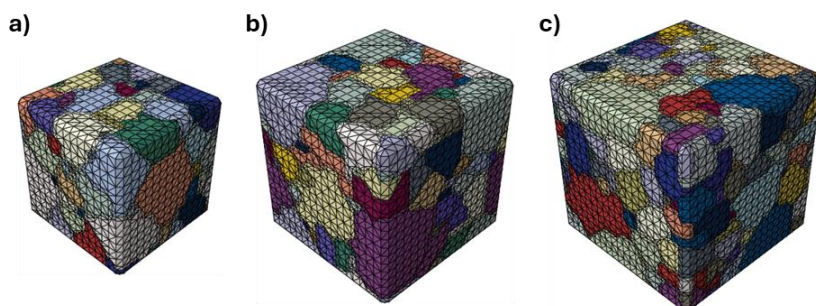


Figure 2.15. 3D finite element (FE) models generated using the representative volume element (RVE) approach, containing a) 98, b) 140, and c) 243 grains. Panels are adapted from Zhang *et al.* [136] by permission of IOP Publishing.

Another popular approach involves extracting a 2D projection of the material's microstructure and extruding it along the specimen's thickness to create a 2.5D FE model [124, 126, 137]. While the model extends the 2D surface microstructure into a third dimension, it does not account for variations in grain geometry through the depth of the specimen, making it a pseudo-3D representation [138]. The projection approach was used in a 2022 study by Abdolvand [124] to investigate the nucleation and propagation of cavities, where a 2.5D hexahedral model was constructed from a 2D EBSD map. The EBSD map and 2.5D FE model are presented in Figure 2.16.

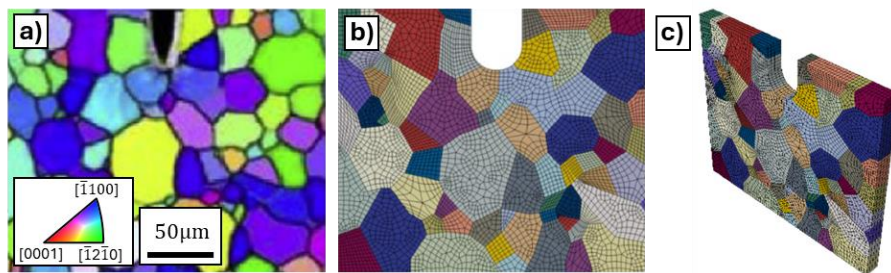


Figure 2.16. Generation of a 2.5D finite element (FE) model using the projection approach. Panel a) shows an electron backscatter diffraction (EBSD) map coloured with respect to IPF- $x$ , while panels b) and c) show the resulting 2.5D FE model in top and angled views, respectively. Panels are adapted from Abdolvand [124] by permission of Elsevier.

While RVE models provide generalised representations of material microstructures, they are typically more computationally expensive and require large amounts of data to achieve statistical equivalency. In contrast, projected models incur reduced computational cost and can reproduce the complex microstructural features of a specific specimen with higher fidelity. However, these projected models are inherently limited to representing the specimens they were projected from, resulting in poor generalisability to other microstructures. Ultimately, both RVE and projection approaches have their advantages, with preference depending on the application, available experimental data, and computational resources.

## 2.5. Material model calibration

Conventional material models — such as those discussed in Section 2.4 — typically have a set of adjustable constitutive parameters that govern their simulated response. One of the first steps in the deployment of these materials models in engineering analyses is to calibrate them. The calibration process of a material model involves identifying suitable values for its constitutive parameters to align the simulated responses with the experimentally observed material behaviour. Traditionally, material models were calibrated using manual trial-and-error methods. These methods were often subjective and time-consuming, particularly for more complex models with expansive parameter spaces and higher computational costs [16, 27, 28]. These methods also heavily relied on the analyst's understanding of the constitutive parameters and the theoretical framework underlying the material model. As such, various optimisation algorithms have since been developed to automate and streamline the calibration process of material models. However, these algorithms often require a substantial number of model evaluations, which can become prohibitive when calibrating semi-empirical or physics-based models that have high computational costs.

To explore the concepts of material model calibration, the following section begins with an overview of these optimisation algorithms and how they differ in search scope, navigation strategy, and determinism (Section

2.5.1). The section continues with an introduction to the genetic algorithm (GA; Section 2.5.2) and its extension to multi-objective optimisation in the multi-objective genetic algorithm (MOGA; Section 2.5.3). Finally, the section concludes with a discussion of popular methods in literature to reduce the computational costs of calibrating complex material models (Section 2.5.4).

### 2.5.1. Optimisation algorithms

Optimisation algorithms can be used to automatically calibrate material models by identifying parameter values that align the simulated response from the material model with experimental observations [118]. Optimisation algorithms achieve this by heuristically navigating the parameter space consisting of all the possible combinations of the model's constitutive parameters [118]. These algorithms repeatedly assess different parameter combinations using an objective function that quantifies the discrepancies between the experimental and simulated responses. These algorithms will use the values obtained from the objective function (i.e., objective values) to guide the search towards more promising regions of the parameter space [118]. During this search, optimisation algorithms may encounter local optima, representing parameter values that yield improved objective values relative to surrounding parameters. The goal of the optimisation algorithm is to find the global optimum, representing parameter values that yield the best objective value across the entire parameter space. By continually pursuing parameter combinations that yield lower discrepancies while avoiding local optima, optimisation algorithms may gradually converge towards the global optimum, obtaining a set of parameter values that most accurately align the simulated response with the experimental data.

Over the years, many optimisation algorithms have been employed for the calibration of material models. These optimisation algorithms can be categorised based on how extensively they explore the parameter space. Local optimisation algorithms, such as linear regression, gradient descent, and Nelder-Mead, search for parameter values within a limited region of the parameter space, typically near user-defined initial values [139]. These algorithms are simple and computationally efficient, making them suitable for the calibration of simpler empirical models that contain a few parameters. This was demonstrated by Garcia *et al.* [139] who successfully used linear regression to calibrate a two-parameter creep life model. However, local algorithms rely heavily on their initial values and are therefore prone to getting stuck in local optima, limiting their effectiveness for more complex models [15, 140, 141]. To address this limitation, global optimisation algorithms can be employed to explore the entire parameter space, enabling a more comprehensive search for the global optimum. While this broader search strategy enhances the calibration robustness and consistency, these algorithms require substantially more computational resources.

These algorithms can also be categorised based on their navigation strategy. Gradient-based optimisation algorithms, such as gradient descent, Adam, and the Newton's methods, are guided by the derivative of the objective function [142-144]. However, these algorithms require differentiability in their objective functions, in which noise in the experimental data could deteriorate convergence behaviour [27]. Additionally, gradient-based algorithms are typically local methods, making them heavily reliant on initial values and prone to converging at local optima. In contrast, direct-search optimisation algorithms do not rely on gradient information, making them generally more robust and better suited for exploring diverse regions of large parameter spaces [15, 29]. Depending on their implementation, these algorithms can be both local or global

algorithms, such as with Nelder-Mead and simulated annealing. However, direct-search algorithms generally require a greater number of objective function evaluations, which may result in slower convergence.

Another way to categorise optimisation algorithms is based on their determinism. Deterministic optimisation algorithms, such as gradient descent and Nelder-Mead, produce the same result given the same initial conditions and settings [145]. Deterministic algorithms follow a defined path through the parameter space by exploiting known features of the optimisation problem, such as gradient or geometric information. As a result, these algorithms are typically designed for problems with smooth, unimodal objective functions that have distinct, well-defined global solutions [145]. In contrast, stochastic algorithms, like simulated annealing, incorporate randomness in the search process [146]. These algorithms are able to more effectively escape local minima, making them particularly useful for complex and multimodal problems [145]. However, due to their inherent randomness, stochastic optimisation algorithms will generate different solutions across multiple runs and may require more computational resources to converge. This was demonstrated by Stewart *et al.* [80], who successfully calibrated the semi-empirical KR model using simulated annealing, but reported significant computational demands.

The choice of optimisation algorithm is crucial in the calibration of semi-empirical and physics-based models, which have high-computational costs, large parameter spaces, and strong interdependencies between their constitutive parameters [30-33]. Given these challenges, global optimisation algorithms are ideal due to their enhanced robustness, consistency, and ability to search for global optima. Direct-search algorithms are also well-suited for these complex models since they do not require gradient information, making them applicable to non-differentiable objective functions or noisy experimental data [27, 142]. Finally, stochastic algorithms are effective at avoiding local optima and navigating complex, multimodal parameter spaces. The integration of global, direct-search, and stochastic optimisation techniques offers an effective approach to calibrating complex material models. A popular example of this integration is the genetic algorithm (GA), which is a population-based metaheuristic technique inspired by the mechanisms of biological evolution and natural selection [15, 147]. The GA has been applied extensively to the calibration of complex material models [15, 27, 29, 148], such as the semi-empirical KR model in Ref. [15] as well as physics-based CP constitutive laws in Refs. [27, 33, 34]. In these studies, the GA has demonstrated its ability to handle non-linear and non-convex problems while exploring expansive parameter spaces, making it a promising candidate for the calibration of the semi-empirical EVP models as well as the physics-based CPFEM models.

### 2.5.2. Genetic algorithm

The genetic algorithm (GA) is a randomised search technique within the wider spectrum of evolutionary algorithms, inspired by the principles of biological evolution and natural selection [15]. As such, GAs use terminology related to genetics, such as *gene*, *chromosome*, *population*, *mating*, *crossover*, and *mutation* [15, 149-151]. In the context of GAs for material model calibration, a gene represents a parameter, a chromosome represents a set of parameters, and a population represents a collection of parameter sets. A summary of the GA workflow is presented in Figure 2.17.

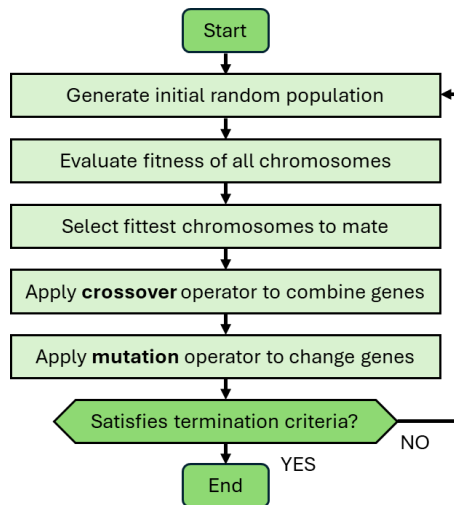


Figure 2.17. Flowchart of the genetic algorithm workflow.

The aim of the GA is to produce a population of the fittest chromosomes, where the fitness of a chromosome corresponds to the minimality of the resulting objective function. To achieve this aim, the GA begins with an initial population of chromosomes with randomly generated genes. Every generation, the GA selects the fittest chromosomes in the population to mate and produce the next generation of chromosomes, which allows the chromosomes with higher fitness levels to pass on their genetic information to their offspring. The mating of two chromosomes primarily relies on two genetic operations — crossover and mutation. The crossover operation selects a subset of the genes from each chromosome to produce the offspring chromosome, whereas the mutation operation applies small changes to one or more genes in the offspring chromosome. The crossover and mutation operations occur based on defined probabilities, namely the crossover probability and mutation probability. In general, a higher crossover probability encourages better convergence of the GA towards the minimum value of the objective function [15, 150], while a higher mutation probability encourages the GA to explore the parameter space and escape local minima [15, 149, 150].

The GA will continue this mating process and evolve the population until a specified termination condition is met. This condition can be when a specified subset of the population has approximately equal fitness levels, when the fittest chromosome has not improved in a specified number of generations, when the population has evolved after a specified number of generations, when a specified amount of time has elapsed, when a specified number of resources have been consumed, or a combination of the aforementioned. If the hyperparameters (e.g., population size, offspring size, crossover probability, mutation probability) have been defined appropriately, the GA will terminate with a population that contains a quasi-optimal chromosome (i.e., set of parameters), which corresponds to a quasi-minimal objective value [15, 27].

### 2.5.3. Multi-objective genetic algorithm

In the context of material model calibration, the GA relies on an objective function that quantifies the discrepancy between the experimentally observed material response and the simulated response from the calibrated model. The aim of the GA is to minimise (or maximise) this objective function, thereby minimising the discrepancy and aligning the model's simulated response with the experimental data. However, the material response may involve multiple distinct properties, each contributing to a separate source of discrepancy. This is

particularly relevant when the calibration is performed to capture deformation behaviour under various loading modes. For instance, in the calibration of creep models, relevant properties might include the minimum-creep-rate, time-to-failure, and strain-to-failure [15], each of which may vary depending on the applied stress and temperature conditions. However, minimising multiple sources of errors can be challenging for the traditional GA, since it only considers a single objective function. A typical solution is to combine the discrepancies into a single weighted function. However, selecting an appropriate formulation and meaningful weights can be challenging, particularly with conflicting objective functions and interdependent parameters. An alternate approach is to define separate objective functions for each distinct material property. Once defined, multi-objective optimisation (MOO) can be employed to simultaneously minimise the objective functions. The multi-objective genetic algorithm (MOGA) combines the concepts of the GA and MOO, with a popular implementation being the non-dominated sorting genetic algorithm-II (NSGA-II) [152].

The goal of a MOO problem is to determine an optimal parameter set (i.e., solution) that best satisfies multiple objective functions. The optimal solution,  $x^*$ , of a MOO problem with  $N$  objective functions,  $f_{1..N}$ , can be represented by the expression in Eq. (5).

$$x^* = \underset{x=x^*}{\operatorname{argmin}} \{f_1(x), f_2(x), \dots, f_N(x)\} \quad (5)$$

In MOO, a solution dominates another solution if it has smaller or equal objective values, with at least one objective value being smaller. The requirements for a solution  $x_1$  to dominate another solution  $x_2$ , can be expressed by Eqs. (6) and (7).

$$\exists i \in \{i = 1..N\} : f_i(x_1) < f_i(x_2) \quad (6)$$

$$\forall i \in \{i = 1..N\} : f_i(x_1) \leq f_i(x_2) \quad (7)$$

A solution is considered Pareto efficient if no other solution dominates it, in which none of its objective values can be improved without increasing at least one other objective value [153]. The collection of all such solutions forms the Pareto front. While every solution on the Pareto front is optimal in a Pareto sense, some may be more desirable than others. In practice, the optimiser distinguishes among the Pareto-efficient solutions using subjective preference information, obtained either before the optimisation (a priori), after the optimisation (a posteriori), or during the optimisation (interactive) [153].

A common strategy for selecting the final solution is to select the knee point from the Pareto front, where further improvement in one objective causes disproportionately large deterioration in another. The knee-point solution thus reflects the most balanced trade-off between multiple competing objectives, representing the most practical solution. Many approaches have been proposed in the literature to identify the knee point from a set of Pareto-optimal solutions. A popular approach is to evaluate the local geometric curvature by measuring angles between a solution and its neighbours in the objective space, with the knee point identified as the solution with the largest such angle [154]. Another method involves estimating each solution's expected utility and selecting the solution whose removal would cause the greatest loss in utility [154]. Although widely used, these knee-point identification methods are generally complex and computationally demanding when applied to high-dimensional objective spaces and large Pareto sets.

In practice, simpler distance-based knee-point identification methods are often sufficient, particularly when solutions exhibit similar trade-offs and a rough approximation of the knee point is acceptable. One such method is the Utopia-point approach, which selects the solution with the smallest Euclidean distance from a reference point (i.e., Utopia point) in the objective space, as illustrated in Figure 2.18a [155]. This approach has been successfully employed in material model calibration, such as by Muránsky *et al.* [156], who trained a physics-informed neural network to minimise deviations from both experimental observations (data loss) and physics-based model predictions (physics loss), as illustrated in Figure 2.18b.

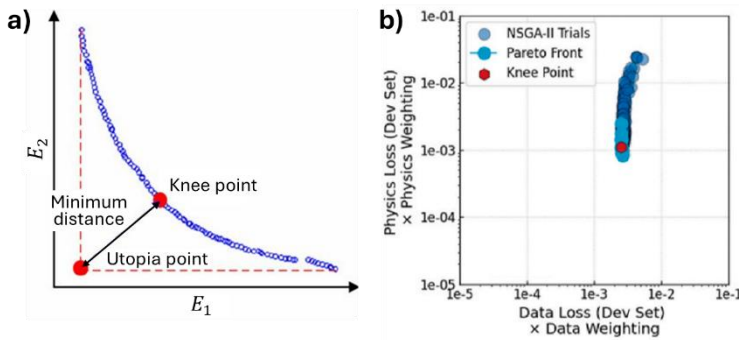


Figure 2.18. Illustration and example of the utopia-point approach. Panel a) shows an illustration adapted from Gu *et al.* [155] by permission of Springer Nature, while panel b) shows an example adapted from Muránsky *et al.* [156] by permission of Elsevier.

#### 2.5.4. Improving calibration efficiency

Optimisation algorithms are essential for automating and streamlining the calibration of material models. However, calibrating complex models — such as semi-empirical and physics-based models — can be challenging due to their large number of constitutive parameters and highly non-linear parameter spaces. As a result, these algorithms often require a substantial number of computationally expensive model evaluations to identify suitable parameter values, which can limit their practicality in engineering analyses. To address this, various optimisation techniques have been proposed in the literature to reduce computational requirements and simplify the calibration process.

A common approach is to shrink the parameter space and narrow the search in more promising regions, such as through active-subspace techniques [157]. These techniques reduce the dimensionality of high-dimensional parameter spaces by identifying the most influential directions (i.e., where the model outputs vary most) and projecting the original parameters onto a lower-dimensional subspace. Active-subspace techniques have been coupled with optimisation algorithms across various domains [158, 159], notably with the genetic algorithm in a recent study by Demo *et al.* [160]. However, these techniques typically rely on gradient information to identify the influential directions, which can be expensive or difficult to obtain. The lower-dimensional subspace may also struggle to capture non-linear parameter interactions — such as those inherent to EVP and CPFEM models — leading to suboptimal calibration results.

A similar strategy to reduce calibration costs involves multi-stage optimisations, where subsets of material parameters are optimised sequentially in multiple stages rather than simultaneously in a single stage, effectively reducing a high-dimensional parameter space into multiple lower-dimensional spaces. This strategy was

employed recently by Saji *et al.* [161] to calibrate a continuum damage mechanics model against experimental force–displacement responses. In their study, each stage targeted specific parameters corresponding to key features of the force–displacement curve — i.e., maximum force, peak position, total work, and overall curve shape — with some parameters refined across multiple stages to account for their influence on multiple features. Honório *et al.* [162] also recently adopted a similar multi-stage approach to calibrate a 19-parameter multi-physics model, yielding robust and accurate results. While this strategy has proven successful, it can still struggle to capture interdependencies between parameter subsets. Additionally, errors introduced in early stages may propagate through subsequent stages, potentially compromising the overall calibration accuracy.

Another approach involves reduced order models (ROMs), which use lower-dimensional approximations to simplify the governing mechanics of high-fidelity, physics-based models while retaining their essential behaviour. By considering fewer degrees of freedom, ROMs can capture the response of complex models at a fraction of the computational cost. A recent example of its application can be found in Patel *et al.* [163], where a ROM was developed for a symmetric 16-ply laminate FE model by representing it as an equivalent 8-ply model, roughly halving the number of elements and, consequently, the simulation time. Another example is with Deng *et al.* [164], who similarly developed a ROM for a FE model by applying spatial domain decomposition to group neighbouring nodes into representative clusters, significantly reducing the degrees of freedom in the model. Despite their efficiency, ROMs may not fully capture the behaviour of their original models, which can lead to inaccuracies when approximating highly localised responses or beyond specific loading conditions.

A closely related technique to ROMs for reducing calibration costs is surrogate modelling, which approximates complex models using data-driven relationships rather than physics-based simplifications. Unlike ROMs, which preserve the models' governing equations, surrogate models rely purely on sampled input–output data without explicitly encoding the underlying mechanics. Surrogate modelling techniques and their application in material model calibration are explored in further depth in Section 2.6.

## 2.6. *Surrogate modelling*

In the calibration of material models, optimisation algorithms evaluate parameter sets using objective functions that compare the model's simulated response with experimentally observed material behaviour. Each evaluation requires a full run of the model, and a single calibration can involve thousands of such evaluations [15]. This can be computationally prohibitive for complex semi-empirical or physics-based models, such as the CPFEM model, where a single run may take days [32]. The computational burden of the calibration process can be reduced by developing a surrogate model to efficiently approximate the behaviour of the material model. This surrogate model takes the parameters of the material model and predicts the corresponding simulated response at a fraction of the original computational cost, allowing the surrogate model to replace the material model during the calibration process. Once the optimal parameters are identified using the surrogate model, they can be applied to the original material model, completing the calibration with substantially fewer computational resources. To provide a deeper understanding of surrogate-based calibration, the following section first discusses the training process of surrogate models (Section 2.6.1). The section continues with an overview of surrogate modelling techniques (Section 2.6.2), and concludes with a discussion of artificial neural networks (ANNs) and their application in the surrogate modelling of physics-based models (Section 2.6.3).

### 2.6.1. Training process

Before a surrogate model can be used for calibration, it must be trained to accurately replicate the behaviour of the material model. For a model with  $N$  constitutive parameters, the possible combinations of parameter values define an  $N$ -dimensional design space [165]. The training process involves sampling a set of points from this space and evaluating both the original material model and the surrogate model at these points. The outputs are then compared, and the surrogate model's hyperparameters are optimised to minimise their discrepancies.

The sample points must be carefully selected from the design space to ensure adequate coverage of the design space [165]. Sampling strategies can divided into stationary and adaptive strategies [165]. Stationary sampling strategies select sample points based on a fixed scheme, independent of any model or analysis results. A basic approach is random sampling, where points are chosen randomly within the design space. While easy to implement, this approach often results in uneven coverage which may cause some regions to be sparsely sampled, reducing the accuracy of the surrogate model. More structured strategies include the two-level factorial design, which for  $P$  parameters, evaluates the  $2^P$  combinations of lower and upper parameter values. However, this strategy assumes linear relationships between the parameters and outputs, which may not adequately represent the behaviour of complex models [16, 27]. The three-level factorial design extends this strategy by evaluating the  $3^P$  combinations for the lower, middle, and upper parameter values. While this strategy can capture non-linear effects through second-degree polynomials, the number of evaluations is unfeasible for high-dimensional design spaces. To address this, the central composite design evaluates the  $2^P$  combinations of upper and lower values,  $2P$  axial points (at a distance  $\alpha$  from the centre), and  $C$  central points, capturing non-linear trends while using fewer evaluations ( $2^P + 2P + C$ ) [27]. Another popular approach is the Latin hypercube sampling (LHS) scheme [166], which divides each parameter range into equal intervals and ensures that each interval is sampled exactly once. The LHS scheme allows for an arbitrary number of sample points, providing flexible control over coverage of the design space and the computational cost of training the surrogate model. Illustrations of the different stationary sampling strategies are presented in Figure 2.19.

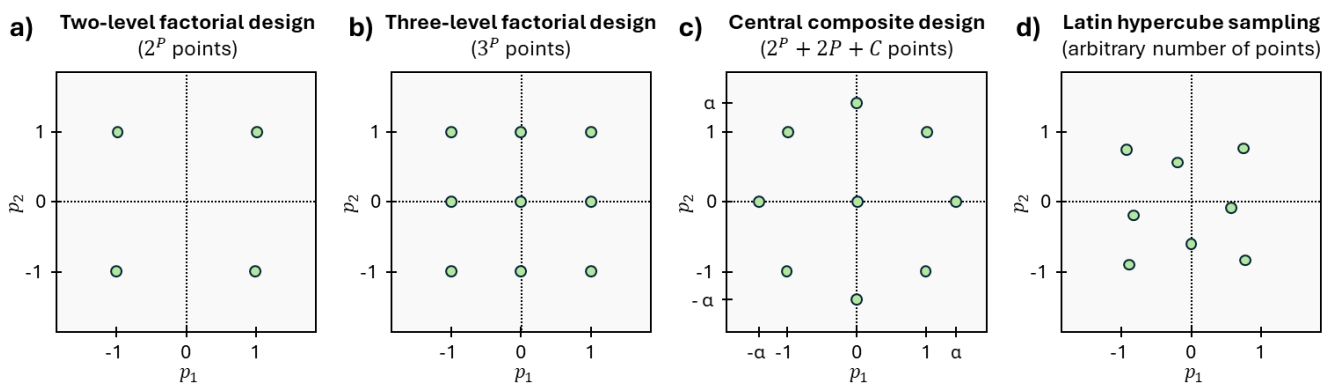


Figure 2.19. Examples of stationary sampling strategies for two parameters: a) two-level factorial design, b) three-level factorial design, c) central composite design, and d) Latin hypercube sampling.

Adaptively sampling strategies typically begin with a small number of sample points determined through a stationary sampling strategy. These strategies then iteratively improve the surrogate model by adding new sample points where they are most needed, usually based on regions of the design space with high prediction

error, steep gradients, or potential optima [165]. While adaptive sampling strategies are more complex and harder to implement than stationary sampling strategies, they have been demonstrated to improve the accuracy of the surrogate model with significantly fewer sample points [167].

### 2.6.2. Modelling techniques

Surrogate modelling techniques can be classified as interpolating and non-interpolating [168]. Interpolation-based methods construct approximations that pass exactly through the sampled points from the training dataset, resulting in zero training error. In these methods, predictions at a new point in the design space are computed as a weighted combination of the sampled points, with weights determined based on their distance or similarity to the new point. A popular example is the Kriging method [169], which determines the weights using a covariance (kernel) function, typically selected from polynomial, exponential, or Gaussian forms [165]. Another common approach is the radial basis function (RBF) method [170], where each sampled point is associated with a radial function, and the weights are determined by solving a linear system of the functions' coefficients. Interpolation-based methods are flexible through different kernels and basis functions and provide strong local accuracy near the sampled points [168]. However, these methods are sensitive to noise, computationally expensive for large datasets, and perform poorly when extrapolating beyond the sampled regions of the design space [168].

In contrast, non-interpolation-based methods create approximations that are not required to pass through the sampled points. These methods make predictions using a global model that is fitted by minimising a predefined error metric over the entire training dataset [168]. One of the earliest approaches is the response surface methodology [171], which fits a low-order polynomial to approximate the model outputs. More recent approaches include support vector regression [172], which fits a function within a margin of tolerance to balance accuracy and model complexity, as well as artificial neural networks, which learn complex relationships through interconnected layers of neurons. In general, non-interpolation-based methods can suffer from reduced local accuracy at the sampled points and often require careful hyperparameter tuning to avoid under- or overfitting. However, compared to interpolating methods, they are typically more robust to noise, scale better with large datasets, and provide improved generalisation beyond the sampled design space, enabling their successful application in surrogate-based calibration of physics-based models over the years [27, 173-175].

### 2.6.3. Artificial neural network

Artificial neural networks (ANNs) are a powerful and widely used non-interpolating surrogate modelling technique inspired by the structure of biological neural systems [176]. ANNs are composed of interconnected computational units called *neurons*, which calculate an output based on a linear combination of inputs that is passed through a non-linear activation function, such as a sigmoid, step function, or rectified linear unit. The operation is described in Eq. (8), where  $y$  represents the output,  $x_i$  represents an input value,  $w_i$  represents the corresponding weight,  $b$  represents a bias term, and  $f(\cdot)$  represents the activation function.

$$y = f(x_1 w_1 + x_2 w_2 + \dots + x_N w_N + b) \quad (8)$$

An ANN is formed by arranging these neurons in layers, with an input layer to receive the data, hidden layers to extract non-linear patterns, and an output layer to generate predictions. The weights and biases of each

neuron are iteratively adjusted to minimise a predefined loss function, enabling the ANN to learn complex, non-linear relationships between the inputs (i.e., constitutive material parameters) and outputs (i.e., simulated material response). Annotated schematics of a neuron and a simple neural network are presented in Figure 2.20a and b, respectively.

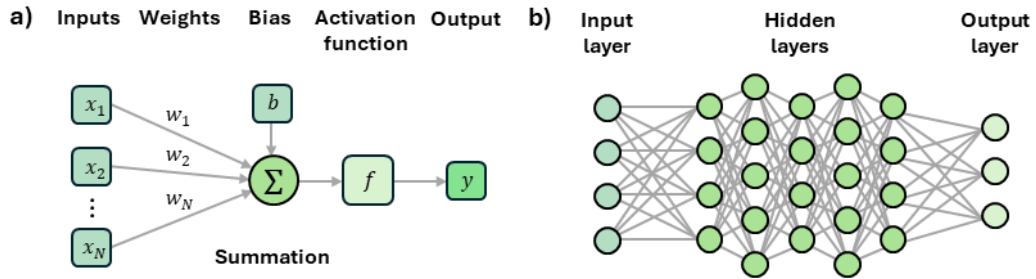


Figure 2.20. Annotated schematic of a) a neuron and b) a simple neural network.

ANNs have been extensively employed as surrogate models for physics-based material models, due to their ability to capture complex, high-dimensional relationships and generalise effectively to unseen data. Among non-interpolating methods, ANNs offer greater adaptability to different input–output patterns through their diverse network architectures. Feed-forward neural networks (FFNNs) are the simplest architecture, where information flows in one direction from the input to output layer. FFNNs are particularly suited for structured, fixed-size predictions, such as to predict the stress–strain response of a viscoplastic RVE model [177] or the plastic anisotropy of CP-simulated texture [178]. In contrast, convolutional neural networks (CNNs) are effective at capturing spatial correlations, making them useful for image-like representations of microstructural data. For instance, Khorrami *et al.* [179] developed a CNN-based surrogate model to predict the von Mises stress fields generated by numerical simulations of polycrystalline microstructures, achieving accurate predictions 500 times faster than the original solver. Another popular architecture is the recurrent neural network (RNN), which is designed to handle sequential or time-dependent data by storing information from previous inputs. Recently, RNNs have been used to predict fracture behaviour from FEM simulations [180] as well as plastic deformation under multiaxial loading simulated by the radial return method [181]. The widespread application of these ANNs underscore their reliability and robustness in surrogate-based calibration of complex material behaviours.

## 2.7. Symbolic regression

Conventional material models, such as those discussed in Section 2.4, are capable of capturing a wide range of material behaviour. However, these models rely on fixed functional forms, which restrict their ability to capture complex or unexpected material behaviours outside of their formulation. These models also require calibration, which can be difficult and computationally prohibitive for more sophisticated formulations. Recent advances in data-driven machine learning methods aim to overcome these limitations by learning constitutive relationships directly from experimental data. Among these approaches, symbolic regression (SR) stands out by generating explicit, interpretable equations that can capture non-linear material behaviours without predefined forms. To explore SR, the following section first outlines the limitations of classical material models (Section 2.7.1). The section then describes the underlying methodology of SR and how it overcomes these limitations (Section 2.7.2), and finally discusses its applications in material modelling (Section 2.7.3).

### 2.7.1. Classical material models

Traditionally, material models were developed to generalise experimentally observed material behaviour through manual trial-and-error methods [182]. Their parameters and functional forms were progressively refined as experiments were performed on a wider range of materials and under more diverse loading conditions. As experimental techniques advanced, researchers gained a deeper understanding of the underlying deformation mechanisms at micro- and mesoscale levels. Incorporating these mechanistic insights into the modelling process enabled researchers to include physically meaningful behaviour — such as dislocation slip, twinning, and void formation — allowing material models to evolve from purely empirical fits (Section 2.4.1) towards more physically informed formulations (Sections 2.4.2 and 2.4.3).

The development of complex materials exhibiting non-linear behaviour has pushed the development of more sophisticated material models [182]. While these models can capture more detailed mechanical responses, their added complexity introduces higher computational cost and greater calibration difficulty, due to larger parameter sets, more intricate constitutive formulations, and the need for a deep understanding of the underlying theoretical framework [182]. In addition, these models are constrained by their fixed functional forms, preventing them from fully utilising the detailed information provided by modern experimental techniques or adapting to material behaviours beyond their original design [182-184]. To overcome these limitations, data-driven machine learning methods have been increasingly employed to extract constitutive relationships from rich experimental datasets without relying on predefined model assumptions.

### 2.7.2. Automated model discovery

Machine learning has emerged as a powerful tool in data-driven constitutive modelling, enabling predictions that extend beyond the capabilities of traditional models. Over the years, machine learning methods such as gradient boost regression, support vector regression, and artificial neural networks have been applied to predict creep rates, time-to-failure, and full creep responses under various stress–temperature conditions [185-188]. These methods have also been applied to predict tensile properties such as ultimate tensile strength, yield strength, and elongation as well as the overall stress–strain response [189-191]. While these studies reported significant improvements over traditional empirical models [187], the resulting models typically function as black-box models that lack interpretability, provide limited insight into the underlying physical mechanisms, and require large experimental datasets to develop.

Among these approaches, symbolic regression (SR) stands out in its ability to discover interpretable mathematical expressions directly from experimental data without predefined assumptions about the model's functional form. The SR process is commonly driven by genetic programming, an evolutionary optimisation technique that evolves a population of candidate expressions through biological operations across multiple generations, similar to the genetic algorithm (Section 2.5.2). The process begins with an initial population of candidate expressions that randomly combine primitive mathematical building blocks, such as variables, constants, operators, and functions. These candidates are often represented as unary-binary expression trees, where nodes represent operators or functions, and leaves represent variables or constants. An example of an expression tree is presented in Figure 2.21, adapted from Makke *et al.* [192].

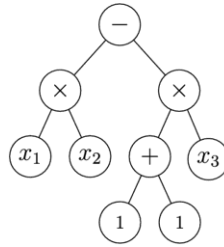


Figure 2.21. Illustration of a unary-binary expression tree that encodes  $f(x) = x_1x_2 - 2x_3$ , adapted from Makke *et al.* [192] by permission of Springer Nature.

Every generation, each candidate in the population is evaluated against two metrics: 1) the agreement of the model's predictions with the experimental data, and 2) the complexity of the mathematical expression based on the number of terms, depth of nested functions, or types of operators [192]. The candidates that achieve the most favourable balance between predictive accuracy and simplicity are combined to produce offspring for the next generation through crossover and mutation operations. The crossover operation involves exchanging subtrees between parent expressions to generate offspring, while the mutation operation involves randomly altering subtrees to explore new functional forms, as illustrated in Figure 2.22 [192]. Together, these operations allow the search process to efficiently explore a vast space of potential functional relationships.

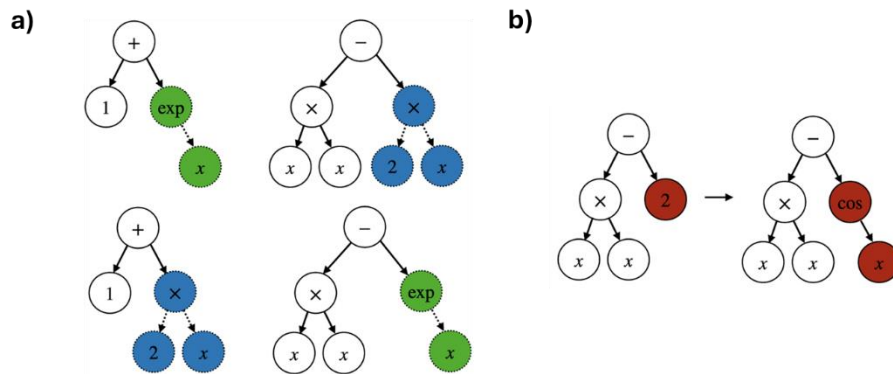


Figure 2.22. Illustrations of the a) crossover and b) mutation operations on exemplary expression trees, adapted from Makke *et al.* [192] by permission of Springer Nature.

Over successive generations, the population of candidates is progressively refined, converging towards expressions that accurately fit the experimental data without becoming unnecessarily complex. By optimising both the functional form and model coefficients, SR provides a powerful means of deriving flexible yet interpretable models directly from experimental data, complementing and extending traditional modelling approaches [193, 194].

### 2.7.3. Applications in material modelling

Although SR has demonstrated success in a variety of scientific domains such as computer, physical, and social sciences, its application in material science has remained relatively limited [193]. This under-utilisation is evident when comparing the number of SR-related contributions to scientific journals from different research fields, as illustrated in Figure 2.23 [193].

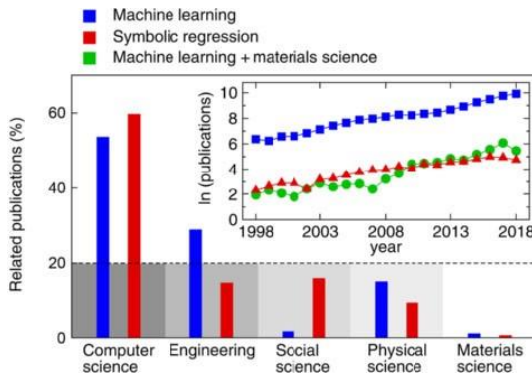


Figure 2.23. Comparison of contributions related to machine learning machine learning and symbolic regression (SR) from different research fields to scientific journals from 1998 to 2018, reproduced from Wang *et al.* [193] by permission of Springer Nature.

However, recent studies have begun to demonstrate the potential of SR in materials science [193]. For instance, Baraldi *et al.* [194] trained SR models to reproduce the creep-rate response from a logistic creep strain model across a wide range of stress–temperature conditions, as shown in Figure 2.24. More recently, Li *et al.* [195] coupled SR with physics-informed constraints to predict the time-to-failure of Ni-based superalloys. The SR-derived equations successfully extended predictions beyond the training data and revealed the mechanistic influence of key microstructural factors, such as  $\gamma'$  phase stability and lattice misfit, on creep behaviour. SR has also been applied to tensile behaviour, with Kabliman *et al.* [196] predicting the stress–strain response of aluminium alloys, and Millner *et al.* [197] predicting the tensile strength of low-carbon steels, which yielded slightly less accurate but more interpretable results compared to artificial neural networks.

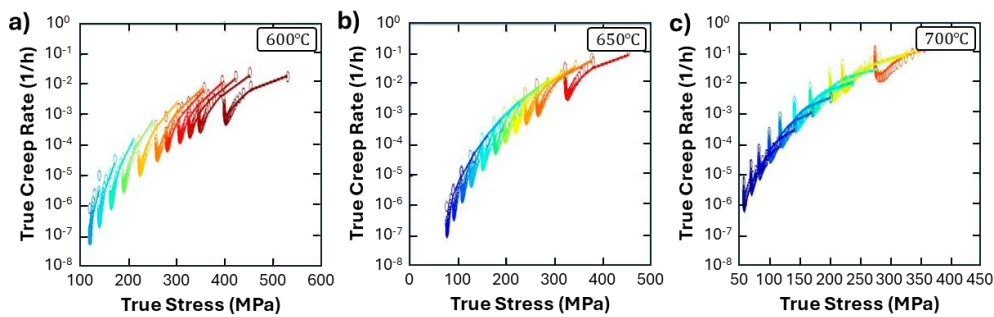


Figure 2.24. Plots of the true creep rate and true stress at a) 600°C, b) 650°C, and c) 700°C, showing the predictions by the symbolic regression (SR) model (lines) and logistic model (ovals). Panels are adapted with permission from D. Baraldi, S. Holmström, K.-F. Nilsson, M. Bruchhausen, and I. Simonovski, *316L(N) Creep Modeling with Phenomenological Approach and Artificial Intelligence Based Methods* [194]; published by MDPI, 2021.

Beyond standalone discovery, SR has also been integrated with established material modelling frameworks to improve their applicability and predictive performance. For instance, Dong *et al.* [198] employed SR as a surrogate model (Section 2.6) to reduce the computational cost of evaluating computationally expensive CPFEM models. Additionally, Subber *et al.* [199] used SR to discover correctional terms for an established predictive corrosion model, applying the Kennedy-O'Hagan method [200] to reduce discrepancies between the model predictions and experimental data. Despite these promising applications, SR remains under-utilised in material science, presenting a valuable opportunity to explore its broader application in material modelling.

## 2.8. Conclusion

The following section provides a brief summary of the review (Section 2.8.1) and highlights the critical gaps in the existing literature (Section 2.8.2).

### 2.8.1. Review summary

Alloy 617 is widely employed in critical engineering systems due to its exceptional thermal stability, mechanical strength, and corrosion-resistance. As such, understanding how the alloy responds to operational, in-service conditions — including its creep and tensile behaviour — is essential for ensuring the safety, reliability, and economic viability of these critical systems. While experimental tests can be performed to characterise the alloy's behaviour under specific conditions, covering the full range of operational conditions is often infeasible due to the extensive time, cost, and resources required, particularly for elevated stress–temperature applications. Material models address this challenge by enabling the prediction of material behaviour across a wide range of conditions while reducing the need for exhaustive experimental testing.

Over the years, various material models have been developed to predict the creep and tensile behaviour of Alloy 617, ranging from simple empirical models that rely on observable experimental trends, to more semi-empirical models that embed simplified physical concepts, and physics-based models that directly represent the governing deformation and degradation processes. In general, models that are more physically grounded provide enhanced predictive accuracy, deeper mechanistic insights, and improved generalisability, but this comes at the cost of higher computational expense and implementation complexity. The deployment of these materials models requires their calibration, which involves identifying suitable constitutive parameter values to align their simulated responses with experimentally observed material behaviour. Optimisation algorithms, such as the multi-objective genetic algorithm (MOGA), are often employed to automate the calibration process.

The main challenge for the calibration of material models with optimisation algorithms is that they typically require a large number of model evaluations, which can be prohibitive for complex semi-empirical and physics-based models that have high computational costs. As such, specialised optimisation strategies — such as active-subspace techniques, multi-stage approaches, and reduced order modelling — are often employed to lower computational costs and simplify the calibration process. A notable strategy is to train a surrogate model to approximate the input–output behaviour of the material model at a fraction of the original computational cost. By replacing the material model with the trained surrogate model during the calibration process, this approach indirectly calibrates the material model using significantly fewer computational resources.

While these material models can capture a wide range of material behaviour, their fixed functional forms, high computational costs, and inherent calibration difficulties limit their practicality for representing complex responses or unexpected behaviours beyond their original formulation. These limitations have motivated increasing interest in data-driven machine learning methods that learn constitutive relationships directly from experimental data. Among these methods, symbolic regression (SR) stands out for its ability to discover explicit, interpretable mathematical expressions without predefined model assumptions.

### 2.8.2. Research gaps

Over the years, significant progress has been made in calibrating material models of varying complexity to capture the creep and tensile behaviour of Alloy 617. However, there are notable areas in the literature that could benefit from further exploration. These gaps are summarised in Table 2.2, with each assigned a label (RG-x) for reference throughout the thesis.

Table 2.2. Summary of research gaps in the literature.

<b>Modelling framework</b>	<b>Research gap</b>	
Empirical and symbolic regression (SR) models	RG-1	Limited use of SR models for the creep prediction for Alloy 617 across a wide stress–temperature range
	RG-2	No assessment of SR models for predicting creep mechanism shifts
	RG-3	Limited evaluation of the robustness of SR models when calibrated with sparse high-temperature datasets
	RG-4	No direct comparison between empirical and SR models for the creep prediction of Alloy 617
Semi-empirical elastic-viscoplastic (EVP) models	RG-5	Limited use of multiple optimisation stages for EVP models
	RG-6	Limited use of multiple objective functions for EVP models
	RG-7	No simultaneous modelling of creep and tensile behaviour using EVP models
	RG-8	No direct comparison between creep damage (CD) and work damage (WD) models
Physics-based crystal plasticity finite element method (CPFEM) models	RG-9	Limited approaches for lowering the development cost of CPFEM surrogate models
	RG-10	Limited use of multiple objective functions for CPFEM model calibration
	RG-11	Limited inclusion of grain-scale metrics in calibration process of CPFEM models
	RG-12	No direct comparison between Voce hardening (VH) and latent hardening (LH) formulations
	RG-13	Limited evaluation of parameter transferability across microstructural fidelities for CPFEM models

While SR has been employed across various domains, its application in material science remains relatively limited, especially for modelling the creep behaviour of Alloy 617. Existing studies primarily employ SR models to predict specific creep characteristics under restricted conditions, without evaluating their ability to handle mechanism shifts. Addressing these limitations is critical for ensuring that SR models can reliably reproduce the deformation behaviour of Alloy 617 across its full range of operating, in service conditions. Additionally, most SR studies rely on comprehensive experimental datasets, in which few studies have assessed the robustness of SR models when trained against sparse datasets, which is crucial since high-temperature data is often expensive and difficult to obtain. Notably, there are no direct comparisons between SR models and established empirical

models for Alloy 617, which can be useful for exploring the applicability and potential advantages of SR models in creep prediction.

Beyond empirical and SR models, semi-empirical elastic-viscoplastic (EVP) models coupled with damage evolution laws have been extensively explored in the literature. However, most existing calibration approaches simultaneously optimise all model parameters using a single objective function. This strategy can lead to inefficient parameter searches and suboptimal parameter sets that fail to capture the intricate interactions between viscoplastic deformation and damage accumulation across different conditions. Additionally, existing work often focuses on capturing either creep or tensile behaviour in isolation, rather than both responses simultaneously. Developing unified models that capture both responses is crucial since in-service components may experience concurrent creep and tensile deformation under complex loading conditions. Furthermore, there exists no direct comparisons of the classical creep damage (CD) and work-based damage (WD) models in the literature, which can be useful for understanding their relative performance and applicability.

At a finer scale, studies on calibrating crystal plasticity finite element method (CPFEM) models often employ surrogate modelling techniques to accelerate their calibration process. However, the development of surrogate models still requires substantial resources, highlighting the need for more efficient strategies. Additionally, existing work has primarily targeted macroscale behaviour, such as the stress–strain response and overall texture evolution. Few studies incorporate multiple objectives and grain-level metrics in the calibration process — such as the rotation of individual grains — which provide critical insight into micromechanical mechanisms that drive plastic deformation. Moreover, few studies evaluate the transferability of calibrated parameters from low- to high-fidelity microstructural models, which is useful for further reducing calibration costs while maintaining predictive accuracy. Finally, no studies directly compare the Voce hardening (VH) and latent hardening (LH) formulations, which can provide critical insight into how different assumptions about slip-system interactions affect predictions of multiscale behaviour.

# Chapter 3

## Research objectives

There remain notable gaps in the literature on the calibration of empirical, symbolic regression (SR), semi-empirical elastic-viscoplastic (EVP) models, and physics-based crystal plasticity finite element method (CPFEM) models for the prediction of creep and tensile behaviour. Research objectives were defined to address these gaps, as summarised in Table 3.1, with each objective (RO-x) aligned to the corresponding gaps (RG-x) identified in Section 2.8.2. The following chapter explains the research objectives in further depth for the empirical and SR models (Section 3.1), EVP models (Section 3.2), and CPFEM models (Section 3.3). The objectives in each section guide the studies presented in Chapter 4, Chapter 5, and Chapter 6, respectively.

Table 3.1. Summary of research objectives for the thesis.

Modelling framework	Research objective		Research gaps
Empirical and symbolic regression (SR) models	RO-1	Evaluate the applicability of SR in predicting mechanism-shifted creep behaviour	RG-1, RG-2
	RO-2	Compare the empirical and SR models for predicting the creep behaviour of Alloy 617 using sparse experimental datasets across a wide stress–temperature range	RG-1, RG-2, RG-3, RG-4
Semi-empirical elastic-viscoplastic (EVP) models	RO-3	Develop a multi-objective multi-stage calibration workflow for EVP models	RG-5, RG-6, RG-7
	RO-4	Compare the creep damage (CD) and work damage (WD) models for predicting the creep and tensile behaviour of Alloy 617	RG-8
Physics-based crystal plasticity finite element method (CPFEM) models	RO-5	Develop a multi-objective surrogate-assisted calibration workflow for the CPFEM models	RG-9, RG-10, RG-11
	RO-6	Compare the Voce hardening (VH), two-coefficient latent hardening (LH2), and six-coefficient latent hardening (LH6) formulations for predicting the multiscale tensile behaviour of Alloy 617	RG-12
	RO-7	Evaluate the transferability of the calibrated parameters across microstructural fidelities	RG-13

### 3.1. Empirical and symbolic regression models

The main objectives for the empirical and SR models are to:

- **Evaluate the applicability of SR in the prediction of mechanism-shifted creep behaviour.** This objective will be achieved by applying SR to reproduce mechanism-shifted strain–time responses, which exhibit atypical behaviour in their tertiary regime attributed to the effects of surface oxidation.

- **Directly compare the accuracy, robustness, and calibration difficulty of empirical and SR models for predicting the creep behaviour of Alloy 617 when calibrated using sparse experimental datasets across a wide range of stress–temperature conditions.** This objective will be achieved by calibrating established empirical models and SR models against experimental data of the minimum creep rate, time-to-failure, strain-to-failure, regular strain–time response, and mechanism-shifted strain–time responses. The empirical and SR models will be calibrated five independent times using twelve experimental datasets across different stress-temperatures conditions. The accuracy, robustness, and calibration difficulty of the calibrated models will then be compared.

The objective will be addressed in Chapter 4, which presents original work focusing on the calibration of the empirical and SR models for predicting the elevated-temperature creep behaviour of Alloy 617.

### *3.2. Semi-empirical elastic-viscoplastic models*

The main objectives for the semi-empirical EVP models are to:

- **Develop a multi-objective multi-stage calibration workflow for EVP models to capture the creep and tensile behaviour of Alloy 617.** This objective will be achieved by defining multiple objective functions for the target features and partitioning the model parameters into groups based on their roles. The performance of the developed workflow will be evaluated in its calibration of the EVP models across ten independent runs.
- **Directly compare the accuracy, robustness, and calibration difficulty of the creep damage (CD) and work damage (WD) models for predicting the creep and tensile behaviour of Alloy 617.** This objective will be achieved by coupling the EVP model with the creep damage (CD) and work damage (WD) models. The coupled EVP-CD and EVP-WD models will then be calibrated using the developed multi-objective multi-stage calibration workflow against the experimental creep and tensile data of Alloy 617. The accuracy, robustness, and calibration difficulty of the calibrated models will then be compared.

These objectives will be addressed in Chapter 5, which adapts work published by the author focusing on the calibration of semi-empirical EVP models for capturing the elevated-temperature creep and tensile behaviour of Alloy 617 [201].

### *3.3. Physics-based crystal plasticity finite element method models*

The main objectives for the physics-based CPFEM models are to:

- **Develop a multi-objective surrogate-assisted calibration workflow for the CPFEM models to capture the multiscale tensile behaviour of Alloy 617.** This objective will be achieved by defining multiple objective functions for the target features and developing an adaptive training strategy for the surrogate model. The performance of the developed workflow will be evaluated in its calibration of the CPFEM models across five independent runs.
- **Directly compare the accuracy, robustness, and calibration difficulty of the Voce hardening (VH), two-coefficient latent hardening (LH2), and six-coefficient latent hardening (LH6) formulations for predicting the multiscale tensile behaviour of Alloy 617.** This objective will be achieved by performing in situ electron backscatter diffraction (EBSD) on an Alloy 617 specimen to obtain experimental data of

the macroscale stress–strain response and grain rotation behaviour. Crystal plasticity (CP) hardening models — i.e., Voce hardening (VH), two-coefficient latent hardening (LH2) and six-coefficient latent hardening (LH6) formulations — will then be coupled with a finite element (FE) model of the specimen. Once coupled, the CPFEM models will be calibrated using the developed multi-objective surrogate-assisted workflow against the experimentally observed stress–strain response, grain reorientation trajectories, and overall texture evolution. The accuracy, robustness, and calibration difficulty of the calibrated models will then be compared.

- **Evaluate the transferability of the calibrated parameters from low- to high-fidelity microstructural FE models.** This objective will be achieved by developed low- and high-fidelity FE models, and coupling them with the VH, LH2, and LH6 formulations. The low-fidelity CPFEM models will then be calibrated using the developed workflow, and the calibrated parameters will be applied to the high-fidelity CPFEM models. The alignment of the low- and high-fidelity CPFEM responses at the calibrated parameters will then be evaluated.

These objectives will be addressed in Chapter 6, which adapts work published by the author focusing on the calibration of CPFEM models for capturing the multiscale tensile behaviour of Alloy 617 [202].

# Chapter 4

## Calibration of empirical and symbolic regression models for the elevated-temperature creep behaviour of Alloy 617

This chapter presents original work that has not been published or included in any prior publication.

### 4.1. *Introduction*

Alloy 617 is widely used in elevated-temperature applications due to its thermal stability, mechanical strength, and corrosion resistance [203]. Under extreme operating conditions, the alloy can experience significant creep damage over its service life, which if left unmanaged, may lead to unexpected failure. Such failures can reduce the operational lifespan of the larger system and compromise its overall economic viability. As such, the ability to predict the creep behaviour and the accumulation of creep damage is of great importance, particularly for engineers involved in the design and maintenance of elevated-temperature systems. Traditionally, empirical material models have been used to predict creep behaviour by establishing relationships between observable material responses in the experimental data. These empirical creep models generally fall into two categories — characteristic-based and strain–time models. Characteristic-based models focus on capturing key creep characteristics (e.g., minimum creep rate, time-to-failure, and strain-to-failure), while strain–time models describe the accumulation of creep strain as a function of time across individual or multiple creep regimes (i.e., primary, secondary, and tertiary). These models predict creep behaviour across various stress–temperature conditions usually by directly incorporating stress and temperature in their functional forms and / or by representing their constitutive parameters as explicit functions of stress and temperature [102, 115].

Today, empirical creep models are still widely used for long-term predictions due to their simplicity, flexibility, and low computational costs [17, 18, 26, 117]. However, the calibration of these models often requires extensive experimental data, which can be time-consuming and expensive to obtain. The accuracy of empirical models also strongly depends on the material, loading conditions, and the specific form of their parameter functions [204]. Additionally, their fixed functional forms prevent them from capturing complex or unexpected behaviours beyond their original design. These limitations not only complicate the calibration of these empirical models but also restrict their predictive capability to novel or untested conditions [15, 16]. Consequently, there is growing interest in data-driven machine learning approaches that can overcome the rigidity of traditional empirical models and better capture complex material behaviours. Among these, symbolic regression (SR) has emerged as a powerful tool for automatically discovering interpretable, constitutive relationships directly from experimental data.

In this study, twelve established empirical material models were calibrated using the genetic algorithm (GA) to predict key creep characteristics (i.e., minimum creep rate, time-to-failure, strain-to-failure) and the overall creep strain–time response (regular and mechanism-shifted) of Alloy 617 across multiple elevated stress–temperature conditions. In parallel, SR was employed to automatically discover alternative constitutive expressions for the same target responses. The empirical and SR models were calibrated five independent times against short-term creep datasets and validated against longer-term datasets to assess their accuracy in

extrapolating beyond the training domain. Overall, the empirical models predicted the creep behaviour fairly accurately but showed heavy reliance on trends in the experimental data. In comparison, the SR models showed higher accuracy in reproducing the short-term creep behaviour, generally improved the longer-term predictions, and showed low variability across independent runs. The SR models also more accurately reproduced the mechanism-shifted strain–time behaviour attributed to the effects of surface oxidation. These results demonstrate the significant potential of SR as a complementary framework to traditional empirical modelling, providing an automated approach that does not rely on the analyst’s prior knowledge for model selection or initial parameter assumptions.

#### 4.2. Experimental data

To support the certification of Alloy 617 for high-temperature nuclear pressure vessel applications, Idaho National Laboratory (INL) conducted a comprehensive suite of creep tests at various stress–temperature conditions [50, 85, 205]. These tests were performed on an as-received, solution-annealed plate of Alloy 617 Heat 314626 manufactured by ThyssenKrupp Vereinigte Deutsche Metallwerke (VDM) [206]. The chemical composition of the Alloy 617 plate is listed in Table 4.1.

Table 4.1. Chemical composition of solution-annealed plate of Alloy 617 Heat 314626 in weight percent [85].

Ni	Cr	Co	Mo	Al	Ti	Fe	Mn	Cu	Si	C	S	B
54.1	22.2	11.6	8.6	1.1	0.4	1.6	0.1	0.04	0.1	0.05	<0.002	<0.001

The creep tests were performed in accordance with ASTM E139-11 [81] under constant temperature and uniaxial stress conditions at 800°C (60MPa, 65MPa, 70MPa, 80MPa), 900°C (26MPa, 28MPa, 31MPa, 36MPa), and 1000°C (11MPa, 12MPa, 13MPa, 16MPa). The minimum creep rate ( $\dot{\varepsilon}_m$ ) from these tests range between  $9.9 \times 10^{-6} \text{ h}^{-1}$  and  $2.33 \times 10^{-4} \text{ h}^{-1}$ . These experimental creep datasets were made available by INL to support the calibration and validation of the empirical and symbolic regression models. In this study, the experimental datasets were employed as strain–time curves to failure, as presented in Figure 4.1.

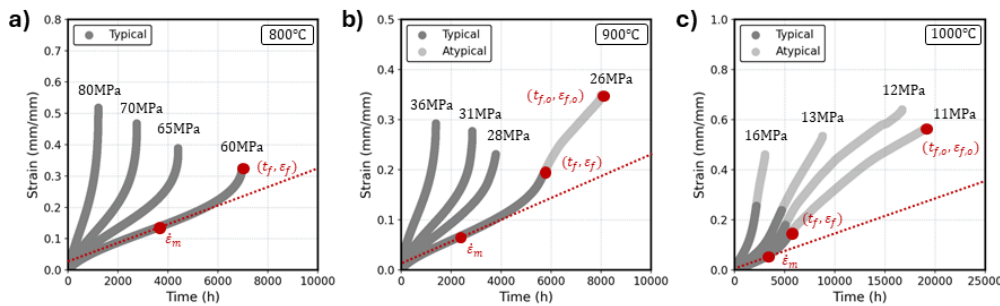


Figure 4.1. Annotated plots of the experimental creep data of Alloy 617 from the Idaho National Laboratory at a) 800°C, b) 900°C, and c) 1000°C. The typical and atypical portions of the creep responses are shown in dark grey and light grey, respectively.

The creep curves in Figure 4.1 show that the creep life of Alloy 617 is predominantly in the secondary and tertiary creep regimes, with a limited amount in the primary regime [50, 205]. Additionally, some of the creep curves exhibit atypical behaviour characterised by a decreasing strain rate in the tertiary regime. This behaviour

is notable in the creep curves at 900°C (26MPa) and 1000°C (11MPa, 12MPa, 13MPa, 16MPa), and is attributed to the creep tests being conducted in air, causing significant surface oxidation [9, 84, 207]. Since oxidation is a diffusion-controlled process, the effects of the surface oxidation are more pronounced at lower stresses as these lead to longer exposure times [207]. The creep curves that were visibly affected by the surface oxidation effects were partitioned at the inflection corresponding to their maximum strain rate — i.e., where the curvature of the strain–time response changes signs from positive to negative. This partitioning strategy was employed to approximately separate the typical creep response from the later-stage atypical behaviour, enabling the assessment of the empirical and symbolic regression models in capturing both the regular creep response as well as the mechanism-shifted behaviour. This partitioning is shown in Figure 4.1, where the typical and atypical portions of the creep response are shown in dark grey and light grey, respectively. Additionally, in these plots,  $t_f$  and  $\varepsilon_f$  represent the time- and strain-to-failure of the typical response, while  $t_{f,o}$  and  $\varepsilon_{f,o}$  represent the true time- and strain-to-failure of the oxidation-affected creep curves.

A summary of the experimental creep datasets is also presented in Table 4.2, where  $T$  represents the temperature and  $\sigma$  represents the applied stress. In this summary, the short-term datasets correspond to the two highest stresses at each temperature, while the longer-term datasets correspond to the two lowest stresses at each temperature.

Table 4.2. Summary of experimental creep data of Alloy 617 from Idaho National Laboratory.

Sample	Time scale	$T$ (°C)	$\sigma$ (MPa)	$\dot{\varepsilon}_m$ ( $10^{-5} \text{h}^{-1}$ )	$t_f$ (h)	$t_{f,o}$ (h)	$\varepsilon_f$ (mm/mm)	$\varepsilon_{f,o}$ (mm/mm)
G32	Longer-	800	60	2.89	6949.7	—	0.328	—
G33	Longer-	800	65	5.04	4404.1	—	0.390	—
G44	Short-	800	70	9.03	2750.7	—	0.468	—
G25	Short-	800	80	23.3	1208.1	—	0.518	—
G59	Longer-	900	26	2.19	5706.1	7983.8	0.193	0.349
G45	Longer-	900	28	3.53	3781.8	—	0.231	—
G50	Short-	900	31	5.37	2846.1	—	0.277	—
G22	Short-	900	36	12.2	1380.4	—	0.293	—
G39	Longer-	1000	11	1.29	5404.8	18923	0.139	0.565
G48	Longer-	1000	12	0.990	5026.9	16696	0.177	0.641
G30	Short-	1000	13	2.66	4688.3	8768.1	0.239	0.535
G18	Short-	1000	16	6.76	2154.6	3034.1	0.255	0.462

### 4.3. Empirical creep models

In this study, twelve empirical models were selected to provide representative examples from the literature for capturing the creep response of Alloy 617 across multiple stress–temperature conditions. The following section outlines the selected empirical models used to predict the minimum creep rate (Section 4.3.1), time-to-

failure (Section 4.3.2), strain-to-failure (Section 4.3.3), and overall strain–time response (Section 4.3.4). A summary of the constitutive parameters for the selected empirical models can be found in Appendix A.1.

#### 4.3.1. Minimum creep rate models

Empirical minimum creep rate models capture the steady-state strain rate and are essential for time-to-failure correlations, creep life extrapolations, as well as the analysis of creep deformation mechanisms. One of the earliest and most widely used empirical models is Norton's power law [11], as expressed in Eq. (4). To account for the influence of temperature, Sherby *et al.* [208] extended this formulation by incorporating an Arrhenius-type temperature dependence. The Norton-Arrhenius model is shown in Eq. (9), where  $R$  represents the universal gas constant (i.e.,  $8.314 \text{ Jmol}^{-1}\text{K}^{-1}$ ) and  $A_{NA}$ ,  $n_{NA}$ , and  $Q_{NA}$  represent the model's three adjustable constitutive parameters.

$$\dot{\epsilon}_m = A_{NA}\sigma^{n_{NA}}\exp(-Q_{NA}/RT) \quad (9)$$

Altenbach *et al.* [209] further extended the Norton-Arrhenius model by introducing a linear term to the power-law dependence to better capture creep behaviour at lower stresses. The Altenbach-Arrhenius model is shown in Eq. (10), where  $A_{AA}$ ,  $B_{AA}$ ,  $n_{AA}$ , and  $Q_{AA}$  are four adjustable parameters.

$$\dot{\epsilon}_m = A_{AA}\sigma(1 + (B_{AA}\sigma)^{n_{AA}})\exp(-Q_{AA}/RT) \quad (10)$$

Another popular approach was introduced by Barnes *et al.* [210] who instead combined the Arrhenius term with Garofalo's hyperbolic-sine law [211] to cover a wider stress range. The Garofalo-Arrhenius model is shown in Eq. (11), where  $A_{GA}$ ,  $\beta_{GA}$ ,  $n_{GA}$ , and  $Q_{GA}$  are the model's four parameters.

$$\dot{\epsilon}_m = A_{GA}\sinh(\beta_{GA}\sigma)^{n_{GA}}\exp(-Q_{GA}/RT) \quad (11)$$

#### 4.3.2. Time-to-failure models

Empirical time-to-failure models estimate the lifespan of materials under operational conditions, which is a primary consideration in high-temperature structural design and component assessment. A popular approach involves the Monkman-Grant relation [105], which correlates the minimum creep rate ( $\dot{\epsilon}_m$ ) with the time-to-failure ( $t_f$ ). The general form of the model assumes an inverse power-law relationship, as shown in Eq. (12), where  $c_{MG}$  and  $m_{MG}$  represent the model's two parameters.

$$t_f = (c_{MG}/\dot{\epsilon}_m)^{m_{MG}} \quad (12)$$

While the minimum creep rate can be used directly as an input to the Monkman-Grant relation, it could also be predicted through a separate constitutive model, such as those described in Section 4.3.1. A notable example is the Dorn-Shepherd model [212], which replaces the minimum creep rate with the Norton-Arrhenius model [113]. The resulting formulation is shown in Eq. (13), where  $D_{DS}$ ,  $n_{DS}$ , and  $Q_{DS}$  are three adjustable parameters which effectively incorporate the original Monkman-Grant parameters (i.e.,  $c_{MG}$  and  $m_{MG}$ ).

$$t_f = D_{DS}\sigma^{-n_{DS}}\exp(Q_{DS}/RT) \quad (13)$$

An alternate approach for time-to-failure predictions involves time-temperature-parameter (TTP) methods, which combine the time-to-failure and temperature into a single parameter to improve extrapolation to

untested conditions. The most prominent TTP method is the Larson-Miller method [100], as shown in Eq. (14), where  $P_{LM}$  represents the Larson-Miller parameter and  $C_{LM}$  represents an adjustable material constant. Other established TTP methods, such as the Orr-Sherby-Dorn [213], Manson-Succop [214], and Manson-Haferd [101] methods, adjust the functional form to improve predictive accuracy for specific materials and temperature ranges. Since TTP methods do not inherently account for multiple stresses, their parameters are often expressed as functions of stress. For the Larson-Miller method, a logarithmic representation has been shown to provide the best fit [215, 216], as presented in Eq. (15) whose parameters are  $a_{LM}$ ,  $b_{LM}$ , and  $c_{LM}$ . Consequently, the combined model contains four adjustable parameters.

$$t_f = \exp(P_{LM}/T - C_{LM}) \quad (14)$$

$$P_{LM} = -a_{LM}\ln(\sigma) - b_{LM}\sigma + c_{LM} \quad (15)$$

#### 4.3.3. Strain-to-failure models

Empirical strain-to-failure models predict the total creep strain accumulated at rupture. These models are less extensively researched compared to other empirical models because strain-to-failure is highly sensitive to the material's microstructure, loading condition, and environmental factors [217]. That said, empirical strain-to-failure models are included in this study for completeness. One of these models was introduced by Dobes *et al.* [218] who incorporated the strain-to-failure into the Monkman-Grant relation [105] to improve correlations between the minimum creep rates and times-to-failure. The Dobes model can be rearranged in terms of the strain-to-failure, as shown in Eq. (16), where  $c_{Do}$  and  $m_{Do}$  are the model's two adjustable parameters.

$$\varepsilon_f = t_f / (c_{Do}/\dot{\varepsilon}_m)^{m_{Do}} \quad (16)$$

A more popular approach was introduced by Evans *et al.* [102] who originally developed the strain-to-failure model within the theta projection framework, which is discussed further in Section 4.3.4. The Evans model is shown in Eq. (17), where  $a_{Ev}$ ,  $b_{Ev}$ ,  $c_{Ev}$ , and  $d_{Ev}$  represent the model's four adjustable parameters. Compared to the Dobes model, the Evans model provides a direct empirical link between the strain-to-failure and the applied stress and temperature.

$$\varepsilon_f = a_{Ev} + b_{Ev}\sigma + c_{Ev}T + d_{Ev}\sigma T \quad (17)$$

More recently, Soares *et al.* [115] extended the Dobes model to provide a more flexible formulation for predicting the strain-to-failure across varying stress–temperature conditions. The Soares model is shown in Eq. (18), where  $a_{So}$ ,  $b_{So}$ ,  $c_{So}$ ,  $d_{So}$ , and  $e_{So}$  are five adjustable parameters.

$$\varepsilon_f = a_{So} + b_{So}/T + c_{So}\sigma/T + d_{So}\log(1/T) + e_{So}\sigma \quad (18)$$

#### 4.3.4. Strain–time models

Empirical strain–time models capture the accumulation of creep strain as a function of time, typically in terms of its individual regimes [108]. In most formulations, primary and tertiary components are additively coupled to form a single unified expression that describes the material's creep response across multiple regimes. These components naturally produce a near-constant strain rate in the intermediate regime, effectively capturing the overall creep response without requiring a separate term for the secondary regime [108]. Additionally, these

models typically only capture the strain–time response at a single stress–temperature condition, requiring parameter functionalisation to extend their applicability across multiple conditions. An example is the omega model [109] shown in Eq. (19), where  $\Omega_{1,0m}$ ,  $\Omega_{2,0m}$ ,  $\Omega_{3,m}$ , and  $\Omega_{4,0m}$  represent the model’s parameters. A common approach to functionalise these parameters is through the Norton–Arrhenius model [102, 204], as given in Eq. (20), with  $A_{i,0m}$ ,  $n_{i,0m}$ ,  $Q_{i,0m}$  denoting the corresponding coefficients for  $i = 1..4$ . The combined model therefore contains a total of 12 adjustable coefficients.

$$\varepsilon = \ln(\Omega_{1,0m}\Omega_{2,0m}t + 1) / \Omega_{2,0m} - \ln(1 - \Omega_{3,0m}\Omega_{4,0m}t) / \Omega_{4,0m} \quad (19)$$

$$\Omega_{i,0m} = A_{i,0m}\sigma^{n_{i,0m}}\exp(-Q_{i,0m}/RT) \quad (20)$$

Another example is the Phi model [106, 219] shown in Eq. (21), with the parameters  $\phi_{1,Ph}$ ,  $\phi_{2,Ph}$ ,  $\phi_{3,Ph}$ , and  $\phi_{4,Ph}$ . Since the model is less commonly used in the literature, the parameters are also functionalised using the Norton–Arrhenius model, which was found through preliminary testing to provide the most consistent and accurate representation among other approaches. The  $\phi_{i,Ph}$  parameters are therefore expressed by Eq. (22) with coefficients  $A_{i,Ph}$ ,  $n_{i,Ph}$ , and  $Q_{i,Ph}$  for  $i = 1..4$ , again giving the model a total of 12 adjustable coefficients.

$$\varepsilon = (\phi_{1,Ph}(1 + \phi_{2,Ph})t)^{1/(1+\phi_{2,Ph})} + (\phi_{3,Ph}(1 - \phi_{4,Ph})t)^{1/(1-\phi_{4,Ph})} \quad (21)$$

$$\phi_{i,Ph} = A_{i,Ph}\sigma^{n_{i,Ph}}\exp(-Q_{i,Ph}/RT) \quad (22)$$

In contrast, one of the most extensively researched empirical strain–time models is the theta projection model [13, 102], shown in Eq. (23), where  $\theta_{1,TP}$ ,  $\theta_{2,TP}$ ,  $\theta_{3,TP}$ , and  $\theta_{4,TP}$  represent the model’s parameters. While the Norton–Arrhenius model could be applied, Evans *et al.* [102] found it impractical for rapid computation in modern finite element frameworks. They instead expressed each parameter as a multilinear expression of stress and temperature terms, as given in Eq. (24), with coefficients  $a_{i,TP}$ ,  $b_{i,TP}$ ,  $c_{i,TP}$ , and  $d_{i,TP}$  for  $i = 1..4$ . This has become a standard approach for the theta projection model, giving a total of 16 adjustable coefficients.

$$\varepsilon = \theta_{1,TP}(1 - \exp(-\theta_{2,TP}t)) + \theta_{3,TP}(\exp(\theta_{4,TP}t) - 1) \quad (23)$$

$$\ln(\theta_{i,TP}) = a_{i,TP} + b_{i,TP}\sigma + c_{i,TP}T + d_{i,TP}\sigma T \quad (24)$$

#### 4.4. Calibration methodology

Empirical and symbolic regression (SR) models were calibrated to capture the minimum creep rate, time-to-failure, strain-to-failure, and strain–time response of Alloy 617 across various elevated stress–temperature conditions. For the empirical models, this involved optimising their constitutive parameters using a genetic algorithm (GA) implemented in the PYMOO library [220]. For the SR models, this involved optimising their functional forms and coefficients using the PySR library [221]. The following section first describes how the experimental datasets are processed and divided into calibration and validation subsets (Section 4.4.1). The section then outlines the GA-based optimisation workflow for the empirical models (Section 4.4.2) as well as the discovery procedure for the SR models (Section 4.4.3).

#### 4.4.1. Data preparation

As discussed in Section 4.2, twelve experimental creep datasets were provided by INL across 800°C, 900°C, and 1000°C. These datasets are divided into two subsets for calibrating and validating the empirical and SR models. Specifically, the models are calibrated using six short-term datasets corresponding to the two highest-stress tests at each temperature. Once calibrated, the models are validated using a separate set of six longer-term datasets corresponding to the two lowest-stress tests at each temperature. This partitioning strategy is employed to assess the models' ability to extrapolate and predict longer-term creep behaviour using only short-term experimental creep data.

Some of the experimental creep datasets exhibited atypical behaviour in the tertiary regime, which was attributed to the effects of surface oxidation [9, 84, 207]. For the calibrations targeting the key creep characteristics, the experimental values are extracted from the typical creep responses that exclude the oxidation-affected behaviour to ensure that the calibration targets reflect the intrinsic material behaviour. This is shown in Figure 4.1, where the minimum creep rate values ( $\dot{\varepsilon}_m$ ) are defined at the secondary regime, while the time- and strain-to-failure values ( $t_f$  and  $\varepsilon_f$ ) are defined at either the point of fracture or at the transition to atypical creep behaviour, whichever comes first. In contrast, the calibrations targeting the strain-time response are performed using two approaches; the first approach only uses the typical creep response with the atypical creep behaviour removed, while the second approach uses the full creep curves that includes both the typical and atypical creep behaviour. These two approaches enable the assessment of the strain-time models in their ability to capture both regular and mechanism-shifted creep behaviour.

Prior to calibrating the empirical and SR models, the stresses and temperatures were normalised by their respective maxima ( $\hat{\sigma} = \sigma/80$  and  $\hat{T} = T/1000$ ) to improve numerical stability and convergence consistency. For the strain-time models, the time values were additionally normalised by the time-to-failure to effectively map each experimental curve onto a normalised domain of  $\hat{t} \in [0,1]$ . This normalisation was performed using  $t_f$  for the regular strain-time curves ( $\hat{t} = t/t_f$ ) and  $t_{f,o}$  for the mechanism-shifted curves ( $\hat{t} = t/t_{f,o}$ ). This scaling focuses the model calibration on how stress and temperature alter the shape of the strain-time curve rather than on its absolute time scale or strain-rate magnitudes.

#### 4.4.2. Parameter optimisation using genetic algorithm

The calibration of an empirical model involves identifying suitable values for their constitutive parameters to align the model's responses with the experimental data. In this study, the empirical models were calibrated using a genetic algorithm (GA; Section 2.5.2) configured with a population size of 500, offspring size of 500, crossover rate of 90%, and mutation rate of 1%. The GA optimisations were terminated after 1000 generations, and the parameters with the lowest objective value were extracted from the final population. The parameter bounds employed for each empirical model are summarised in Appendix A.1.

The empirical characteristic-based models were calibrated directly against the experimental minimum creep rate, time-to-failure, and strain-to-failure values extracted from the typical creep responses (Section 4.4.1). The calibrations for the minimum creep rate were guided by the  $E_{\dot{\varepsilon}_m}$  objective function, which minimises the discrepancy between the steady-state gradient of the experimental and simulated creep curves. The objective

function is defined in Eq. (25), where  $N$  represents the number of datasets,  $\dot{\varepsilon}_{m,exp}$  represents the experimental minimum creep rate, and  $\dot{\varepsilon}_{m,sim}$  represents the simulated minimum creep rate.

$$E_{\dot{\varepsilon}_m} = \sqrt{\frac{1}{N} \sum_{i=1}^N \left( \frac{(\dot{\varepsilon}_{m,exp})_i - (\dot{\varepsilon}_{m,sim})_i}{(\dot{\varepsilon}_{m,exp})_i} \right)^2} \quad (25)$$

The time-to-failure calibrations were guided by the  $E_{t_f}$  objective function, which minimises the horizontal distance between the endpoints of the experimental and simulated creep curves. The objective function is defined in Eq. (26), where  $t_{f,exp}$  represents the experimental time-to-failure and  $t_{f,sim}$  represents the simulated time-to-failure.

$$E_{t_f} = \sqrt{\frac{1}{N} \sum_{i=1}^N \left( \frac{(t_{f,exp})_i - (t_{f,sim})_i}{(t_{f,exp})_i} \right)^2} \quad (26)$$

Additionally, the strain-to-failure calibrations were guided by the  $E_{\varepsilon_f}$  objective function, which minimises the vertical distance between the endpoints of the experimental and simulated creep curves. The objective function is defined in Eq. (27), where  $\varepsilon_{f,exp}$  represents the experimental strain-to-failure and  $\varepsilon_{f,sim}$  represents the simulated strain-to-failure.

$$E_{\varepsilon_f} = \sqrt{\frac{1}{N} \sum_{i=1}^N \left( \frac{(\varepsilon_{f,exp})_i - (\varepsilon_{f,sim})_i}{(\varepsilon_{f,exp})_i} \right)^2} \quad (27)$$

In contrast, the empirical strain–time models were calibrated using a two-stage approach, commonly used in the literature [102, 115, 204]. In the first stage, the parameters of the model were optimised against individual experimental strain–time curves. These parameters were optimised using the  $E_\varepsilon$  objective function, which minimises the common area between the experimental and simulated creep curves, by assessing the strain values of the creep curves at evenly spaced time intervals. The objective function is defined in Eq. (28), where  $M$  represents the number of assessed values,  $\varepsilon_{exp}$  represents an experimental strain value,  $\varepsilon_{sim}$  represents a simulated strain value, and  $\bar{\varepsilon}_{exp}$  represents the average of the experimental strain values. In this study,  $M = 50$  is used to obtain a sufficient approximation of the area while reducing the number of evaluations. Note that the  $\tilde{\varepsilon}$  term is used instead of the  $\tilde{\varepsilon}$  term to prevent the relative errors of the small experimental strain values from dominating the objective value.

$$E_\varepsilon = \sqrt{\frac{1}{NM} \sum_{i=1}^N \sum_{j=1}^M \left( \frac{(\varepsilon_{exp})_{i,j} - (\varepsilon_{sim})_{i,j}}{(\bar{\varepsilon}_{exp})_i} \right)^2} \quad (28)$$

In the second stage, the coefficients of the strain–time model’s parameter functions were optimised against the parameters obtained from the first stage. These coefficients were optimised using the  $E_p$  objective function defined in Eq. (29), where  $p_{opt}$  represents an optimised parameter value from the first stage and  $p_{fun}$  represents the corresponding parameter value evaluated by the parameter function.

$$E_p = \sum_{i=1}^N \left( \frac{(p_{opt})_i - (p_{fun})_i}{(p_{opt})_i} \right)^2 \quad (29)$$

This two-stage procedure greatly simplified the calibration process and reduced its computational burden. Preliminary tests showed that simultaneously optimising all the coefficients of the parameter functions would result in convergence failures due to the excessively large search space.

#### 4.4.3. Model discovery using symbolic regression

Symbolic regression (SR) was employed to automatically discover alternative constitutive expressions to capture the same target responses as the selected empirical models. These expressions were developed as functions of normalised stress and temperature ( $\hat{\sigma}$  and  $\hat{T}$ ) for the characteristic-based models (minimum creep rate, time-to-failure, and strain-to-failure) and as functions of normalised stress, temperature, and time ( $\hat{\sigma}$ ,  $\hat{T}$ , and  $\hat{t}$ ) for the strain–time models. These SR models were developed using the same building blocks in traditional empirical models, which include their input variables ( $\hat{\sigma}$ ,  $\hat{T}$ , and  $\hat{t}$ ), binary operators (i.e., addition, subtraction, multiplication, division, and exponentiation), and unary functions (i.e., exponential and logarithmic). To promote simpler expressions and avoid overfitting, the exponentiation operator was constrained to exclude nested expressions, and the maximum expression size was limited to 32.

The SR search was performed with 50 populations of 50 solutions, over 250 iterations for the characteristic-based predictions and over 1000 iterations for the strain–time predictions. Every iteration, the error of each candidate expression was calculated using the same objective functions as the empirical models —  $E_{\dot{\varepsilon}_m}$ ,  $E_{t_f}$ ,  $E_{\varepsilon_f}$ , and  $E_\varepsilon$ , as defined in Section 4.4.2. The complexity of each expression was also calculated based on the total number of variables (i.e.,  $\hat{\sigma}$ ,  $\hat{T}$ , and  $\hat{t}$ ), operators, and functions. Upon termination, the best expression is selected from the candidate expressions based on how well they balance accuracy and simplicity, thereby ensuring that the final model is both robust and interpretable.

#### 4.5. *Results and discussion*

The empirical and symbolic regression (SR) models were calibrated using experimental creep data of Alloy 617 at 800°C, 900°C, and 1000°C. The models were calibrated against six short-term experimental datasets and validated against six longer-term datasets. The calibrations targeting the minimum creep rate ( $\dot{\varepsilon}_m$ ), time-to-failure ( $t_f$ ), and strain-to-failure ( $\varepsilon_f$ ) used experimental values from the typical creep responses using normalised stress and temperature inputs ( $\hat{\sigma}$  and  $\hat{T}$ ). The strain–time calibrations were performed on both the typical creep responses as well as the full creep responses (including the atypical tertiary behaviour), using normalised time, stress, and temperature inputs ( $\hat{t}$ ,  $\hat{\sigma}$ , and  $\hat{T}$ ). Each calibration was performed five independent times to assess the robustness and variability of the results.

The following section analyses the performance of the empirical and SR models in reproducing the minimum creep rate (Section 4.5.1), time-to-failure (Section 4.5.2), and strain-to-failure (Section 4.5.3). The section then evaluates the models in capturing the typical creep strain–time response (Section 4.5.4) as well as the full, mechanism-shifted creep curves (Section 4.5.5). Finally, the section concludes with a comparison of the overall accuracy, robustness, and consistency of the discussed models across the five calibration runs (Section 4.5.6).

#### 4.5.1. Minimum creep rate predictions

Three empirical models — Norton-Arrhenius, Altenbach-Arrhenius, and Garofalo-Arrhenius models — were calibrated to capture the minimum creep rate ( $\dot{\epsilon}_m$ ) of Alloy 617 across five independent runs. In parallel, SR was applied to discover five alternative constitutive expressions to capture the same stress- and temperature-dependent behaviour. The SR models were calibrated on the log-transformed minimum creep rate values due to their small magnitudes in the calibration datasets (i.e.,  $\sim 10^{-8} \text{ s}^{-1}$ ). The calibration and validation results for the empirical and SR models are presented in Figure 4.2. In this figure, the top row of plots (Figure 4.2a, c, e, and g) compares the experimental and simulated minimum creep rates, with each plot showing the line of best fit (LOBF) for the calibration and validation datasets corresponding to the run that achieved the lowest objective value. In the bottom row, the boxplots (Figure 4.2b, d, and f) present the optimised parameter distributions for the empirical models across the five optimisation runs, while the equations in Figure 4.2h present the constitutive expressions discovered using SR.

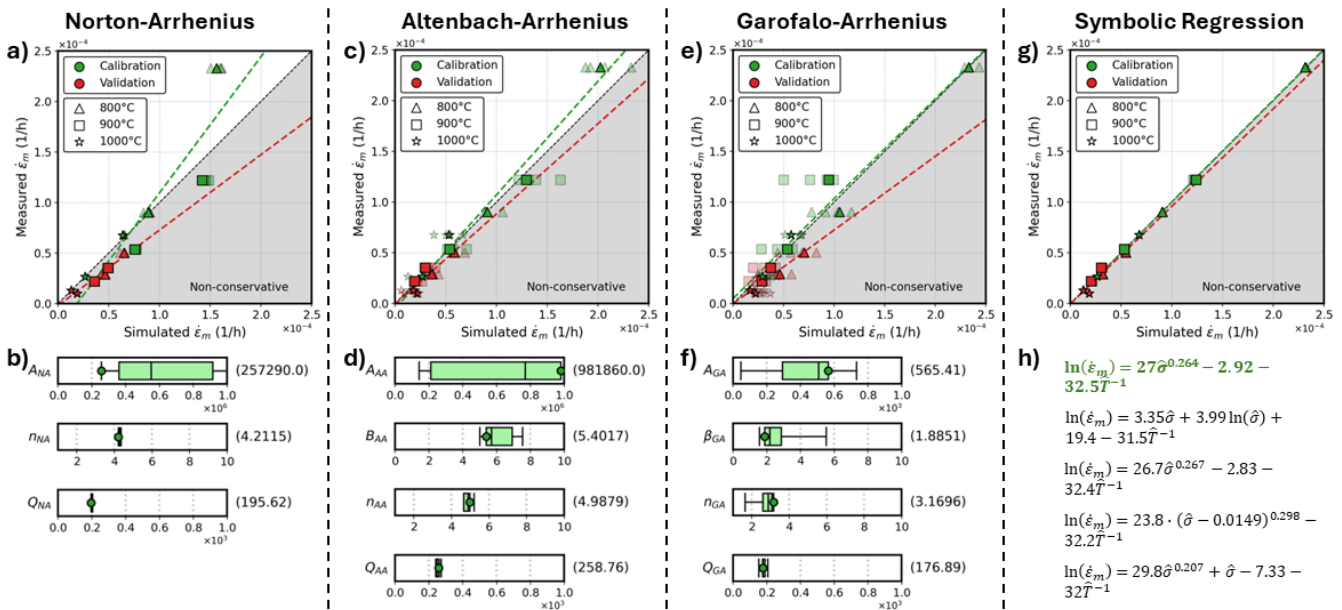


Figure 4.2. Calibration and validation results for the Norton-Arrhenius, Altenbach-Arrhenius, Garofalo-Arrhenius, and symbolic regression (SR) models in predicting the minimum creep rate across five independent runs. Plots a), c), e), and g) compare the experimental and simulated minimum creep rate values for the calibration (green) and validation (red) datasets, with the dashed lines representing the line of best fit (LOBF) corresponding to the run that achieved the lowest objective value. Panels b), d), and f) show the parameter distributions for the empirical models, with the mean (black line), standard deviation (box), range (whiskers), bounds (limits), and best-performing values (green circle and number). Panel h) shows the SR-derived constitutive expressions with the best-performing expression highlighted in green.

The performance of the empirical and SR models was quantified through two metrics — the relative error (RE) to measure the accuracy of the minimum creep rate predictions against the experimental data, and the coefficient of variation (CV) to measure the consistency of the predictions across independent runs. For each model, the RE and CV values were averaged over five runs for the calibration (green) and validation (red) datasets, as presented in Figure 4.3.

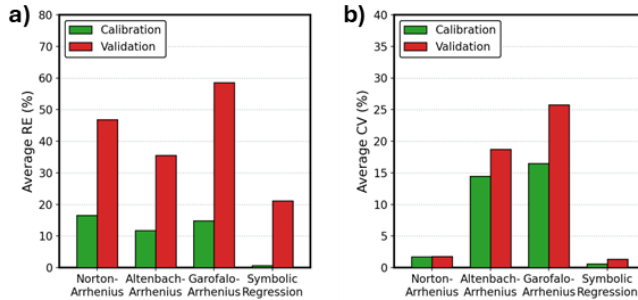


Figure 4.3. Comparison of empirical and symbolic regression (SR) models in reproducing the minimum creep rate from the calibration (green) and validation (red) datasets. Plot a) compares the average relative errors (RE) while plot b) compares the average coefficient of variation (CV).

In general, the empirical models were able to reproduce the minimum creep rates from calibration datasets fairly well across five runs. This is demonstrated by the proximity of the individual symbols to the ideal 1:1 line (Figure 4.2a, c, and e) as well as their RE values that ranged from 11.8% to 16.5% (Figure 4.3a). However, the accuracy was notably lower for the validation datasets due to their exclusion from the calibration process, with REs increasing to 35.5–58.6%. The reduced accuracy also reflects the slight inconsistencies in how the experimentally observed minimum creep rate varies with stress and temperature between the calibration and validation datasets [11, 209]. These inconsistencies are illustrated by the plots of  $\ln(\dot{\epsilon}_m)$  against  $1/\hat{T}$  and  $\ln(\hat{\sigma})$  presented in Figure 4.4. Since all three models rely directly on these trends, their inconsistencies between datasets likely contributed to the models' reduced predictive performance. However, these trends are well defined within the calibration datasets, leading to narrow spreads in the activation energy parameters (i.e.,  $Q_{NA}$ ,  $Q_{AA}$ , and  $Q_{GA}$ ) as well as the stress rate sensitivity parameters (i.e.,  $n_{NA}$ ,  $n_{AA}$ , and  $n_{GA}$ ). In contrast, the other parameters act primarily as scaling factors, producing broader distributions that manifest as higher run-to-run variability in the minimum creep rate values simulated by the Altenbach-Arrhenius and Garofalo-Arrhenius models. This increased variability is demonstrated in Figure 4.3b, with the models showing substantially higher CVs (14.4–25.8%) compared to the Norton-Arrhenius model (~1.7%), particularly for the validation datasets.

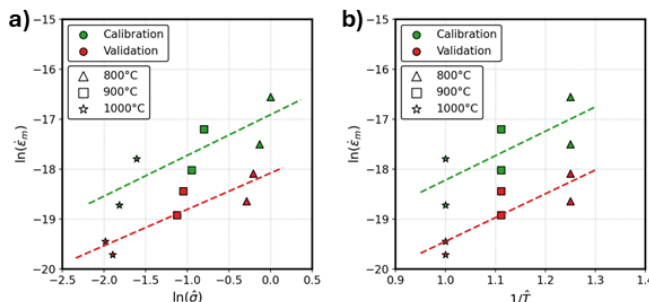


Figure 4.4. Experimental correlations between a)  $\ln(\dot{\varepsilon}_m)$  and  $\ln(\hat{\sigma})$  and b)  $\ln(\dot{\varepsilon}_m)$  and  $1/\hat{T}$  for Alloy 617 at 800°C, 900°C, and 1000°C, showing calibration (green) and validation (red) datasets with dashed lines indicating the lines of best fit (LOBF).

Compared to the empirical models, the SR models showed improved accuracy for both calibration and validation datasets, as reflected by their lower REs in Figure 4.3a (0.6% and 21.1%). The SR models also exhibited significantly lower variability across independent runs, indicated by the reduced scatter of the symbols in Figure 4.2g and the lower CVs (0.6% and 1.3%) in Figure 4.3b. Notably, the discovered expressions were relatively simple and closely resembled conventional empirical forms, incorporating Arrhenius-type  $1/\hat{T}$  dependencies and stress-exponent terms. This resemblance is likely a consequence of the log transformation of the minimum creep rate values, which implicitly enforced an exponential form and power-law relationships. To assess the effect of the transformation, SR was also employed directly to the untransformed minimum creep rate values, as presented in Appendix A.2. In general, this alternate approach yielded similar predictive accuracy but higher run-to-run variability. The resulting expressions were also more complex, containing large exponents (e.g.,  $\hat{\sigma}^{22.2}$ ) and exponential functions to accommodate the small minimum creep rate values. Since the normalisation of the stress and temperature inputs (i.e.,  $\hat{\sigma} = \sigma/80$  and  $\hat{T} = T/1000$ ) constrained them to values  $\leq 1$ , the SR models were stable within the employed calibration and validation ranges. However, extrapolation beyond 80MPa or 1000°C (where  $\hat{\sigma} > 1$  and  $\hat{T} \geq 1$ ) could lead to the significant overprediction of the minimum creep rate values. These results highlight the importance of log-transforming the minimum creep rates for discovering simple, stable, and interpretable expressions.

#### 4.5.2. Time-to-failure predictions

The empirical Monkman-Grant, Dorn-Shepherd, and Larson-Miller models were calibrated five times to capture the time-to-failure ( $t_f$ ) of Alloy 617, while SR was again applied to discover five alternative constitutive expressions. Similar to the minimum creep rate predictions, the SR models were calibrated on the log-transformed time-to-failure values due to their large magnitudes in the calibration datasets ( $\sim 10^7$ s). The calibration and validation results are presented in Figure 4.5, while the average RE and CV values are shown in Figure 4.6.

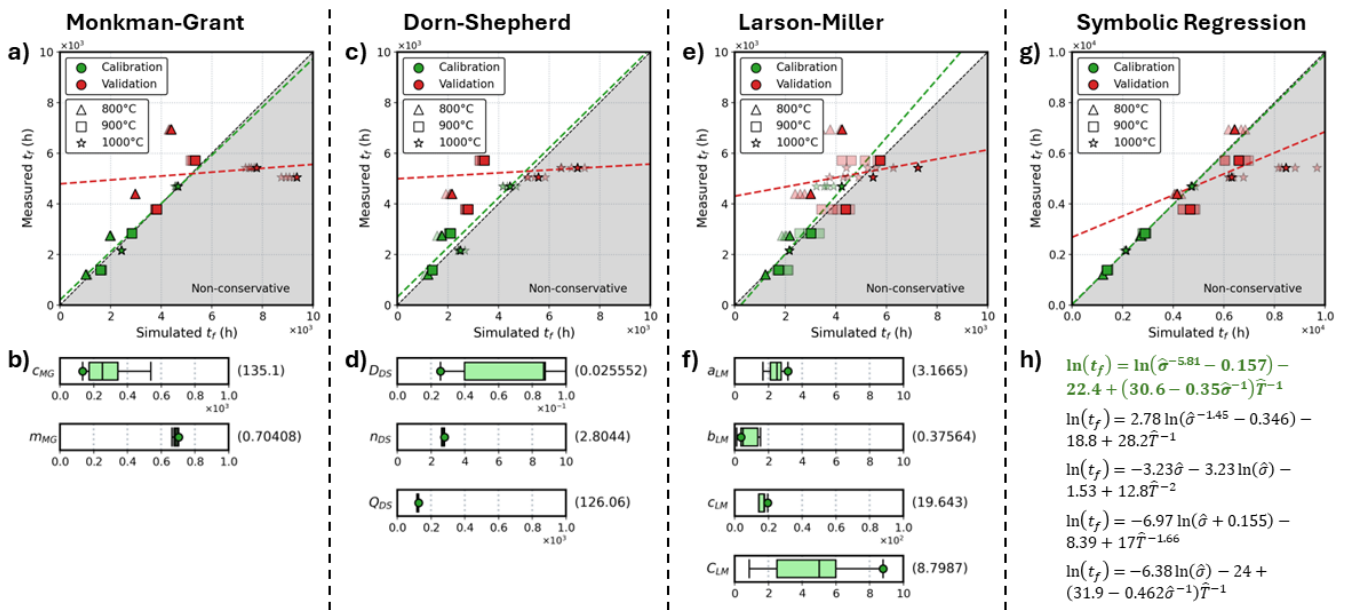


Figure 4.5. Calibration and validation results for the Monkman-Grant, Dorn-Shepherd, Larson-Miller, and symbolic regression (SR) models in predicting the time-to-failure across five independent runs. Plots a), c), e), and g) compare the experimental and simulated time-to-failure values for the calibration (green) and validation (red) datasets, with the dashed lines representing the line of best fit (LOBF) corresponding to the run that achieved the lowest objective value. Panels b), d), and f) show the parameter distributions for the empirical models, with the mean (black line), standard deviation (box), range (whiskers), bounds (limits), and best-performing values (green circle and number). Panel h) shows the SR-derived constitutive expressions with the best-performing expression highlighted in green.

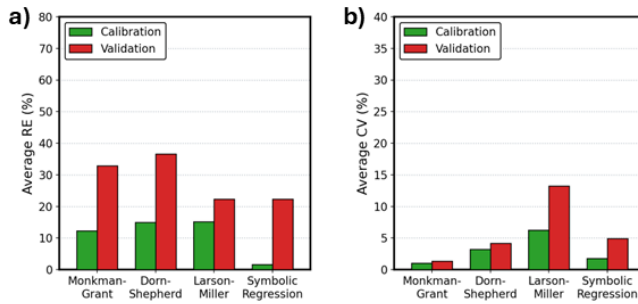


Figure 4.6. Comparison of empirical and symbolic regression (SR) models in reproducing the time-to-failure from the calibration (green) and validation (red) datasets. Plot a) compares the average relative errors (RE) while plot b) compares the average coefficient of variation (CV).

Similar to the minimum creep rate predictions, the empirical models accurately captured the time-to-failure from the calibration datasets, achieving REs of 12.2–15.1% as shown in Figure 4.6a. The models also showed a notable reduction in accuracy for the validation datasets, particularly at 1000°C, with REs increasing to 22.3–36.5%. This reduction again reflects the inconsistencies between the calibration and validation datasets in how  $\ln(t_f)$  varies with  $\ln(\dot{\varepsilon}_m)$ ,  $\ln(\hat{\sigma})$ , and  $1/\hat{T}$ , as shown in Figure 4.7. The relationships in the calibration datasets constrain the parameters of the empirical models. In particular, the  $m_{MG}$  parameter is constrained by the strong linearity between  $\ln(t_f)$  and  $\ln(\dot{\varepsilon}_m)$  [105], and the  $n_{DS}$  and  $Q_{DS}$  parameters are constrained by the relationships

of  $\ln(t_f)$  with  $\ln(\hat{\sigma})$  and  $1/\hat{T}$  [212]. These well-defined trends result in low variability for the Monkman-Grant and Dorn-Shepherd models' responses across independent calibration runs, with CVs of 1.0–4.1% as shown in Figure 4.6b. In contrast, the Larson-Miller parameters are not as well constrained leading to higher run-to-run variability, with CVs of 6.2% and 13.2% for the calibration and validation datasets, respectively.

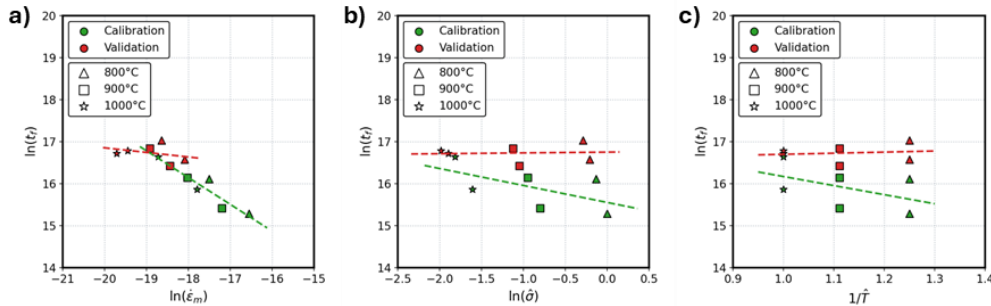


Figure 4.7. Experimental correlations between a)  $\ln(t_f)$  and  $\ln(\dot{\varepsilon}_m)$ , b)  $\ln(t_f)$  and  $\ln(\hat{\sigma})$ , and c)  $\ln(t_f)$  and  $1/\hat{T}$  for Alloy 617 at  $800^\circ\text{C}$ ,  $900^\circ\text{C}$ , and  $1000^\circ\text{C}$ , showing calibration (green) and validation (red) datasets with dashed lines indicating the lines of best fit (LOBF).

The SR models showed improved accuracy in the time-to-failure predictions compared to the empirical models, with lower REs for the calibration (1.6%) and validation datasets (22.3%), as shown in Figure 4.6a. The models also showed comparably low variability to the Monkman-Grant and Dorn-Shepherd models, with CVs of 1.7% and 4.9%, as shown in Figure 4.6b. Furthermore, many of the discovered expressions contained Arrhenius-type  $1/\hat{T}$  dependencies and stress-exponent terms, similar to those found in the minimum creep rate models, reflecting the intrinsic relationship between the two properties. Applying SR to the untransformed time-to-failure values (Appendix A.2) yielded comparable accuracy but higher run-to-run variability. The expressions also contained extreme exponents (e.g.,  $\hat{T}^{-44.9}$ ) that become unstable beyond the employed calibration and validation ranges, again underscoring the importance of log-transforming the time-to-failure values.

#### 4.5.3. Strain-to-failure predictions

The empirical (Dobes, Evans, and Soares) and SR models were calibrated to capture the strain-to-failure ( $\varepsilon_f$ ) of Alloy 617. Unlike the minimum creep rate or time-to-failure predictions, SR was applied directly on the strain-to-failure values since they do not span extreme magnitudes. The calibration and validation results are presented in Figure 4.8 and Figure 4.9.

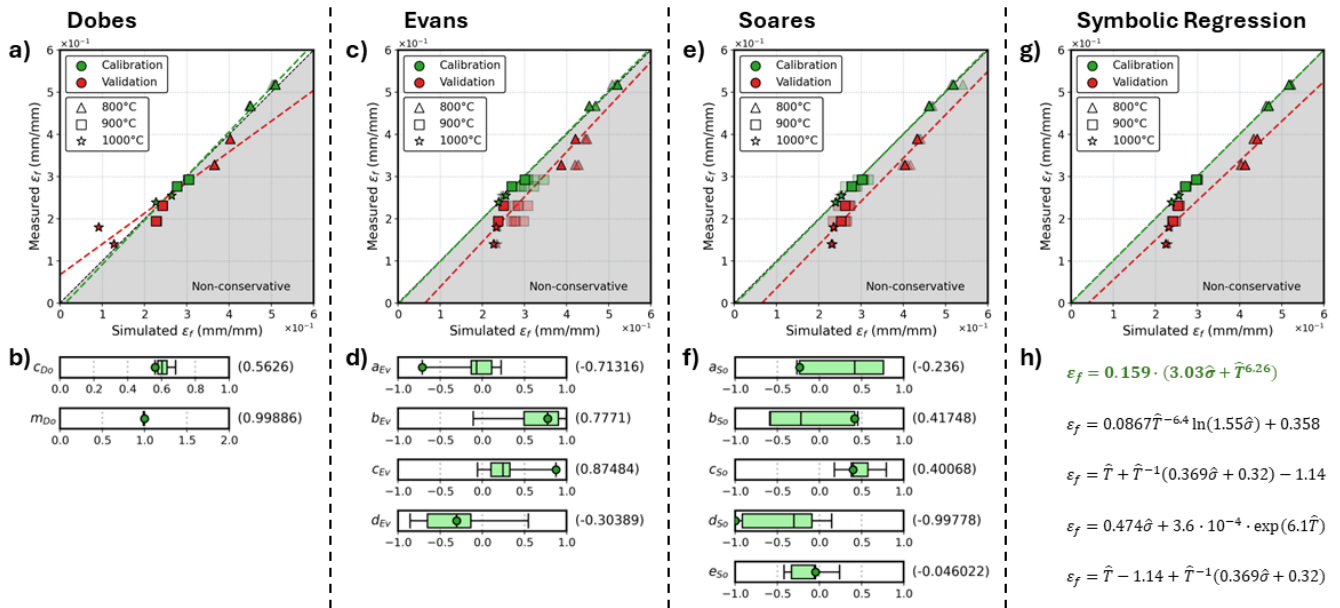


Figure 4.8. Calibration and validation results for the Dobes, Evans, Soares, and symbolic regression (SR) models in predicting the strain-to-failure across five independent runs. Plots a), c), e), and g) compare the experimental and simulated strain-to-failure values for the calibration (green) and validation (red) datasets, with the dashed lines representing the line of best fit (LOBF) corresponding to the run that achieved the lowest objective value. Panels b), d), and f) show the parameter distributions for the empirical models, with the mean (black line), standard deviation (box), range (whiskers), bounds (limits), and best-performing values (green circle and number). Panel h) shows the SR-derived constitutive expressions with the best-performing expression highlighted in green.

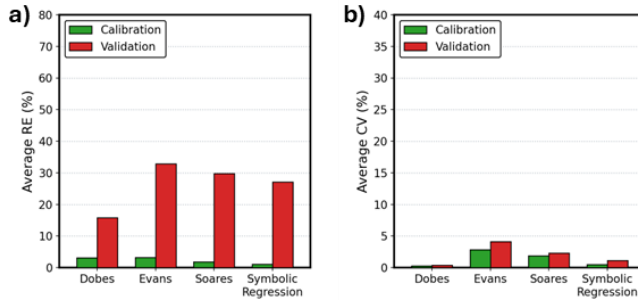


Figure 4.9. Comparison of empirical and symbolic regression (SR) models in reproducing the strain-to-failure from the calibration (green) and validation (red) datasets. Plot a) compares the average relative errors (RE) while plot b) compares the average coefficient of variation (CV).

As seen in Figure 4.9a, the empirical models accurately reproduced the strain-to-failure for the calibration datasets, with REs of 1.8–3.2%, but showed significantly reduced accuracy for the validation datasets, where REs increased to 15.8–32.8%. Additionally, the LOBFs in Figure 4.8a, c, and e show that the strains-to-failure in the validation datasets were consistently overpredicted. Between the models, the Dobes model shows the highest validation accuracy (RE of 15.8%; Figure 4.9a) and lowest variability (CV of 0.3–0.4%; Figure 4.9b), owing to the strong linear relationship between  $\varepsilon_f$  and  $\dot{\varepsilon}_m t_f$  and the similarity of this relationship across calibration and validation datasets, as shown in Figure 4.10. The linear relationship also tightly constrained the model's parameters, resulting in the narrow distributions of  $c_{D_0}$  and  $m_{D_0}$  (Figure 4.8b) and the consistent convergence

of  $m_{Do}$  towards unity [218]. In contrast, the Evans and Soares models show broader spreads and slightly higher CVs of up to 4.1% (Figure 4.9b), suggesting that the models are over-parameterised, with interdependent terms compensating for one another. This over-parameterisation likely contributed to the higher validation errors observed for the Evans and Soares models, whose flexible functional form make them more prone to overfitting compared to the Dobes model.

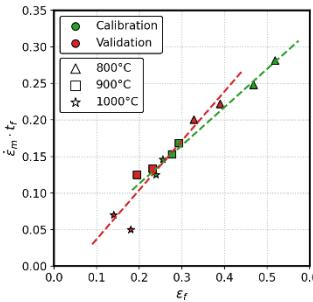


Figure 4.10. Experimental correlations between  $\dot{\varepsilon}_m \cdot t_f$  and  $\varepsilon_f$  for Alloy 617 at 800°C, 900°C, and 1000°C, showing calibration (green) and validation (red) datasets with dashed lines indicating the lines of best fit (LOBF).

Unlike the other target responses, the SR models did not outperform the empirical models in reproducing the experimental strain-to-failure values, with REs of 0.4% and 30.6% for the calibration and validation datasets, respectively (Figure 4.9a). The SR models also exhibited low run-to-run variability, with CVs of 0.3% and 0.9%, which is comparable to the empirical models (Figure 4.9b). In addition, the SR-derived expressions were relatively simple and did not contain steep functional forms, likely due to the narrow range of the strain-to-failure values. Consequently, calibrating the SR models against the log-transformed strain-to-failure values (Appendix A.2) offered no noticeable improvement in predictive accuracy, simplicity, or stability.

#### 4.5.4. Regular strain–time predictions

The empirical omega, phi, and theta projection models were calibrated to capture the regular strain–time response of Alloy 617 which excluded the atypical behaviour in the tertiary regime. In these calibrations, the time-to-failure was considered at either the fracture point or the transition point to atypical behaviour, whichever came first. The time values were thus normalised using  $\hat{t} = t/t_f$  to map the experimental creep curves onto a domain of  $\hat{t} \in [0,1]$ . Initially, attempts were made to simultaneously optimise all the coefficients of each model’s parameter functions. However, the simple single-stage calibration process consistently failed to reliably describe the experimental data due to the high dimensionality of the models’ parameter search spaces. As such, the strain–time models were instead calibrated following a two-stage approach that involved 1) optimising the parameters of the model against individual strain–time curves, then 2) optimising the coefficients of the parameter functions against the resulting parameter sets.

This two-stage calibration approach was applied five times for each empirical strain–time model. The results for the omega model are presented in Figure 4.11, while the results for the phi and theta projection models can be found in Appendix A.3. The top row of these figures (a-c) shows the experimental and simulated strain–time responses across 800°C, 900°C, and 1000°C, while the bottom row (d) shows the coefficient distributions for the model’s parameter functions from five optimisation runs. In parallel to the calibrations of the empirical

strain–time models, SR was applied to obtain five alternative constitutive expressions, formulated in terms of normalised time, stress, and temperature. The results for the SR models are presented in Figure 4.12, showing the strain–time responses across all three temperatures (Figure 4.12a-c) as well as the discovered expressions (Figure 4.12d). Additionally, the RE and CV values for the empirical and SR models were calculated at 32 equally spaced time intervals for each curve and averaged across all the curves in each dataset over five runs, as shown in Figure 4.13.

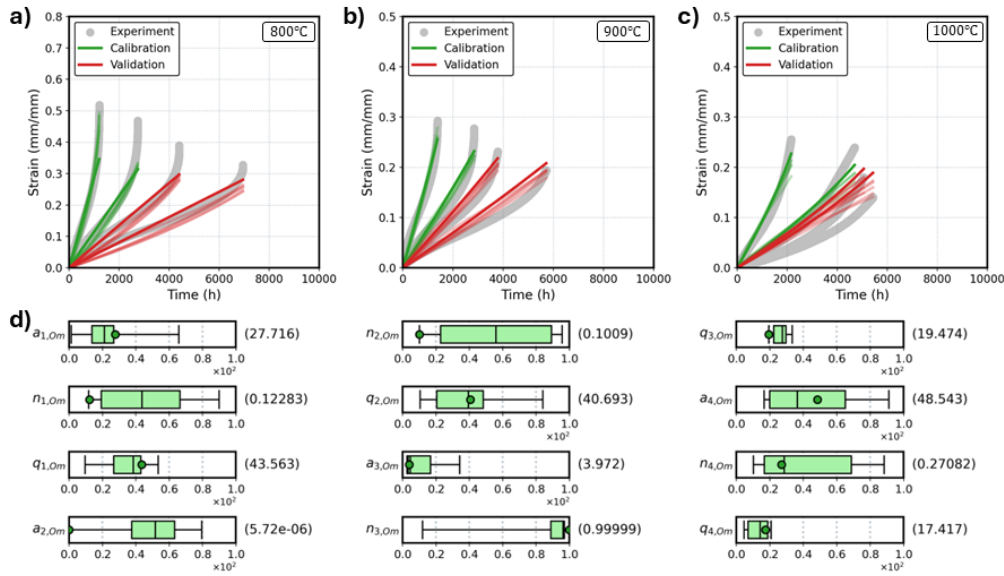


Figure 4.11. Calibration and validation results for the omega model in predicting the regular strain–time response across five independent runs. Plots a), b), and c) compare the experimental and simulated strain–time curves at 800°C, 900°C, and 1000°C, respectively, for the calibration (green) and validation (red) datasets. Panels d), e), and f) show the model’s parameter distributions, with the mean (black line), standard deviation (box), range (whiskers), bounds (limits), and best-performing values (green circle and number).

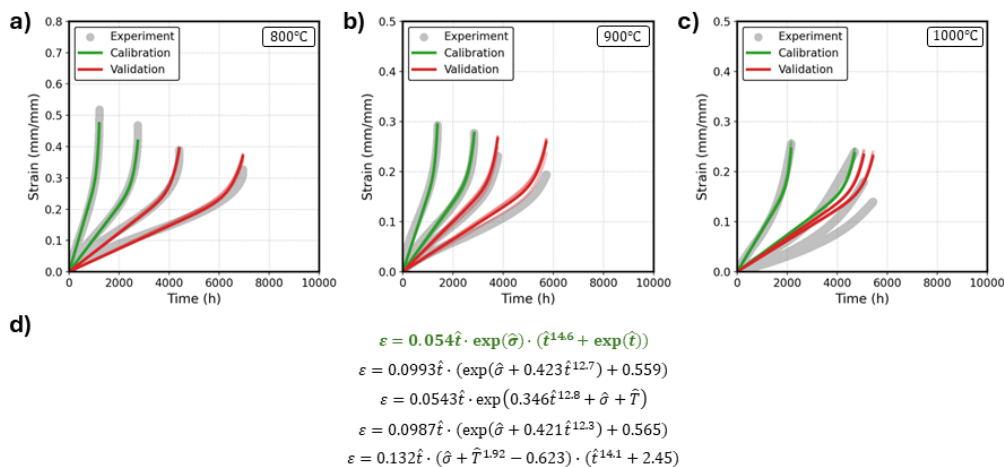


Figure 4.12. Calibration and validation results for the symbolic regression (SR) model in predicting the regular strain–time response across five independent runs. Plots a), b), and c) compare the experimental and simulated strain–time

curves at 800°C, 900°C, and 1000°C, respectively, for the calibration (green) and validation (red) datasets. Panel d) shows the SR-derived constitutive expressions with the best-performing expression highlighted in green.

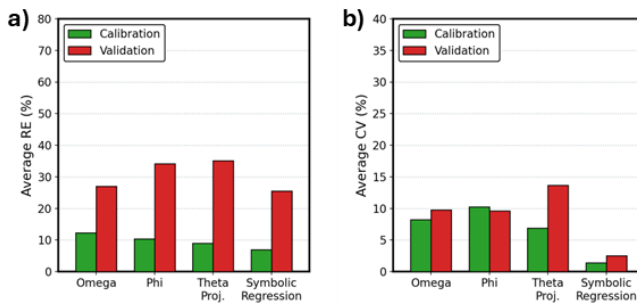


Figure 4.13. Comparison of empirical and symbolic regression (SR) models in reproducing the regular strain–time responses from the calibration (green) and validation (red) datasets. Plot a) compares the average relative errors (RE) while plot b) compares the average coefficient of variation (CV).

All three empirical models accurately and consistently reproduced the individual creep curves across during the first calibration stage, achieving average RE values below 5% for all the curves. However, their accuracy decreased when the models were extended across multiple stresses and temperatures in the second stage, with REs increasing to 8.9–12.3% for the calibration datasets (Figure 4.13a). The empirical models tended to underrepresent the characteristic curvatures of the creep regimes, most noticeable in the primary regime, reflecting the limited primary creep present in the experimental data [50, 205]. For the validation datasets, the REs further increased to 27.0–35.1% (Figure 4.13a), and the models consistently overpredicted the strain values, most notably at 1000°C. Across five calibration runs, the omega model showed broader parameter distributions compared to the phi and theta projection models. However, all three models exhibited similarly high run-to-run variability in their simulated strain–time responses, with CVs ranging from 6.9–10.3% and 9.6–13.6% for the calibration and validation datasets, respectively (Figure 4.13b). This variability reflects the dependence of the empirical models on the uniqueness of the first-stage parameters, where variations in their values carry over into the coefficients in the second stage. These results also suggest that the bounds for the second-stage coefficients were poorly defined, highlighting the importance of specifying tighter coefficient bounds for individual parameters rather than applying uniform constraints across all parameters.

The simulated strain–time responses from the SR models closely aligned with the experimental data at 800°C and 900°C. Additionally, the SR models showed slightly higher overall accuracy compared to the empirical models, with REs of 6.9% and 25.5% for the calibration and validation datasets, respectively (Figure 4.13a). While the SR models continued to underrepresent the primary regime, they more accurately reproduced the curvature across the secondary and tertiary regimes. The SR models achieved this by using a multiplicative  $\hat{t}$  term to represent the near-constant strain rate of the secondary regime as well as high time exponents (12-15) to reproduce the accelerated strain growth in the tertiary regime. Notably, the discovered expressions were simple and compact, containing very few terms. The expressions were also relatively consistent across independent SR runs, resulting in low run-to-run variability across all three temperatures (CVs of 0.5% and 1.1%; Figure 4.13b). However, at 1000°C, the SR models showed reduced accuracy and, similar to the empirical models, overpredicted the strain values for the validation datasets. These discrepancies likely arise from residual surface

oxidation effects which the employed partitioning strategy (Section 4.2) could not fully exclude. Notably, some of the SR-derived expressions (i.e., first, second, and fourth) are independent of temperature, suggesting that the normalised strain–time response of Alloy 617 is governed primarily by stress within the calibrated temperature range, with temperature effects largely absorbed by the normalisation procedure (i.e.,  $\hat{t} = t/t_f$ ).

#### 4.5.5. Mechanism-shifted strain–time predictions

The empirical strain–time models were calibrated using the same two-stage approach to capture the full, mechanism shifted strain–time response of Alloy 617, which included the atypical tertiary behaviour attributed to surface oxidation effects [9, 84, 207]. SR was then applied five times to capture the same target response. In these calibrations, the time values were normalised as  $\hat{t} = t/t_{f,o}$  for the creep curves that were affected by the surface oxidation effects, and as  $\hat{t} = t/t_f$  for the unaffected curves, effectively mapping all responses onto the same domain of  $\hat{t} \in [0,1]$ . The results for the omega and SR models across five runs are presented in Figure 4.14 and Figure 4.15, respectively, while the results for the phi and theta projection models can be found in Appendix A.4. Additionally, the RE and CV values for the empirical and SR models are presented in Figure 4.16.

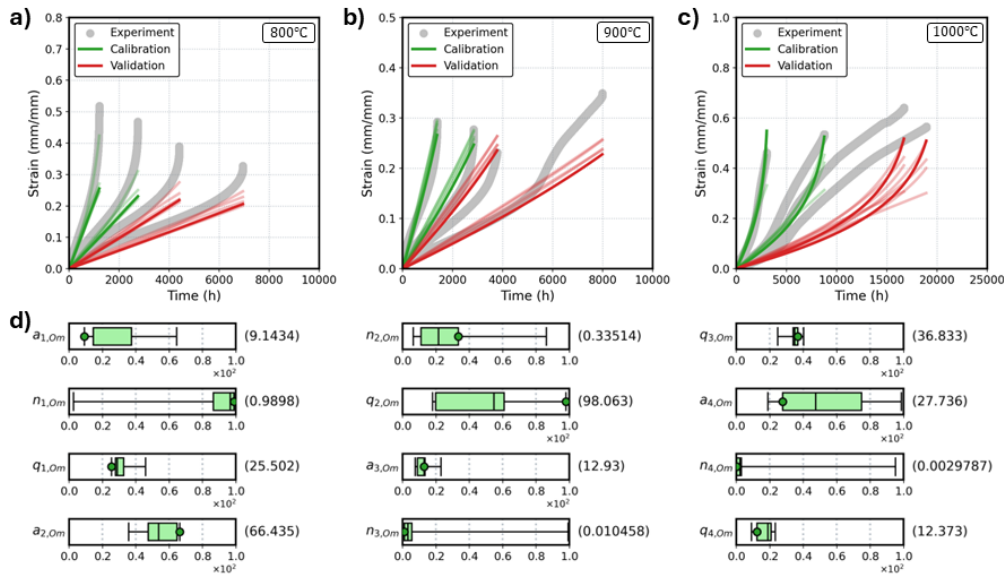


Figure 4.14. Calibration and validation results for the omega model in predicting the mechanism-shifted strain–time response across five independent runs. Plots a), b), and c) compare the experimental and simulated strain–time curves at 800°C, 900°C, and 1000°C, respectively, for the calibration (green) and validation (red) datasets. Panels d), e), and f) show the model's parameter distributions, with the mean (black line), standard deviation (box), range (whiskers), bounds (limits), and best-performing values (green circle and number).

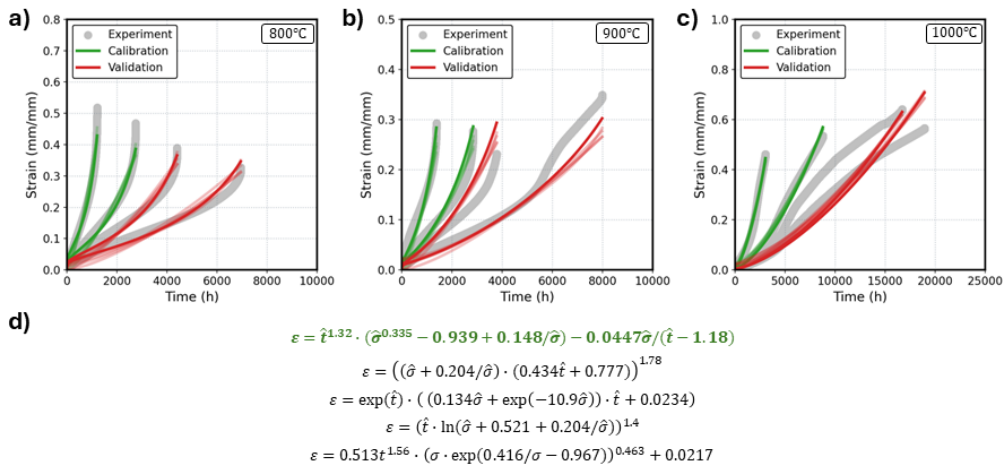


Figure 4.15. Calibration and validation results for the symbolic regression (SR) model in predicting the mechanism-shifted strain–time response across five independent runs. Plots a), b), and c) compare the experimental and simulated strain–time curves at 800°C, 900°C, and 1000°C, respectively, for the calibration (green) and validation (red) datasets. Panel d) shows the SR-derived constitutive expressions with the best-performing expression highlighted in green.

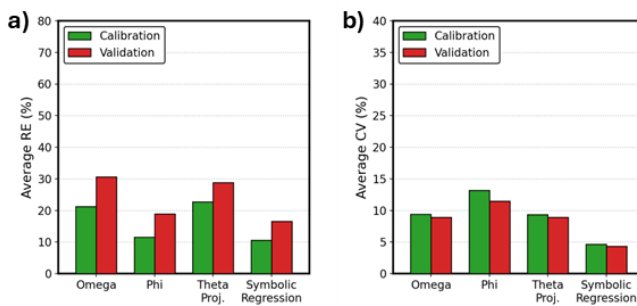


Figure 4.16. Comparison of empirical and symbolic regression (SR) models in reproducing the mechanism-shifted strain–time responses from the calibration (green) and validation (red) datasets. Plot a) compares the average relative errors (RE) while plot b) compares the average coefficient of variation (CV).

In the first calibration stage, the empirical models accurately reproduced the regular strain–time behaviour but failed to capture the mechanism-shifted curves. These discrepancies carried over to the second stage where the model was extended across multiple stress–temperature conditions, reducing the accuracy of both the regular and mechanism-shifted responses. This is reflected in their higher RE values for the calibration datasets (11.5–22.7%; Figure 4.16a) compared to those for the regular strain–time predictions (8.9–12.3%; Figure 4.13a). The reduced accuracy is expected, since the empirical models were not formulated to account for the atypical accumulation of creep plasticity measured in the experiments. Despite this, the models showed similar run-to-run variability to the regular strain–time predictions, with CVs of 9.3–13.2% and 8.9–11.5% for the calibration and validation datasets, respectively (Figure 4.16b).

In contrast, the SR models showed higher accuracy (REs of 10.6% and 16.5%; Figure 4.16a) and lower run-to-run variability (CVs of 4.7% and 4.3%; Figure 4.16b) compared to all three empirical models. While the SR models captured the strain–time responses at 800°C reasonably well, their performance deteriorated at 900°C and 1000°C, particularly for the mechanism-shifted curves. To improve model performance, the mechanism-shifted

curves were renormalised using  $\hat{t} = t/t_f$  (baseline time-to-failure) instead of  $\hat{t} = t/t_{f,o}$  (actual time-to-failure), so that  $\hat{t} \in [0,1]$  corresponds to the typical creep response,  $\hat{t} = 1$  corresponds to the shift in the dominant deformation mechanism, and  $\hat{t} > 1$  corresponds to the atypical, oxidation-driven behaviour. This alternate approach fixes the mechanism shift point to a consistent value across all curves, enabling the SR algorithm to more easily discover a single expression that behaves differently before and after the shift. The calibration results using this approach are presented in Figure 4.17.

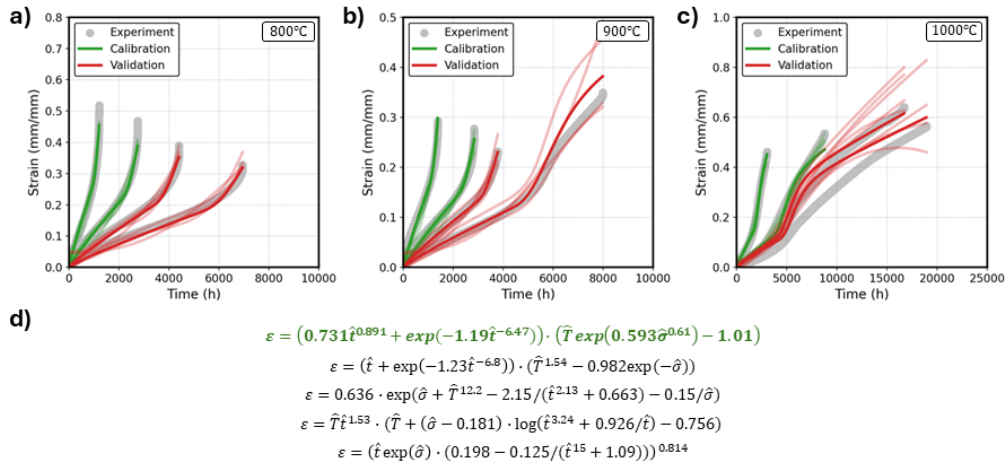


Figure 4.17. Supplementary calibration and validation results for the symbolic regression (SR) model in predicting the mechanism-shifted strain–time response across five independent runs using renormalised time values. Plots a), b), and c) compare the experimental and simulated strain–time curves at 800°C, 900°C, and 1000°C, respectively, for the calibration (green) and validation (red) datasets. Panel d) shows the SR-derived constitutive expressions with the best-performing expression highlighted in green.

Compared to the initial SR modelling approach (Figure 4.15), the alternate approach more effectively reproduced the curvatures of the individual regimes in both the regular and mechanism-shifted strain–time responses. This is reflected in their lower REs for both the calibration (7.4%) and validation datasets (13.4%). The approach also showed a clearer transition from regular to oxidation-induced behaviour in the mechanism-shifted curves. However, the curves showed substantially higher run-to-run variability (CVs of 15.6% and 26.0%) and the post-shift response from the validation datasets at 1000°C still showed notable discrepancies. Moreover, applying this approach to capture mechanism-shifted curves requires the times-to-failure corresponding to the regular (oxidation-unaffected) creep responses under the same stress–temperature conditions. While this study approximates those values by excluding the oxidation-affected portions from the creep curves (Section 4.2), such an approximation may be unreliable in practice, which limits the practicality of this alternate approach.

#### 4.5.6. Comparison of empirical and symbolic regression models

For the minimum creep rate, time-to-failure, and strain-to-failure predictions, the empirical models exhibited higher accuracy and lower run-to-run variability in reproducing the short-term creep behaviour (i.e., calibration datasets) compared to the longer-term behaviour (i.e., validation datasets). Notably, the accuracy of the empirical models showed no clear correlation with their number of adjustable parameters, demonstrating that

greater model complexity does not inherently enhance generalisability. Instead, the empirical models with more parameters generally exhibited greater run-to-run variability in their simulated responses, reflecting the increased calibration difficulty associated with higher dimensional parameter spaces. The variability of the models is also influenced by how effectively their functional forms capture the well-defined trends in the calibration datasets. In particular, the low variability of the Norton-Arrhenius and Dorn-Shepherd models arises from the log-linear dependence of their target responses on stress and temperature. Among the empirical models, the Monkman-Grant and Dobes models exhibit the lowest variability, owing to their inclusion of properties (i.e., minimum creep rate and time-to-failure) that follow strongly linear trends in the data (i.e.,  $\ln(t_f)$  versus  $\ln(\dot{\varepsilon}_m)$  in Figure 4.7 and  $\varepsilon_f$  versus  $\dot{\varepsilon}_m t_f$  in Figure 4.10). That said, reliance on these properties can limit practicality, since they often require additional testing or prior knowledge, which may not be readily available. Compared to the empirical models, the SR models more accurately reproduced the short-term creep behaviour, owing to their more flexible and adaptable functional forms. The SR models also showed higher accuracy for the longer-term minimum creep rate and time-to-failure predictions, which is particularly valuable since long-term experiments are often time-consuming and costly, in which reliable predictions can reduce the need for extensive testing. In contrast, the SR models showed comparable accuracy for the longer-term strain-to-failure predictions, highlighting the persisting risk of overfitting the calibration data. That said, the SR models showed low run-to-run variability across all three target responses, demonstrating strong reproducibility and model stability across independent runs. Additionally, the discovered expressions were generally simple, with those derived from the log-transformed minimum creep rate and time-to-failure data resembling conventional empirical forms. Notably, when SR was applied directly to the untransformed minimum creep rate and time-to-failure values (Appendix A.2), the predictions showed greater run-to-run variability. In addition, the resulting expressions were more complex and adopted numerically unstable functional forms to accommodate the extreme magnitudes of the target values. Although these alternate expressions performed adequately within the calibration and validation ranges, they risk overpredicting the responses when extrapolated beyond 80MPa or 1000°C, underscoring the importance of appropriate data scaling.

For the regular strain-time responses, all three empirical models reproduced the short-term behaviour reasonably well but showed a moderate decline in accuracy for the longer-term predictions. The models also showed comparably high variability across independent runs, reflecting their reliance on the uniqueness of the optimised parameters during their first calibration stage. Between the empirical models, the theta projection model exhibited the highest accuracy in reproducing the short-term responses but the lowest accuracy in the longer-term responses, suggesting that the increased flexibility of the model's parameter function made it more prone to overfitting. When the full, mechanism-shifted creep curves were included, all three models showed reduced accuracy and higher run-to-run variability for the short-term predictions. This degradation in performance underscores the inability of the models to account for the atypical accumulation of creep plasticity measured in the experiments. Compared to the empirical models, the SR models exhibited higher accuracy and lower run-to-run variability for both the regular and mechanism-shifted strain-time responses. For the regular responses, the SR models more effectively captured the characteristic curvatures of the individual creep regimes, yielding compact and interpretable expressions. While the SR models similarly outperformed the empirical models for the mechanism-shifted responses, they still struggled to reproduce the post-shift response. To address this, an alternate approach (Figure 4.17) was employed to renormalise the mechanism-shifted curves

so that  $\hat{t} \in [0,1]$  corresponds to the typical creep response and  $\hat{t} > 1$  corresponds to the atypical behaviour. Although the alternate approach more effectively captured the curvature of the creep curves and the transition between typical and atypical behaviour, its reliance on oxidation-unaffected time-to-failure values limits its practicality.

In addition to the predictive performance of the empirical and SR models, their practical applicability also depends on their computational requirements. As such, a comparison of the computational cost of calibrating the empirical and SR models is presented in Figure 4.18. All the calibrations were performed on a single core of a 3.80 GHz Intel Core i7-10700KF processor, with the costs calculated for each target response and averaged across five independent runs. In general, the calibration of the SR models incurred higher computational costs compared to the empirical models. For the characteristic-based predictions (i.e., minimum creep rate, time-to-failure, and strain-to-failure), the empirical models required roughly 1 minute compared to 15 minutes for the SR models. Additionally, for the regular and mechanism-shifted strain-time predictions, the empirical models required around 30 minutes while SR models required 60 minutes.

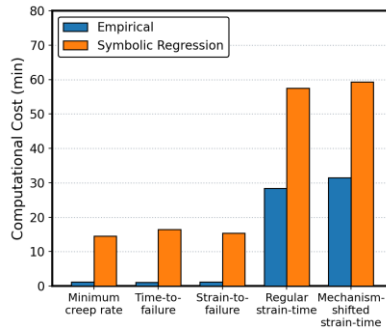


Figure 4.18. Comparison of the computational requirements for the calibration of the empirical models (in blue) and symbolic regression (SR) models (in orange), averaged across five independent runs. The costs were calculated for the predictions of the minimum creep rate, time-to-failure, strain-to-failure, regular strain-time response, and mechanism-shifted strain-time response.

Despite the higher calibration costs, SR provided a more streamlined and automated framework that consistently discovered simple and interpretable expressions. The SR models also outperformed the empirical models in reproducing the short-term creep behaviour, generally improved the longer-term predictions, and consistently showed low variability across independent runs. In addition, the SR models were able to better capture the effects of surface oxidation in the full strain-time responses, demonstrating their ability to adapt to changes in the operative deformation mechanisms. These results suggest that SR can serve as a complementary tool to empirical models, enhancing predictions without relying on the analyst's prior knowledge for model selection or initial parameter assumptions. That said, further testing under a wider range of loading conditions and across different materials may be needed to fully establish their generalisability and robustness.

#### 4.6. Conclusion

In this study, empirical and symbolic regression (SR) models were calibrated to predict key creep characteristics (i.e., minimum creep rate, time-to-failure, strain-to-failure) and the overall creep strain-time response (regular and mechanism-shifted) of Alloy 617 across multiple elevated stress-temperature conditions.

For each target response, three empirical models of varying complexities were calibrated using the genetic algorithm (GA). The calibration of the empirical characteristic-based models was performed directly against those scalar responses, while the empirical strain–time models were calibrated following a two-stage approach that involved 1) optimising the model’s parameters against individual strain–time curves, then 2) optimising the parameter function’s coefficients against the resulting parameter sets. In parallel, SR was applied to discover alternate constitutive expressions using building blocks (i.e., input variables, binary operators, and unary functions) commonly found in conventional empirical models. The empirical and SR models were calibrated five independent times against short-term experimental creep datasets provided by Idaho National Laboratory and subsequently validated against longer-term datasets to assess their predictive accuracy.

Overall, the empirical models reproduced the short-term creep behaviour (i.e., calibration datasets) reasonably well but showed lower accuracy for the longer-term predictions (i.e., validation datasets). Notably, the parameter spread and run-to-run variability of the empirical models was strongly dependent on the clarity of the trends in the experimental data. For the regular strain–time responses, the empirical models underrepresented the characteristic curvatures of all three creep regimes, overpredicted the longer-term strain values, and showed high run-to-run variability. When the mechanism-shifted responses were included in the calibration, the short-term predictions showed substantially reduced accuracy and higher run-to-run variability, underscoring the models’ inability to account for atypical creep behaviour.

In comparison, the SR models exhibited higher accuracy and mostly lower run-to-run variability in the short-term responses. The SR models also generally improved predictions for the longer-term behaviour, which is significant since long-term experiments are often more time-consuming and costly to perform. That said, the longer-term strain-to-failure predictions showed slightly reduced accuracy compared to the empirical models, underscoring the persisting risk of overfitting the calibration data. Notably, the discovered expressions were simple and interpretable, some of which resembled conventional empirical forms. For the strain–time responses, the SR models more accurately reproduced the curvature of the secondary and tertiary regimes but continued to underrepresent the primary regime. While the SR model showed improved accuracy in capturing the mechanism-shifted responses, they still showed notable discrepancies in the longer-term predictions.

In this work, the empirical models required careful selection of constitutive forms suited to the material, target response, and loading conditions, as well as the identification of suitable parameter bounds based on prior knowledge and iterative refinement. The empirical strain–time models additionally required multiple, separate optimisations for individual curves and parameter functions. While the calibration of the SR models incurred higher computational costs, SR offered a substantially more streamlined and automated framework, demonstrating its potential as a complementary framework to traditional empirical modelling. However, the SR models can produce unstable expressions that are difficult to interpret and lack physical meaning. As such, future work should focus on incorporating physical constraints, guiding the symbolic search with known constitutive relationships, and implementing cross-validation strategies to improve model robustness and reliability. Future work could also involve calibrating the SR models across different materials and a wider range of loading conditions, particularly those that exhibit mechanism shifts, to enhance the generalisability of the discovered expressions.

# Chapter 5

## Calibration of semi-empirical elastic-viscoplastic models for the elevated-temperature creep and tensile behaviour of Alloy 617

The work presented in this chapter was published by the author as ‘Multi-Objective Calibration of Elastic-Viscoplastic Models to capture the Elevated-Temperature Creep and Tensile Behaviour of Alloy 617’ in the International Journal of Pressure Vessels and Piping, December 2025 [201]. This work was produced in collaboration with Ondrej Muránsky, Mark Messner, Jay Kruzic, and Michael McMurtrey. The presented text has been adapted from the published version to include additional content, reduce repetition, and improve consistency in notation, terminology, and formatting with the rest of the thesis.

### 5.1. *Introduction*

Empirical material models, such as Norton’s power law [11], the theta projection model [12, 13], and Hollomon’s equation [14], are characterised by their simple definitions and low computational costs [15]. However, these models often struggle to accurately describe the ongoing deformation and degradation mechanics of materials under operating in-service conditions. Furthermore, these models are prone to over-conservatism and poor extrapolations beyond tested scenarios [15, 16]. Semi-empirical material models improve upon empirical models by incorporating the underlying physical mechanisms that govern material behaviour under elevated stress and temperature conditions. This enables semi-empirical models to more reliably extrapolate beyond test conditions, capture mechanism shifts, and accommodate different loading scenarios. Well-established examples include the Kachanov-Rabotnov [17, 18] model, ductility exhaustion models [26, 222, 223], and elastic-viscoplastic (EVP) models [224, 225]. However, the main challenge when using semi-empirical models lies in their calibration, which involves finding the set of unknown material parameters that best describes the experimentally observed material response.

Traditionally, manual trial-and-error methods were employed to calibrate material models. However, these methods were often subjective, time-consuming, and heavily dependent on prior knowledge of the underlying modelling framework. As such, gradient-based and direct-search optimisation methodologies are often employed to automate and streamline the calibration process of semi-empirical models [15, 226]. Gradient-based optimisation methods, such as gradient descent, Adam, and Newton-type methods, are efficient and well-suited for high-dimensional problems [142, 227]. However, these methods rely heavily on the initial parameter values and often converge towards local minima, particularly in the complex and non-linear parameter spaces characteristic of semi-empirical models [27, 142]. Gradient-based methods also require differentiability in their objective functions, in which noise in the experimental data could deteriorate convergence behaviour [27]. In contrast, direct-search optimisation methods do not rely on gradient information, making them generally more robust and better suited for exploring diverse regions of large parameter spaces [15, 29]. A notable example is the genetic algorithm (GA), which has been widely used in the calibration of complex material models due to its effectiveness at locating global minima and simultaneous handling of multiple objective functions [15, 27, 33, 34, 151]. However, despite these advantages, direct-search methods typically require a substantial number of evaluations to achieve convergence.

In the present work, a novel multi-objective three-stage calibration workflow was developed using a multi-objective genetic algorithm (MOGA) to efficiently calibrate two semi-empirical material models to capture the elevated-temperature creep and tensile behaviour of Alloy 617. The semi-empirical models employed a temperature-dependent elastic-viscoplastic (EVP) constitutive model, coupled with either a classical creep damage (CD) or work-based damage (WD) model to capture the failure response. The calibration of the EVP-CD and EVP-WD models was performed against elevated-temperature experimental creep and tensile datasets collected by the Idaho National Laboratory (INL) [85]. The calibration workflow involved 1) determining the material parameters for the EVP model, 2) identifying the parameters for the damage models (CD, WD), and subsequently 3) fine-tuning the parameters together. The models were calibrated using the short-term creep and tensile datasets and validated using longer-term creep datasets. This approach allowed the assessment of the models' accuracy in extrapolating beyond the calibration datasets, thereby evaluating their predictive capabilities. From these assessments, it is shown that both damage models can capture elevated -temperature creep and tensile yielding behaviour, with the WD model producing more accurate tensile stress–strain curves to failure at the cost of being more difficult to calibrate.

## 5.2. *Experimental data*

This study employs experimental creep and tensile data of Alloy 617 to support the calibration and validation of the semi-empirical material models. The experimental creep data used in this study are the same as those used in Chapter 4, which were obtained from creep tests conducted at Idaho National Laboratory (INL) on an as-received, solution-annealed plate of Alloy 617 (Heat 314626) to support the certification of the alloy for high-temperature nuclear pressure vessel applications. The creep tests were performed in accordance with ASTM E139-11 [81] under constant temperature and uniaxial stress conditions at 800°C (60MPa, 65MPa, 70MPa, 80MPa), 900°C (26MPa, 28MPa, 31MPa, 36MPa), and 1000°C (11MPa, 12MPa, 13MPa, 16MPa). As discussed in Section 4.2, some of the creep curves exhibited atypical behaviour characterised by a decreasing strain rate in the tertiary regime, which was attributed to the creep tests being conducted in air causing surface oxidation effects [9, 84, 207]. For this work, the atypical tertiary behaviour was excluded to assess the typical prediction capabilities of the semi-empirical models, which were not designed to capture the effects of oxidation. The employed creep strain–time curves are presented in Figure 4.1 and summarised in Table 4.2.

Additionally, the experimental tensile data were obtained from tests conducted by INL on specimens from the same Alloy 617 plate, following ASTM E8-11 [73]. The tensile tests were performed at the same constant temperatures (i.e., 800°C, 900°C, and 1000°C) under a constant strain rate of approximately  $10^{-4}\text{s}^{-1}$ . The tensile data is employed in the form of stress–strain tensile curves up to 80% of the maximum true stress (i.e., stress-at-ductility). The tensile data are presented in Figure 5.1, showing each curve annotated with the yield stress ( $\sigma_y$ ), maximum true stress ( $\sigma_M$ ), the strain-at-ductility ( $\varepsilon_d$ ), and the stress-at-ductility ( $\sigma_d$ ). Note that the tensile data was originally provided in engineering stress–strain values and converted to homogeneous true stress–strain values using standard relations.

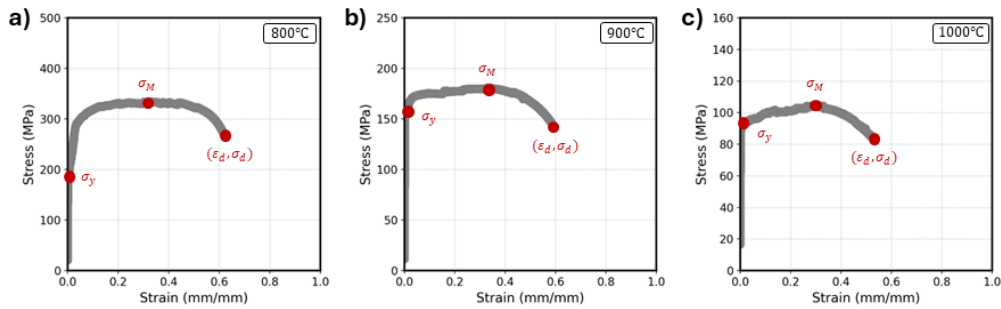


Figure 5.1. Annotated plots of the experimental tensile data of Alloy 617 from the Idaho National Laboratory at a) 800°C, b) 900°C, and c) 1000°C.

A summary of the experimental tensile data is presented in Table 5.1, where  $\dot{\varepsilon}$  represents the strain rate and  $\sigma_{UTS}$  represents the ultimate tensile stress. Note that the values for  $\dot{\varepsilon}$ ,  $\varepsilon_f$ ,  $\sigma_y$ , and  $\sigma_{UTS}$  are reported in terms of engineering stress and strain, while the values for  $\sigma_M$ ,  $\sigma_d$ , and  $\varepsilon_d$  are reported in true stress and strain.

Table 5.1. Summary of experimental tensile data of Alloy 617 from Idaho National Laboratory.

Sample	Time scale	T (°C)	$\dot{\varepsilon}$ ( $10^{-4} \text{h}^{-1}$ )	$\varepsilon_f$ (mm/mm)	$\sigma_y$ (MPa)	$\sigma_{UTS}$ (MPa)	$\sigma_M$ (MPa)	$\sigma_d$ (MPa)	$\varepsilon_d$ (mm/mm)
D7	Short-term	800	1.04	0.940	189	289.5	334.3	267.0	0.622
D10	Short-term	900	1.00	1.033	163	166.2	180.7	144.4	0.587
D12	Short-term	1000	1.03	0.987	90	123.6	104.6	83.6	0.527

### 5.3. Elastic viscoplastic material models

Semi-empirical models combine theoretical principles with the existing experimental datasets to describe material behaviour under varying loading conditions. By considering the underlying deformation and degradation mechanisms, semi-empirical models can reliably extrapolate beyond test conditions, capture mechanism shifts, and accommodate different loading scenarios. One of the most popular semi-empirical models is the elastic-viscoplastic (EVP) model [224, 225], which describes the time-dependent plastic behaviour as attributed to the motion of dislocations, formation of cavities, and the sliding of grain boundaries [119]. While the EVP model is unable to capture damage by itself, it can be readily coupled with a classical creep damage (CD) model or a work damage (WD) model to capture the material's entire service life. Both the EVP-CD and EVP-WD models were implemented using the nuclear engineering material model library (NEML) [228]. For the creep simulations, the models were terminated when the damage reached a value of 0.95; for the tensile simulations, the models were terminated when the stress dropped to 80% of the maximum true stress (i.e., stress-at-ductility). The following section defines the EVP model (Section 5.3.1) and its coupling with the CD model (Section 5.3.2) and WD model (Section 5.3.3). Additionally, a summary of the material parameters for the EVP, CD, and WD models can be found in Appendix B.1.

### 5.3.1. Definition of elastic-viscoplastic model

In this study, the elastic-viscoplastic (EVP) model was employed to characterise deformation behaviour under high-temperature loading by coupling elastic and viscoplastic mechanisms. The model is formulated within the infinitesimal strain framework [23, 25, 229], where the total strain rate ( $\dot{\epsilon}$ ) of the material is additively decomposed into second order tensors of the elastic strain rate ( $\dot{\epsilon}_e$ ) and viscoplastic strain rate ( $\dot{\epsilon}_{vp}$ ), as expressed in Eq. (30). It is acknowledged that the experimental creep and tensile data used in this study (Section 5.2) involves strains of up to 64.1%, which exceeds the validity limit of the infinitesimal strain theory. While a finite strain formulation would offer a more rigorous approach for modelling large deformations, the infinitesimal strain approach was adopted to reduce computational complexity and ensure compatibility with existing model formulations.

$$\dot{\epsilon} = \dot{\epsilon}_e + \dot{\epsilon}_{vp} \quad (30)$$

In this study, elastic deformation is assumed to be isotropic, and as such, the elastic component of the proposed EVP model can be represented by the conventional form of Hooke's law. This is shown in Eq. (31), where  $\dot{\sigma}$  represents the stress rate and  $\mathbf{C}$  represents the isotropic elasticity tensor described by the elastic modulus ( $E$ ) and Poisson's ratio ( $\nu$ ).

$$\dot{\sigma} = \mathbf{C} : \dot{\epsilon}_e \quad (31)$$

The expanded matrix form of the employed Hooke's law is shown in Eq. (32).

$$\begin{bmatrix} \dot{\sigma}_{11} \\ \dot{\sigma}_{22} \\ \dot{\sigma}_{33} \\ \dot{\sigma}_{23} \\ \dot{\sigma}_{13} \\ \dot{\sigma}_{12} \end{bmatrix} = \frac{E}{(1+\nu)(1-2\nu)} \begin{bmatrix} 1-\nu & \nu & \nu & 0 & 0 & 0 \\ \nu & 1-\nu & \nu & 0 & 0 & 0 \\ \nu & \nu & 1-\nu & 0 & 0 & 0 \\ 0 & 0 & 0 & \frac{1-2\nu}{2} & 0 & 0 \\ 0 & 0 & 0 & 0 & \frac{1-2\nu}{2} & 0 \\ 0 & 0 & 0 & 0 & 0 & \frac{1-2\nu}{2} \end{bmatrix} \begin{bmatrix} \dot{\epsilon}_{e,11} \\ \dot{\epsilon}_{e,22} \\ \dot{\epsilon}_{e,33} \\ \dot{\epsilon}_{e,23} \\ \dot{\epsilon}_{e,13} \\ \dot{\epsilon}_{e,12} \end{bmatrix} \quad (32)$$

The viscoplastic component of the EVP model is represented by the Perzyna viscoplastic flow rule [230] within a power-law framework, which relates the viscoplastic strain rate ( $\dot{\epsilon}_{vp}$ ) to the applied stress ( $\sigma$ ) and two temperature-dependent material parameters. The viscoplastic model is defined in Eq. (33) [230], where  $f_{PF}$  is the yield function,  $n_{PF}$  represents the flow surface exponent, and  $\eta_{PF}$  represents the viscosity parameter.

$$\dot{\epsilon}_{vp} = \left( \frac{\langle f_{PF}(\sigma, \sigma_h, T) \rangle}{\eta_{PF}} \right)^{n_{PF}} \quad (33)$$

The  $\langle \cdot \rangle$  notation in Eq. (33) represents the McCauley brackets. The definition of  $\langle x \rangle$  for a value  $x$  is defined by the expression in Eq. (34) [230].

$$\langle x \rangle = \begin{cases} 0, & x < 0 \\ x, & x \geq 0 \end{cases} \quad (34)$$

The yield function ( $f_{PF}$ ) from Eq. (33) is defined by the expression in Eq. (35). In this expression,  $J_2$  represents the deviatoric stress invariant,  $T$  represents the temperature,  $\sigma$  represents the applied stress, and  $\sigma_h$  represents the hardening stress [25].

$$f_{PF}(\sigma, \sigma_h, T) = J_2(\sigma) + \sqrt{\frac{2}{3}}\sigma_h \quad (35)$$

The  $J_2$  function describes the von Mises effective stress [25], and is defined in Eq. (36).

$$J_2(\sigma) = \sqrt{\frac{3}{2} \operatorname{dev}(\sigma) : \operatorname{dev}(\sigma)} \quad (36)$$

The  $\operatorname{dev}$  notation in Eq. (36) denotes the deviator function. The definition of  $\operatorname{dev}(X)$  for some second order tensor  $X$  is shown in Eq. (37), where  $\operatorname{tr}$  is the trace, and  $I$  is the identity tensor.

$$\operatorname{dev}(X) = X - \frac{1}{3} \operatorname{tr}(X)I \quad (37)$$

In addition to isotropic elastic behaviour, the material is assumed to exhibit isotropic viscoplastic behaviour. Hence, the hardening stress ( $\sigma_h$ ) is obtained using the Voce isotropic hardening rule [104], as defined by the expression in Eq. (38). In this expression,  $\sigma_{y,0}$  represents the initial yield stress,  $R_{VIH}$  represents the isotropic hardening modulus, and  $d_{VIH}$  represents the isotropic hardening rate [231]. Note that  $d_{VIH}$  controls the rate of hardening whereas  $R_{VIH}$  controls the magnitude of the hardening [232].

$$\sigma_h = \sigma_{y,0} + R_{VIH}(1 - e^{-d_{VIH}/\varepsilon_{vp}}) \quad (38)$$

Once combined, the EVP model contains five material parameters. The first three parameters ( $\sigma_{y,0}$ ,  $R_{VIH}$ , and  $d_{VIH}$ ) come from the Voce isotropic hardening rule [104], whereas the remaining parameters ( $n_{PF}$  and  $\eta_{PF}$ ) come from the Perzyna viscoplastic flow rule [230]. The values of these parameters must be calibrated for the EVP model to capture the deformation behaviour of Alloy 617.

### 5.3.2. Coupling with a classical creep damage model

The elastic-viscoplastic creep damage (EVP-CD) model couples the EVP model with the Hayhurst-Leckie-Kachanov-Rabotnov creep damage (CD) model [233], which characterises damage accumulation based on the local reduction in the material's cross-sectional area, as a function of time. The CD model relies on a damage state variable,  $\omega$ , such that  $\omega = 0$  when the material is in its undamaged state and  $\omega = 1$  when the material is ruptured. In the CD model,  $\omega$  is defined by Eq. (39), where  $A_{CD}$  represents the stress prefactor,  $\xi_{CD}$  represents the stress power law exponent, and  $\phi_{CD}$  represents the damage power law exponent [234]. For this study, the effective stress is defined by the  $J_2$  function described in Eq. (36).

$$\dot{\omega} = \left( \frac{J_2(\sigma)}{A_{CD}} \right)^{\xi_{CD}} (1 - \omega)^{\xi_{CD} - \phi_{CD}} \quad (39)$$

The addition of the CD model introduces three material parameters ( $A_{CD}$ ,  $\xi_{CD}$ , and  $\phi_{CD}$ ), which results in the coupled EVP-CD model having a total of eight material parameters.

### 5.3.3. Coupling with a work damage model

The elastic-viscoplastic work damage (EVP-WD) model couples the EVP model with the work damage (WD) model. The WD model shares functionality with ductility exhaustion models [26, 222, 223] that evaluate material failure based on ductility decline but differ in their characterisation of damage as a function of plastic work density rather than strain. In the WD model, the damage state variable,  $\omega$ , is defined by Eq. (40), where  $W$  represents the plastic work density,  $W_{crit}$  represents the critical plastic work density, and  $n_d$  represents the damage exponent that controls the onset of damage in the material flow stress.

$$\dot{\omega} = \frac{n_d \omega^{\frac{n_d-1}{n_d}} \dot{W}}{W_{crit}} \quad (40)$$

The WD model defines the critical work density ( $W_{crit}$ ) and the damage exponent ( $n_d$ ) as piecewise functions of the logarithmised work density rate (i.e.,  $\log_{10}(\dot{W})$ ) controlled by six parameters ( $A_{WD}$ ,  $a_{WD}$ ,  $B_{WD}$ ,  $b_{WD}$ ,  $\alpha_{WD}$ , and  $\beta_{WD}$ ), resulting in the coupled EVP-WD model having a total of eleven material parameters. The critical work density is represented as a bilinear function, where  $A_{WD}$  and  $a_{WD}$  control the linear relationship for creep and  $B_{WD}$  and  $b_{WD}$  control the linear relationship for tensile. The damage exponent is represented as a step function where  $\alpha_{WD}$  and  $\beta_{WD}$  represent the damage exponent values for creep and tensile, respectively. These representations were inspired by the relationship of the critical work density and average work density rate in the experimental creep and tensile data, from which the values of  $A_{WD}$ ,  $a_{WD}$ ,  $B_{WD}$ , and  $b_{WD}$  were calculated to be 15.063s, 103.03MPa, 264.45s, and 599.01MPa. As such,  $A_{WD} < B_{WD}$  and  $a_{WD} < b_{WD}$  are enforced to preserve the experimentally observed relationship. The critical work density and damage exponent functions are discussed in further depth in Appendix B.2.

## 5.4. *Calibration methodology*

The semi-empirical models must be calibrated before they can be used to capture creep and tensile behaviour. In this study, the EVP-CD and EVP-WD models were calibrated using the genetic algorithm (GA) in a multi-objective three-stage calibration workflow, which involved 1) finding the elastic-viscoplastic parameters, 2) finding the damage parameters, and 3) fine-tuning the combined parameters. This procedure was repeated ten times for the EVP-CD and EVP-WD models to investigate the repeatability and robustness of the developed approach. Once calibrated, the semi-empirical models were assessed based on their individual performance at each optimisation stage, as well as their relative performance after the three-stage calibration.

The following section begins by describing how the experimental datasets were processed and separated into calibration and validation subsets (Section 5.4.1). The section continues with an overview of the multi-objective genetic algorithm (MOGA; Section 5.4.2) as well as the developed three-stage calibration workflow (Section 5.4.3). The developed calibration workflow is also summarised in the flowchart in Figure 5.2.

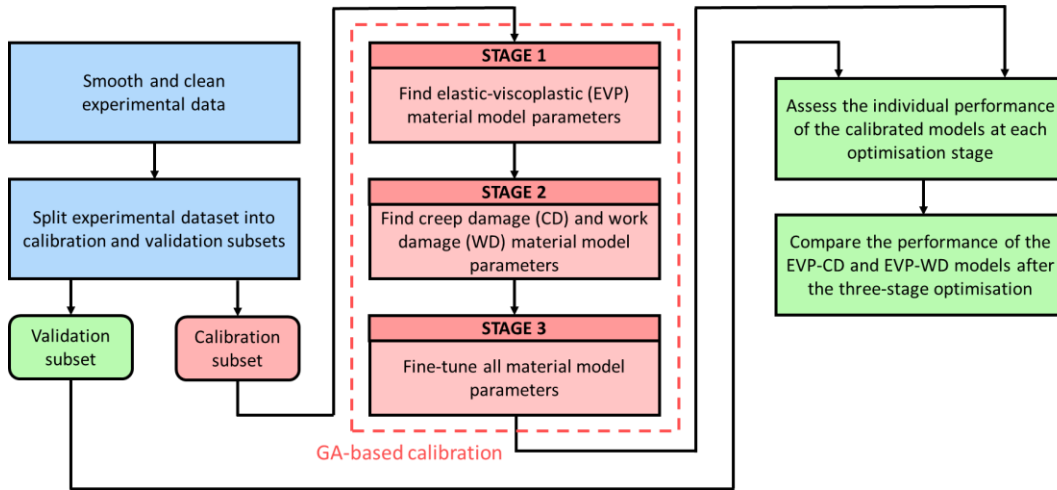


Figure 5.2. Flowchart of multi-objective three-stage calibration workflow.

#### 5.4.1. Splitting the experimental datasets

This study uses a similar partitioning strategy as Chapter 4, in which the short-term experimental datasets are used for calibration, and the longer-term experimental datasets are used for validation. The experimental data provided by INL includes tests at three temperatures (800°C, 900°C, and 1000°C), with each comprising four creep curves and one tensile curve. At each temperature, the semi-empirical models are calibrated using the two highest stress creep curves and the tensile curve (i.e., short-term data), while validation is performed using the two lowest stress creep curves (i.e., longer-term data). This data selection strategy allows for a demonstration of the models' ability to capture multiple loading configurations, as well as their ability to extrapolate and predict longer-term material behaviour using only short-term experimental data.

#### 5.4.2. Multi-objective genetic algorithm optimisation

The EVP-CD and EVP-WD models were calibrated using the multi-objective genetic algorithm (MOGA), which combines the concepts of the genetic algorithm (GA; Section 2.5.2) with multi-objective optimisation (MOO; Section 2.5.3). This study employed the non-dominated sorting genetic algorithm-II (NSGA-2) implementation of the MOGA to simultaneously minimise multiple objective functions and capture the material properties from the experimental creep and tensile datasets. The MOGA was configured with a population size of 100, offspring size of 50, crossover rate of 80%, and mutation rate of 1. The lower and upper bounds for the material parameters were determined based on literature [231, 234-236] and refined through trial-and-error, as summarised in Appendix B.1. These bounds were selected such that the parameter space would be small enough for the MOGA to converge in a reasonable amount of time, but large enough to showcase the MOGA's optimisation capabilities [15].

To guide the MOGA in its search for suitable material parameters for the semi-empirical models, objective functions were implemented to minimise the discrepancies between certain material properties extracted from the experimentally observed and simulated creep and tensile curves. These material properties were selected based on their importance in the analysis of engineering systems. The schematic in Figure 5.3 visualises these objective functions on a creep and tensile curve.

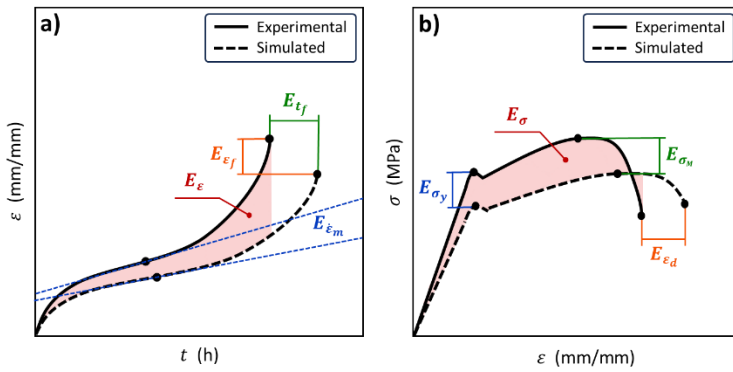


Figure 5.3. Schematics of an experimentally observed and simulated a) creep curve and b) tensile curve, annotated with the discrepancies that the implemented objective functions aim to minimise.

For the creep curves, four objective functions were used to minimise discrepancies in the strain values ( $E_\varepsilon$ ), minimum creep rate ( $E_{\dot{\varepsilon}_m}$ ), time-to-failure ( $E_{t_f}$ ), and strain-to-failure ( $E_{\varepsilon_f}$ ). These objective functions are consistent to those introduced in Chapter 4 (Section 4.4.2), as defined in Eqs. (28), (25), (26), and (27), respectively. For the tensile curves, four additional objective functions were implemented to minimise discrepancies in the stress values ( $E_\sigma$ ), yield stress ( $E_{\sigma_y}$ ), maximum true stress ( $E_{\sigma_M}$ ), and strain-at-ductility ( $E_{\varepsilon_d}$ ). In these objective functions,  $N$  represents the number of calibration datasets. Since the semi-empirical models are calibrated against the two lowest-stress creep curves and one tensile curve for each temperature (Section 5.4.1), the creep objective functions set  $N = 2$  while the tensile objective functions set  $N = 1$ .

The  $E_\sigma$  objective function minimises the common area between the experimental and simulated tensile curves, by assessing the stress values of the tensile curves at evenly spaced strain intervals. The objective function is defined in Eq. (41),  $M$  represents the number of assessed values,  $\sigma_{exp}$  represents an experimental stress value,  $\sigma_{sim}$  represents a simulated stress value, and  $\bar{\sigma}_{exp}$  represents the average of the experimental stress values. In this study,  $M = 50$  is used to obtain a sufficient approximation of the area while reducing the number of evaluations.

$$E_\sigma = \sqrt{\frac{1}{NM} \sum_{i=1}^N \sum_{j=1}^M \left( \frac{(\sigma_{exp})_{i,j} - (\sigma_{sim})_{i,j}}{(\bar{\sigma}_{exp})_i} \right)^2} \quad (41)$$

The  $E_{\sigma_y}$  objective function minimises the discrepancy between the yield stress of the experimental and simulated tensile curves. The objective function is defined in Eq. (42), where  $\sigma_{y,exp}$  represents the experimental yield stress and  $\sigma_{y,sim}$  represents the simulated yield stress.

$$E_{\sigma_y} = \sqrt{\frac{1}{N} \sum_{i=1}^N \left( \frac{(\sigma_{y,exp})_i - (\sigma_{y,sim})_i}{(\sigma_{y,exp})_i} \right)^2} \quad (42)$$

In addition, the  $E_{\sigma_M}$  objective function minimises the discrepancy between the maximum true stress of the experimental and simulated tensile curves. The objective function is defined in Eq. (43), where  $\sigma_{M,exp}$  represents the experimental maximum true stress and  $\sigma_{M,sim}$  represents the simulated maximum true stress.

$$E_{\sigma_M} = \sqrt{\frac{1}{N} \sum_{i=1}^N \left( \frac{(\sigma_{M,exp})_i - (\sigma_{M,sim})_i}{(\sigma_{M,exp})_i} \right)^2} \quad (43)$$

Finally, the  $E_{\varepsilon_d}$  objective function minimises the horizontal distance between the endpoints of the experimental and simulated tensile curves. The objective function is defined in Eq. (44), where  $\varepsilon_{d,exp}$  represents the experimental strain-at-ductility and  $\varepsilon_{d,sim}$  represents the simulated strain-at-ductility.

$$E_{\varepsilon_d} = \sqrt{\frac{1}{N} \sum_{i=1}^N \left( \frac{(\varepsilon_{d,exp})_i - (\varepsilon_{d,sim})_i}{(\varepsilon_{d,exp})_i} \right)^2} \quad (44)$$

After each optimisation run, the square sum of the defined objectives values was calculated for each solution (i.e., set of parameter values) in the final population. The best solution (i.e., most optimal set of parameter values) was identified as the solution with the minimal square sum, representing the solution that provides the best tradeoff between all eight objectives.

#### 5.4.3. Multi-objective three-stage calibration workflow

Calibrating the semi-empirical models can be challenging due to their complexity and the high dimensionality of the parameter space. As such, directly optimising the models could incur convergence issues, overfitting, and substantial computational costs. To simplify the calibration process and reduce the computational costs, the optimisation problem was separated into three smaller optimisation stages.

The first optimisation stage (stage 1) involved finding the EVP parameters ( $\sigma_{y,0}$ ,  $R_{VIH}$ ,  $d_{VIH}$ ,  $n_{PF}$ , and  $\eta_{PF}$ ) using only the experimental elastic-plastic creep and tensile data. The values of the EVP parameters in the initial population of the MOGA were randomly generated within their defined bounds. When calibrating the EVP model against creep data, the MOGA optimised with the objective functions for the strain values ( $E_\varepsilon$ ) and minimum creep rate ( $E_{\dot{\varepsilon}_m}$ ) using the creep data up to the minimum creep rate (i.e., onset of tertiary creep). When calibrating against the tensile data, the MOGA optimised with the objective functions for the stress values ( $E_\sigma$ ) and yield stress ( $E_{\sigma_y}$ ) using the tensile data up to the maximum true stress. For this stage, the MOGA was terminated after 250 generations.

The second optimisation stage (stage 2) involved fixing the values of the optimised EVP parameters from the first stage (i.e.,  $\sigma_{y,0}$ ,  $R_{VIH}$ ,  $d_{VIH}$ ,  $n_{PF}$ , and  $\eta_{PF}$ ) before searching for the remaining damage parameters of the semi-empirical models. For the EVP-CD model, the MOGA searched for the  $A_{CD}$ ,  $\xi_{CD}$ , and  $\phi_{CD}$  parameters; and for the EVP-WD model, the MOGA searched for the  $A_{WD}$ ,  $a_{WD}$ ,  $B_{WD}$ ,  $b_{WD}$ ,  $\alpha_{WD}$ , and  $\beta_{WD}$  parameters. The values of the CD and WD parameters in the initial population of the MOGA were, once again, randomly generated within their defined bounds. When calibrating against creep data, the MOGA optimised with the objective

functions for the strain values ( $E_\varepsilon$ ), minimum creep rate ( $E_{\dot{\varepsilon}_m}$ ), time-to-failure ( $E_{t_f}$ ), and strain-to-failure ( $E_{\varepsilon_f}$ ). When calibrating against tensile data, the MOGA optimised with the objective functions for the stress values ( $E_\sigma$ ), yield stress ( $E_{\sigma_y}$ ), maximum true stress ( $E_{\sigma_M}$ ), and strain-at-ductility ( $E_{\varepsilon_d}$ ). For this stage, the MOGA was terminated after 250 generations for the EVP-CD model, and 500 generations for the EVP-WD model.

The third optimisation stage (stage 3) involved simultaneously fine-tuning the optimised material parameters of the EVP and damage models from the previous optimisation stages. This correctional optimisation aimed to better capture the parameter interactions and resolve any coupling issues between the EVP and damage models. To do this, the initial population of the MOGA was defined with the optimised EVP-CD and EVP-WD parameters from the second optimisation stage. With the initialised parameters, this correctional optimisation was conducted using the same objective functions, calibration data, and number of generations as the second optimisation stage.

### *5.5. Results and discussion*

In an ideal scenario, the calibration of materials models should be a straightforward process. However, the complexity of semi-empirical material models — with many unknown material parameters — often complicates this process. A single-stage calibration process, which employs an optimisation algorithm trying to simultaneously find all eight or eleven unknown material parameters, is only applicable in limited cases when calibrating simpler material models [15, 26, 118] in a relatively tight parameter space. Attempts were made to calibrate EVP-CD and EVP-WD models with a single-stage calibration process against the available experimental creep and tensile datasets. However, the simple single-stage calibration process consistently failed to reliably describe the experimental data due to the many unknown material parameters. It thus became clear that employing a simple single-stage approach is not effective for calibrating advanced models such as EVP-CD and EVP-WD. Hence, the multi-objective three-stage calibration workflow was employed to calibrate the EVP-CD and EVP-WD material models against the INL-provided creep and tensile experimental datasets for Alloy 617 at 800°C, 900°C, and 1000°C. The workflow involved identifying the material parameters of the EVP model and damage (CD, WD) model through two separate optimisations (stages 1 and 2), followed by a correctional optimisation (stage 3) to resolve interdependencies between the two sets of material parameters. The calibration results on the 800°C datasets are shown in the following section, while the results for the 900°C and 1000°C datasets can be found in Appendix B.3.

The following section first presents the calibration results for the EVP-CD model (Section 5.5.1) and EVP-WD model (Section 5.5.2). The section then provides a discussion the developed multi-objective three-stage calibration process (Section 5.5.3), followed by an assessment of the calibrated EVP-CD and EVP-WD models (Section 5.5.4), as well as an overview of the computational resources required to calibrate these semi-empirical models (Section 5.5.5).

#### 5.5.1. Calibration of elastic-viscoplastic creep damage model

Calibrating the EVP-CD model requires finding the five material parameters defining the EVP model ( $\sigma_{y,0}$ ,  $R_{VIH}$ ,  $d_{VIH}$ ,  $n_{PF}$ ,  $\eta_{PF}$ ) and the three parameters defining the CD model ( $A_{CD}$ ,  $\xi_{CD}$ , and  $\phi_{CD}$ ). The three-stage calibration process was conducted ten times to find these unknown material parameters. The calibration results

for the EVP-CD model at each optimisation stage are shown in Figure 5.4, with each plot (a-f) containing the experimental creep and tensile curves (in grey) with the corresponding ten sets of simulated creep and tensile curves (in green or red). To assess the robustness of the developed workflow, the boxplots (g) show the distribution of the found material parameters resulting from the ten independent calibration runs. The material parameters for the best optimised calibration run are shown in Figure 5.4g, and the corresponding curves are highlighted with increased opacity in Figure 5.4a-f. Note that the best of the ten independent calibration runs were identified based on the minimality of the square sum of the objective values after the final optimisation stage, as described in Section 5.4.2.

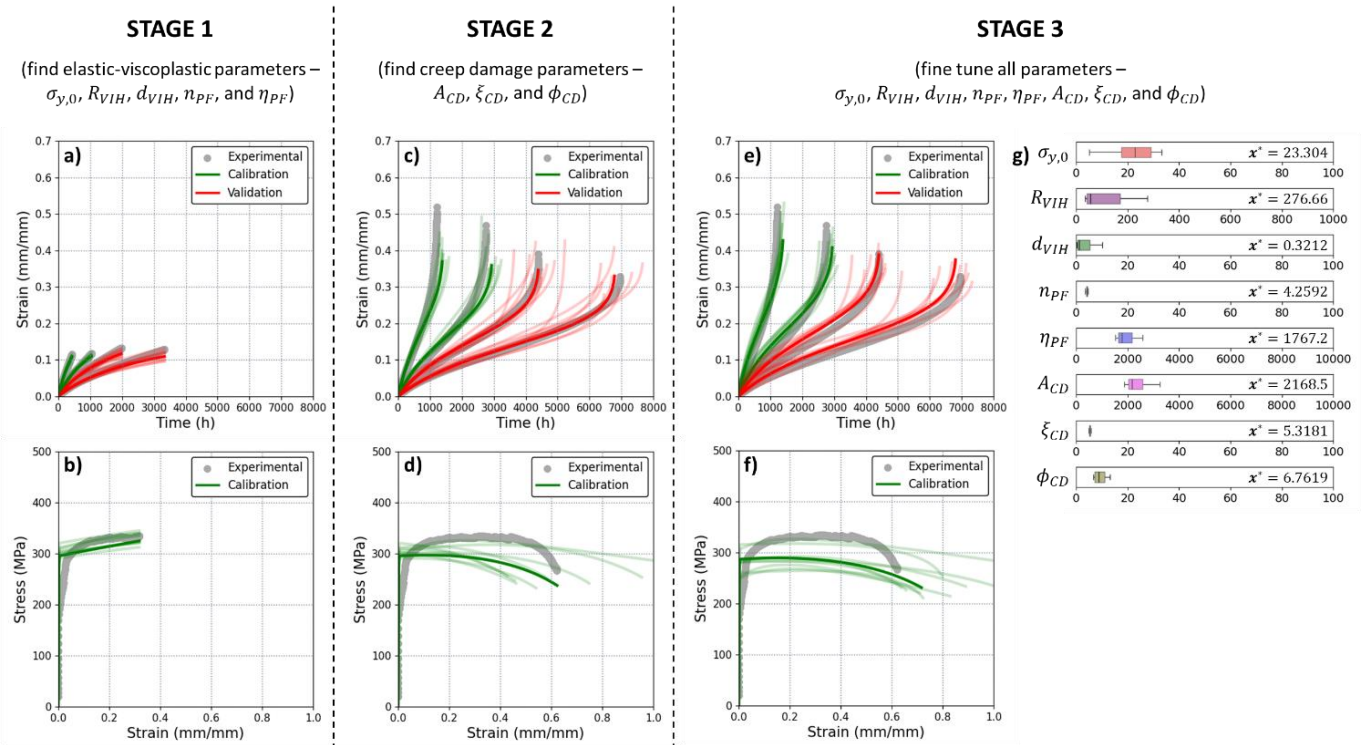


Figure 5.4. Calibration results for the EVP-CD model at 800°C, calibrated with short-term creep curves (70MPa and 80MPa) and tensile curve, and validated with longer-term creep curves (60MPa and 65MPa). The top row of plots (a, c, e) shows the creep results while the bottom row of plots (b, d, and f) shows the tensile results after stages 1, 2, and 3. The experimental datasets are in grey, the simulated curves used for calibration are in green, and the simulated curves used for validation are in red. The boxplots (g) show the distribution of the found parameters, where  $x^*$  represents the optimal parameter value, the vertical line represents the mean, the boxes represent the standard deviations, and the whiskers represent the ranges.

The plots in the first column show the results from the initial optimisation (stage 1), where the EVP model was calibrated using the short-term creep curves up to the minimum creep rate ( $\dot{\epsilon}_m$ ) and a tensile curve up to the maximum true stress ( $\sigma_M$ ). It is clear from Figure 5.4a that the elastic-plastic creep behaviour was captured accurately and consistently, as demonstrated by the narrow spread of the simulations and their proximity to the experimental data. While the simulated tensile curves in Figure 5.4b have a more noticeable spread, the simulations are still of acceptable accuracy. The plots in the second column of Figure 4 show the results from the second optimisation (stage 2), where the CD model is being calibrated using full creep and tensile curves while the EVP parameters found in the first stage are fixed. The times-to-failure of the creep curves were

accurately captured, as shown in Figure 4c. In particular, the times-to-failure for the longer-term creep curves were predicted exceptionally well, despite them not being used in the calibration process. However, the strains-to-failure were not very accurate, though they are still conservative. While the tensile damage was not captured very well, the EVP-CD model was still able to simulate the strain-at-ductility with reasonable accuracy, as shown in Figure 5.4d. The plots in the third column show the results from the correctional optimisation (stage 3), where the EVP and CD parameters were fine-tuned using full creep and tensile curves. As shown in Figure 5.4e, the accuracy and consistency of the creep curves were slightly improved in the correctional optimisation, particularly for the strains-to-failure. However, as shown in Figure 5.4f, there were no noticeable improvements in the accuracy of the tensile damage, with the strain-at-ductility being worse.

The three-stage optimisation of the EVP-CD model was also conducted using experimental creep and tensile data at 900°C and 1000°C, the results of which can be found in Appendix B.3. At 900°C, the minimum creep rates and yield stress were accurately captured in the initial optimisation (stage 1). However, the times-to-failure, strains-to-failure, and maximum true stress were not captured very accurately in the second optimisation (stage 2). While the accuracy of the strain-at-ductility improved in the correctional optimisation (stage 3), there were minimal improvements for the other material properties. The short-term creep curves were captured with reasonable accuracy at 1000°C, but the longer-term creep simulations were demonstrably worse, and the tensile failure was poorly predicted.

### 5.5.2. Calibration of elastic-viscoplastic work damage model

The EVP-WD model is defined by the five material parameters from the EVP model ( $\sigma_{y,0}$ ,  $R_{VIH}$ ,  $d_{VIH}$ ,  $n_{PF}$ ,  $\eta_{PF}$ ) and the six material parameters from the WD model ( $A_{WD}$ ,  $a_{WD}$ ,  $B_{WD}$ ,  $b_{WD}$ ,  $\alpha_{WD}$ , and  $\beta_{WD}$ ). As with the EVP-CD model, the three-stage calibration process was conducted ten times to find these unknown material parameters. The calibration results at 800°C are presented in Figure 5.5, while the results for the 900°C and 1000°C datasets can be found in Appendix B.3.

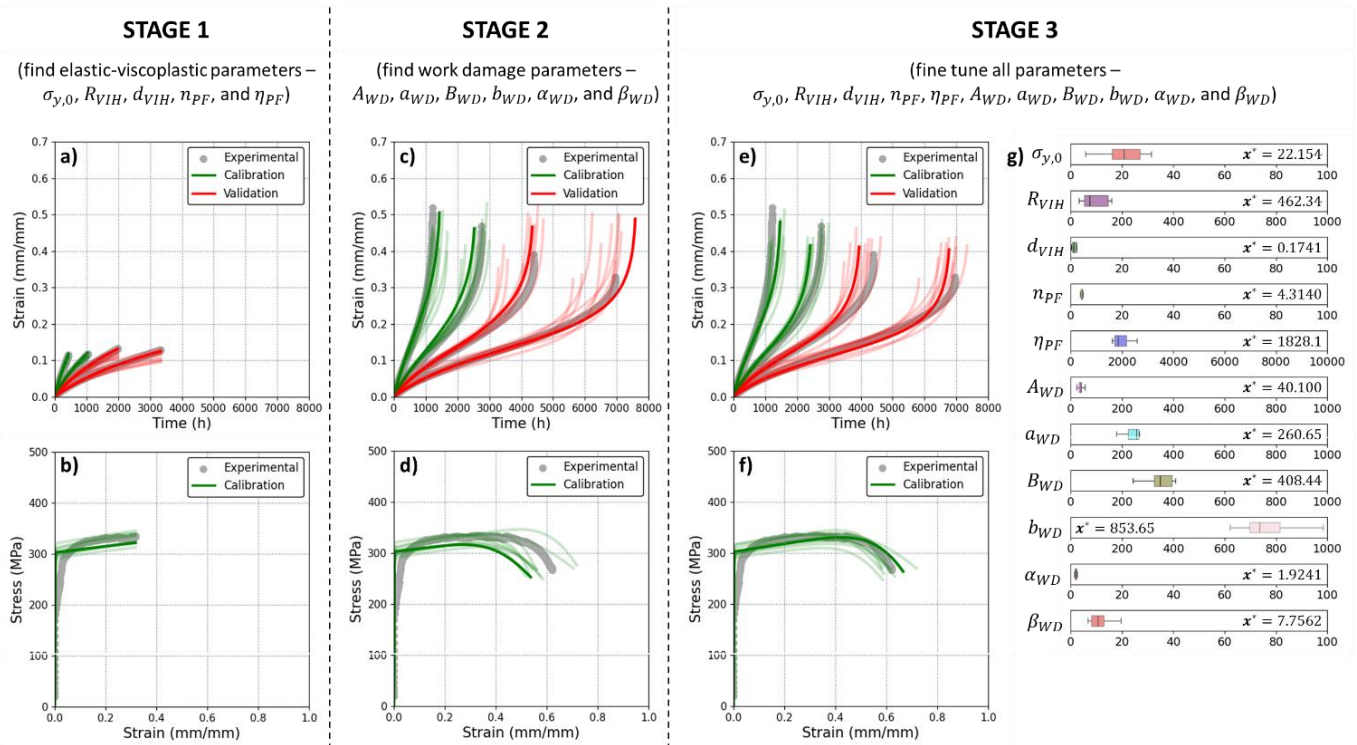


Figure 5.5. Calibration results for the EVP-WD model at 800°C, calibrated with short-term creep curves (70 MPa and 80 MPa) and tensile curve, and validated with longer-term creep curves (60 MPa and 65 MPa). The top row of plots (a, c, e) shows the creep results while the bottom row of plots (b, d, and f) shows the tensile results after stages 1, 2, and 3. The experimental datasets are in grey, the simulated curves used for calibration are in green, and the simulated curves used for validation are in red. The boxplots (g) show the distribution of the found parameters, where  $x^*$  represents the optimal parameter value, the vertical line represents the mean, the boxes represent the standard deviations, and the whiskers represent the ranges.

The optimisation results for the EVP-WD model are somewhat consistent with that observed for the EVP-CD model. Specifically, the elastic-plastic behaviour was accurately captured in the initial optimisation (stage 1), and the damage behaviour was captured with less accuracy in the second optimisation (stage 2), particularly for the strains-to-failure for the longer-term creep curves and the strain-at-ductility in the tensile curve. However, the accuracy of the simulations was improved in the correctional optimisation (stage 3), especially for the tensile response. While the EVP-WD model captured the creep behaviour with comparable accuracy to the EVP-CD model, the EVP-WD model was able to capture the tensile behaviour significantly better, specifically regarding the yield stress, maximum true stress, and strain-at-ductility. The improvement from the correctional optimisation (stage 3) was also more significant for the EVP-WD model than for the EVP-CD model.

The three-stage optimisation of the EVP-WD model was also conducted at 900°C and 1000°C (Appendix B.3), which show that the EVP-WD model was similarly able to outperform the EVP-CD model at those temperatures, particularly with the accuracy of the tensile simulations. Notably, the longer-term creep predictions were improved significantly during the correctional optimisation at 900°C. However, the EVP-WD model struggled to accurately capture and predict the creep behaviour at 1000°C.

### 5.5.3. Assessment of calibration process

Preliminary trials were undertaken to simultaneously search for all the parameters of the EVP-CD and EVP-WD models in a single optimisation stage. However, the calibrations were computationally expensive and consistently failed. Hence, a modular approach was undertaken to calibrate the models in three separate stages. In the initial optimisation (stage 1, shown in Figure 5.4a-b and Figure 5.5a-b), the EVP model accurately captured the elastic-plastic behaviour of the experimental creep and tensile data. In the subsequent optimisation (stage 2, shown in Figure 5.4c-d and Figure 5.5c-d), the coupled EVP-CD and EVP-WD models were not very accurate in capturing damage behaviour, particularly for the strains-to-failure. Specifically, for the best calibration run at 800°C, the average relative errors of the strains-to-failure for the EVP-CD and EVP-WD models were 16% and 18%, respectively. These inaccuracies could be attributed to the limitations of the infinitesimal strain theory, which disregards the effects of large deformations, rotations, and non-linear material behaviour. Additionally, the modular approach of the separate optimisations simplified and reduced the computational burden of the calibration process, by splitting the high-dimensional parameter space into two lower-dimensional parameter spaces. However, separate optimisations can overlook the interactions between the viscoplastic response and damage accumulation — such as the effects of localised plastic deformation on damage initiation and growth rates, and the effects of damage evolution on the strain rate sensitivity, creep deformation rate, and strain hardening behaviour. The neglect of these interactions combined with the limitations of the infinitesimal strain theory likely contributed to the decreased accuracy in capturing the damage behaviour during the second optimisation.

The correctional optimisation (stage 3, shown in Figure 5.4e-f and Figure 5.5e-f) aimed to better capture the parameter interactions by simultaneously fine-tuning the parameters of the EVP and damage (CD, WD) models. The overall accuracy of both models improved in the correctional optimisation — for instance, for the best calibration run at 800°C, the averaged objective values for the EVP-CD and EVP-WD models decreased by 14% and 27%, respectively. Notably, the EVP-WD model showed more substantial improvements, which was attributed to the larger number of material parameters in the WD model as well as the tighter coupling between the EVP and WD models, particularly with the WD model's reliance on the loading history and accumulated work. While initialising the parameters helped reduce the computational burden by allowing for faster convergence, the effectiveness of the correctional optimisation still hinges on the assumption that the separately optimised parameters are close to their optimal values. This can be problematic for more complex models (e.g., physics-based models), where the correctional optimisation could further worsen the simulations by overfitting the calibration datasets.

The boxplots in Figure 5.4g and Figure 5.5g show the optimised parameters for the EVP-CD and EVP-WD models after the three-stage calibration runs at 800°C. The optimised parameters at all three temperatures are also tabulated in Appendix B.4. During the calibration runs, the MOGA converged towards a spread of different parameter values. This lack of uniqueness in the optimised parameters is attributed to the non-deterministic nature of the GA, the non-linearity of the objective functions, the predefined termination of the MOGA (after 250 or 500 generations), as well as the optimisation problem not being sufficiently constrained. The spread could potentially be reduced by introducing additional calibration datasets, reducing the size of the searched parameter space, and further tuning the MOGA's hyperparameters. That said, the spread of the parameters was

relatively narrow compared to the applied bounds, which demonstrates the repeatability of the calibration process and the sufficiency of the current setup for optimising the EVP-CD and EVP-WD models. The boxplots in Figure 5.5g also show that there were inconsistencies between the optimised values for the  $A_{WD}$ ,  $a_{WD}$ ,  $B_{WD}$ , and  $b_{WD}$  parameters and the experimentally observed values discussed in Section 5.3.3. These inconsistencies were due to the optimised values being based at one temperature, while the experimentally observed values were calculated from all three temperatures. It is worth noting that attempts were made to fix these parameters, which did not yield models that predicted the data well. However, the optimised values are still of the same order of magnitude, which suggests that the experimentally observed parameter values should only be used to determine the bounds of the parameters for the calibration process.

The robustness of the multi-objective three-stage calibration workflow depends on the underlying microstructural stability of the material. The success of the calibration workflow in capturing the behaviour of Alloy 617 can be attributed to its high microstructural stability, which minimises phase transformations and limits the influence of thermodynamic effects on deformation [237]. However, materials that are prone to phase changes, carbide coarsening, or grain boundary evolution, can undergo significant microstructural changes over prolonged high-temperature loading. These changes can trigger shifts in the dominant deformation and degradation mechanisms, which in turn alter the material's mechanical response [238-240]. For these microstructurally unstable materials, the mechanical response captured during stage 1 (initial yielding) and stage 2 (damage progression) may reflect drastically different microstructural states. This can cause the correctional optimisation to over-fit either the yielding or damage response, rather than achieving a balanced fit across the entire deformation history. To address this issue, the calibration workflow can be extended with additional stages spaced across narrower intervals, allowing the parameter subsets to adapt progressively to the material's evolving behaviour.

#### 5.5.4. Performance of calibrated models

As discussed in Section 5.3.1, the semi-empirical models were formulated within the infinitesimal strain framework [23, 25, 229] despite the experimental data exceeding the framework's validity limit. Consequently, these models were empirically calibrated to reproduce the relevant macroscopic behaviours observed in tensile and creep tests. In this sense, the EVP-CD and EVP-WD models are suitable for fitness-for-service assessments where deformation paths remain within the calibrated range.

To evaluate the predictive capabilities of the fully calibrated EVP-CD and EVP-WD models (i.e., after stage 3), a detailed comparison was performed between experimentally observed and simulated material properties under creep and tensile loading at 800°C, 900°C, and 1000°C. The comparisons for the best calibration run are shown in Figure 5.6 with the plots in the top row (a, b, c, and d) comparing the total creep deformation ( $\varepsilon_{area}$ ), minimum creep rate ( $\dot{\varepsilon}_m$ ), time-to-failure ( $t_f$ ), and strain-to-failure ( $\varepsilon_f$ ) for the creep curves, and the plots in the bottom row (e, f, g, and h) comparing the toughness ( $\sigma_{area}$ ), yield stress ( $\sigma_y$ ), maximum true stress ( $\sigma_M$ ), and strain-at-ductility ( $\varepsilon_d$ ) for the tensile curves. These plotted material properties correspond to the objective functions used for the MOGA optimisation, as described in Section 5.4.2, and the accuracies in capturing the material properties are indicated by the proximity of the individual symbols to the ideal 1:1 line.

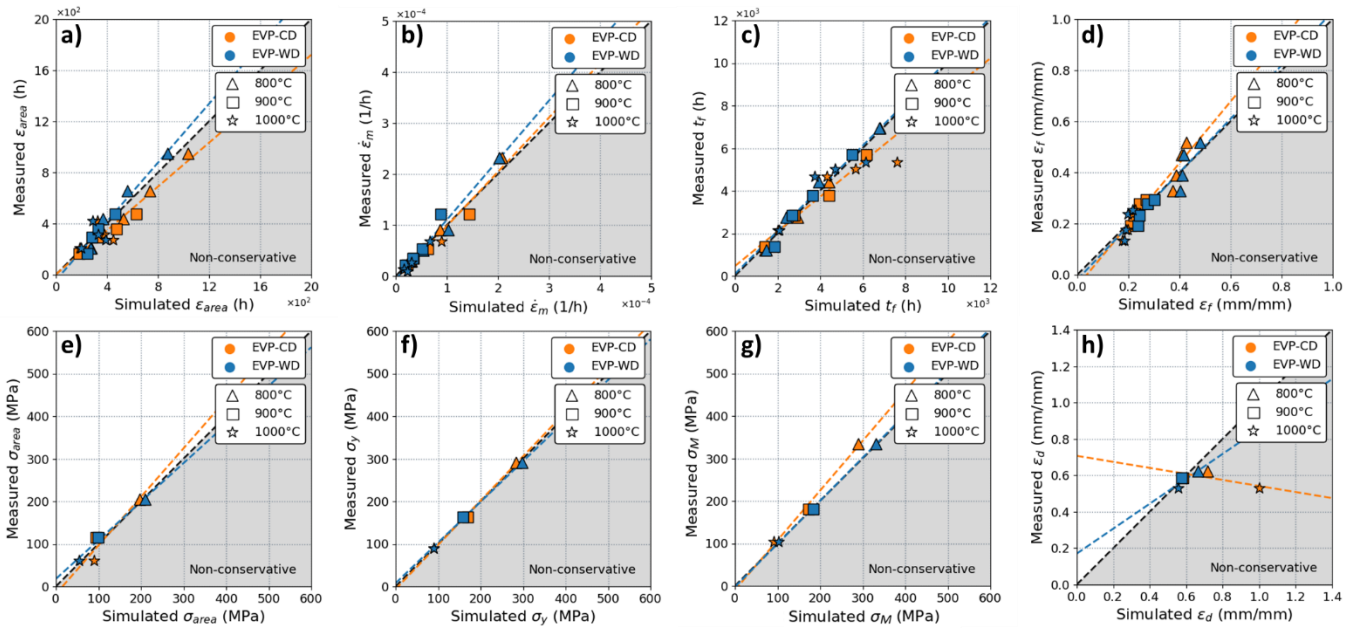


Figure 5.6. Assessment of simulated material properties by the EVP-CD model (orange) and EVP-WD model (blue) at 800°C, 900°C, and 1000°C. The plots in a), b), c), and d) compare the total creep deformation, minimum creep rate, time-to-failure, and strain-to-failure of the experimental and simulated creep curves. The plots in e), f), g), and h) compare the toughness, yield stress, maximum tensile stress, and strain-at-ductility of the experimental and simulated tensile curves.

As seen in Figure 5.6, the EVP-CD and EVP-WD models capture the creep behaviour of Alloy 617 with comparable accuracy, with the EVP-WD model slightly outperforming for the times- and strains-to-failure. In addition, most of the material properties captured by the EVP-WD model are conservative, which is useful for capturing the safe lifetimes of materials under in-service operating conditions. Both models were able to accurately predict the longer-term creep curves (i.e., validation data), which showcase their capacity to encapsulate the physical processes inherent to the material. These results also demonstrate that short-term experimental data can sufficiently calibrate the EVP-CD and EVP-WD model to predict longer-term behaviour, which is significant since short-term data is easier and less costly to obtain than longer-term experimental data. However, in this study, the longer-term validation data only captures times-to-failure out to around one year, while VHTR designs will require 100,000 hours or more of component lifetime. Thus, future work will be required to understand if accurate extrapolations can be made out to 100,000 hours, and if so, what times-to-failure would be required for the calibration data. Additionally, the accuracy of the time-to-failure predictions is shown to decrease with increasing temperature (Figure 5.6c). This was attributed to the increasing effect of the in-air oxidation during the creep testing [9, 84, 207] at higher temperatures (i.e., 1000°C), which the models and the data removal (Section 5.2) were unable to account for. That said, reduced time-to-failure accuracy at 1000°C is not a concern for VHTR designs using ASME Code Case N-898, which limits the temperature to 954°C and below.

When it comes to tensile behaviour, both models accurately captured the yield stress and toughness. This is expected since both models share the EVP model, which is mostly responsible for capturing those material properties. The greatest discrepancies in the performance of the two models lie in the capturing of the maximum true stress and strain-at-ductility. This is demonstrated in Figure 5.6g-h, with the EVP-WD model substantially outperforming the EVP-CD model. These discrepancies can be attributed to the fact that the CD

model posits that damage accumulates as a function of time instead of strain or plastic work density [233]. As such, the CD model is not mathematically suited to capture failure in tensile deformation, especially at the comparatively high strain rates of the tensile data (i.e.,  $1.0 \times 10^{-4}\text{s}^{-1}$ ). However, the WD model defines the damage accumulation using piecewise correlations that simulate separate behaviours depending on the plastic work density rate, allowing the WD model to account for the contrastingly different strain rates observed in creep and tensile experiments. These results suggest that the WD model could be extended to capture additional loading configurations (e.g., fatigue data) by defining the critical plastic work density ( $W_{crit}$ ) with an  $N$ -linear function and the damage exponent ( $n_d$ ) with an  $N$ -step function, where  $N$  refers to the number of loading configurations to be captured.

### 5.5.5. Computational costs

While the EVP-WD model can capture tensile damage with greater accuracy compared to the EVP-CD model, the EVP-WD model suffers from a more complex implementation, larger number of material parameters, and higher evaluation times. Specifically, each evaluation of the EVP-WD model took an average of 1.395s of CPU time on a single core of a 3.80 GHz Intel Core i7-10700KF processor, while each evaluation of the EVP-CD model took an average of only 0.595s. The EVP-WD model was also found to require more generations (500) to reach a suitable set of material parameter values compared to the EVP-CD model (250). This was attributed to the larger parameter space as well as the tighter coupling between the EVP and WD models. As such, with the higher evaluation time and number of generations, the EVP-WD model requires significantly more computational resources to calibrate.

### 5.6. Conclusion

In this study, a three-stage calibration framework was developed to simultaneously calibrate semi-empirical material models to the high-temperature creep and tensile behaviour of Alloy 617 at 800°C, 900°C, and 1000°C. The models employed a temperature-dependent elastic-viscoplastic (EVP) formulation coupled with either classical creep damage (EVP-CD) or work-based damage (EVP-WD) model. A multi-objective genetic algorithm (MOGA) was utilised to concurrently fit both model variants to short-term creep and tensile datasets provided by Idaho National Laboratory (INL). Validation was subsequently performed against independent longer-term creep measurements, allowing assessment of the models' predictive capabilities beyond the calibration dataset.

The three-stage calibration consisted of 1) the identification of EVP parameters, 2) the calibration of damage parameters (CD or WD), and 3) the joint fine-tuning of all parameters. This staged approach enabled robust and efficient calibration against the short-term experimental data. The repeatability of the calibration was assessed through ten independent optimisation runs, revealing some variability due to the stochastic nature of the genetic algorithm and the inherent non-linearity of the calibration problem. It is therefore recommended to perform multiple calibration runs to ensure the identification of robust and representative parameter sets.

Once calibrated, both EVP-CD and EVP-WD models successfully captured the creep response of Alloy 617 at 800°C and 900°C with comparable accuracy. However, predictive performance decreased at 1000°C due to surface oxidation effects leading to atypical tertiary creep behaviour, which the current models were not formulated to describe. Overall, the EVP-WD model demonstrated superior accuracy in reproducing the full tensile stress-strain response compared to the EVP-CD model, although at the cost of increased computational

complexity and calibration effort. Additionally, the WD formulation, by capturing deformation history through plastic work density, holds potential for extension to other loading scenarios, such as fatigue or thermo-mechanical cycling.

It is important to acknowledge that the constitutive models employed here were based on the infinitesimal strain theory, thus their accuracy at large deformations — such as those near tensile failure — may be limited. Nevertheless, they remain practically applicable and reliable for moderate strains, typical of creep deformation and inelastic service conditions. The newly developed three-stage calibration workflow addresses the significant challenge of simultaneously calibrating material models against distinct mechanical responses, offering a structured foundation for extending this approach to alternative constitutive frameworks or different material systems in future research.

# Chapter 6

## Calibration of physics-based crystal plasticity finite element method models for the multiscale deformation behaviour of Alloy 617

The work presented in this chapter was published by the author as ‘Multi-Objective Surrogate-Assisted Calibration of CPFEM Models Using Macroscopic Response and In Situ EBSD Measurements of Grain Reorientation Trajectories’ in *Acta Materialia*, 2026 [202]. This work was produced in collaboration with Ondrej Muránsky, Mark Messner, Tao Wei, Tianchen Hu, Jay Kruzic, and Michael McMurtrey. Similar to Chapter 5, the presented text has been adapted from the published version to include additional content, reduce repetition, and improve consistency.

### 6.1. *Introduction*

Material models are of technological importance in materials science and engineering, enabling the prediction of material behaviour under various conditions. Empirical and semi-empirical elasto-plastic models are widely utilised in engineering applications due to their straightforward implementation and computational efficiency [15, 22, 118, 241], relying primarily on experimental data to establish relationships between stress and strain. However, these models do not directly consider the alloy’s microstructural influences on their elasto-plastic behaviour. To address this limitation, microstructure-informed models have been developed and are widely adopted by the research community [135, 242-245]. In particular, crystal plasticity finite element method (CPFEM) models simulate the elasto-plastic deformation of polycrystalline materials at the crystal scale by considering the alloy’s microstructure, deformation mechanisms, and grain-to-grain interactions [124, 126]. While CPFEM models offer enhanced accuracy by integrating detailed microstructural information, they are significantly more computationally expensive, posing challenges for their use in practical engineering applications [16, 27].

One of the first steps in the deployment of CPFEM models in engineering finite element analyses is to calibrate these models against experimental data to ensure that the simulated responses accurately reflect observed material behaviour under simple experimental loading conditions. The calibration process of CPFEM models involves the numerical identification of the constitutive material parameters that govern the material’s behaviour at the microstructural level, such as the slip system strengths, hardening coefficients, and interaction terms. The existing literature frequently relies on manual trial-and-error methods to calibrate CPFEM models against a single objective, such as a uniaxial stress-strain curve. However, this approach depends heavily on prior knowledge of the constitutive parameters and can be extremely time consuming, given the extensive parameter space of CPFEM models necessitating numerous evaluations [16, 27, 28]. In addition, calibrating against a single objective often leads to an under-constrained problem where multiple sets of parameters yield similar results, leading to ambiguity and reduced reliability in the calibrated models. Hence, many authors use additional data as objectives to constrain the large parameter space, such as the internal lattice strains of grain families [246-248], reorientation trajectories of individual grains [249], or overall texture evolution [250-252]. However, the calibration of models against multiple objectives introduces complexities that make the process

even more computationally expensive. As such, various optimisation methodologies have been employed for the multi-objective calibration of CPFEM models [28, 126, 249, 253].

These optimisation methods are broadly categorised into gradient-based and direct-search optimisation methods, each with their own advantages and limitations. Gradient-based optimisation methods, such as gradient descent, Adam, and Newton's methods, are efficient and well-suited for high-dimensional problems [142-144]. However, these methods rely heavily on the initial parameter values and are highly susceptible to converging towards local minima, particularly in the complex and non-linear parameter spaces characteristic of CPFEM simulations [27, 142]. Gradient-based methods also require differentiability in their objective functions, in which noise in the experimental data could deteriorate convergence behaviour [27]. In contrast, direct-search optimisation methods do not rely on gradient information, making them generally more robust and better suited for exploring diverse regions of large parameter spaces [15, 29]. These methods are also more effective at locating global minima and can handle multiple objective functions simultaneously. A popular example is the genetic algorithm (GA), which has been used extensively to identify the constitutive parameters in various crystal plasticity (CP) constitutive laws [27, 33, 34]. Despite these advantages, direct-search methods typically require a substantial number of evaluations to achieve convergence, which can be prohibitive given the high computational cost of each CPFEM simulation.

To address the computational challenges associated with calibrating CPFEM models using direct-search optimisation, surrogate modelling techniques have emerged as a viable solution to approximate the input-output relationships of computationally expensive models with significantly reduced computational costs. A notable example of such techniques is symbolic regression, which has recently been used in Ref. [198] to derive interpretable mathematical relationships from CPFEM simulations of Ti–6Al–4V. Other well-established techniques include the response surface methodology [171], Kriging method [169], and deep neural networks (DNNs) [254]. By developing a surrogate model, the calibration process can leverage these faster approximations to explore the parameter space more efficiently. This enables the application of direct-search optimisation methods to the surrogate model, thereby minimising the number of required CPFEM simulations [255, 256]. Once an optimal set of constitutive parameters is identified through the surrogate-based optimisation, these parameters can be used to calibrate the original CPFEM model with much lower computational overhead. Consequently, surrogate modelling not only alleviates the computational burden but also facilitates the practical application of robust optimisation techniques in the calibration of complex microstructure-informed material models [126, 255, 256].

In the present work, *in situ* electron backscatter diffraction (EBSD) was performed on an Alloy 617 specimen under uniaxial tensile loading at room temperature to obtain both the macroscopic stress–strain response and grain-scale reorientation trajectories. These experimental datasets were used to calibrate CPFEM models with three CP formulations: (i) a Voce hardening (VH) formulation, (ii) a two-coefficient latent hardening (LH2) formulation, and (iii) a six-coefficient latent hardening (LH6) formulation — implemented within low- and high-fidelity finite element (FE) microstructural representations of the specimen gauge. The calibration employed a multi-objective surrogate-assisted workflow in which a multi-objective genetic algorithm (MOGA) was coupled with an adaptively trained deep neural network (DNN) surrogate model to efficiently identify CP parameters that reproduce both the macroscopic stress–strain curve and the reorientation trajectories of eight selected

grains in the low-fidelity model. The performance of the CPFEM models was then validated against the trajectories of eight additional grains and the overall texture evolution. Finally, the optimised parameter sets from the low-fidelity calibrations were applied to the corresponding high-fidelity CPFEM models to assess their transferability across different microstructural fidelities within the FE framework.

## 6.2. *Experimental data*

The following section describes the experimental procedures and datasets used in this study. The section includes details on the Alloy 617 material (Section 6.2.1), the data acquisition during the *in situ* EBSD-based tensile testing (Section 6.2.2), the analysis of grain reorientation across EBSD maps (Section 6.2.3), and the generation of finite element (FE) microstructural models from the initial EBSD map (Section 6.2.4).

### 6.2.1. Material

Alloy 617 is a solid solution and precipitation strengthened Ni-Cr-Co alloy, offering an exceptional combination of thermal, mechanical, physical, and corrosion-resistance [1]. In particular, the alloy maintains high strength and excellent creep resistance at elevated temperatures. In addition, its corrosion resistance supports applications in chemical processing environments [2, 3], while its high ductility and toughness at lower temperatures allow for use in certain cryogenic systems [4]. These properties allow Alloy 617 to perform reliably across a broad temperature range, expanding its versatility in critical engineering applications. In particular, the nuclear industry is pursuing the alloy as structural material for intermediate heat exchangers in the next generation (Gen IV) of nuclear reactor systems [5], which are expected to operate at significantly higher temperatures (up to 950°C) [1, 6, 7] than the current fleet of nuclear reactor systems (300°C). The aerospace industry also employs Alloy 617 in the combustion chambers and exhaust systems of jet engines and gas turbines due to the alloy's ability to withstand thermal and mechanical stresses [8-10]. The alloy studied in the present work has been provided by Idaho National Laboratory and was a part of the material used for the development of the ASME Section III, Division 5 code case permitting the use of Alloy 617 in nuclear high-temperature applications [50].

### 6.2.2. Data acquisition during tensile loading

The *in situ* tensile testing was performed using a Zeiss UltraPlus scanning electron microscope (SEM) equipped with a Kammrath & Weiss GmbH tensile loading stage. The test was conducted at room temperature at a post-yield displacement rate of  $0.224\mu\text{ms}^{-1}$  and strain rate of  $10^{-4}\text{s}^{-1}$ , following a stepwise loading approach in crosshead control mode. At each step, the miniaturised tensile specimen (see Figure 6.1a) was first loaded to a specified displacement level and then unloaded to 15MPa to facilitate the acquisition of the electron backscatter diffraction (EBSD) data. The EBSD measurements were performed using an electron beam energy of 20kV, with each map taking approximately 30 minutes to acquire. After the data was collected, the specimen was reloaded to a higher displacement level in the subsequent step and unloaded again for further EBSD mapping. In total, 24 EBSD orientation maps were acquired, each corresponding to a different level of imparted plastic strain. These maps are presented in Appendix C.1.

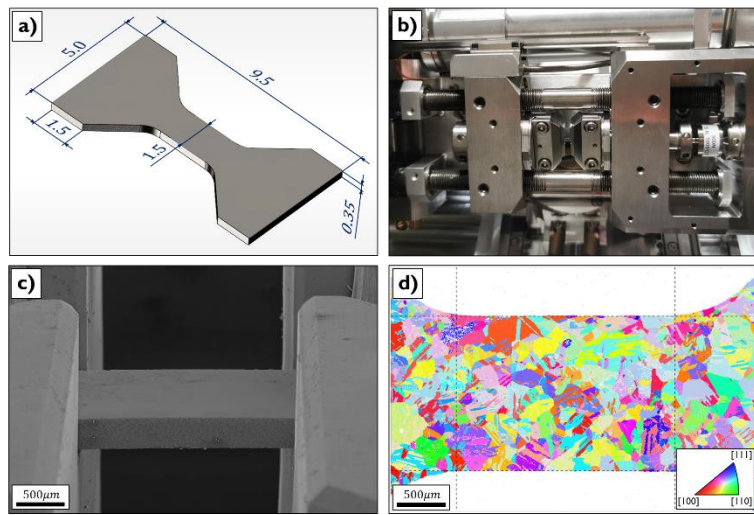


Figure 6.1. Images of the experimental data acquisition — a) dimensioned drawing of the specimen, b) photograph of the specimen in the loading stage, c) SEM micrograph of the specimen in the loading stage, and d) initial EBSD map shown as IPF- $x$  coloured map.

The plot in Figure 6.2 presents the true stress–strain response for the miniaturised tensile specimen with the unloading/reloading portions removed. In this plot, the dashed blue lines mark the points at which the EBSD datasets were collected. The plot also compares this response with that of a standard-sized specimen tested at Idaho National Laboratory under identical strain rate and temperature conditions following ASTM E8-11 [73, 77]. The close agreement of the two responses suggest that the stepwise loading procedure and the specimen-size differences have minimal influence on the measured mechanical behaviour. Additionally, the EBSD maps were acquired at a magnification of  $30 \times$  with a  $120\mu\text{m}$  aperture and a spatial resolution of  $5\mu\text{m}$ . This configuration enabled relatively fast data acquisition of around 10 to 30 minutes per map, depending on the level of imparted plastic strain. The map size of  $2865\mu\text{m} \times 1920\mu\text{m}$  was sufficient to capture nearly the entire initial gauge section of the specimen, which has approximate dimensions of  $2200\mu\text{m} \times 1560\mu\text{m}$ . However, as shown in Figure 6.1c, partial shadowing from the loading stage obstructed the EBSD detector, resulting in missing data along the upper edges of the specimen.

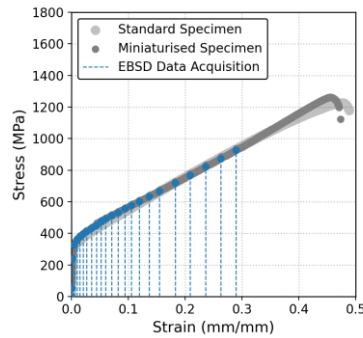


Figure 6.2. Comparison of the recorded true stress–strain curves obtained during the in-situ EBSD experiment on the miniaturised tensile specimen (Figure 6.1) and on a standard tensile specimen [77]. Dashed blue lines indicate the stress–strain positions at which the EBSD datasets were collected (Figure C.1).

### 6.2.3. Grain reorientation trajectories

Grain tracking is essential for understanding the evolution of crystallographic texture as a function of plastic deformation in the specimen gauge during tensile loading. In this work, an automated grain-tracking algorithm was developed to monitor the orientation of individual grains across the sequence of 24 EBSD maps, as described in Appendix C.2. The algorithm operates by matching grains between consecutive maps based on the normalised distance between their centroids and the similarity of their crystallographic orientations. A grain in a subsequent EBSD map is considered a match if its centroid lies within a predefined distance threshold and its orientation difference is within an acceptable tolerance relative to the grain in the preceding map. This iterative matching procedure enables continuous tracking of individual grains from the initial undeformed state to high levels of plastic strain. Once tracked, the reorientation trajectories of individual grains were constructed by stitching their crystallographic orientations throughout their deformation sequence. The constructed reorientation trajectories exhibited notable noise due to measurement variability, which was mitigated through smoothing using spherical linear interpolation (SLERP). Once smoothed, the reorientation trajectories were manually inspected to ensure that they did not significantly deviate from the raw data.

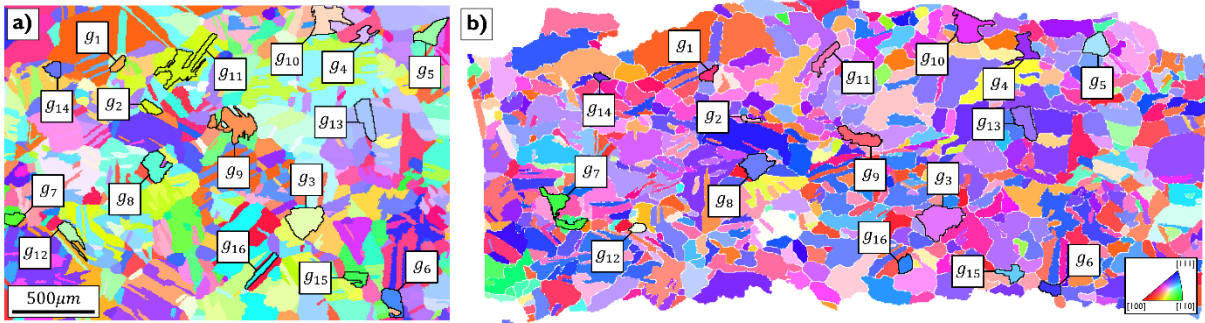


Figure 6.3. Selected grains ( $g_{1..16}$ ) on the a) initial EBSD map ( $\varepsilon = 0.0\%$ ) and b) final EBSD map ( $\varepsilon = 29.0\%$ ) shown as IPF- $x$  coloured maps.

In this study, the reorientation trajectories of 16 grains ( $g_{1..16}$ ) were selected from the tracked EBSD dataset for use in the calibration and validation procedures. These grains were chosen to span a broad range of initial orientations relative to the loading axis, to provide diverse spatial distribution across the specimen, and to ensure well-tracked reorientation trajectories throughout the deformation process. The location of the selected grains on the initial ( $\varepsilon = 0.0\%$ ) and final ( $\varepsilon = 29.0\%$ ) EBSD maps are shown in Figure 6.3, while their deformation paths are summarised in Appendix C.2. In addition, the inverse pole figures (IPFs) in Figure 6.4 compare the raw and SLERP-smoothed reorientation trajectories of  $g_{1..16}$  in the loading direction ( $x$ ).

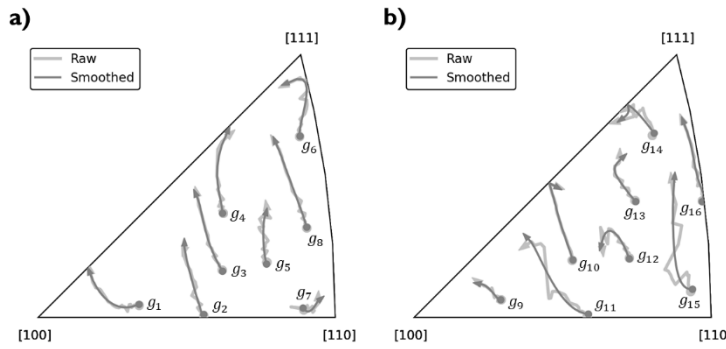


Figure 6.4. Inverse pole figures (IPFs) of the raw and SLERP-smoothened reorientation trajectories of grains a)  $g_{1..8}$  and b)  $g_{9..16}$  in the  $x$ -direction.

#### 6.2.4. Finite element model generation

Initial analysis of the collected EBSD orientation data and subsequent grain segmentation was performed using the MTEX MATLAB toolbox [257]. In the first EBSD map (Figure 6.1d), any missing data was reconstructed by extrapolating crystal orientations from neighbouring regions, which enabled the generation of finite element (FE) microstructural models of the specimen gauge. This EBSD dataset contains a total of 571 grains and was acquired before tensile testing at a spatial resolution of  $5\mu\text{m}$ . The EBSD data was downsampled using the MTEX function, ‘reduce’, and used to generate microstructural FE models of the specimen gauge. The models were generated by creating a 2.5D volumetric representation from the initial 2D EBSD orientation map. This was accomplished by replicating the 2D data along the specimen thickness (z-axis), thereby forming a voxelated volume. The voxellation was then converted into a hexahedral (hex) mesh using the ‘Sculpt’ module in Cubit Coreform 2022.4 [258] and scaled to  $300\mu\text{m}$  to reflect the actual thickness of the specimen. This process produces a 2.5D representation of the specimen [138], since the mesh extends the 2D surface microstructure into a third dimension but does not account for variations in grain geometry through the depth of the specimen. In this conversion process, voxels corresponding to individual grains were mapped onto FE blocks, where each block is formed from a subset of hex elements used to represent that grain. It should be noted that some grains were lost during the conversion from the voxellation into the 2.5D mesh due to limitations inherent in the voxel merging and meshing process.

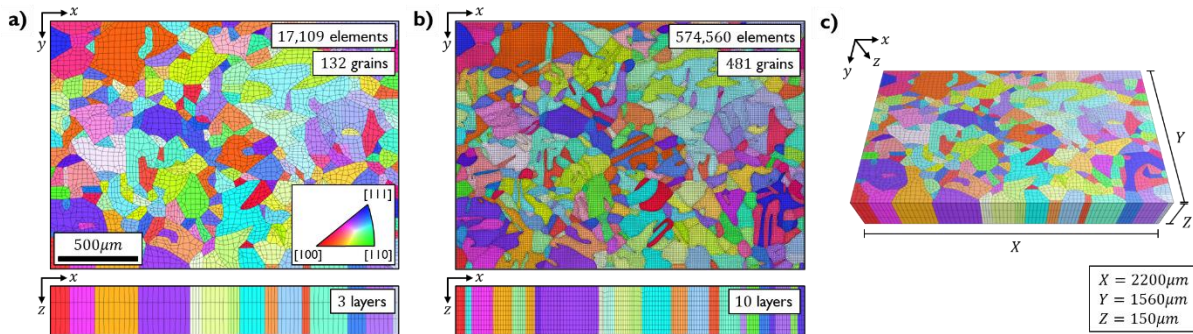


Figure 6.5. IPF- $x$  coloured maps of a) the low-fidelity mesh (top and side view), b) the high-fidelity mesh (top and side view), and c) the low-fidelity mesh (angled view).

Using the meshing processes, a low- and high-fidelity FE model was generated at a downsampled resolution of 40 $\mu\text{m}$  (containing 132 grains) and 10 $\mu\text{m}$  (containing 481 grains), respectively, as shown in Figure 6.5. These resolutions were selected based on a sensitivity study to examine the effects of mesh resolution on the morphology and response of the FE models, as shown in Appendix C.3. The low-fidelity model was generated with three layers of elements along the specimen's thickness, containing a total of 17,109 hex elements. In contrast, the high-fidelity mesh was generated with ten layers of elements, containing a total of 574,560 hex elements. While the high-fidelity model offered a more accurate representation of the microstructure, its higher element count substantially amplified the computational costs of each CPFEM evaluation.

### 6.3. *Microstructure-informed material models*

In this study, the crystal plasticity finite element method (CPFEM) was utilised to simulate the multiscale behaviour of the Alloy 617 specimen under uniaxial tensile loading. The crystal plasticity (CP) formulations were implemented in the nuclear engineering material library (NEML) [228] to describe the mechanical and microstructural response of the tested alloy. The CP formulations were integrated with the finite element (FE) models through Deer [259], an application of the open-source multiphysics object-oriented simulation environment (MOOSE) [260] that links to NEML. The formulations include a Voce hardening (VH) formulation [104], a two-coefficient latent hardening (LH2) formulation [261], and a six-coefficient latent hardening (LH6) formulation [261]. These phenomenological formulations were chosen to represent progressively increasing levels of model complexity and parameterisation, while remaining widely used in CPFEM literature. While other hardening formulations (e.g., Kocks-Mecking and dislocation-density-based) could provide additional mechanistic insights [262-264], they were not considered in this work as they are not yet available within the current MOOSE-NEML framework. Accordingly, the following section will provide an overview of CP (Section 6.3.1), as well as descriptions of the VH (Section 6.3.2), LH2 (Section 6.3.3), and LH6 (Section 6.3.4) formulations. In addition, a summary of the constitutive parameters for all three formulation can be found in Appendix C.4.

#### 6.3.1. Crystal plasticity formulation

Crystal plasticity (CP) formulations were defined to simulate the multiscale behaviour of Alloy 617. In these formulations, the plastic velocity gradient ( $L^p$ ) of a single crystal is defined as a sum of the shear deformation of each slip system [265]. The slip rate of a slip system ( $\dot{\gamma}_\alpha$ ) is defined using the standard power law model, as shown in Eq. (45), where  $\dot{\gamma}_0$  represents the reference slip rate,  $n$  represents the strain rate sensitivity parameter,  $\tau_\alpha$  represents the resolved shear stress (RSS), and  $\tau_\alpha^*$  represents the critical resolved shear stress (CRSS).

$$\dot{\gamma}_\alpha = \dot{\gamma}_0 \left| \frac{\tau_\alpha}{\tau_\alpha^*} \right|^{n-1} \left( \frac{\tau_\alpha}{\tau_\alpha^*} \right) \quad (45)$$

The reference slip rate ( $\dot{\gamma}_0$ ) is defined based on the uniaxial strain rate ( $\dot{\varepsilon}$ ) and Taylor factor ( $M$ ) [266], as shown in Eq. (46). The Taylor factor for face-centred cubic (FCC) polycrystalline metals with random orientations under uniaxial tensile deformation has been previously calculated to be 3.07 using a full constraint Taylor model [31, 266-268]. As such, with a post-yield strain rate of  $10^{-4}\text{s}^{-1}$  (Section 6.2.2), the reference slip rate was set to  $3.25 \times 10^{-5}\text{s}^{-1}$  to reduce the rate sensitivity in the model response.

$$\dot{\gamma}_0 = \dot{\varepsilon}/M \quad (46)$$

The CRSS of a slip system ( $\tau_\alpha^*$ ) describes the threshold shear stress required to initiate slip. When the RSS exceeds the CRSS, dislocations will begin moving along the slip system, and the crystal will begin plastically deforming [59]. The CP formulations define the CRSS of a slip system as the sum of its static strength ( $\tau_0$ ) and its dynamic strength ( $\tau'_\alpha$ ), as shown in Eq. (47). In this equation, the static strength represents the inherent resistance of all the slip systems, while the dynamic strength represents the additional resistance that evolves based on time-dependent factors.

$$\tau_\alpha^* = \tau_0 + \tau'_\alpha \quad (47)$$

### 6.3.2. Voce hardening formulation

The Voce hardening (VH) formulation [104] assumes that all slip systems share the same dynamic strength ( $\tau'$ ), accounting for all three stages of single crystal plasticity behaviour. The VH formulation is defined in Eq. (48) [104], where  $b$  represents the saturation rate parameter and  $\tau_s$  represents the saturation strength. Hence, the VH formulation is governed by four adjustable constitutive material parameters —  $\tau_0$ ,  $n$ ,  $b$ , and  $\tau_s$ .

$$\dot{\tau}' = b(\tau_s - \tau') \sum_{\alpha \in A} |\dot{\gamma}_\alpha| \quad (48)$$

### 6.3.3. Two-coefficient latent hardening formulation

In contrast, the latent hardening formulations [261] assume that the dynamic strength of the slip systems ( $\tau'_\alpha$ ) evolve independently, accounting for only the first two stages of single crystal plasticity behaviour (i.e., easy glide and linear hardening). The latent hardening formulations simulate hardening behaviour by considering the interaction strengths between slip systems, as shown in Eq. (49) [261]. In this equation,  $H_{\alpha,\beta}$  represents an element of the interaction matrix that quantifies how much slip system  $\beta$  contributes to the hardening of slip system  $\alpha$ .

$$\dot{\tau}'_\alpha = \sum_{\beta \in A} H_{\alpha,\beta} |\dot{\gamma}_\beta| \quad (49)$$

For FCC crystal structures with 12 independent  $\{111\}\langle 110 \rangle$  slip systems, the interaction matrix is a  $12 \times 12$  matrix designed to capture the influence of dislocation interactions between the slip systems. The 144 elements of the interaction matrix are typically reduced to two independent coefficients [269-271]. In this two-coefficient interaction matrix ( $\mathbf{H}_2$ ), the diagonal elements (i.e.,  $\alpha = \beta$ ) correspond to the self-hardening coefficient ( $h_{\alpha\alpha}$ ) and the off-diagonal elements (i.e.,  $\alpha \neq \beta$ ) correspond to the latent hardening coefficient ( $h_{\alpha\beta}$ ). The two-coefficient latent hardening (LH2) formulation employs the  $\mathbf{H}_2$  interaction matrix and is thus governed by four adjustable constitutive material parameters —  $\tau_0$ ,  $n$ ,  $h_{\alpha\alpha}$ , and  $h_{\alpha\beta}$ .

### 6.3.4. Six-coefficient latent hardening formulation

According to Franciosi *et al.* [62], the elements of the interaction matrix can also be reduced to six independent coefficients due to the diagonal symmetry of the matrix and the ternary symmetry of the four  $\langle 111 \rangle$  axes [65]. The six-coefficient interaction matrix ( $H_6$ ) is shown in Eq. (50), in which the diagonal elements correspond to the self-hardening coefficient ( $h_{\alpha\alpha}$ ) and the off-diagonal elements correspond to five distinct latent hardening coefficients ( $h_1, h_2, h_3, h_4$ , and  $h_5$ ). The latent hardening coefficients represent the strengths of the coplanar, Hirth lock, collinear, glissile junction, and sessile junction interactions [65, 272], respectively.

$$H_6 = \begin{bmatrix} h_{\alpha\alpha} & h_1 & h_1 & h_3 & h_4 & h_4 & h_2 & h_4 & h_5 & h_2 & h_5 & h_4 \\ h_1 & h_{\alpha\alpha} & h_1 & h_4 & h_2 & h_5 & h_4 & h_3 & h_4 & h_5 & h_2 & h_4 \\ h_1 & h_1 & h_{\alpha\alpha} & h_4 & h_5 & h_2 & h_5 & h_4 & h_2 & h_4 & h_4 & h_3 \\ h_3 & h_4 & h_4 & h_{\alpha\alpha} & h_1 & h_1 & h_2 & h_5 & h_4 & h_2 & h_4 & h_5 \\ h_4 & h_2 & h_5 & h_1 & h_{\alpha\alpha} & h_1 & h_5 & h_2 & h_4 & h_4 & h_3 & h_4 \\ h_4 & h_5 & h_2 & h_1 & h_1 & h_{\alpha\alpha} & h_4 & h_4 & h_3 & h_5 & h_4 & h_2 \\ h_2 & h_4 & h_5 & h_2 & h_5 & h_4 & h_{\alpha\alpha} & h_1 & h_1 & h_3 & h_4 & h_4 \\ h_4 & h_3 & h_4 & h_5 & h_2 & h_4 & h_1 & h_{\alpha\alpha} & h_1 & h_4 & h_2 & h_5 \\ h_5 & h_4 & h_2 & h_4 & h_4 & h_3 & h_1 & h_1 & h_{\alpha\alpha} & h_4 & h_5 & h_2 \\ h_2 & h_5 & h_4 & h_2 & h_4 & h_5 & h_3 & h_4 & h_4 & h_{\alpha\alpha} & h_1 & h_1 \\ h_5 & h_2 & h_4 & h_4 & h_3 & h_4 & h_4 & h_2 & h_5 & h_1 & h_{\alpha\alpha} & h_1 \\ h_4 & h_4 & h_3 & h_5 & h_4 & h_2 & h_4 & h_5 & h_2 & h_1 & h_1 & h_{\alpha\alpha} \end{bmatrix} \quad (50)$$

The six-coefficient latent hardening (LH6) formulation employs the  $H_6$  interaction matrix and is thus governed by eight adjustable constitutive material parameters —  $\tau_0, n, h_{\alpha\alpha}, h_1, h_2, h_3, h_4$ , and  $h_5$ .

## 6.4. *Calibration methodology*

In this study, the multi-objective genetic algorithm (MOGA) was combined with a deep neural network (DNN) surrogate model to calibrate the CPFEM models against the experimental in situ EBSD data. A multi-objective surrogate-assisted calibration workflow was developed to iteratively reduce the discrepancies between the responses produced by the CPFEM and surrogate models. The following section will provide overviews of the MOGA optimisation (Section 6.4.1) and DNN surrogate model (Section 6.4.2), as well as describe how the MOGA and surrogate model were integrated into the calibration workflow (Section 6.4.3).

### 6.4.1. Multi-objective genetic algorithm optimisation

Similar to Chapter 5, the CPFEM models were calibrated using the non-dominated sorting genetic algorithm-II (NSGA-2) implementation of the multi-objective genetic algorithm (MOGA) [220]. Following Ref. [15, 27, 148] and optimisations with similar material models, the MOGA was configured with a population size of 100, offspring size of 100, crossover rate of 80%, and mutation rate of 1. In addition, bounds were also defined for each constitutive parameter to control the shape and size of the MOGA's search space. The bounds for the VH, LH2, and LH6 formulations were initially defined based on literature and adjusted using a Taylor mean field model [228] to ensure the optimisations remained confined to feasible and physically meaningful regions of the parameter space. The parameter bounds and the referenced literature are summarised in Appendix C.4.

In this study, the MOGA was used to minimise two objective functions. The first objective function ( $E_\sigma$ ) calculates the discrepancies between the experimental and simulated stress–strain curves using the normalised root mean square error (NRMSE), expressed as a dimensionless decimal value. The objective function follows the same definition as the  $E_\sigma$  objective function used in Chapter 5, as shown in Eq. (41). This objective function is used to assess the alignment of the experimental and simulated stress–strain responses at 32 uniformly spaced strain intervals along the curves. As such, this study uses  $M = 1$  and  $N = 32$ . Since the calibration focuses on plastic deformation rather than the elastic regime, this resolution is sufficient for capturing the relevant behaviour.

The second objective function ( $E_\phi$ ) calculates discrepancies between the experimental and simulated grain reorientation trajectories using the mean geodesic distance, expressed in radians. This is shown in Eq. (51), where  $q_{exp}$  represents a quaternion from an experimental trajectory,  $q_{sim}$  represents a quaternion from a simulated trajectory, and  $G$  represents the number of grains being evaluated. This objective function is used to assess the alignment of the experimental and simulated reorientation trajectories similarly at  $N = 32$  uniformly spaced strain intervals along the trajectories. Note that that the geodesic distance was chosen for the objective function over the misorientation to reduce the computational cost of the calibration process. As long as the orientations being compared are fairly close together in the 3D rotation space (i.e., SO(3)), this measure is identical to a misorientation calculation accounting for crystal symmetry.

$$E_\phi = \frac{1}{GN} \sum_{i=1}^G \sum_{j=1}^N 2 \cos^{-1}((q_{exp})_{i,j} \cdot (q_{sim})_{i,j}) \quad (51)$$

Once the MOGA terminates, the best solution (i.e., the knee point) is identified from the Pareto front based on the minimal squared sum of the normalised objective values, as detailed in Appendix C.5. The knee-point parameters represent the optimal trade-off between the objectives and are used to calibrate the material model, yielding simulated responses that best align with the experimentally observed material behaviour.

#### 6.4.2. Deep neural network surrogate modelling

The MOGA assesses the optimality of a set of constitutive parameters by evaluating multiple objective functions. When calibrating a material model, these objective functions require the model’s simulated response to compare with the experimentally observed material behaviour. In a single calibration, the MOGA will assess numerous parameter sets across multiple generations, which necessitates running the model a substantial number of times. However, the high computational cost of running the CPFEM models makes their direct calibration using the MOGA impractical [15, 27, 151]. The computational burden of the calibration process can be reduced by developing a surrogate model to approximate the behaviour of the CPFEM model more efficiently. Given a set of constitutive parameters, the surrogate model can approximate the stress–strain response and reorientation trajectories simulated by the CPFEM model at a fraction of the original computational cost. By employing the surrogate model to evaluate the objective functions, the MOGA is able to obtain an optimal set of constitutive parameters to calibrate the CPFEM model much faster by using significantly fewer resources.

In this study, the surrogate model was developed using a deep neural network (DNN) implemented in PyTorch [273]. The input layer of the DNN contains  $P + 1$  features, which include the  $P$  adjustable constitutive parameters of the CPFEM model and a strain value. The input layer feeds into three hidden layers with 128, 256, and 512 neurons, respectively, each followed by a rectified unit linear activation function. The output layer contains  $4G + 1$  features, consisting of four quaternion components for each of the  $G$  grains selected as well as a stress value. By predicting the macroscale stresses and grain orientations at various strains, the DNN can approximate the entire stress–strain response and  $G$  reorientation trajectories for a given set of constitutive parameters. The training dataset for the DNN was composed of the results of multiple CPFEM simulations. For each simulation, the macroscale stress and  $G$  grain orientations were extracted from the simulated material response at 32 evenly spaced strain intervals. Consequently, each CPFEM simulation provided 32 input–output pairs, with each pair corresponding to the  $P + 1$  input features and the  $4G + 1$  output features. The extracted input–output pairs from all the CPFEM simulations were then compiled to form the training dataset.

Once the training dataset was generated, the input and output features were normalised through linear and logarithmic scaling to lie within a  $[0,1]$  range. The dataset was then partitioned using K-fold cross validation with five splits, ensuring that the entire dataset would be used for training and validating the DNN across five iterations. The DNN was trained using the Adam optimiser and a  $L_1$  regularisation coefficient of  $1 \times 10^{-7}$ . The training process was guided by the mean square error (MSE) loss function to minimise the discrepancies between the DNN-predicted and CPFEM-simulated material responses. The training was performed with an initial learning rate of  $1 \times 10^{-3}$ , which was adaptively reduced by a factor of 10 with a patience of 100 epochs. The DNN was trained for up to 2000 epochs, with early termination triggered when the learning rate dropped below  $1 \times 10^{-7}$  to prevent overfitting.

#### 6.4.3. Multi-objective surrogate-assisted calibration workflow

In initial tests, surrogate models were trained against a dataset of 16 CPFEM evaluations and calibrated using the MOGA. While the surrogate models reliably reproduced the calibration dataset, the optimised parameters consistently showed poor transferability to the CPFEM models, resulting in substantial discrepancies between the CPFEM responses and the experimental data. While the accuracy of the CPFEM models improved when using larger training datasets, they required additional CPFEM evaluations that significantly increased the computational expense. As such, a multi-objective surrogate-assisted calibration workflow was developed to effectively and efficiently calibrate the CPFEM models, as summarised in Figure 6.6.

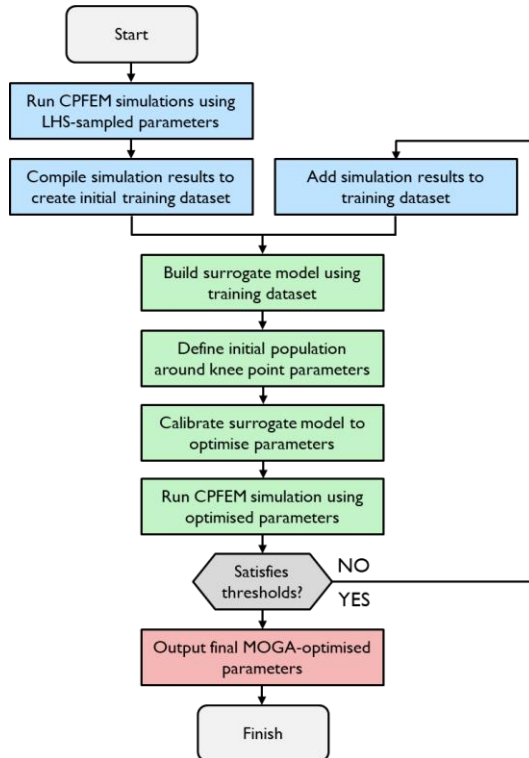


Figure 6.6. Flow chart of the multi-objective surrogate-assisted calibration workflow.

The workflow begins by sampling the parameter space using the Latin hypercube sampling (LHS) scheme within the bounds defined in Appendix C.4. A sampling size of  $2P$  was adopted to ensure a fair comparison across the CPFEM models, where  $P$  represents the number of adjustable constitutive parameters. The sampling size was chosen following Refs. [274-276] and a sensitivity study presented in Appendix C.6. For each sampled set of parameters, the CPFEM model is evaluated, and the simulated material responses are compiled to generate an initial training dataset. The surrogate model is then trained using the training dataset and calibrated using the MOGA. These MOGA optimisations use an initial population that is seeded with the knee-point parameters (Appendix C.5) from the previous CPFEM evaluations, which minimised both objective functions ( $E_\sigma$  and  $E_\phi$ ) most optimally. The CPFEM model is then evaluated using the optimised parameters, and the discrepancies between the surrogate model's approximations and the CPFEM responses are calculated by repurposing the objective functions in Eqs. (41) and (51).

If  $E_\sigma < 1\%$  and  $E_\phi < 0.1^\circ$ , the calibration workflow terminates, and the final knee-point parameters are extracted. If the criteria are not met, the CPFEM response at the MOGA-optimised parameters is incorporated into the training dataset, after which the surrogate model is retrained, and the optimisation and evaluation steps are repeated. The iterative refinement of the surrogate model at the MOGA-optimised parameters ensures that the surrogate model is most accurate in the regions of the parameter space that are actively explored by the MOGA. This refinement process continues, with each cycle improving the surrogate model's accuracy, until the accuracy thresholds ( $E_\sigma < 1\%$  and  $E_\phi < 0.1^\circ$ ) are satisfied. Although these thresholds were not selected through formal optimisation, preliminary testing indicated that they provided a practical balance between surrogate fidelity and computational cost. Importantly, the termination criterion is governed by the accuracy of the surrogate model in approximating the CPFEM responses, rather than the accuracy of the CPFEM

model in reproducing the experimentally observed behaviour. This choice was made to improve the generalisability of the calibration workflow by accommodating for biases in the calibration dataset, such as reorientation trajectories that are inherently less reproducible due to inaccuracies in the FE models.

## 6.5. Results and discussion

In this study, a calibration workflow was developed that couples a multi-objective genetic algorithm (MOGA) with an adaptively trained deep neural network (DNN) surrogate model. While the MOGA offers strong global search capabilities for multi-objective optimisation, it typically requires a large number of model evaluations — something that becomes computationally prohibitive when each evaluation involves a computationally expensive CPFEM simulation. To address this, the direct MOGA–CPFEM interaction is replaced with a DNN surrogate model that was adaptively trained to emulate the CPFEM predictions at a fraction of the computational cost. Each CP formulation (VH, LH2, and LH6) was coupled with a low-fidelity FE model and calibrated five independent times, with a new surrogate model developed in each run to avoid bias from the initial dataset or network realisation. The best-performing parameter set obtained using the low-fidelity CPFEM model was then applied to the high-fidelity microstructural model to assess both the performance and robustness of the developed calibration workflow as well as the transferability of the optimised parameters across microstructural fidelities.

The following section will first discuss the development and accuracy of the DNN surrogate models (Section 6.5.1) before evaluating the predictive performance of the calibrated CPFEM models, comparing the stress–strain response, grain reorientation trajectories, and overall texture evolution across the three CP formulations (Section 6.5.2). The section will then assess the variability of the optimised parameters across independent calibration runs (Section 6.5.3) and discuss the impact of mesoscale constraints on the calibration results (Section 6.5.4). Finally, the section will evaluate the transferability of the optimised parameters from the low- to high-fidelity microstructural FE models (Section 6.5.5). In addition, an assessment of the calibration costs for each CPFEM model can be found in Appendix C.7.

### 6.5.1. Performance of trained surrogate models

Deep neural network (DNN) surrogate models were adaptively trained to replicate the predictions of the low-fidelity CPFEM models, reproducing both the macroscopic stress–strain response (Figure 6.2) and the mesoscale reorientation trajectories of eight grains ( $g_{1..8}$ ; Figure 6.4). The surrogate models were trained using an initial dataset of 8 simulations for the VH and LH2 formulations, and 16 simulations for the LH6 formulation to accommodate its larger number of material parameters. The surrogate model was iteratively refined using additional low-fidelity CPFEM simulations evaluated at the MOGA-optimised parameter values, until the surrogate model satisfied the accuracy thresholds,  $E_\sigma < 1\%$  and  $E_\phi < 0.1^\circ$ . This adaptive training strategy allowed the surrogate model to become progressively more accurate in regions of the parameter space that are most relevant to the calibration, where the CPFEM responses aligned closest with the experimental observations. However, this strategy limits the generalisability of the surrogate models beyond the explored regions of the parameter space, preventing its direct application to other experimental datasets without further training.

A new surrogate model was developed from scratch for each independent calibration run to avoid bias from any particular initial dataset or DNN realisation. Figure 6.7 presents the evolution of the surrogate model accuracy as more CPFEM simulations are progressively added into the DNN training set across five independent calibration runs of the VH formulation. The surrogate model accuracy is measured using the objective functions,  $E_\sigma$  and  $E_\phi$  (Eqs. (41) and (51)), which in this case quantify the deviation (error) between the surrogate model predictions and the CPFEM predictions across the full range of strain values used in the calibration process. As shown in Figure 6.7, the VH formulation achieved the accuracy thresholds after an average of 13 re-training cycles which corresponds to 21 CPFEM evaluations in the training set. The LH2 formulation required an average of 16 cycles (24 evaluations) to reach the same accuracy, while the more complex LH6 formulation required an average of 22 cycles (38 evaluations), reflecting the higher dimensionality of its parameter space. The variability in the number of re-training cycles required to converge reflects the stochastic nature of the employed LHS scheme and the MOGA optimisation process.

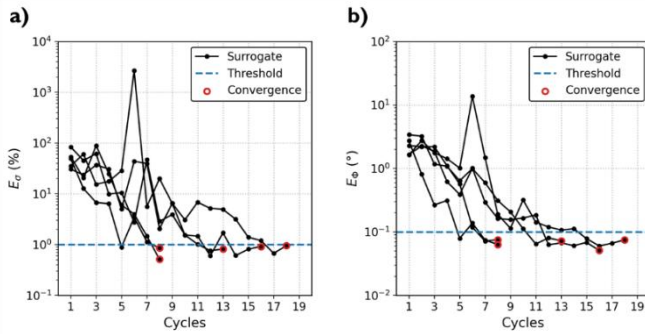


Figure 6.7. Discrepancies between the surrogate model approximations and the low-fidelity VH simulations across five calibration runs using an initial dataset size of 8. Plot a) shows the discrepancies in the stress–strain response (%) while plot b) shows the discrepancies in the reorientation trajectories (°). Each plot shows the discrepancies (black line), accuracy threshold (blue dashed line), and the termination cycle (red circle) for each calibration run.

Once the DNN surrogate models achieved the predefined accuracy thresholds ( $E_\sigma < 1\%$  and  $E_\phi < 0.1^\circ$ ), they consistently reproduce the CPFEM predictions, regardless of how many CPFEM evaluations were used during their training process. A representative example of the surrogate model’s accuracy is presented in Figure 6.8, showing its predictions (black) with the corresponding low-fidelity CPFEM model’s predictions (red), and the experimental data (grey). The close agreement between both models for the stress–strain responses (Figure 6.8a) and grain  $g_{1..8}$  reorientation trajectories (Figure 6.8b) confirms that the adaptively trained DNN surrogate model can provide an accurate representation of the CPFEM model. Reaching this level of surrogate accuracy is a critical prerequisite for the proposed workflow, enabling the MOGA-based CPFEM model calibration to be achieved at a fraction of the computation cost without compromising accuracy.

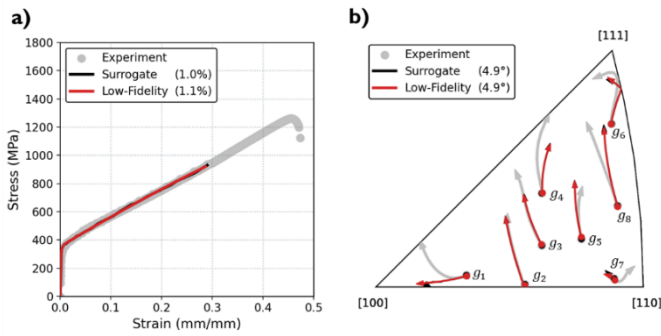


Figure 6.8. Comparison of the surrogate model approximations and the low-fidelity VH simulations, with the experimental data in grey, the approximations in black, and the VH responses in red. These plots compare the a) stress–strain responses and b) reorientation trajectories of  $g_{1..8}$ , including the corresponding objective values ( $E_\sigma$  and  $E_\phi$  from Eqs. (41) and (51)).

### 6.5.2. Performance of calibrated models

The trained surrogate DNN models described in Section 6.5.1 were next deployed within the MOGA-based calibration workflow (Figure 6.6) to replace the computationally expensive CPFEM evaluations. To evaluate the robustness and repeatability of the complete workflow — encompassing both adaptive surrogate model development and MOGA-based optimisation — each of the three CP formulations (VH, LH2, and LH6) was integrated with the low-fidelity FE model and calibrated five times. As outlined above, the multi-objective calibration simultaneously targeted the experimental stress–strain response and the reorientation trajectories of eight selected grains ( $g_{1..8}$ ), while validation was performed against the trajectories of eight additional grains ( $g_{9..16}$ ) and the overall texture evolution. The calibration and validation results for the VH, LH2, and LH6 models are presented in Figure 6.9, Figure 6.10, and Figure 6.11, respectively, comparing the simulated stress–strain responses, reorientation trajectories, and texture evolution with the experimental measurements. In these figures, the best calibration run is identified based on the minimal squared sum of the normalised objective values (Appendix C.5) and is shown in red, while the other runs are shown in green. The overall texture is characterised using contoured  $\{111\}$  pole figures at  $\varepsilon = 0.0\%$ ,  $10.6\%$ , and  $29.0\%$ , complemented by texture indexes calculated over the same strain range. Note that the influence of the selected calibration grain reorientation trajectories is examined in Appendix C.8, where the calibration and validation grains are swapped to demonstrate that the workflow is largely insensitive to the choice of calibration grains.

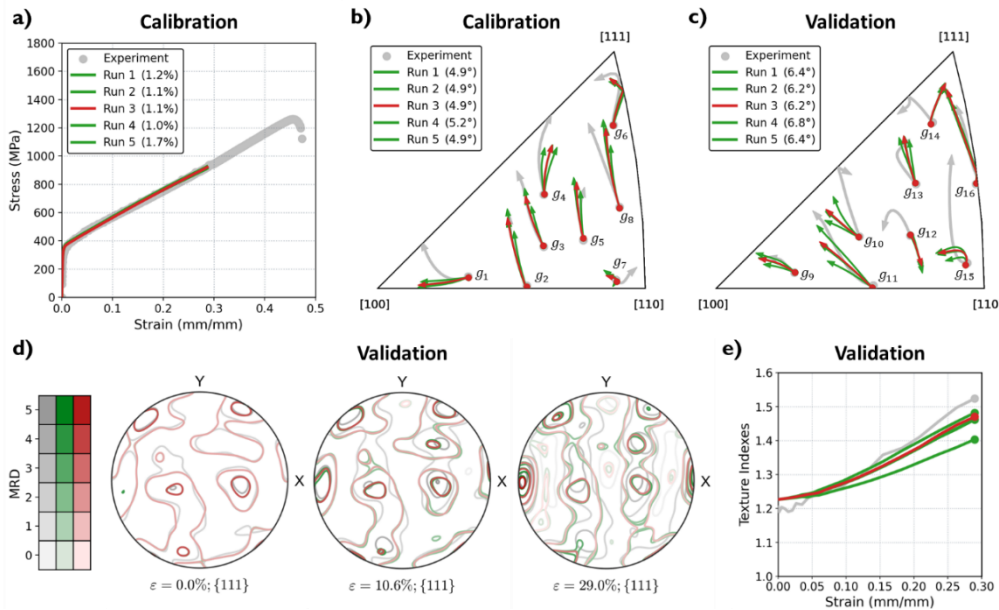


Figure 6.9. Calibration and validation results for the VH formulation after five runs, comparing the experimental data in grey with the simulated responses in green (all runs) and red (best run). The plots in the top row compare the a) stress–strain responses (calibration), b) reorientation trajectories of  $g_{1..8}$  (calibration), and c) reorientation trajectories of  $g_{9..16}$  (validation), including the corresponding objective values ( $E_\sigma$  and  $E_\phi$  from Eqs. (41) and (51)). The plots in the bottom row compare the overall texture evolution (validation) using d) contoured  $\{111\}$  pole figures at  $\varepsilon = 0.0\%$ ,  $10.6\%$ , and  $29.0\%$ , and e) texture indexes over  $0.0\%$  to  $29.0\%$ .

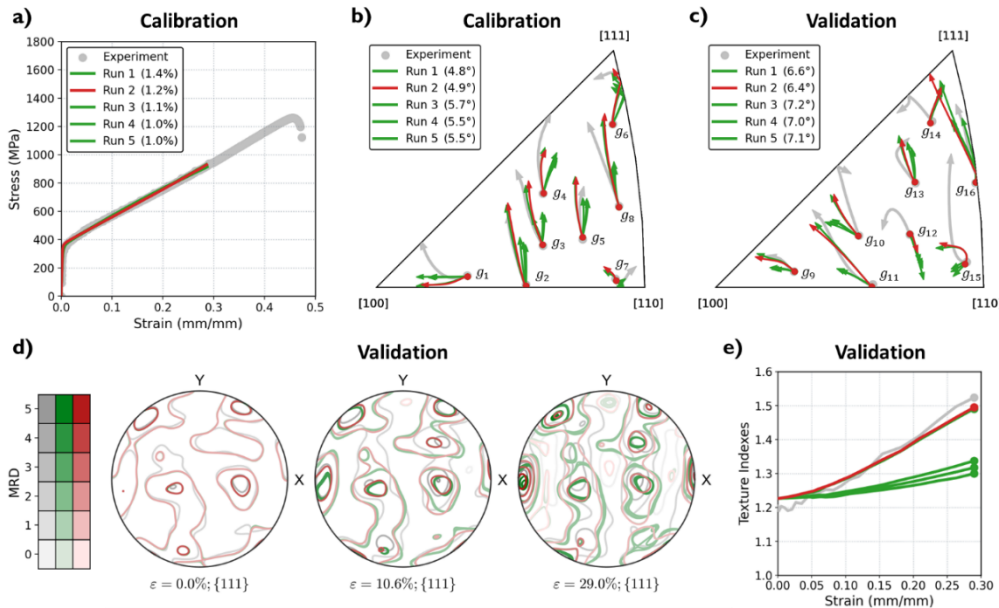


Figure 6.10. Calibration and validation results for the LH2 formulation after five runs, comparing the experimental data in grey with the simulated responses in green (all runs) and red (best run). The plots in the top row compare the a) stress–strain responses (calibration), b) reorientation trajectories of  $g_{1..8}$  (calibration), and c) reorientation trajectories of  $g_{9..16}$  (validation), including the corresponding objective values ( $E_\sigma$  and  $E_\phi$  from Eqs. (41) and (51)). The plots in the bottom row compare the overall texture evolution (validation) using d) contoured  $\{111\}$  pole figures at  $\varepsilon = 0.0\%$ ,  $10.6\%$ , and  $29.0\%$ , and e) texture indexes over  $0.0\%$  to  $29.0\%$ .

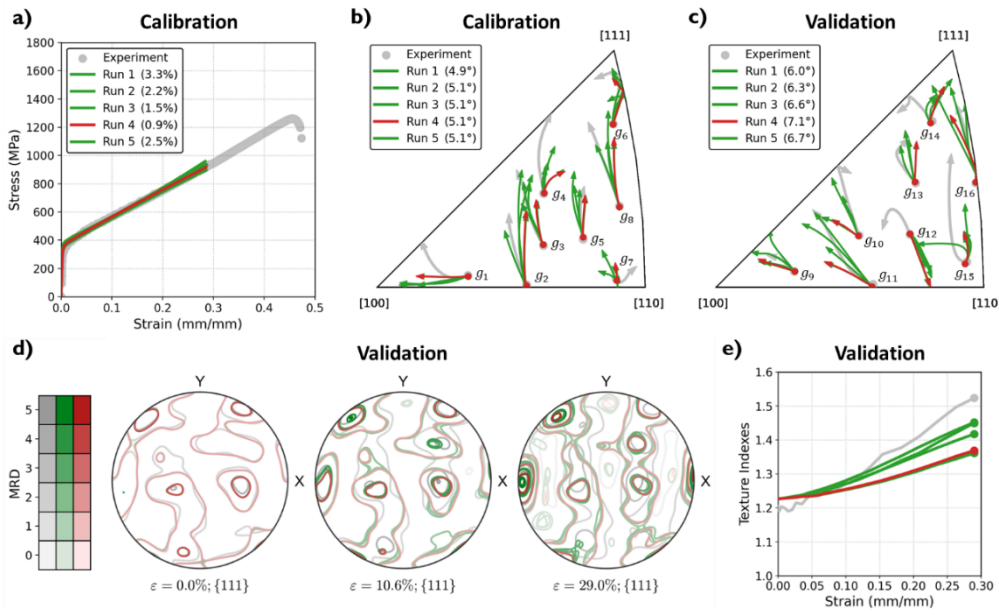


Figure 6.11. Calibration and validation results for the LH6 formulation after five runs, comparing the experimental data in grey with the simulated responses in green (all runs) and red (best run). The plots in the top row compare the a) stress–strain responses (calibration), b) reorientation trajectories of  $g_{1..8}$  (calibration), and c) reorientation trajectories of  $g_{9..16}$  (validation), including the corresponding objective values ( $E_\sigma$  and  $E_\phi$  from Eqs. (41) and (51)). The plots in the bottom row compare the overall texture evolution (validation) using d) contoured  $\{111\}$  pole figures at  $\varepsilon = 0.0\%$ , 10.6%, and 29.0%, and e) texture indexes over 0.0% to 29.0%.

Across all three formulations, the simulated stress–strain responses (Figure 6.9a, Figure 6.10a, and Figure 6.11) showed excellent agreement with the experimental data. The VH and LH2 formulations exhibited minimal variability across the five calibration runs, with a mean standard deviation (SD) of 3.76MPa and 5.05MPa across the strain range, respectively. This consistency highlights the robustness of the calibration workflow and demonstrates that even the simplest VH formulation can reliably reproduce the macroscopic mechanical response of Alloy 617 under uniaxial loading. In contrast, the LH6 formulation exhibited noticeably greater run-to-run variability with a SD of 10.6MPa, suggesting less stable convergence of the optimisation process due to the formulation’s larger parameter space.

The reorientation trajectories of the eight calibration grains ( $g_{1..8}$ ; Figure 6.9b, Figure 6.10b, and Figure 6.11b) were reproduced with reasonable accuracy for all three CPFEM models. Grains exhibiting complex, non-monotonic rotation paths in orientation space showed poorer agreement than those following simpler, monotonic trajectories. This behaviour reflects the local nature of grain interactions as well as the limitations associated with constructing a 3D volumetric mesh from a single 2D EBSD orientation map. In this 2.5D representation (Section 6.2.4), the through-thickness microstructural variations — such as grain morphology, local neighbourhood topology, or orientation gradients — are not captured, which can influence the predicted slip activity and rotation behaviour of individual grains. These simplifications likely contributed to the discrepancies observed for certain grain trajectories. Introducing stochastic orientation perturbations or randomised microstructural layers along the specimen thickness could, in future, help quantify the sensitivity of the calibration to such assumptions and provide a measure of robustness. Notably, the run-to-run variability in

the simulated  $g_{1..8}$  trajectories was most pronounced for the LH2 and LH6 formulations, with standard deviations of  $0.908^\circ$  and  $0.859^\circ$ , respectively, compared with  $0.256^\circ$  for the VH formulation.

The reorientation trajectories of the eight validation grains ( $g_{9..16}$ ; Figure 6.9c, Figure 6.10c, and Figure 6.11) exhibited greater run-to-run variability to the calibration grains, with SDs of  $0.53^\circ$ ,  $1.68^\circ$ , and  $1.15^\circ$  for the VH, LH2, and LH6 formulations, respectively. The simulated trajectories also showed a clear decline in accuracy, as indicated by their higher  $E_\phi$  values. The reduced consistency and predictive accuracy of the  $g_{9..16}$  trajectories is expected due to their exclusion from the calibration dataset, further exacerbated by complex rotation paths that the FE model was unable to reliably reproduce. In many cases, these grains (i.e.,  $g_{11}$ ,  $g_{12}$ ,  $g_{14}$ ,  $g_{15}$ , and  $g_{16}$ ) were located near mesh boundaries or affected by segmentation artefacts — such as merging or splitting during grain tracking — which likely degraded their correspondence between the experimental microstructure and the low-fidelity model (see Appendix C.2 for details of the grain-tracking algorithm applied to the in-situ EBSD maps). While the LH2 and LH6 formulations offered greater flexibility in simulating non-monotonic reorientation behaviour, they also showed higher sensitivity to noise in the calibration data. In contrast, the VH formulation delivered more consistent predictions across runs, suggesting a more favourable balance between model complexity and the level of experimental constraint provided under uniaxial loading.

Despite the variability in the mesoscale reorientation trajectory predictions, all three CPFEM models showed good performance in predicting the overall texture evolution (Figure 6.9d-e, Figure 6.10d-e, and Figure 6.11d-e). The simulated  $\{111\}$  pole figures and texture indexes were generally in good agreement with the experimental data, particularly at lower and intermediate strain levels. At higher strains, the VH and LH2 formulations continued to capture the dominant texture components well, while the LH6 formulation displayed some misalignment in both intensity and orientation. Notably, for the LH6 formulation, some runs produced texture indexes well below the experimental value despite similar accuracy in the calibration grain trajectories. These results highlight a limitation of relying on a restricted set of grain reorientation trajectories in the calibration process. In other words, accurately reproducing the mesoscale grain trajectories may not necessarily guarantee accurate texture predictions.

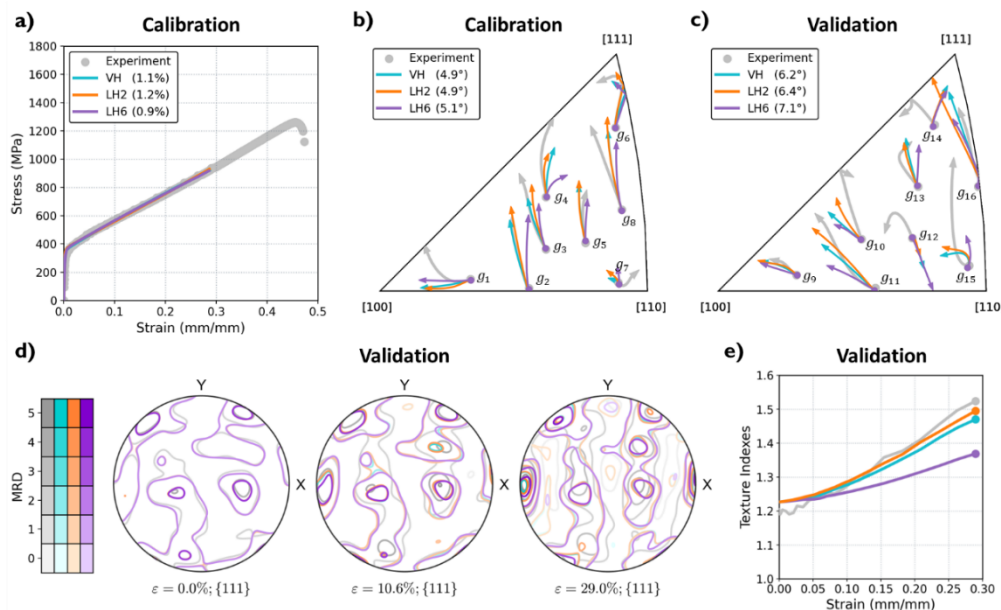


Figure 6.12. Comparison of the low-fidelity responses of the three CPFEM models, with the experimental data in grey, the VH responses in cyan, the LH2 responses in orange, and the LH6 responses in purple. The plots in the top row compare the a) stress-strain responses (calibration), b) reorientation trajectories of  $g_{1..8}$  (calibration), and c) reorientation trajectories of  $g_{9..16}$  (validation), including the corresponding objective values ( $E_\sigma$  and  $E_\phi$  from Eqs. (41) and (51)). The plots in the bottom row compare the overall texture evolution (validation) using d) contoured {111} pole figures at  $\varepsilon = 0.0\%$ , 10.6%, and 29.0%, and e) texture indexes over 0.0% to 29.0%.

The simulated results from the best calibration run of each CPFEM formulation are presented in Figure 6.12, comparing the VH (cyan), LH2 (orange), and LH6 (purple) responses — these are the best of five calibration runs discussed above and presented in Figure 6.9, Figure 6.10, and Figure 6.11. It becomes clear from Figure 6.12 that all three models reproduced the stress-strain response with excellent accuracy (Figure 6.12a), confirming that the calibration workflow can reliably capture the macroscopic mechanical behaviour of Alloy 617 under uniaxial loading. The grain reorientation trajectories of  $g_{1..16}$  (Figure 6.12b-c) were also predicted with broadly similar accuracy, although the LH6 responses consistently exhibited larger deviations and greater run-to-run scatter than the VH and LH2 responses, despite its greater flexibility and larger parameter space. A comparable trend is observed for the overall texture evolution (Figure 6.12d-e), where the VH and LH2 formulations more accurately tracked the intensity and orientation of the dominant texture components, while the LH6 formulation displayed larger deviations in the pole figure contours and final texture index, along with greater run-to-run variability.

Overall, the present results demonstrate that all three tested CP formulations can capture the key aspects of Alloy 617's deformation behaviour under uniaxial tensile loading, including the macroscopic stress-strain response, individual grain rotation behaviour, and texture evolution as a function of imparted plastic strain. Of the three, the VH formulation delivered the most consistent and robust performance, providing the best balance between accuracy and reliability. The LH2 formulation achieved comparable accuracy in many cases and offered greater flexibility for modelling complex grain rotations, but at the cost of increased sensitivity to noise and reduced parameter identifiability. In contrast, the LH6 formulation — despite its broader representational capacity — did not outperform the simpler CP formulations and showed substantially greater variability between calibration runs in all evaluated metrics. Additionally, the VH formulation was substantially cheaper to calibrate, requiring an average of 4.83 CPU-hours on 192 cores (dual AMD EPYC 96-core processors), compared with 35.04 hours for LH2 and 55.48 hours for LH6 (see Appendix C.7). These findings show that VH is the most practical formulation for this application, underscoring the need to match model complexity to the available experimental data.

### 6.5.3. Robustness of calibration workflow

As discussed in Sections 6.5.1 and 6.5.2, the developed calibration workflow — combining adaptively trained DNN surrogate models with a MOGA — enables efficient calibration of computationally expensive CPFEM models. To assess its robustness, five independent calibration runs were performed for each CP formulation. These runs revealed some variability in the simulated responses, particularly in the mesoscale reorientation trajectories of individual grains. Such variability reflects the inherent sensitivity of CPFEM simulations to the chosen material parameters and raises the question of how consistently these parameters can be identified. To explore this, Figure 6.13 presents the distributions of the optimised material parameters for the VH, LH2, and

LH6 formulations across their five calibration runs. These distributions include  $\{\tau_0, n, b, \tau_s\}$  for the VH formulation,  $\{\tau_0, n, h_{\alpha\alpha}, h_{\alpha\beta}\}$  for the LH2 formulation, and  $\{\tau_0, n, h_{\alpha\alpha}, h_1, h_2, h_3, h_4, h_5\}$  for the LH6 formulation.

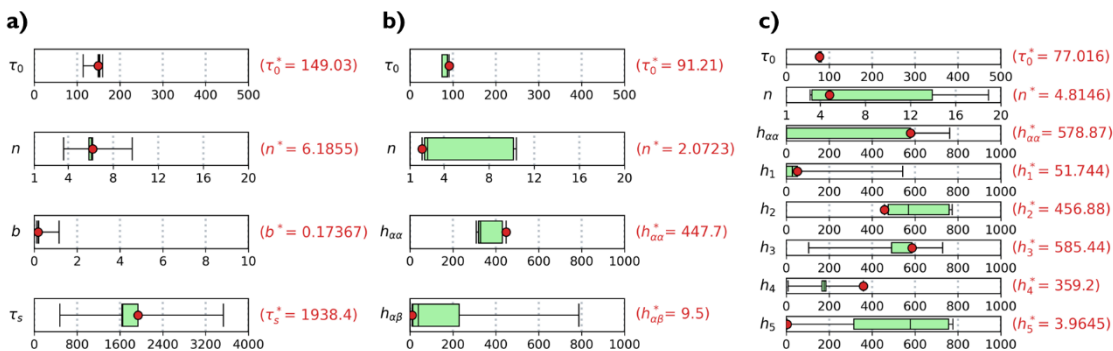


Figure 6.13. Boxplots of the optimised parameters for the a) VH formulation, b) LH2 formulation, and c) LH6 formulation across five calibration runs, showing the mean (black horizontal line), standard deviation (box), range (whiskers), and bounds (limits). The knee-point values are overlaid as red circles, with their exact values annotated on the right.

It is clear from Figure 6.13 that the variability of the identified material parameters differs substantially between CPFEM models, suggesting that the robustness of the calibration workflow varies with the employed CP formulation. For the VH formulation (Figure 6.13a),  $\tau_0$  (initial slip system strength) and  $b$  (hardening rate) exhibit narrow distributions across calibration runs, indicating that these parameters are well constrained by the available experimental datasets. In contrast,  $n$  (strain-rate sensitivity) and  $\tau_s$  (saturation strength) display broader spreads, reflecting the absence of calibration data at multiple strain rates and into the late-stage saturation regime (Stage III), limiting the constraint of these two material parameters. The inclusion of grain reorientation trajectories in the objective function appears to reinforce the stability of the VH formulation, as  $\tau_0$  and  $b$  strongly influence the primary slip system activation and are already tightly constrained by the stress-strain curve. The LH2 formulation (Figure 6.13b) retains relatively low variability in  $\tau_0$ , but shows significantly wider spreads for  $n$ ,  $h_{\alpha\alpha}$  (self-hardening strength), and  $h_{\alpha\beta}$  (latent hardening strength). Under a single monotonic tensile path, the additional reorientation data only moderately reduces the parameter non-uniqueness, as many slip system interactions remain weakly activated and therefore do not leave a distinct signature in the orientation trajectories. The LH6 formulation (Figure 6.13c) shows a similar pattern for  $\tau_0$ , which remains relatively consistent between runs, but displays pronounced variability in  $n$ ,  $h_{\alpha\alpha}$  (self-hardening strength), and  $h_{1..5}$  (latent hardening strengths). The variability of these parameters reflects their poor constraint due to the limited activation of secondary slip systems under uniaxial tensile loading [75]. Without more diverse deformation paths — such as multiaxial or non-monotonic loading — to stimulate these interactions, the optimiser struggles to distinguish among multiple mathematically viable but physically inconsistent solutions [75]. This further highlights a need to match the model complexity to the type of available experimental datasets.

The optimised parameter values from the best calibration runs (Appendix C.5) of all three formulations are presented in Figure 6.13 as red symbols. It should be noted upfront that the strain-rate sensitivity parameter,  $n$ , should be interpreted with caution across all formulations. Its variation between the VH, LH2, and LH6

formulations primarily reflects the lack of experimental data at multiple strain rates to constrain it — if such data were available,  $n$ , would be expected to converge to a consistent value independent of the chosen CP formulation. With this limitation in mind, the remaining parameters reveal distinct trends across the three models. The optimised material parameters for the VH formulation ( $\tau_0^* = 149.03\text{MPa}$ ,  $n^* = 6.1855$ ,  $b^* = 0.1737$ , and  $\tau_s^* = 1938.4\text{MPa}$ ) indicate a high initial slip system strength and moderate hardening rate. In the LH2 formulation, the optimised parameters ( $\tau_0^* = 91.21\text{MPa}$ ,  $n^* = 2.0723$ ,  $h_{\alpha\alpha}^* = 447.7\text{MPa}$ , and  $h_{\alpha\beta}^* = 9.5\text{MPa}$ ) indicate a decrease in initial strength and suggest that most of the additional hardening is concentrated in self-hardening rather than latent interactions. Finally, the LH6 formulation exhibits an even lower initial strength ( $\tau_0^* = 77.016\text{MPa}$ ,  $n^* = 4.8146$ ,  $h_{\alpha\alpha}^* = 578.87\text{MPa}$ ) and highly scattered latent hardening values ( $h_1^* = 51.744\text{MPa}$ ,  $h_2^* = 456.88\text{MPa}$ ,  $h_3^* = 585.44\text{MPa}$ ,  $h_4^* = 359.2\text{MPa}$ , and  $h_5^* = 3.9645\text{MPa}$ ), underscoring the poor constraint of these parameters under the present uniaxial loading condition.

The contrast between the VH and LH2 formulations further highlights how parameter identifiability depends on model structure. Although both formulations involve fitting only four material parameters, the inclusion of latent hardening terms in the LH2 formulation changes the allocation of hardening between  $\tau_0$  and the interaction coefficients. This reallocation is a mathematical consequence of parameter coupling, in which the absence of data that explicitly constrains latent hardening allows the optimiser to reduce  $\tau_0$  and adjust  $h_{\alpha\alpha}$  and  $h_{\alpha\beta}$  to reproduce the same macroscopic stress–strain curve. As a result,  $\tau_0$  becomes model-dependent rather than a unique estimate of the critical resolved shear stress (CRSS) for the active slip system. Determining the true value of  $\tau_0$  would thus require independent experimental constraints, such as multiple strain-rate curves to decouple  $\tau_0$  from  $n$ , or non-proportional and multiaxial loading to activate and constrain latent hardening. This issue becomes even more pronounced in the LH6 formulation, where the expanded parameter space further amplifies coupling effects. Without sufficiently diverse experimental loading conditions to activate secondary slip systems, the optimiser distributes hardening across many poorly constrained interaction terms, yielding parameter sets that lack physical uniqueness.

This non-uniqueness is a well-recognised characteristic of inverse CPFEM calibration problems, where several parameter sets can yield comparable macroscopic and mesoscale responses. In the present study, the inclusion of grain reorientation trajectories helps to filter out non-physical solutions but cannot fully remove this degeneracy because the available experimental data provide only limited independent constraints. The issue is analogous to other under-constrained inverse problems, such as nano-indentation, where distinct constitutive parameter combinations can reproduce similar load–displacement curves. As demonstrated in indentation studies, introducing additional physically measurable quantities — such as the plastic-zone radius [277] — can improve parameter identifiability. By analogy, CPFEM calibrations could incorporate physics-informed observations (e.g., local lattice strains, slip activity maps, or orientation-gradient fields) to further constrain the feasible parameter space and enhance uniqueness [247, 278].

Taken together, these results show that, given the single monotonic tensile curve at one strain rate available for calibration, the VH formulation provides the most reliable and interpretable parameter set. The parameters governing the initial slip system strength and hardening rate are well constrained, whereas the strain-rate sensitivity parameter remains weakly constrained across all formulations. This limitation reflects the lack of experimental data at multiple strain rates rather than any deficiency of the CP formulations themselves. The

LH2 formulation can reproduce the same stress–strain response, but the additional latent hardening terms are only loosely identifiable under simple uniaxial loading. The LH6 formulation is clearly over-parameterised for the available dataset and produces parameter sets that lack physical uniqueness, consistent with the large spreads and run-to-run variability observed in stress–strain, grain reorientation, and texture predictions (Section 6.5.2). Based on this variability analysis alone, the inclusion of grain reorientation trajectories provides only a moderate reduction in parameter non-uniqueness. Overall, the VH formulation yields the most robust and interpretable parameters, the LH2 formulation introduces moderate ambiguity, and the LH6 formulation is over-parameterised under the present calibration conditions.

#### 6.5.4. Impact of mesoscale constraints on model calibration

As shown in Section 6.5.3, the inclusion of mesoscale grain reorientation trajectories in the multi-objective calibration framework has only a limited effect on reducing the statistical variability of material parameters under the present loading conditions. However, it plays an important role in filtering out physically unrealistic solutions that would otherwise pass undetected in a single-objective framework. To clarify this distinction, the VH formulation was calibrated without mesoscale constraints, using only the macroscopic stress–strain curve while excluding the reorientation trajectories from the calibration process. This single-objective approach mirrors the most common practice in CPFEM parameter identification, where model fitting is performed exclusively against the stress–strain response without incorporating additional experimental datasets capable of constraining the parameter space. The predictions obtained from the VH formulation calibrated using single-objective approach are presented in Figure 6.14, while the corresponding distributions of the optimised parameters are presented in Figure 6.15.

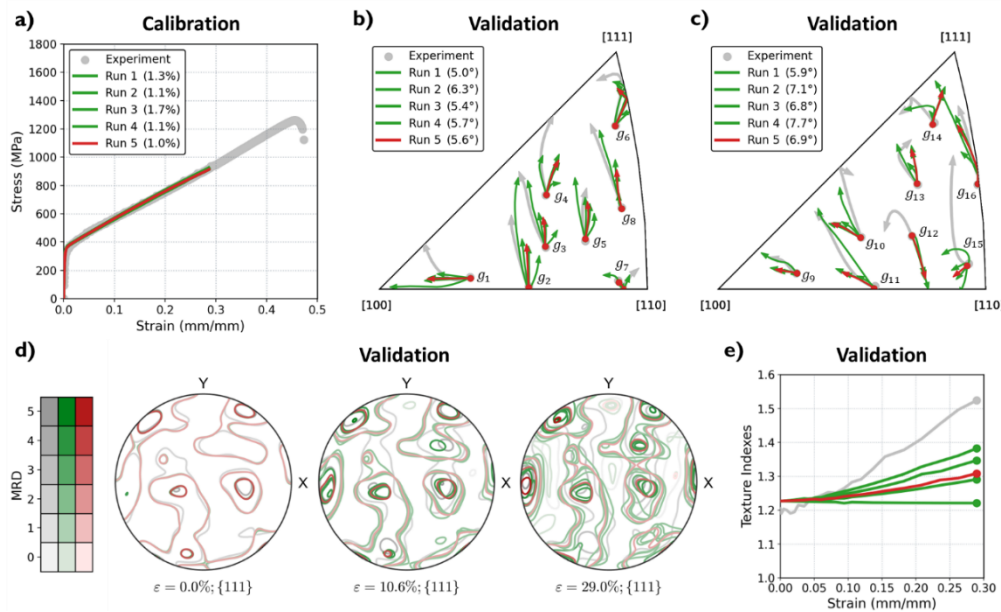


Figure 6.14. Supplementary calibration and validation results for the VH formulation after five single-objective runs, comparing the experimental data in grey with the simulated responses in green (all runs) and red (best run). The plots in the top row compare the a) stress–strain responses (calibration), b) reorientation trajectories of  $g_{1..8}$  (validation), and c) reorientation trajectories of  $g_{9..16}$  (validation), including the corresponding objective values ( $E_\sigma$  and  $E_\phi$  from Eqs. (41)

and (51)). The plots in the bottom row compare the overall texture evolution (validation) using d) contoured {111} pole figures at  $\varepsilon = 0.0\%$ , 10.6%, and 29.0%, and e) texture indexes over 0.0% to 29.0%.

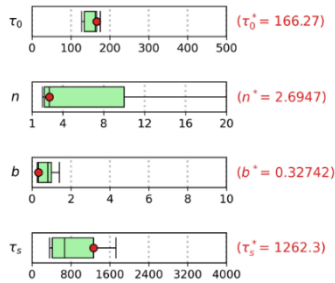


Figure 6.15. Supplementary boxplots of the optimised parameters for the VH formulation across five single-objective calibration runs, showing the mean (black horizontal line), standard deviation (box), range (whiskers), and bounds (limits). The knee-point values are overlaid as red circles, with their exact values annotated on the right.

The results in Figure 6.14 can be directly compared with those in Figure 6.9, which shows the VH responses from the developed multi-objective calibration workflow that also incorporated the grain reorientation trajectories in its objective function. Several observations emerge from this comparison. Firstly, the stress–strain response is predicted with excellent accuracy in both single- (Figure 6.14a) and multi-objective approaches (Figure 6.9a). This demonstrates the strong capacity of the VH formulation in matching the global mechanical response even when unconstrained by mesoscale reorientation behaviour. Secondly, the predictions for the  $g_{1..16}$  trajectories remain reasonably accurate despite their exclusion from the calibration, with the average geodesic distance error ( $E_\phi$ ) increasing only slightly from  $5.68^\circ$  (Figure 6.9b-c) to  $6.24^\circ$  (Figure 6.14b-c). Thirdly, and most critically, the predictions for texture evolution show greater discrepancies in the single-objective approach. This can be seen in the best single-objective calibration run, which yields a final texture index of approximately 1.30 (Figure 6.14). In contrast, the best multi-objective run yields a final index of 1.47 (Figure 6.9e), which is much closer to the experimental value of 1.52.

At first glance, these findings may appear to contradict the results of Section 6.5.3, which indicates that the inclusion of the grain reorientation trajectories in the calibration process has only a moderate effect on constraining the statistical spread of parameters. In reality, the two sets of results are consistent once the distinction between parameter identifiability and physical plausibility is recognised. Under the present loading conditions — single-path monotonic tension at a single strain rate — grain reorientation trajectories and the stress–strain curve are not strongly independent constraints for material parameters. Consequently, their inclusion as an objective function does not sharply reduce the run-to-run variability of these parameters, as illustrated by the box plots in Figure 6.13 and Figure 6.15. Instead, these mesoscale constraints act as a decisive physical filter. Many parameter combinations can match the macroscopic stress–strain response, but only a subset produce microstructural evolution consistent with the measured reorientation behaviour and the resulting texture. Without these mesoscale constraints, the optimisation can converge to mathematically valid yet physically inconsistent material parameter sets, leading to degraded predictions of texture evolution despite an equally accurate macroscopic fit.

Thus, in the present study, the value of including grain trajectories lies less in tightening the statistical identifiability of weakly constrained parameters and more in ensuring that the selected material parameter set is physically consistent across scales. This conclusion is particularly relevant because single-objective, stress-strain-only calibration remains the dominant approach in CPFEM modelling. The present results therefore provide strong evidence that developed MOGA-based model calibration incorporating mesoscale constraints should be adopted more widely to obtain parameter sets that are both mathematically optimal and physically meaningful.

### 6.5.5. Transferability across microstructural fidelities

All calibration runs in previous sections were performed using a 2.5D low-fidelity FE microstructural representation of the Alloy 617 specimen gauge, comprising 132 grains (from the experimentally identified 571 grains) and 17,109 hexahedral elements. While this model is referred to as ‘low fidelity’, it still captures nearly one quarter of the measured grains, preserving a representative subset of the microstructure. To assess the transferability of the found material parameters to a more realistic microstructural representation, the knee-point parameters from the best calibration run of each CP formulation (VH, LH2, and LH6; Figure 6.9, Figure 6.10, and Figure 6.11) were applied without modification to a 2.5D high-fidelity FE model of the same specimen, comprising 481 grains and 574,560 hexahedral elements. This high-fidelity FE model of the microstructure preserves a much larger fraction of the experimentally measured grain structure and neighbourhood topology, thereby modifying the local interaction fields experienced by individual grains. The plots in Figure 6.16, Figure 6.17, and Figure 6.18 compare the low- and high-fidelity predictions for the VH, LH2, and LH6 formulations, respectively, showing the stress–strain curves, reorientation trajectories of  $g_{1..16}$ , and overall texture evolution.

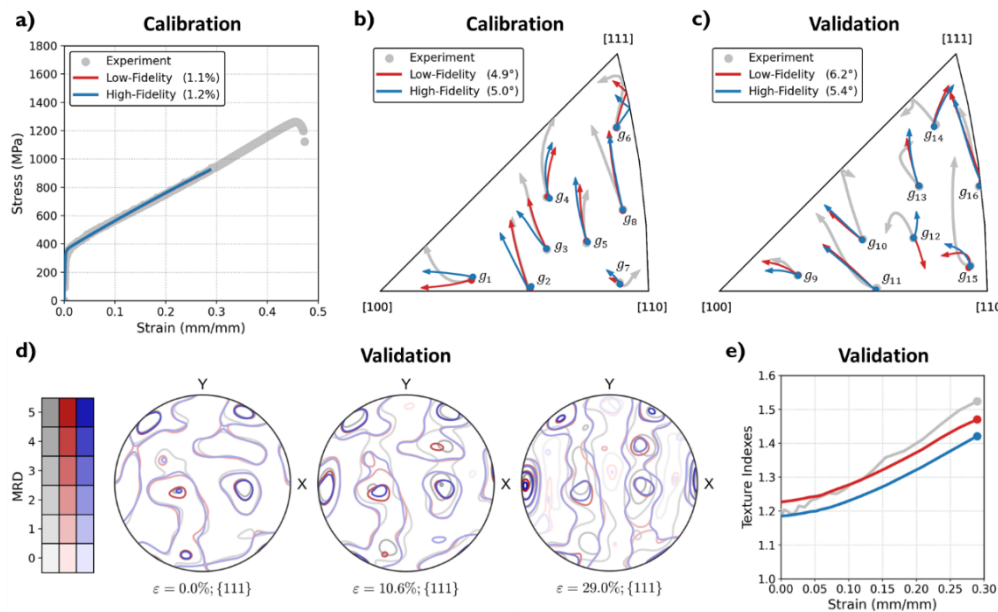


Figure 6.16. Comparison of the low- and high-fidelity responses from the VH formulation, with the experimental data in grey, the low-fidelity responses in red, and the high-fidelity responses in blue. The plots in the top row compare the a) stress–strain responses (calibration), b) reorientation trajectories of  $g_{1..8}$  (calibration), and c) reorientation trajectories of  $g_{9..16}$  (validation), including the corresponding objective values ( $E_\sigma$  and  $E_\phi$  from Eqs. (41) and (51)). The plots in the

bottom row compare the overall texture evolution (validation) using d) contoured {111} pole figures at  $\varepsilon = 0.0\%$ , 10.6%, and 29.0%, and e) texture indexes over 0.0% to 29.0%.

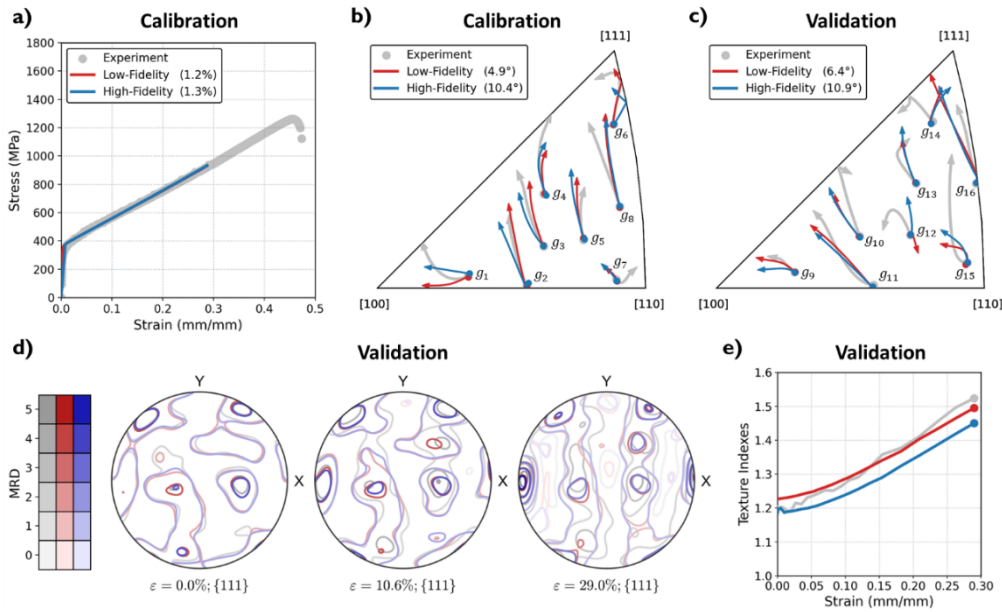


Figure 6.17. Comparison of the low- and high-fidelity responses from the LH2 formulation, with the experimental data in grey, the low-fidelity responses in red, and the high-fidelity responses in blue. The plots in the top row compare the a) stress–strain responses (calibration), b) reorientation trajectories of  $g_{1..8}$  (calibration), and c) reorientation trajectories of  $g_{9..16}$  (validation), including the corresponding objective values ( $E_\sigma$  and  $E_\phi$  from Eqs. (41) and (51)). The plots in the bottom row compare the overall texture evolution (validation) using d) contoured {111} pole figures at  $\varepsilon = 0.0\%$ , 10.6%, and 29.0%, and e) texture indexes over 0.0% to 29.0%.

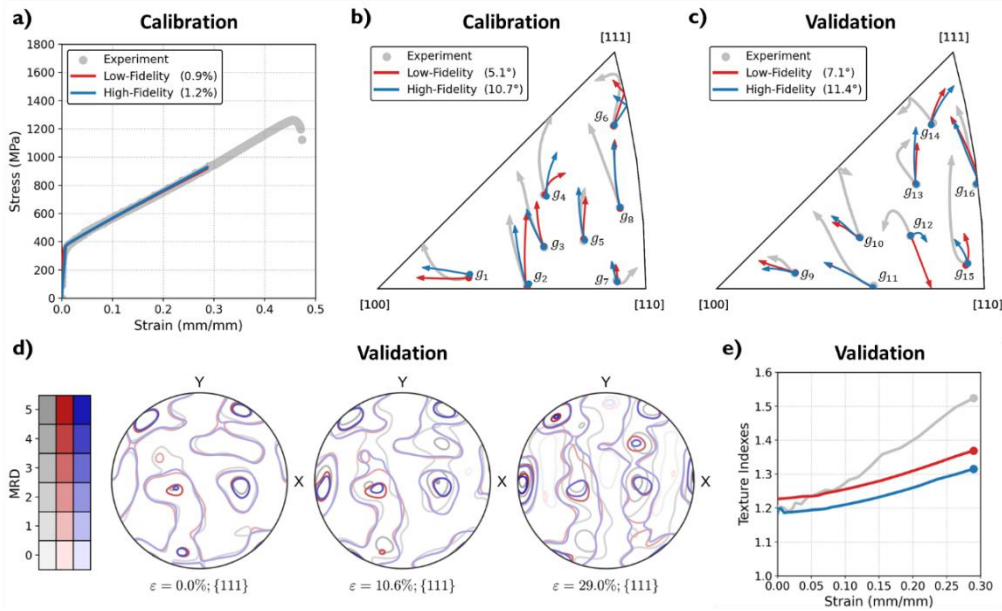


Figure 6.18. Comparison of the low- and high-fidelity responses from the LH6 formulation, with the experimental data in grey, the low-fidelity responses in red, and the high-fidelity responses in blue. The plots in the top row compare the a) stress–strain responses (calibration), b) reorientation trajectories of  $g_{1..8}$  (calibration), and c) reorientation trajectories of  $g_{9..16}$  (validation), including the corresponding objective values ( $E_\sigma$  and  $E_\phi$  from Eqs. (41) and (51)). The

plots in the bottom row compare the overall texture evolution (validation) using d) contoured  $\{111\}$  pole figures at  $\varepsilon = 0.0\%$ ,  $10.6\%$ , and  $29.0\%$ , and e) texture indexes over  $0.0\%$  to  $29.0\%$ .

Across all three formulations, the stress–strain curves (Figure 6.16a, Figure 6.17a, and Figure 6.18a) remain in excellent agreement with the experimental data and are virtually indistinguishable between low- and high-fidelity CPFEM models. This demonstrates that the macroscopic mechanical response is largely insensitive to microstructural resolution, at least within the range examined here, and that the calibrated parameters capture the bulk deformation behaviour in a transferable manner. From an engineering perspective, this suggests that moderate-fidelity microstructures, such as the 132-grain model used for calibration, are sufficient for identifying parameters that govern global stress–strain behaviour, offering substantial computational savings without compromising accuracy.

For the VH formulation (Figure 6.16b-c), the average geodesic distance error for  $g_{1..16}$  remains essentially unchanged when moving from the low- to high-fidelity model, with certain grains (e.g.,  $g_{12}$ ) even exhibiting improvements in accuracy. In contrast, the LH2 and LH6 formulations show reduced accuracy in the reorientation trajectory predictions, with average geodesic distance errors ( $E_\phi$ ) increasing from  $\sim 6^\circ$  in the low-fidelity calibration to  $\sim 11^\circ$  in the high-fidelity predictions (Figure 6.17b-c and Figure 6.18b-c). This reduction in accuracy reflects the greater sensitivity of the latent-hardening-based formulations to local neighbourhood changes, which are significantly altered by the more complete grain topology in the high-fidelity representation. These results build on the findings of Section 6.5.2, confirming that the VH formulation delivers the most stable and repeatable (robust) predictions when it comes to grain reorientation trajectories, both within the low-fidelity calibration model and when transferred to a higher-fidelity representation.

For the overall texture evolution, both low- and high-fidelity models reproduce the main features of the measured  $\{111\}$  pole figures (Figure 6.16d-e, Figure 6.17d-e, and Figure 6.18d-e). Consistent with the mesoscale predictions of grain reorientation trajectories discussed above, the VH formulation provides the most stable predictions, whereas the LH2 and LH6 formulations show greater sensitivity to the higher-resolution microstructural topology. Across all three formulations, however, the high-fidelity models yield texture indices that are about 0.45 units lower than their low-fidelity counterparts, corresponding to an underprediction of texture sharpness. This reduction can be attributed to the greater microstructural detail in the high-fidelity FE models, which disperses dominant orientations that may be artificially concentrated in the lower-fidelity representation.

Overall, these results show that transferring calibrated parameters from low- to high-fidelity microstructural models is entirely feasible for capturing the global stress–strain response and predicting the texture evolution. While the VH formulation yields reliable grain rotation predictions, the LH2 and LH6 formulations exhibit degraded accuracy due to their increased sensitivity to local interaction effects at higher microstructural resolutions. While direct calibration on a high-fidelity model would likely improve these mesoscale predictions, the associated computational cost is substantial. As such, for applications focused on reproducing the macroscopic response or achieving stable mesoscale predictions, it is effective to calibrate FE models that use moderately reduced fidelities and VH-type formulations.

## 6.6. Conclusion

This study presented a multi-objective surrogate-assisted calibration workflow for crystal plasticity finite element method (CPFEM) models, combining a multi-objective genetic algorithm (MOGA) with an adaptively trained deep neural network (DNN) surrogate model. The calibration workflow was demonstrated on three crystal plasticity (CP) formulations — a Voce hardening (VH) model, a two-coefficient latent hardening (LH2) model, and a six-coefficient latent hardening (LH6) model — coupled with a 2.5D low-fidelity microstructural finite element (FE) model of the specimen gauge. The CPFEM models were calibrated in five independent runs to confirm the repeatability of the workflow and enable direct analysis of variability in the optimised material parameters. Across all formulations, the macroscopic stress–strain response was reproduced reliably. The VH formulation delivered the most consistent results across calibration runs, with stable predictions of grain reorientation trajectories and texture evolution. The LH2 formulation matched the macroscopic accuracy of VH but showed higher sensitivity to noise in the calibration data and to changes in the fidelity of microstructural representation. The LH6 formulation exhibited substantial run-to-run variability across all assessed metrics, indicating that its larger parameter space is under-constrained under the present single-rate, monotonic loading conditions.

Analysis of the calibrated material parameters explains these trends. In the VH formulation, the initial slip system strength and hardening rate were tightly constrained, whereas the strain-rate sensitivity remained weakly constrained across all formulations due to the absence of multi-rate data. Adding latent hardening terms in the LH2 and LH6 formulations increased modelling flexibility but reduced parameter identifiability. Different parameter combinations could reproduce the same macroscopic response, reflecting parameter compensation effects and weak constraints on latent interactions under the given loading path. Including grain reorientation trajectories in the multi-objective calibration only moderately reduced statistical variability but acted as an important mesoscale filter, removing physically inconsistent solutions that could otherwise degrade texture evolution predictions. The transferability of the calibrated material parameters was also examined by applying the optimised parameter sets from the low-fidelity calibrations to a 2.5D high-fidelity microstructural FE model of the same specimen. Across all formulations, the prediction of the macroscopic stress–strain response was clearly preserved. At the mesoscale, the VH formulation retained good prediction of grain rotations and overall texture evolution, whereas the CPFEM predictions implementing the LH2 and LH6 formulations showed larger discrepancies, highlighting their sensitivity to local neighbourhood changes introduced by the higher fidelity of the FE microstructural model.

Overall, under the present single-rate, monotonic uniaxial loading, the VH formulation provides the most reliable and interpretable calibration outcome and is recommended for parameter reporting and predictive use in similar conditions. The LH2 and LH6 formulations could be potentially more useful when additional constraints exist, such as multiple strain rates, multiaxial or non-proportional loading, or physics-informed parameter bounds to reduce non-uniqueness and parameter compensation. Regardless of formulation, including grain reorientation trajectories in the objective is recommended. Even when they do not benefit the model stress–strain accuracy, they improve physical consistency and enhance predictions of texture evolution. Calibration on microstructures with moderately reduced fidelities offers an efficient route to reliable macroscopic predictions,

but grain-scale predictions should be validated and, if necessary, refined on higher-fidelity representations of microstructure.

Finally, the adopted 2.5D microstructural representation reduces through-thickness complexity, enabling direct integration of in situ EBSD data while keeping the computational cost tractable. The agreement achieved under uniaxial loading indicates that the key deformation mechanisms were captured. It is recognised that the parameters identified in this framework may not be fully transferable to a fully three-dimensional microstructure, where additional morphological constraints would influence the local deformation behaviour. Extending the same multi-objective surrogate-assisted calibration workflow to fully three-dimensional microstructures, richer loading paths, and additional physics such as creep and damage should further improve parameter identifiability and broaden its applicability to structural materials in demanding environments.

# Chapter 7

## Discussion

The thesis is composed of three studies focusing on the development and calibration of various empirical, semi-empirical, and physics-based material models to capture the creep and tensile behaviour of Alloy 617. In the first study (Chapter 4), empirical and symbolic regression (SR) models were calibrated to capture elevated-temperature creep behaviour. In the second study (Chapter 5), semi-empirical elastic-viscoplastic (EVP) models were calibrated using a multi-objective three-stage calibration workflow to capture elevated-temperature creep and tensile behaviour. In the third study (Chapter 6), physics-based crystal plasticity finite element method (CPFEM) models were calibrated using a multi-objective surrogate-assisted calibration workflow to capture multiscale tensile behaviour.

The following discussion chapter reflects on the outcomes of these three studies. The chapter begins with a brief overview of their research context, modelling frameworks, and calibration methodologies (Section 7.1), followed by a discussion of how the research objectives were addressed (Section 7.2). The chapter continues with a high-level comparison of the empirical, SR, EVP, and CPFEM models (Section 7.3), before identifying the remaining knowledge gaps and potential directions for future work (Section 7.3.3).

### 7.1. Research overview

Alloy 617 is commonly used in crucial engineering systems, making it essential to understand its behaviour across a wide range of operational conditions. Since performing experimental tests across the full range of conditions is infeasible, material models are often used to predict material behaviour while reducing the need for exhaustive experimental testing. Conventional material models range from empirical formulations that rely on observable trends, to semi-empirical models that incorporate basic physical concepts, and physics-based models that are grounded in fundamental mechanisms. To ensure accurate predictions, these material models are calibrated against experimental data, often using optimisation algorithms to automate and streamline the process. For complex semi-empirical and physics-based models, calibration can be difficult and computationally expensive, highlighting the need for more efficient calibration approaches, such as multi-stage workflows and surrogate-assisted techniques. Beyond conventional models that rely on fixed functional forms, symbolic regression (SR) provides a data-driven approach to discover flexible and interpretable constitutive expressions directly from experimental data. Despite significant progress in applying these modelling and calibration techniques to capture the creep and tensile behaviour of Alloy 617, there remain notable gaps in the literature regarding the prediction of creep mechanism shifts, use of multi-objective calibration, inclusion of grain-scale metrics, evaluation of parameter transferability, and the lack of direct comparisons between modelling frameworks. These gaps form the basis of the three studies presented in this thesis.

In the first study (Chapter 4), empirical and SR models were calibrated to predict key creep characteristics (i.e., minimum creep rate, time-to-failure, strain-to-failure) and the overall creep strain–time response (regular and mechanism-shifted) of Alloy 617 across multiple stress–temperature conditions (800°C, 900°C, and 1000°C). For each target response, three representative empirical models were calibrated using the genetic

algorithm (GA). The empirical characteristic-based models were calibrated directly against the scalar responses, while the empirical strain–time models were calibrated following a two-stage approach, which involved 1) optimising the model’s parameters against individual strain–time curves and 2) optimising the parameter function’s coefficients against the optimised model parameters. In parallel, SR was applied to discover alternative constitutive expressions of input variables, binary operators, and unary functions. The empirical and SR models were calibrated five independent times against short-term experimental creep datasets and validated against longer-term datasets to assess their robustness and predictive accuracy.

In the second study (Chapter 5), semi-empirical elastic-viscoplastic (EVP) models were calibrated to simultaneously predict the creep and tensile behaviour of Alloy 617 at elevated-temperatures conditions (800°C, 900°C, or 1000°C). The models employed an elastic-viscoplastic (EVP) formulation coupled with a classical creep damage (EVP-CD) or work-based damage (EVP-WD) model. The EVP-CD and EVP-WD models were calibrated using a multi-objective genetic algorithm (MOGA) through three optimisation stages. This multi-objective three-stage calibration workflow involves 1) optimising the parameters of the EVP model, 2) optimising the parameters of the damage (CD or WD) model, and 3) jointly refining all the parameters. The EVP-CD and EVP-WD models were each calibrated ten independent times against short-term creep and tensile datasets, then subsequently validated against longer-term datasets.

In the third study (Chapter 6), physics-based crystal plasticity finite element method (CPFEM) models were calibrated to capture the multiscale tensile behaviour of Alloy 617 at room temperature. The models employed a crystal plasticity (CP) formulation — a Voce hardening (VH) model, a two-coefficient latent hardening (LH2) model, and a six-coefficient latent hardening (LH6) model — coupled with a 2.5D low-fidelity microstructural finite element (FE) model of the specimen gauge. The CPFEM models were calibrated using a workflow that combined a MOGA with a deep neural network (DNN) surrogate model, which was adaptively trained in regions of the parameter space actively explored during the optimisation. The CPFEM models were calibrated five independent times against the macroscale stress–strain response and reorientation trajectories of eight grains, then validated against eight additional grain trajectories and the overall texture evolution.

## 7.2. *Addressing research objectives*

Seven research objectives (RO-1 to RO-7) were defined in Chapter 3 (Table 3.1) to target gaps in the literature concerning the calibration of the empirical models, SR models, semi-empirical EVP models, and physics-based CPFEM models. The following section outlines how each research objective was addressed in the three studies. The section begins by evaluating the use of SR to predict mechanism-shifted creep behaviour (Section 7.2.1) and comparing the empirical and SR models (Section 7.2.2). The section continues by describing the development of a multi-objective multi-stage calibration workflow (Section 7.2.3) and comparing the CD and WD models (Section 7.2.4). Finally, the section concludes by outlining the development of a multi-objective surrogate-assisted calibration workflow (Section 7.2.5), comparing the VH, LH2, and LH6 formulations (Section 7.2.6), and evaluating the transferability of parameters across microstructural fidelities (Section 7.2.7).

### 7.2.1. Application of symbolic regression for mechanism-shifted creep behaviour

To address the first objective of the first study (RO-1), SR was applied to a combination of regular and mechanism-shifted strain–time responses. These mechanism-shifted responses exhibited atypical behaviour in

the tertiary regime attributed to the effects of surface oxidation. In one approach, the time values of each strain–time curve were normalised by their respective times-to-failure, so that  $\hat{t} \in [0,1]$  across all curves. This method captured the regular strain–time responses reasonably well but failed to reproduce the post-shift behaviour for the mechanism-shifted responses.

An alternate approach normalised the time values so that  $\hat{t} \in [0,1]$  corresponded to the typical creep response,  $\hat{t} = 1$  corresponded to the shift in the dominant deformation mechanism, and  $\hat{t} > 1$  corresponded to the atypical, oxidation-driven behaviour. By fixing the mechanism shift to a consistent value across curves, this method more effectively reproduced the curvatures of both the regular and mechanism-shifted strain–time responses and provided a clearer transition from regular to oxidation-induced behaviour. However, this alternate approach requires prior knowledge of the mechanism-shift point for each curve, which is generally unavailable for new materials or untested conditions, limiting its practical application. Nevertheless, the results highlight the potential of SR for capturing mechanism-shifted creep behaviour when relevant experimental data are available.

### 7.2.2. Comparison of empirical and symbolic regression models

To address the second objective of the first study (RO-2), the empirical and SR models were calibrated five independent times against the experimentally observed minimum creep rate, time-to-failure, strain-to-failure, regular strain–time response, and mechanism-shifted strain–time response. The calibrations were performed against six short-term experimental datasets and validated against six longer-term datasets across various stresses at 800°C, 900°C, and 1000°C. The calibrated models were then compared based on their accuracy, robustness, and calibration difficulty.

Although both empirical and SR models performed reasonably well, the SR models consistently outperformed the empirical models in reproducing the short-term experimental data (i.e., calibration datasets). This discrepancy is reflected in their average relative errors across all five target responses, which were 12.0% for the empirical models and 3.3% for the SR models. The SR models also achieved improved predictions for most of the longer-term responses, as reflected in their relative errors of 33.9% and 22.6% for the empirical and SR models, respectively. The only exception was the strain-to-failure predictions with relative errors of 30.6% and 26.1%, reflecting the SR models' persisting risk of overfitting the calibration data.

The empirical and SR models yielded consistent predictions across independent runs despite being calibrated with only six datasets. However, the SR models exhibited lower variability in their predicted responses across five independent runs, with an average coefficient of variation of 2.3% across all target responses compared to 8.0% for the empirical models. The SR models also more accurately captured the surface oxidation effects in the full strain–time responses, highlighting their ability to adapt to changes in the operative deformation mechanisms. While the SR-discovered expressions were not identical between runs, they retained similar functional structures with multiple terms recurring across solutions. In contrast, the parameters of the empirical models were highly sensitive to trends in the experimental data, leading to broad parameter distributions and considerable run-to-run variability.

Compared to the empirical models, the calibration of the SR models incurred higher computational costs. For characteristic-based predictions, the empirical models required around 1 minute of CPU time compared to 15

minutes for the SR models, while for the strain–time predictions, the empirical models required roughly 30 minutes compared to 60 minutes for the SR models. Despite this discrepancy, the SR framework offered a more automated and generalisable approach, allowing it to explore a broad space of functional forms and discover interpretable expressions that, in some cases, resembled conventional empirical models. In contrast, the calibration process for the empirical models required greater manual effort and relied heavily on the analyst’s expertise, particularly for selecting the empirical model and defining the parameter bounds. Additionally, calibrating the empirical strain–time models required multi-stage optimisations due to their large number of adjustable parameters. That said, the empirical models typically had simpler functional forms with well-established parameter meanings, providing clearer insight into trends in the experimental data.

In general, the SR models outperformed the empirical models in capturing the short-term creep behaviour, generally improved longer-term predictions, and consistently showed low run-to-run variability. The SR models also better captured the surface oxidation effects in the strain–time responses. While the SR models incurred higher calibration costs, they provided a more streamlined and automated framework that discovered relatively simple and interpretable expressions, suggesting that SR can serve as a complementary tool to empirical models. That said, a more comprehensive comparison could be achieved in the future by calibrating the models using experimental datasets that span a wider range of stress–temperature conditions, mechanical loading modes, and material types.

### 7.2.3. Development of multi-objective multi-stage calibration workflow

To address the first objective of the second study (RO-3), a multi-objective multi-stage calibration workflow was developed with the MOGA to efficiently calibrate the EVP-CD and EVP-WD models to capture creep and tensile behaviour. Eight objective functions were defined for the strain values ( $E_\varepsilon$ ), minimum creep rate ( $E_{\dot{\varepsilon}_m}$ ), time-to-failure ( $E_{t_f}$ ), strain-to-failure ( $E_{\varepsilon_f}$ ), stress values ( $E_\sigma$ ), yield stress ( $E_{\sigma_y}$ ), maximum true stress ( $E_{\sigma_M}$ ), and strain-at-ductility ( $E_{\varepsilon_d}$ ). Additionally, the parameters of each model were partitioned into two groups governing the yielding and damage responses. The workflow was applied to calibrate the EVP-CD and EVP-WD models by 1) optimising the EVP parameters, 2) optimising the CD / WD parameters, and 3) fine tuning them together to resolve parameter interdependencies.

In the first optimisation stage, the EVP model accurately and consistently captured the yielding response of the creep and tensile data. In the second stage, the CD and WD models showed reduced accuracy in predicting the damage response, particularly in the strain-to-failure predictions. In the final correctional stage, the accuracy of the predictions improved, as reflected in their averaged objective values decreasing by 14% and 27% for the EVP-CD and EVP-WD models, respectively. The improvements were more substantial with the EVP-WD model due to the larger number of material parameters in the WD model and the tighter coupling between the EVP and WD models.

Overall, the multi-stage calibration workflow demonstrated greater consistency and computational efficiency than a single-stage approach where all the parameters were optimised simultaneously. When attempting to calibrate the EVP-CD and EVP-WD models in a single stage, the MOGA was unable to efficiently search their high-dimensional parameter spaces and the models consistently failed to reproduce the experimental creep and tensile behaviour. Despite these improvements, the performance of the developed workflow still depends on

the accuracy of the separately optimised parameters, as the final correctional stage assumes that the parameters are close to their optimal values. This reliance can limit the applicability of the workflow for more complex models (e.g., physics-based models), where parameter interactions are stronger and the correctional stage may degrade the models' predictive performance due to overfitting.

#### 7.2.4. Comparison of creep and work damage models

To address the second objective of the second study (RO-4), the developed workflow was used to calibrate the EVP-CD and EVP-WD models against experimentally observed creep and tensile behaviour at 800°C, 900°C, and 1000°C. At each temperature the models were calibrated ten independent times against the short-term creep and tensile datasets, then validated against the longer-term datasets. The calibrated models were then compared based on their accuracy, robustness, and calibration difficulty.

For creep behaviour, both EVP-CD and EVP-WD models produced accurate predictions at 800°C but showed reduced accuracy at 900°C and 1000°C, due to the increasing surface-oxidation effects at those temperatures. While the EVP-CD model was slightly more accurate for the minimum creep rate predictions, the EVP-WD model performed better for the time- and strain-to-failure predictions. Notably, the material properties captured by the EVP-WD model were mostly conservative, which is useful for estimating safe in-service lifetimes. For tensile behaviour, both the EVP-CD and EVP-WD models accurately captured the yield stress and toughness, which is expected since these properties are largely governed by the shared EVP framework. However, the EVP-WD model substantially outperformed the EVP-CD model in capturing the maximum true stress, strain-at-ductility, and overall tensile damage response. These discrepancies stem from the CD model basing damage accumulation on time, limiting its ability to capture the high strain-rate tensile behaviour. In contrast, the WD model employed piecewise correlations based on plastic work density to capture separate strain-rate effects, enabling accurate creep and tensile predictions.

The EVP-CD and EVP-WD models exhibited similar robustness in their calibration against creep and tensile behaviour. At 800°C, both models produced consistent predictions across ten independent runs. However, their run-to-run variability showed a notable increase at 900°C and 1000°C, again attributed to surface-oxidation effects at those temperatures. Despite this increased variability, the distributions of the optimised parameters for both models remained comparably narrow relative to the applied bounds at all three temperatures. These results suggest that the experimental data sufficiently constrained both models, allowing for reliable parameter identification.

Despite the improved accuracy of the EVP-WD model in capturing tensile damage, the model suffered from a more complex implementation. The EVP-WD model also incurred higher computational costs, with each evaluation taking an average of 1.395s of CPU time compared to only 0.595s for the EVP-CD model. Furthermore, the EVP-WD model required 500 generations to converge while the EVP-CD model required only 250. This discrepancy was attributed to the larger number of material parameters in the EVP-WD model (eleven versus eight) and the tighter coupling between its EVP and damage components. As such, with the higher evaluation time and number of generations, the EVP-WD model required significantly more computational resources to calibrate (~19.8 hours) compared to the EVP-CD model (~5.2 hours).

Overall, the EVP-CD and EVP-WD models exhibited similar accuracy for the creep predictions and comparable robustness. Despite the higher computational costs and calibration effort, the EVP-WD model demonstrated superior accuracy in reproducing the full tensile stress–strain response and holds potential for extension to other loading scenarios, such as fatigue or thermo-mechanical cycling. Consequently, the choice between EVP-CD and EVP-WD models should be guided by the available computational resources and required accuracy for the tensile predictions.

#### **7.2.5. Development of multi-objective surrogate-assisted calibration workflow**

To address the first objective of the third study (RO-5), a multi-objective surrogate-assisted calibration workflow was developed with the MOGA to efficiently calibrate the CPFEM models to capture multiscale tensile behaviour. Two objective functions were defined, with one for the macroscale stress–strain response ( $E_\sigma$ ) and the other for the grain reorientation trajectories ( $E_\phi$ ). Guided by these objective functions, a DNN surrogate model was trained from an initial dataset generated through the Latin hypercube sampling (LHS) scheme and adaptively refined at the MOGA-optimised parameters. This training strategy progressively improved the surrogate model in regions of the parameter space that were actively explored by the MOGA, thereby avoiding unnecessary sampling in uninformative regions and avoiding the risk of overfitting.

Using this strategy, the surrogate models were trained with significantly fewer CPFEM evaluations than a uniformly sampled or full pre-trained surrogate model, with the VH, LH2, and LH6 formulations calibrated using an average of only 21, 24, and 38 evaluations. Once trained, the surrogate models reliably reproduced the CPFEM predictions, enabling the MOGA-based calibration to be performed at a fraction of the computational cost without compromising accuracy. However, the strategy limited the generalisability of the surrogate models beyond the explored regions of the parameter space, preventing their direct application to other experimental datasets without additional training.

#### **7.2.6. Comparison of crystal plasticity hardening models**

To address the second objective of the third study (RO-6), the developed workflow was used to calibrate the VH, LH2, and LH6 formulations against experimentally observed multiscale tensile behaviour. The CPFEM models were calibrated five independent times against the macroscale stress–strain response and eight grain reorientation trajectories, then validated against eight additional trajectories and the overall texture evolution. The calibrated models were then compared based on their accuracy, robustness, and calibration difficulty.

Across all three formulations — VH, LH2, and LH6 — the simulated stress–strain responses showed excellent agreement with the experimental data, with their best calibration runs yielding  $E_\sigma$  objective values of 1.1%, 1.2%, and 0.9%, respectively. The models also reproduced the reorientation trajectories reasonably well for the calibration datasets ( $E_\phi = 4.9^\circ$ ,  $4.9^\circ$ , and  $5.1^\circ$ ) but the accuracy decreased for the validation dataset ( $E_\phi = 6.2^\circ$ ,  $6.4^\circ$ , and  $7.1^\circ$ ). Notably, the LH6 formulations showed reduced accuracy in capturing the trajectories for both datasets compared to the VH and LH2 formulations. A similar trend was observed in the predictions for the overall texture evolution, in which the VH and LH2 formulations accurately tracked the intensity and orientation of the dominant texture components, while the LH6 formulation exhibited larger deviations in the pole figure contours and final texture index. The reduced accuracy of the LH6 formulation was attributed to its more

complex implementation and larger number of parameters — eight compared to four in the other models — making its calibration more sensitive and prone to deviation.

In general, the VH formulation showed lower variability across five calibration runs compared to the LH2 and LH6 formulations, as reflected in the mean standard deviations for their stress–strain responses (3.76MPa compared to 5.05MPa and 10.6MPa) as well as their reorientation trajectories ( $0.39^\circ$  compared to  $1.29^\circ$  and  $1.0^\circ$ ). The increased run-to-run variability of the LH2 and LH6 formulations was attributed to their poor constraint due to the limited activation of secondary slip systems under uniaxial tensile loading. Their poor constraint is also reflected in the broad distributions of the self- and latent hardening coefficients ( $h_{\alpha\alpha}$ ,  $h_{\alpha\beta}$ , and  $h_{1..5}$ ), in which the MOGA converged to multiple mathematically viable but physically distinct solutions. In contrast, the parameters in the VH formulation remained relatively well constrained, with the exception of the saturation strength parameter ( $\tau_s$ ) due to the lack of calibration data in the late-stage saturation regime (Stage III). Notably, the inclusion of the mesoscale reorientation trajectories in the calibration process modestly reduced parameter variability while providing a crucial physical filter, ensuring that the optimised parameters produced realistic microstructural evolution consistent with experimental observations.

Among the three CPFEM models, the calibration of the VH formulation was the most computationally efficient. In particular, the VH formulation required an average of only 21 evaluations while the LH2 and LH6 formulations required 24 and 38, respectively. Additionally, the VH formulation was substantially cheaper to evaluate, which each low-fidelity evaluation requiring approximately 0.23 hours of CPU time (on 192 cores) compared to 1.46 hours for the LH2 and LH6 formulations. Consequently, the total CPU time required to calibrate the LH2 and LH6 formulations was approximately 7-12 times greater than that required for the VH formulation.

Overall, the VH formulation demonstrated comparable accuracy, greater robustness, and substantially improved efficiency compared to the other formulations, making it the most suitable choice for the multiscale prediction of Alloy 617 under uniaxial tensile loading. That said, the LH2 and LH6 formulations may provide enhanced performance for applications involving more complex loading paths or multiaxial stress states.

#### 7.2.7. Evaluation of parameter transferability across fidelities

To address the third objective of the third study (RO-7), the transferability of the optimised parameters across microstructural fidelities was evaluated. The CP formulations — VH, LH2, and LH6 — were coupled with a low-fidelity FE model (with 132 grains) and a high-fidelity model (with 481 grains). The low-fidelity CPFEM models were calibrated five times using the developed workflow, and the best set of parameters were used to evaluate the high-fidelity CPFEM models.

Across all three formulations, the stress–strain responses between the low- and high-fidelity models showed close agreement, demonstrating that the macroscopic mechanical response is largely insensitive to microstructural resolution within the examined range. In contrast, the reorientation trajectories showed modest discrepancies between microstructural fidelities, attributed to the higher sensitivity of the CPFEM framework to changes in local grain morphology. While these discrepancies did not affect the accuracy of the trajectory predictions for the VH formulation, the LH2 and LH6 formulations showed reduced accuracy, with their objective values ( $E_\phi$ ) increasing from  $\sim 6^\circ$  in the low-fidelity calibration to  $\sim 11^\circ$  in the high-fidelity predictions. For the

overall texture evolution, the low- and high-fidelity models showed consistent predictions for all three formulations. However, the high-fidelity models showed a slight underprediction of texture sharpness, as reflected in their texture indices being about 0.45 units lower than the low-fidelity models. This underprediction was attributed to the increased microstructural resolution of the high-fidelity FE models, which dispersed dominant orientations across the grains, reducing the artificial concentration observed in the lower-fidelity representation.

Overall, these results showed that the optimised parameters could be feasibly transferred from the low- and high-fidelity models, with strong alignment for the stress–strain response and texture evolution, and reasonable agreement for the reorientation trajectories — particularly for the VH formulation. As such, calibrations can be performed on moderately reduced-fidelity FE models to maintain reliable macroscopic predictions, although grain-scale predictions may require additional validation or refinement.

### 7.3. *Comparison of modelling frameworks*

The three studies presented in this thesis provided direct comparisons between the empirical and SR models, between the semi-empirical CD and WD models, as well as between the physics-based VH, LH2, and LH6 formulations. Since these studies employed different experimental datasets and focused on distinct material responses, their results cannot be directly compared across modelling frameworks. As such, the following section presents a high-level comparison of these frameworks in terms of their generalisability (Section 7.3.1), interpretability (Section 7.3.2), and practicality (Section 7.3.3) for engineering applications.

#### 7.3.1. Comparison of model generalisability

The ability of material models to generalise beyond their calibration dataset is crucial for reliably predicting material behaviour at untested conditions, reducing the need for extensive experimental testing. The simple forms of empirical models enable them to be easily adapted or combined, enabling predictions across multiple stresses and temperatures. These empirical models exhibited reasonable generalisability, reliably predicting the longer-term creep behaviour of Alloy 617 using only the short-term experimental data. While these models captured the regular creep behaviour at 800°C fairly well, they were less effective in capturing the oxidation-affected creep behaviour at 900°C and 1000°C. The empirical models also showed high sensitivity to experimental trends, which could limit their generalisability across more diverse conditions. In contrast, the SR models offered greater generalisability through their flexible functional forms that discovered relationships directly from the experimental data. They also showed generally improved predictions for the longer-term creep behaviour compared to the empirical models. While the SR models more accurately captured the mechanism-shifted strain–time responses, they required prior knowledge of mechanism-shift points for optimal performance. Additionally, their effectiveness still strongly depended on the quality and range of the calibration data, in which careful validation was required to prevent overfitting and the generation of unstable or non-physical expressions.

Similar to the empirical and SR models, the semi-empirical EVP models could predict longer-term behaviour using only short-term data for calibration. However, instead of targeting individual aspects of creep behaviour, the EVP models provided a unified framework that captured the complete creep response — encompassing the minimum creep rate, time-to-failure, strain-to-failure, and strain–time response — in addition to the full tensile

behaviour. Despite these advantages, the semi-empirical models were restricted to single-temperature applications while the empirical and SR models could reproduce creep behaviour across multiple stress–temperature conditions. Additionally, their performance still diminished under conditions affected by surface oxidation, which could limit their reliability in real service environments.

By explicitly representing microstructural deformation mechanisms, the CPFEM models captured behaviour across multiple length scales. These models accurately captured the macroscale stress–strain response and mesoscale grain reorientation trajectories, while also predicting behaviour beyond their calibration datasets, including additional reorientation trajectories and the overall texture evolution. Importantly, the optimised parameters could be transferred between low- and high-fidelity FE models, yielding good agreement for the stress–strain response and texture evolution, and decent alignment for the reorientation trajectories. While the CPFEM models performed well under the studied condition, further evaluation under different loading conditions and microstructures is necessary to assess their broader generalisability.

### 7.3.2. Comparison of model interpretability

The interpretability of material models is crucial for connecting model behaviour to physical processes, enabling insight into the underlying mechanisms. Among the modelling frameworks, empirical models offer the least physical interpretability. While these models can be calibrated to closely reproduce the experimental creep data, their parameters serve primarily as fitting coefficients, providing minimal mechanistic understanding of the underlying processes. Nevertheless, these parameters can still reveal correlations in the experimental data, such as with the linear relationship between  $\ln(\dot{\varepsilon}_m)$  versus  $\ln(\hat{\sigma})$ ,  $\ln(t_f)$  versus  $\ln(\dot{\varepsilon}_m)$ , and  $\ln(t_f)$  versus  $1/\hat{T}$ . SR models extend conventional empirical models by revealing the experimental correlations without relying on predefined functional forms. For example, the SR-discovered expressions for the minimum creep rate and time-to-failure often included Arrhenius-like terms, capturing the temperature dependence observed in the experiments. Similarly, the strain–time expressions included multiplicative  $\hat{t}$  terms to capture the near-constant strain rate of the secondary regime and high time exponents to represent the accelerated strain growth of the tertiary regime. While the first study did not explicitly examine the physical interpretation of the SR models, the framework has been shown to provide such insights through physics-informed inputs and constraints [195].

In contrast to the empirical and SR models, the semi-empirical EVP models offer greater interpretability by explicitly linking model parameters to deformation mechanisms. For instance, the flow surface exponent ( $n_{PF}$ ) and viscosity parameter ( $\eta_{PF}$ ) reveal how rapidly viscoplastic deformation develops, while the Voce hardening parameters ( $\sigma_{y,0}$ ,  $R_{VIH}$ ,  $d_{VIH}$ ) provide information about the alloy’s hardening behaviour. However, the interpretability of the EVP models is limited by their reliance on simplifying assumptions, such as with isotropic elasticity and the infinitesimal strain theory. Additionally, their use of empirical components — such as the WD model’s piecewise functions — can obscure the link between the parameters and mechanisms, making it challenging to extract mechanistic insight. Finally, the simultaneous calibration of both creep and tensile behaviour can impose competing constraints on the parameters, such as with the initial yield stress parameter ( $\sigma_{y,0}$ ), whose optimised values vary greatly from the experimentally observed yield stress.

The physics-based CPFEM models provide the highest degree of interpretability among the discussed material modelling frameworks, providing parameters that correspond directly to measurable microstructural

processes. For instance, the initial slip system strength ( $\tau_0$ ) and saturation rate ( $b$ ) in the VH formulation directly relate to the initial yield strength and hardening slope of the single stress-strain curve in the calibration dataset. Additionally, the self- and latent hardening parameters ( $h_{\alpha\alpha}$ ,  $h_{\alpha\beta}$ , and  $h_{1..5}$ ) in the LH2 and LH6 formulations provide useful insight into the relative strengths of self- and cross-slip system interactions. However, in the third study, the CPFEM models were under-constrained due to the lack of calibration data at multiple strain rates, in the late-stage saturation regime (Stage III), and under complex loading paths (e.g., multiaxial or non-monotonic). As such, to fully preserve the physical significance of these parameters, future work should focus on expanding the experimental dataset to more sufficiently constrain the CPFEM models.

### 7.3.3. Comparison of model practicality

Beyond their performance, the usefulness of a material model is determined by how readily it can be deployed in practical engineering applications. Empirical models generally incur low computation costs due to their simple implementations, with predictions typically computed within milliseconds on modern hardware. In the first study, the calibration of empirical characteristic-based models was straightforward, requiring roughly a minute of CPU time. In contrast, the empirical strain–time models involved a large number of parameters to account for multiple stress–temperature conditions, necessitating multiple optimisation stages and roughly 30 minutes of calibration. Additionally, since empirical models are typically tailored for specific responses, capturing the complete material behaviour often requires multiple complementary models. For instance, since the employed strain–time models included normalised time terms, representing full creep responses would require separate calibrations of both time-to-failure and strain–time models. Similar to empirical models, evaluating a SR-discovered expression is computationally inexpensive. However, the discovery process can require exploring a large number of functional forms, leading to slightly higher calibration costs. In particular, the calibration of the SR models in the first study required roughly 15 minutes for the characteristic-based predictions and 60 minutes for the strain–time predictions. Despite the higher costs, the SR framework offers a more streamlined and automated modelling approach, which is less reliant on the analyst’s expertise. That said, some manual effort is still required to constrain the model and filter out unstable or non-physical expressions.

Semi-empirical EVP models are inherently more complex to implement than the empirical and SR models. Their development required the careful selection and integration of multiple interacting components through a trial-and-error process. Evaluating these complex models often require specialised numerical routines to solve their non-linear, time-dependent governing equations, resulting in higher computational costs. In particular, each evaluation of the EVP-CD and EVP-WD models required roughly 0.595s and 1.395s of CPU time, respectively. In addition, these models contain a large number of interdependent material parameters, making calibration challenging and necessitating multiple optimisation stages to achieve stable and physically meaningful solutions. Even with the multi-stage calibration workflow, the EVP-CD and EVP-WD models still required approximately 5.2 hours and 19.8 hours to calibrate, respectively.

Among the discussed modelling frameworks, the physics-based CPFEM models have the most complex implementations due to their consideration of crystal-level anisotropy, slip system mechanics, grain-to-grain interactions, and microstructural evolution. These models require accurate FE representations that capture the grain geometries and orientations of the specimen microstructure. They are also substantially more computationally intensive, since the CP equations must be solved at multiple quadrature points for each

element over many timesteps. Even with a low-fidelity FE model containing 17,109 elements evaluated on 192 cores, a single simulation takes  $\sim$ 0.23 hours for the VH formulation and  $\sim$ 1.46 hours for the LH2 and LH6 formulations. While surrogate models can be developed to reduce their calibration costs, their development still required numerous full simulations — i.e., 21, 24, and 38 for the VH, LH2, and LH6 formulations, respectively. Additionally, the development and calibration of the CPFEM models required high-resolution microstructural data, the acquisition of which is often expensive, time-consuming, and involves specialised instrumentation. As such, while CPFEM models offer high predictive accuracy, great generalisability, and rich mechanistic insight, their complexity, computational demands and extensive data requirements limit their routine application.

#### *7.4. Remaining gaps and future work*

Despite the advancements achieved through the three studies, several gaps remain that limit the broader applicability and predictive capability of the discussed modelling frameworks. The following section provides a brief outline of potential future work for the empirical and SR models (Section 7.4.1), semi-empirical EVP models (Section 7.4.2), and physics-based CPFEM models (Section 7.4.3).

##### 7.4.1. Future work for empirical and symbolic regression models

In comparing the empirical and SR models, the first study showed that the SR framework could complement empirical models by enhancing their predictive accuracy and consistency while providing a more streamlined and automated calibration approach. However, a more comprehensive assessment can be achieved by applying cross-validation against experimental datasets spanning different materials and a wider range of loading conditions. Applying SR across multiple materials could also help reveal consistent functional forms that incorporate material-specific parameters, potentially replacing traditional empirical models.

Future work could also focus on using SR to capture mechanism-shifted material behaviour, such as the creep response of Alloy 617 affected by surface oxidation. This could involve applying SR to the differences between the regular and mechanism-shifted responses following the Kennedy-O'Hagan method [200], enabling the discovery of a functional form that captures the isolated effect of the mechanism shift. The SR-discovered expressions could then be integrated with other modelling frameworks to enhance their predictive capability and generalisability. However, implementing this would require experimental datasets under identical loading conditions that included and excluded the mechanism-shifted behaviour.

The SR models were developed to empirically describe the creep behaviour rather than to explicitly capture the underlying physics. As such, future research could enhance the physical fidelity of SR models, such as by incorporating physics-informed inputs and constraints, or by incorporating established constitutive relationships into the set of candidate building blocks. SR could also be integrated into semi-empirical or physics-based modelling frameworks, such as EVP and CPFEM models, to discover functional relationships between key variables. These approaches could enhance the predictive accuracy of the SR models and enable them to provide richer mechanistic insight.

##### 7.4.2. Future work for semi-empirical elastic-viscoplastic models

In the second study, the EVP models were developed based on the infinitesimal strain theory as a simplifying assumption to reduce computational complexity and ensure compatibility with existing model formulations in

the nuclear engineering material library (NEML). However, the experimental creep and tensile data used in this study involved strains of up to 64.1%, which exceeds the validity limit of the infinitesimal strain theory. While the results showed that the models remained applicable using the employed experimental datasets, future work should focus on reformulating the EVP models within the finite-strain framework to improve their accuracy, reliability, and physical consistency when applied to large strains.

When comparing the two EVP models, the EVP-WD model exhibited enhanced accuracy in simultaneously capturing the creep and tensile behaviour. This was achieved by representing the model parameters — namely the critical plastic work density ( $W_{crit}$ ) and the damage exponent ( $n_d$ ) — as piecewise functions of the logarithmised work density rate, allowing the WD model to capture the distinct strain-rate effects characteristic of creep and tensile behaviour. Building on these results, future work could explore the extension of the WD model to additional loading configurations, such as fatigue or thermo-mechanical cycling.

Additionally, it would be useful to calibrate the EVP models on one type of loading (e.g., creep) and validate them on another type of loading (e.g., tensile). This approach would provide a more rigorous assessment of the models' generalisability and ensure that the parameters capture underlying material behaviour.

#### **7.4.3. Future work for physics-based crystal plasticity finite element method models**

In the third study, the multi-objective surrogate-assisted calibration workflow was applied to 2.5D FE models that provided a direct 1:1 representation of the specimen microstructure. This approach enabled the direct integration of the experimental in situ electron backscatter diffraction (EBSD) data as well as reduced the total number of elements, thereby decreasing the computational cost of evaluating the CPFEM models. However, the approach also neglected the variations in the through-thickness morphology of the FE model, which reduced the physical fidelity and accuracy of the CPFEM model. As such, future work could explore how the calibration workflow applies to full 3D microstructural models, which could be developed as statistically equivalent representative volume element (RVE) models or through 3D imaging techniques to preserve the microstructural details of the specimen.

Across five calibration runs, some of the optimised parameters of the CPFEM models exhibited broad distributions due to the under-constraint of their parameters. In particular, the strain rate sensitivity parameter ( $n$ ), saturation strength parameter ( $\tau_s$ ), and the self- and latent hardening coefficients ( $h_{\alpha\alpha}$ ,  $h_{\alpha\beta}$ , and  $h_{1.5}$ ) showed notable variability due to the absence of calibration data at multiple strain rates, in the late-stage saturation regime (Stage III), and under complex deformation paths (e.g., multiaxial or non-monotonic). As such, future work should focus on expanding the experimental dataset to better constrain these parameters, enabling a more comprehensive and reliable comparison of the CP formulations.

Finally, the CPFEM models were calibrated against experimental data from a single Alloy 617 specimen. To more thoroughly evaluate the generalisability of the CPFEM models and calibration workflow, future studies could apply the approach to different materials and across a wider range of material responses, such as creep and damage behaviour. Future work could also focus on applying the calibration workflow to more physically grounded hardening formulations, such as Kocks-Mecking, dislocation-density-based, or geometrically necessary dislocations-based formulations [262-264], which could provide richer mechanistic insight than the employed VH, LH2, LH6 formulations.

# Chapter 8

## Conclusion

Material models can be used to predict material behaviour across a wide range of loading conditions without relying heavily on exhaustive experimental testing. While higher-fidelity models provide enhanced accuracy, applicability, and mechanistic insight, they often involve more complex implementations, higher computational costs, and greater calibration difficulty, necessitating the use of specialised optimisation techniques. To explore these trade-offs, this thesis presented three studies focusing on the development and calibration of empirical, semi-empirical, and physics-based material models to predict the creep and tensile behaviour of Alloy 617.

In the first study, empirical and symbolic regression (SR) models were calibrated to capture elevated-temperature creep behaviour, targeting key creep characteristics and overall strain–time response. While the empirical models captured the short-term creep behaviour reasonably well, they showed lower accuracy for the longer-term predictions. The models also underrepresented the characteristic curvatures of the strain–time responses, especially for mechanism-shifted behaviour. Additionally, their performance was strongly influenced by experimental trends, underscoring their reliance on observed behaviour rather than underlying mechanisms. In comparison, the SR models generally achieved higher accuracy, lower run-to-run variability, and improved adaptability to the mechanism-shifted responses. The SR framework also provided a more streamlined and automated process that yielded relatively simple and interpretable expressions. However, the SR-discovered expressions still required careful validation to prevent overfitting and the generation of unstable or non-physical forms. Overall, SR shows promise as a complementary tool to traditional empirical models, but its applicability could be strengthened through cross-validation, by employing a wider range of loading conditions and different materials, and by incorporating physics-informed constraints.

In the second study, semi-empirical models — coupling the elastic-viscoplastic (EVP) formulation with a classical creep damage (EVP-CD) and work-based damage (EVP-WD) model — were calibrated using a multi-objective three-stage calibration workflow to capture elevated-temperature creep and tensile behaviour. By splitting the high-dimensional parameter space into two lower-dimensional spaces, the calibration workflow improved the consistency and computational efficiency of the calibration process. Using this workflow, both EVP-CD and EVP-WD models produced similarly accurate creep predictions at 800°C and 900°C, but their performance declined at 1000°C due to surface oxidation effects. For the tensile predictions, the EVP-WD model outperformed the EVP-CD model by employing piecewise parameter functions of the work density rate. However, this came at the cost of increased computational complexity and calibration effort. Future work could focus on applying cross-validation, improving the generalisability of the WD model by extending it to additional loading configurations, as well as enhancing the accuracy, reliability, and physical consistency of the EVP models by reformulating them within the finite-strain framework.

In the third study, three physics-based crystal plasticity finite element method (CPFEM) models — coupling the Voce hardening (VH), two-coefficient latent hardening (LH2), and six-coefficient latent hardening (LH6) formulations with a 2.5D finite element (FE) model — were calibrated using a multi-objective surrogate-assisted calibration workflow to capture multiscale tensile behaviour. The results showed that the calibration workflow

produced accurate surrogate models and enabled efficient and robust parameter identification. In applying the workflow, all three formulations accurately captured the macroscale stress–strain response, but the LH6 formulation showed reduced accuracy in capturing the grain reorientation trajectories and texture evolution. The LH2 and LH6 formulations also exhibited greater run-to-run variability due to the limited activation of secondary slip systems in the data. Additionally, the VH formulation incurred substantially lower calibration costs and showed stronger parameter transferability across microstructural fidelities. While the results demonstrated that the VH formulation is the most reliable and interpretable for the investigated loading condition, a more comprehensive comparison can be achieved by employing calibration datasets that include multiple strain rates, late-stage saturation regime (Stage III), and complex deformation paths (e.g., multiaxial or non-monotonic). To further assess the generalisability of the calibration workflow, future work could apply it to full 3D microstructural models and more physically grounded hardening formulations.

Overall, the empirical, SR, semi-empirical EVP, and physics-based CPFEM models offered distinct trade-offs and that align with different modelling priorities. The empirical models provided simplicity, low computational costs, and ease of implementation, making them suitable for quick predictions that do not require detailed mechanistic insight. The SR models provided a more flexible approach to automatically discover constitutive expressions directly from experimental data without relying on the analyst's expertise, though careful validation is required. Additionally, the EVP models captured both creep and tensile behaviour within a unified framework while offering greater interpretability by linking its parameters to deformation mechanisms, albeit with higher calibration costs. Finally, the CPFEM models provided the highest level of physical fidelity, offering rich mechanistic insight and accurately predicting tensile behaviour across multiple length scales, but required substantial computational resources and high-resolution microstructural data. Together, the results of this thesis emphasise that no modelling framework is universally superior, and that model selection should be guided by the required accuracy, generalisability, physical fidelity, and available computational and experimental resources.

## References

- [1] W. Ren, R. Swindeman, A Review on Current Status of Alloys 617 and 230 for Gen IV Nuclear Reactor Internals and Heat Exchangers, *Journal of Pressure Vessel Technology-transactions of The Asme - J PRESSURE VESSEL TECHNOL* 131 (2009) 044002-15.
- [2] K. Maile, Qualification of Ni-Based Alloys for Advanced Ultra Supercritical Plants, *Procedia Engineering* 55 (2013) 214-220.
- [3] X. Xie, C.-y. Chi, S. Zhao, J. Dong, F. Lin, Superalloys and the Development of Advanced Ultra-Supercritical Power Plants, *Materials Science Forum* 747 (2013) 594-603.
- [4] P. Mandal, A. Lalu, A.M. Saji, M. Jacob, Cryogenic Behavior of TIG Welded Ni-Based Superalloy (IN617), 2022, pp. 207-219.
- [5] W. Ren, Considerations of Alloy 617 Application in the Gen IV Nuclear Reactor Systems - Part II: Metallurgical Property Challenges, (2009).
- [6] J.K. Wright, Next Generation Nuclear Plant Steam Generator and Intermediate Heat Exchanger Materials Research and Development Plan, Office of Scientific and Technical Information (OSTI), 2010.
- [7] R.E. Mizia, Next Generation Nuclear Plant Intermediate Heat Exchanger Acquisition Strategy, Office of Scientific and Technical Information (OSTI), 2008.
- [8] Q. Meng, Z. Wang, Creep damage models and their applications for crack growth analysis in pipes: A review, *Engineering Fracture Mechanics* 205 (2019) 547-576.
- [9] L.J. Carroll, C. Cabet, M.C. Carroll, R.N. Wright, The development of microstructural damage during high temperature creep-fatigue of a nickel alloy, *International Journal of Fatigue* 47 (2013) 115-125.
- [10] H.E. McCoy, J.F. King, Mechanical properties of Inconel 617 and 618, United States, 1985.
- [11] F.H. Norton, The Creep of Steel at High Temperatures, McGraw-Hill book Company 1929.
- [12] P. McVetty, Factors affecting choice of working stresses for high-temperature service, (1933).
- [13] R.W. Evans, B. Wilshire, Creep of metals and alloys, IMM North American Pub. Center, Brookfield, VT, United States, 1984.
- [14] J.H. Hollomon, Tensile deformation, *Aime Trans* 12(4) (1945) 1-22.
- [15] J. Choi, L. Bortolan Neto, R.N. Wright, J.J. Kruzic, O. Muránsky, On the prediction of creep behaviour of alloy 617 using Kachanov-Rabotnov model coupled with multi-objective genetic algorithm optimisation, *International Journal of Pressure Vessels and Piping* 199 (2022) 104721.
- [16] A. Venkataraman, M. Messner, An initial framework for the rapid qualification of long-term creep rupture strength via microstructural modeling, Office of Scientific and Technical Information (OSTI), 2021.
- [17] L.M. Kachanov, Time of the Rupture Process under Creep Conditions, *Izvestiia Akademii Nauk SSSR, Otdelenie Tekhnicheskikh Nauk* 8 (1958) 26-31.
- [18] Y.N. Rabotnov, F.A. Leckie, W. Prager, Creep Problems in Structural Members, *Journal of Applied Mechanics* 37(1) (1970) 249-249.
- [19] I.w. Goodall, R.A. Ainsworth, An Assessment Procedure for the High Temperature Response of Structures, 1991.
- [20] Y. Takahashi, B. Dogan, D. Gandy, Systematic Evaluation of Creep-Fatigue Life Prediction Methods for Various Alloys, 2009.
- [21] G. Cheng, A. Plumtree, A fatigue damage accumulation model based on continuum damage mechanics and ductility exhaustion, *International Journal of Fatigue* 20(7) (1998) 495-501.
- [22] P. Zerbe, B. Schneider, E. Moosbrugger, M. Kaliske, A viscoelastic-viscoplastic-damage model for creep and recovery of a semicrystalline thermoplastic, *International Journal of Solids and Structures* 110-111 (2017) 340-350.

- [23] E. Krempl, K. Ho, THE MODELING OF INELASTIC COMPRESSIBILITY AND INCOMPRESSIBILITY USING THE VISCOPLASTICITY THEORY BASED ON OVERSTRESS (VBO), in: M.F. Hassan, S.M. Megahed (Eds.), Current Advances in Mechanical Design and Production VII, Pergamon, Oxford, 2000, pp. 151-160.
- [24] J.P. DeMarco, E.A. Hogan, C.M. Stewart, A.P. Gordon, An Efficient Method for the Optimization of Viscoplastic Constitutive Model Constants, ASME Turbo Expo 2010: Power for Land, Sea, and Air, 2010, pp. 569-580.
- [25] O.M. Heeres, A.S.J. Suiker, R. de Borst, A comparison between the Perzyna viscoplastic model and the Consistency viscoplastic model, European Journal of Mechanics - A/Solids 21(1) (2002) 1-12.
- [26] K. Kan, O. Muránsky, P.J. Bendeich, R.N. Wright, J.J. Kruzic, W. Payten, Assessment of creep damage models in the prediction of high-temperature creep behaviour of Alloy 617, International Journal of Pressure Vessels and Piping 177 (2019) 103974.
- [27] K. Sedighiani, M. Diehl, K. Traka, F. Roters, J. Sietsma, D. Raabe, An efficient and robust approach to determine material parameters of crystal plasticity constitutive laws from macro-scale stress-strain curves, International Journal of Plasticity 134 (2020) 102779.
- [28] B. Clausen, D. Brown, C. Tomé, L. Balogh, S. Vogel, Engineering related neutron diffraction measurements probing strains, texture and microstructure, 31st Riso International Symposium on Materials Science. Technical University of Denmark, Riso National Laboratory for Sustainable Energy (2010).
- [29] J. Fernández, J. Lopez-Campos, A. Segade Robleda, J.A. Vilán, A genetic algorithm for the characterization of hyperelastic materials, Applied Mathematics and Computation 329 (2018) 239-250.
- [30] M. Messner, A. Beaudoin, R. Dodds, Consistent crystal plasticity kinematics and linearization for the implicit finite element method, Engineering Computations 32(6) (2015) 1526-1548.
- [31] K. Zhang, B. Holmedal, T. Mánik, A. Saai, Assessment of advanced Taylor models, the Taylor factor and yield-surface exponent for FCC metals, International Journal of Plasticity 114 (2019) 144-160.
- [32] D. Depriester, J.P. Goulmy, L. Barrallier, Crystal Plasticity simulations of in situ tensile tests: A two-step inverse method for identification of CP parameters, and assessment of CPFEM capabilities, International Journal of Plasticity 168 (2023) 103695.
- [33] P.T.N. Nguyen, F. Abbès, J.S. Lecomte, C. Schuman, B. Abbès, Inverse Identification of Single-Crystal Plasticity Parameters of HCP Zinc from Nanoindentation Curves and Residual Topographies, Nanomaterials (Basel) 12(3) (2022).
- [34] J. Wang, W. Jiang, Numerical assessment on fatigue damage evolution of materials at crack tip of CT specimen based on CPFEM, Theoretical and Applied Fracture Mechanics 109 (2020) 102687.
- [35] E. Merson, R. Brydson, A. Brown, The effect of crystallographic orientation on the mechanical properties of titanium, Journal of Physics: Conference Series 126 (2008) 012020.
- [36] M. Dakshinamurthy, K. Kowalczyk-Gajewska, G. Vadillo, Influence of crystallographic orientation on the void growth at the grain boundaries in bi-crystals, International Journal of Solids and Structures 212 (2021) 61-79.
- [37] P. Gasson, Introduction to Aerospace Materials A. P. Mouritz Woodhead Publishing, 80 High Street, Sawston, Cambridge, CB22 3HJ, UK. 2012. 621pp. Illustrated. £55. ISBN 978-1-85573-946-8, The Aeronautical Journal (1968) 117 (2013) 866 - 867.
- [38] H. Ibach, H. Lüth, L. Mihály, D.G. Mandrus, Solid-State Physics: An Introduction to Theory and Experiment, 1991.
- [39] G.F. Bassani, G.L. Liedl, P. Wyder, Encyclopedia of Condensed Matter Physics, 2005.
- [40] M.R. Ahmadi, E. Povoden-Karadeniz, B. Sonderegger, K.I. Öksüz, A. Falahati, E. Kozeschnik, A model for coherency strengthening of large precipitates, Scripta Materialia 84-85 (2014) 47-50.
- [41] S. Gupta, C.A. Bronkhorst, Crystal plasticity model for single crystal Ni-based superalloys: Capturing orientation and temperature dependence of flow stress, International Journal of Plasticity 137 (2021) 102896.

- [42] Z. Wang, O. Muránsky, H. Zhu, T. Wei, A. Sokolova, K. Short, R.N. Wright, On the kinetics of gamma prime ( $\gamma'$ ) precipitation and its strengthening mechanism in Alloy 617 during a long-term thermal aging, *Materialia* 11 (2020) 100682.
- [43] J.M. Fragomeni, B.M. Hillberry, Predicting the precipitation hardening response of particle strengthened alloys hardened by ordered precipitates, American Society of Mechanical Engineers, Pressure Vessels and Piping Division (Publication) PVP 369 (1997) 355-373.
- [44] W. Ren, R.W. Swindeman, Development of a Controlled Material Specification for Alloy 617 for Nuclear Applications, United States, 2005.
- [45] S. Tang, Z. Zheng, L. Ning, Gamma prime coarsening in a nickel base single crystal superalloy, *Materials Letters* 128 (2014) 388-391.
- [46] S. Haribabu, C. Sudha, P. Ganesh, A. Kumar, Interdiffusion Studies in Alloy 617 and 10Cr Steel Joints Using Diffusion Couple Approach and Simulations, *Journal of Phase Equilibria and Diffusion* 45(3) (2024) 621-638.
- [47] S. Kasahara, Y. Inagaki, M. Ogawa, Process flow sheet evaluation of a nuclear hydrogen steelmaking plant applying very high temperature reactors for efficient steel production with less CO<sub>2</sub> emissions, *Nuclear Engineering and Design* 271 (2014) 11-19.
- [48] OECD, N.E. Agency, Advanced Nuclear Reactor Systems and Future Energy Market Needs, 2021.
- [49] C.W. Forsberg, P.F. Peterson, L. Ott, The Advanced High-Temperature Reactor (AHTR) for Producing Hydrogen to Manufacture Liquid Fuels, United States, 2004, p. 13.
- [50] R.N. Wright, Draft ASME Boiler and Pressure Vessel Code Cases and Technical Bases for Use of Alloy 617 for Constructions of Nuclear Component Under Section III, Division 5, United States, 2021, p. Medium: ED; Size: 384 p.
- [51] J. Avila Molina, O. Muránsky, L. Bortolan Neto, J.J. Kruzic, R.N. Wright, Development and performance of data-driven models for the prediction of the high-temperature fatigue life of alloy 617, *International Journal of Pressure Vessels and Piping* 206 (2023) 105022.
- [52] H.-J. Penkalla, H.-H. Over, F. Schubert, Constitutive Equations for the Description of Creep and Creep Rupture Behavior of Metallic Materials at Temperatures Above 800 °C, *Nuclear Technology* 66(3) (1984) 685-692.
- [53] W.D. Callister Jr, D.G. Rethwisch, Materials science and engineering: an introduction, John wiley & sons2020.
- [54] D.E. Sands, Introduction to crystallography, 1975.
- [55] A.G. Jackson, Slip Systems, in: A.G. Jackson (Ed.), *Handbook of Crystallography: For Electron Microscopists and Others*, Springer New York, New York, NY, 1991, pp. 83-88.
- [56] Slip and Dislocations, in: W.F. Hosford (Ed.), *Fundamentals of Engineering Plasticity*, Cambridge University Press, Cambridge, 2013, pp. 83-117.
- [57] D. Hull, D.J. Bacon, Introduction to Dislocations, *American Journal of Physics* 36 (1968) 174-174.
- [58] E. Schmid, W. Boas, Theorien der Kristallplastizität und -festigkeit, in: E. Schmid, W. Boas (Eds.), *Kristallplastizität: Mit Besonderer Berücksichtigung der Metalle*, Springer Berlin Heidelberg, Berlin, Heidelberg, 1935, pp. 279-301.
- [59] Chapter 6 - Experimental Studies of Peierls–Nabarro-type Friction Forces in Metals and Alloys, in: D. Caillard, J.L. Martin (Eds.), *Pergamon Materials Series*, Pergamon2003, pp. 159-224.
- [60] A.F. Bower, Applied mechanics of solids, Boca Raton : Taylor & Francis, Boca Raton, 2010.
- [61] T.-Y. Wu, J. Bassani, C. Laird, Latent Hardening in Single Crystals I. Theory and Experiments, *Proceedings of The Royal Society A: Mathematical, Physical and Engineering Sciences* 435 (1991) 1-19.
- [62] P. Franciosi, M. Berveiller, A. Zaoui, Latent hardening in copper and aluminium single crystals, *Acta Metallurgica* 28(3) (1980) 273-283.

- [63] B. Devincre, L. Kubin, T. Hoc, Physical analyses of crystal plasticity by DD simulations, *Scripta Materialia* 54(5) (2006) 741-746.
- [64] M. Khadyko, S. Dumoulin, G. Cailletaud, O.S. Hopperstad, Latent hardening and plastic anisotropy evolution in AA6060 aluminium alloy, *International Journal of Plasticity* 76 (2016) 51-74.
- [65] C. Gérard, G. Cailletaud, B. Bacroix, Modeling of latent hardening produced by complex loading paths in FCC alloys, *International Journal of Plasticity* 42 (2013) 194-212.
- [66] H. Mecking, Deformation of Polycrystals, in: P. Haasen, V. Gerold, G. Kostorz (Eds.), *Strength of Metals and Alloys*, Pergamon1979, pp. 1573-1594.
- [67] G. Yang, S.-J. Park, Deformation of Single Crystals, Polycrystalline Materials, and Thin Films: A Review, *Materials*, 2019.
- [68] S. Suwas, S. Mondal, Texture Evolution in Severe Plastic Deformation Processes, *MATERIALS TRANSACTIONS* 60(8) (2019) 1457-1471.
- [69] Z. Huang, D. wen, Y. Xu, Q. Guo, Z. Chen, X. Jiang, A. Wang, Y. Li, B. Zhou, X. Hou, B. Wang, Dislocation slips assisted grain rotation and specific texture evolution in a CoCrNi medium entropy alloy, *Materials Science and Engineering: A* 890 (2024) 145897.
- [70] C.J. Smithells, W.F. Gale, T.C. Totemeier, Smithells metals reference book, 1949.
- [71] N. Saba, M. Jawaid, M.T.H. Sultan, 1 - An overview of mechanical and physical testing of composite materials, in: M. Jawaid, M. Thariq, N. Saba (Eds.), *Mechanical and Physical Testing of Biocomposites, Fibre-Reinforced Composites and Hybrid Composites*, Woodhead Publishing2019, pp. 1-12.
- [72] R. Singh, Chapter 11 - Mechanical Properties and Testing of Metals, in: R. Singh (Ed.), *Applied Welding Engineering*, Butterworth-Heinemann, Boston, 2012, pp. 87-94.
- [73] ASTM E 8-11, Standard Test Methods for Tension Testing of Metallic Materials, ASTM International, 2011.
- [74] H. Talebi-Ghadikolaee, H. Moslemi Naeini, M.J. Mirnia, M.A. Mirzai, S. Alexandrov, H. Gorji, Experimental and numerical investigation of failure during bending of AA6061 aluminum alloy sheet using the modified Mohr-Coulomb fracture criterion, *The International Journal of Advanced Manufacturing Technology* 105(12) (2019) 5217-5237.
- [75] D.W. Moon, Considerations on the present state of lüders band studies, *Materials Science and Engineering* 8(4) (1971) 235-243.
- [76] M. Liesegang, P. Lion, T. Beck, M. Gräf, G. Steidl, Investigation of the tensile deformation behaviour in Ni-based superalloy inconel alloy 617 using EBSD-based finite element simulations and optical flow method, *Journal of Materials Science* 58(21) (2023) 8990-9005.
- [77] J. Wright, N. Lybeck, Tensile properties of alloy 617 bar stock, Idaho National Lab.(INL), Idaho Falls, ID (United States), 2013.
- [78] K. Hrutkay, D. Kaoumi, Tensile behavior of inconel 617 vs. Haynes 230: Effects of temperature and strain rate, *Transactions of the American Nuclear Society* 109 (2013) 644-647.
- [79] 21 - Mechanical testing, in: W.F. Gale, T.C. Totemeier (Eds.), *Smithells Metals Reference Book* (Eighth Edition), Butterworth-Heinemann, Oxford, 2004, pp. 21-1-21-23.
- [80] C. Stewart, A. Gordon, Analytical Method to Determine the Tertiary Creep Damage Constants of the Kachanov-Rabotnov Constitutive Model, 2010.
- [81] ASTM E 139-11, Standard Test Methods for conducting Creep, Creep-Rupture, and Stress Rupture Tests of Metallic Materials, ASTM International, 2011.
- [82] A.M.A. Golshan, H. Aroo, M. Azadi, Sensitivity analysis for effects of heat treatment, stress, and temperature on AlSi12CuNiMg aluminum alloy behavior under force-controlled creep loading, *Applied Physics A* 127(1) (2021) 48.
- [83] M. Pfeifer, *Degradation and Reliability of Materials*, 2009, pp. 161-187.

- [84] C. Jang, S.H. Kim, I. Sah, D. Kim, Creep behavior of Alloy 617 in high temperature air and helium environments—effect of oxidation damage, *Journal of Mechanical Science and Technology* 30(10) (2016) 4433-4438.
- [85] J.K. Wright, L.J. Carroll, R.N. Wright, Creep and Creep-Fatigue of Alloy 617 Weldments, Office of Scientific and Technical Information (OSTI), 2014.
- [86] D. Liebschner, P.V. Afonine, M.L. Baker, G. Bunkóczki, V.B. Chen, T.I. Croll, B. Hintze, L.W. Hung, S. Jain, A.J. McCoy, N.W. Moriarty, R.D. Oeffner, B.K. Poon, M.G. Prisant, R.J. Read, J.S. Richardson, D.C. Richardson, M.D. Sammito, O.V. Sobolev, D.H. Stockwell, T.C. Terwilliger, A.G. Urzhumtsev, L.L. Videau, C.J. Williams, P.D. Adams, Macromolecular structure determination using X-rays, neutrons and electrons: recent developments in Phenix, *Acta Crystallogr D Struct Biol* 75(Pt 10) (2019) 861-877.
- [87] C.G. Shull, E.O. Wollan, X-Ray, Electron, and Neutron Diffraction, *Science* 108(2795) (1948) 69-75.
- [88] K. Fucke, J.W. Steed, X-ray and Neutron Diffraction in the Study of Organic Crystalline Hydrates, Water, 2010, pp. 333-350.
- [89] X. Zou, S. Hovmöller, P. Oleynikov, X. Zou, S. Hovmöller, P. Oleynikov, 11 Electron crystallography - an introduction, *Electron Crystallography: Electron Microscopy and Electron Diffraction*, Oxford University Press2011, p. 0.
- [90] R. Macovez, P. Rudolf, Reference Module in Materials Science and Materials Engineering, 2016.
- [91] R. Son, K. Yamazawa, A. Oguchi, M. Suga, M. Tamura, Y. Murakawa, S. Kume, Morphomics via Next-generation Electron Microscopy, 2021.
- [92] B.J. Inkson, 2 - Scanning electron microscopy (SEM) and transmission electron microscopy (TEM) for materials characterization, in: G. Hübschen, I. Altpeter, R. Tschuncky, H.-G. Herrmann (Eds.), *Materials Characterization Using Nondestructive Evaluation (NDE) Methods*, Woodhead Publishing2016, pp. 17-43.
- [93] L.A. Bendersky, F.W. Gayle, Electron Diffraction Using Transmission Electron Microscopy, *J Res Natl Inst Stand Technol* 106(6) (2001) 997-1012.
- [94] R. Kohli, K.L. Mittal, *Developments in Surface Contamination and Cleaning: Detection, Characterization, and Analysis of Contaminants*, 2012.
- [95] L. Tayebi, K. Moharamzadeh, *Biomaterials for Oral and Dental Tissue Engineering*, 2017.
- [96] K. Mo, G. Lovicu, X. Chen, H.-M. Tung, J. Hansen, J. Stubbins, Mechanism of plastic deformation of a Ni-based superalloy for VHTR applications, *Journal of Nuclear Materials* 441 (2013) 695-703.
- [97] A.J. Schwartz, M. Kumar, B.L. Adams, *Electron Backscatter Diffraction in Materials Science*, 2000.
- [98] V. Randle, Electron backscatter diffraction: Strategies for reliable data acquisition and processing, *Materials Characterization* 60(9) (2009) 913-922.
- [99] S.I. Wright, M.M. Nowell, A Review of In Situ EBSD Studies, in: A.J. Schwartz, M. Kumar, B.L. Adams, D.P. Field (Eds.), *Electron Backscatter Diffraction in Materials Science*, Springer US, Boston, MA, 2009, pp. 329-337.
- [100] J.M. F.R. Larson, A Time-temperature Relationship for Rupture and Creep Stresses, *Transactions of ASME* 1952.
- [101] A.M.H. S.S. Manson, U.S.N.A.C.f. Aeronautics, A Linear Time-temperature Relation for Extrapolation of Creep and Stress-rupture Data, National Advisory Committee for Aeronautics1953.
- [102] R.W. Evans, J.D. Parker, B. Wilshire, The  $\theta$  projection concept—A model-based approach to design and life extension of engineering plant, *International Journal of Pressure Vessels and Piping* 50(1) (1992) 147-160.
- [103] P. Ludwik, *Elemente der technologischen Mechanik*, Springer1909.
- [104] E. Voce, The Relationship between Stress and Strain for Homogeneous Deformation, *Journal of the Institute of Metals* 74 (1948) 537-562.
- [105] F.C. Monkman, An empirical relationship between rupture life and minimum creep rate in creep-rupture tests, *Proc of the ASTM*, 1956, pp. 593-620.

- [106] R. Wu, R. Sandstrom, F. Seitis, Influence of Extra Coarse Grains on the Creep Properties of 9 Percent CrMoV (P91) Steel Weldment, *Journal of Engineering Materials and Technology* 126 (2004) 87.
- [107] A. Graham, K. Walles, Relationships between long and short time creep and tensile properties of a commercial alloy, *J. Iron Steel Inst.* 179 (1955) 105-120.
- [108] R. Sandström, *Basic Modeling and Theory of Creep of Metallic Materials*, 2024.
- [109] M. Prager, Development of the MPC Omega Method for Life Assessment in the Creep Range, *Journal of Pressure Vessel Technology* 117(2) (1995) 95-103.
- [110] J.H. Sung, J.H. Kim, R.H. Wagoner, A plastic constitutive equation incorporating strain, strain-rate, and temperature, *International Journal of Plasticity* 26(12) (2010) 1746-1771.
- [111] B. Seisenbacher, G. Winter, F. Grün, Improved Approach to Determine the Material Parameters for a Combined Hardening Model, *Materials Sciences and Applications* 09 (2018) 357-367.
- [112] Q.T. Pham, Y.-S. Kim, Evaluation on Flexibility of Phenomenological Hardening Law for Automotive Sheet Metals, Metals, 2022.
- [113] J. Weertman, Steady-State Creep through Dislocation Climb, *Journal of Applied Physics* 28 (1957) 362-364.
- [114] G.R. Johnson, A constitutive model and data for metals subjected to large strains, high strain rates and high temperatures, *Proceedings of the 7th International Symposium on Ballistics*, The Hague, Netherlands, 1983, 1983.
- [115] T.R.L. Soares, I. Kieliba, M. Azenha, T. Tonnesen, P.B. Lourenço, A theta projection model for compressive creep behaviour of refractories at high temperature: application to alumina-spinel, *Meccanica* 58(12) (2023) 2401-2420.
- [116] B. Vakhshouri, S. Nejadi, Empirical models and design codes in prediction of modulus of elasticity of concrete, *Frontiers of Structural and Civil Engineering* 13(1) (2019) 38-48.
- [117] S. Li, X. Yu, S. Yang, H. Wang, D. Chen, A Micromechanical-Based Semi-Empirical Model for Predicting the Compressive Strength Degradation of Concrete under External Sulfate Attack, *Materials* 16(16) (2023) 5542.
- [118] C.M. Stewart, A.P. Gordon, Strain and Damage-Based Analytical Methods to Determine the Kachanov–Rabotnov Tertiary Creep-Damage Constants, *International Journal of Damage Mechanics* 21(8) (2012) 1186-1201.
- [119] W. Sumelka, T. Łodygowski, Viscoplasticity, in: H. Altenbach, A. Öchsner (Eds.), *Encyclopedia of Continuum Mechanics*, Springer Berlin Heidelberg, Berlin, Heidelberg, 2018, pp. 1-5.
- [120] F.X. Liu, A.C.F. Cocks, E. Tarleton, Dislocation dynamics modelling of the creep behaviour of particle-strengthened materials, *Proceedings of the Royal Society A: Mathematical, Physical and Engineering Sciences* 477(2250) (2021) 20210083.
- [121] O. Sadiku-Agboola, E.R. Sadiku, Chapter 3 - Theoretical Modeling of Nanostructured Formation in Polymer Blends, in: S. Thomas, R. Shanks, S. Chandrasekharakurup (Eds.), *Nanostructured Polymer Blends*, William Andrew Publishing, Oxford, 2014, pp. 33-99.
- [122] N. Moelans, B. Blanpain, P. Wollants, An Introduction to Phase-Field Modeling of Microstructure Evolution, *Calphad* 32 (2008) 268-294.
- [123] S. Wang, W. Zhuang, J. Cao, J. Lin, Chapter 32 - Micro-mechanics Modeling for Micro-forming Processes, in: Y. Qin (Ed.), *Micromanufacturing Engineering and Technology* (Second Edition), William Andrew Publishing, Boston, 2015, pp. 733-748.
- [124] H. Abdolvand, Development of microstructure-sensitive damage models for zirconium polycrystals, *International Journal of Plasticity* 149 (2022) 103156.
- [125] W. Wang, W. Wen, Modeling in Crystal Plasticity: From Theory to Application, in: F.G. Caballero (Ed.), *Encyclopedia of Materials: Metals and Alloys*, Elsevier, Oxford, 2022, pp. 552-560.
- [126] O. Sedaghat, H. Abdolvand, A non-local crystal plasticity constitutive model for hexagonal close-packed polycrystals, *International Journal of Plasticity* 136 (2021) 102883.

- [127] K.-S. Li, R.-Z. Wang, G.-J. Yuan, S.-P. Zhu, X.-C. Zhang, S.-T. Tu, H. Miura, A crystal plasticity-based approach for creep-fatigue life prediction and damage evaluation in a nickel-based superalloy, *International Journal of Fatigue* 143 (2021) 106031.
- [128] F. Roters, P. Eisenlohr, L. Hantcherli, D.D. Tjahjanto, T.R. Bieler, D. Raabe, Overview of constitutive laws, kinematics, homogenization and multiscale methods in crystal plasticity finite-element modeling: Theory, experiments, applications, *Acta Materialia* 58(4) (2010) 1152-1211.
- [129] J. Liu, W. Xiong, A. Behera, S. Thompson, A.C. To, Mean-field polycrystal plasticity modeling with grain size and shape effects for laser additive manufactured FCC metals, *International Journal of Solids and Structures* 112 (2017) 35-42.
- [130] A. Molinari, S. Ahzi, R. Kouddane, On the self-consistent modeling of elastic-plastic behavior of polycrystals, *Mechanics of Materials* 26(1) (1997) 43-62.
- [131] B. Clausen, D.W. Brown, M.A.M. Bourke, T.A. Saleh, S.A. Maloy, In situ neutron diffraction and Elastic–Plastic Self-Consistent polycrystal modeling of HT-9, *Journal of Nuclear Materials* 425(1) (2012) 228-232.
- [132] R.J. Asaro, A. Needleman, Overview no. 42 Texture development and strain hardening in rate dependent polycrystals, *Acta Metallurgica* 33(6) (1985) 923-953.
- [133] D. Peirce, R.J. Asaro, A. Needleman, An analysis of nonuniform and localized deformation in ductile single crystals, *Acta Metallurgica* 30(6) (1982) 1087-1119.
- [134] X. Zhang, V.-T. Phan, C. Oskay, Microstructural creep, fatigue and creep-fatigue modeling of Nickel-based superalloy Inconel 617 at high temperature, 2016.
- [135] G. Venkataramani, K. Kirane, S. Ghosh, Microstructural parameters affecting creep induced load shedding in Ti-6242 by a size dependent crystal plasticity FE model, *International Journal of Plasticity* 24(3) (2008) 428-454.
- [136] X. Zhang, C. Oskay, Polycrystal plasticity modeling of nickel-based superalloy IN 617 subjected to cyclic loading at high temperature, *Modelling and Simulation in Materials Science and Engineering* 24(5) (2016) 055009.
- [137] J. Thomas, M. Groeber, S. Ghosh, Image-based crystal plasticity FE framework for microstructure dependent properties of Ti–6Al–4V alloys, *Materials Science and Engineering: A* 553 (2012) 164-175.
- [138] S. François, M. Schevenels, P. Galvín, G. Lombaert, G. Degrande, A 2.5D coupled FE–BE methodology for the dynamic interaction between longitudinally invariant structures and a layered halfspace, *Computer Methods in Applied Mechanics and Engineering* 199(23) (2010) 1536-1548.
- [139] J.M. Garcia, L.P. Brando, U.O. Costa, J.V. Salgado, L.F. Nunes, A.D.S. Paula, S.N. Monteiro, Experimental creep behavior and life prediction through observation and numerical analysis for AISI 310, *Journal of Materials Research and Technology* 9(1) (2020) 222-229.
- [140] B. Addis, M. Locatelli, F. Schoen, Local optima smoothing for global optimization, *Optimization Methods and Software* 20(4-5) (2005) 417-437.
- [141] A. Grishchenko, A. Semenov, Effective methods of parameter identification for creep models with account of III stage, *MATEC Web of Conferences* 53 (2016) 01041.
- [142] T. Chen, M.C. Messner, Training material models using gradient descent algorithms, *International Journal of Plasticity* 165 (2023) 103605.
- [143] Z. Yang, A.-W. Elgamal, Application of unconstrained optimization and sensitivity analysis to calibration of a soil constitutive model, *International Journal for Numerical and Analytical Methods in Geomechanics* 27 (2003) 1277-1297.
- [144] A. Andrade-Campos, S. Thuillier, P. Philippe, F. Teixeira-Dias, On the determination of material parameters for internal variable thermoelastic–viscoplastic constitutive models, *International Journal of Plasticity* 23 (2007) 1349.

- [145] M. Francisco, S. Revollar, P. Vega, R. Lamanna, A COMPARATIVE STUDY OF DETERMINISTIC AND STOCHASTIC OPTIMIZATION METHODS FOR INTEGRATED DESIGN OF PROCESSES, IFAC Proceedings Volumes 38(1) (2005) 335-340.
- [146] Y. Eren, İ.B. Küçükdemiral, İ. Üstoğlu, Chapter 2 - Introduction to Optimization, in: O. Erdinç (Ed.), Optimization in Renewable Energy Systems, Butterworth-Heinemann, Boston, 2017, pp. 27-74.
- [147] P.A. Vikhar, Evolutionary algorithms: A critical review and its future prospects, 2016 International Conference on Global Trends in Signal Processing, Information Computing and Communication (ICGTSPICC) (2016) 261-265.
- [148] M. Franulović, R. Basan, I. Prebil, Genetic algorithm in material model parameters' identification for low-cycle fatigue, Computational Materials Science 45(2) (2009) 505-510.
- [149] R.N. Greenwell, J.E. Angus, M. Finck, Optimal mutation probability for genetic algorithms, Mathematical and Computer Modelling 21(8) (1995) 1-11.
- [150] A. Hassanat, K. Almohammadi, E.A. Alkafaween, E. Abunawas, A. Hammouri, V.B.S. Prasath, Choosing Mutation and Crossover Ratios for Genetic Algorithms—A Review with a New Dynamic Approach, Information 10(12) (2019) 390.
- [151] Y. Lin, W. Yang, Application of Multi-Objective Genetic Algorithm Based Simulation for Cost-Effective Building Energy Efficiency Design and Thermal Comfort Improvement, Frontiers in Energy Research 6 (2018).
- [152] K. Deb, A. Pratap, S. Agarwal, T. Meyarivan, A fast and elitist multiobjective genetic algorithm: NSGA-II, IEEE Transactions on Evolutionary Computation 6(2) (2002) 182-197.
- [153] M.T.M. Emmerich, A.H. Deutz, A tutorial on multiobjective optimization: fundamentals and evolutionary methods, Natural Computing 17(3) (2018) 585-609.
- [154] J. Branke, K. Deb, H. Dierolf, M. Osswald, Finding Knees in Multi-objective Optimization, in: X. Yao, E.K. Burke, J.A. Lozano, J. Smith, J.J. Merelo-Guervós, J.A. Bullinaria, J.E. Rowe, P. Tiňo, A. Kabán, H.-P. Schwefel (Eds.) Parallel Problem Solving from Nature - PPSN VIII, Springer Berlin Heidelberg, Berlin, Heidelberg, 2004, pp. 722-731.
- [155] X. Gu, G. Sun, G. Li, L. Mao, Q. Li, A comparative study on multiobjective reliable and robust optimization for crashworthiness design of vehicle structure, 2014.
- [156] O. Muránsky, M.N. Tran, W. Payten, On the application of PINN-style physics-regularised neural networks to high-temperature creep rupture life prediction, International Journal of Pressure Vessels and Piping 219 (2026) 105691.
- [157] P.G. Constantine, Active Subspaces: Emerging Ideas for Dimension Reduction in Parameter Studies, Society for Industrial and Applied Mathematics 2015.
- [158] D. Erdal, S. Xiao, W. Nowak, O.A. Cirpka, Sampling behavioral model parameters for ensemble-based sensitivity analysis using Gaussian process emulation and active subspaces, Stochastic Environmental Research and Risk Assessment 34(11) (2020) 1813-1830.
- [159] A.L. Lewis, R.C. Smith, B.J. Williams, Bayesian model calibration on active subspaces, 2017 American Control Conference (ACC), 2017, pp. 3165-3170.
- [160] N. Demo, M. Tezzele, G. Rozza, A supervised learning approach involving active subspaces for an efficient genetic algorithm in high-dimensional optimization problems, SIAM Journal on Scientific Computing 43(3) (2021) B831-B853.
- [161] R.P. Saji, P. Pantidis, L. Svolos, M.E. Mobasher, Multi-stage calibration framework for continuum damage mechanics models, Engineering Fracture Mechanics 326 (2025) 111341.
- [162] H.T. Honório, M. Houben, K. Bisdom, A.v.d. Linden, K.d. Borst, L.J. Sluys, H. Hajibeygi, A multi-step calibration strategy for reliable parameter determination of salt rock mechanics constitutive models, International Journal of Rock Mechanics and Mining Sciences 183 (2024) 105922.

- [163] D.K. Patel, A.M. Waas, Multiscale modeling of tensile fracture in fiber reinforced composites, Composites Part C: Open Access 2 (2020) 100016.
- [164] S. Deng, C. Mora, D. Apelian, R. Bostanabad, Data-Driven Calibration of Multifidelity Multiscale Fracture Models Via Latent Map Gaussian Process, Journal of Mechanical Design 145(1) (2022).
- [165] J. Kudela, R. Matousek, Recent advances and applications of surrogate models for finite element method computations: a review, Soft Computing 26(24) (2022) 13709-13733.
- [166] M.D. McKay, R.J. Beckman, W.J. Conover, A Comparison of Three Methods for Selecting Values of Input Variables in the Analysis of Output from a Computer Code, Technometrics 21(2) (1979) 239.
- [167] F. Provost, D. Jensen, T. Oates, Efficient progressive sampling, ACM.
- [168] C.K.J. Hou, K. Behdinan, Dimensionality Reduction in Surrogate Modeling: A Review of Combined Methods, Data Science and Engineering 7(4) (2022) 402-427.
- [169] D.G. Krige, A statistical approach to some basic mine valuation problems on the Witwatersrand, by D.G. Krige, published in the Journal, December 1951 : introduction by the author, Journal of the Southern African Institute of Mining and Metallurgy 52(9) (1952) 201-203.
- [170] M.D. Buhmann, Radial basis functions, Acta Numerica 9 (2000) 1-38.
- [171] G.E.P. Box, N.R. Draper, Empirical model-building and response surface, John Wiley & Sons, Inc.1986.
- [172] A.I.J. Forrester, A.J. Keane, Recent advances in surrogate-based optimization, Progress in Aerospace Sciences 45(1) (2009) 50-79.
- [173] E. Noh, S. Hong, Finite Element Analysis and Support Vector Regression-Based Optimal Design to Minimize Deformation of Indoor Bicycle Handle Frame Equipped with Monitor, Applied Sciences 12(6) (2022) 2999.
- [174] S. Singh, A. Gupta, Application of support vector regression in predicting thickness strains in hydro-mechanical deep drawing and comparison with ANN and FEM, CIRP Journal of Manufacturing Science and Technology 3 (2010) 66–72.
- [175] G. Weber, M. Pinz, S. Ghosh, Machine Learning-Aided Parametrically Homogenized Crystal Plasticity Model (PHCPM) for Single Crystal Ni-Based Superalloys, JOM 72(12) (2020) 4404-4419.
- [176] S. Walczak, N. Cerpa, Artificial Neural Networks, in: R.A. Meyers (Ed.), Encyclopedia of Physical Science and Technology (Third Edition), Academic Press, New York, 2003, pp. 631-645.
- [177] J. Geiger, W. Wagner, S. Freitag, Multiscale modeling of viscoelastic shell structures with artificial neural networks, Computational Mechanics 76(3) (2025) 541-565.
- [178] D. Montes de Oca Zapiain, H. Lim, T. Park, F. Pourboghrat, Predicting plastic anisotropy using crystal plasticity and Bayesian neural network surrogate models, Materials Science and Engineering: A 833 (2022) 142472.
- [179] M.S. Khorrami, J.R. Mianroodi, N.H. Siboni, P. Goyal, B. Svendsen, P. Benner, D. Raabe, An artificial neural network for surrogate modeling of stress fields in viscoplastic polycrystalline materials, npj Computational Materials 9(1) (2023) 37.
- [180] B.P. van de Weg, L. Greve, M. Andres, T.K. Eller, B. Rosic, Neural network-based surrogate model for a bifurcating structural fracture response, Engineering Fracture Mechanics 241 (2021) 107424.
- [181] L. Borkowski, C. Sorini, A. Chattopadhyay, Recurrent Neural Network-Based Multiaxial Plasticity Model with Regularization for Physics-Informed Constraints, 2021.
- [182] R. Lourenço, A. Andrade-Campos, P. Georgieva, The Use of Machine-Learning Techniques in Material Constitutive Modelling for Metal Forming Processes, Metals, 2022, p. 427.
- [183] T. Kirchdoerfer, M. Ortiz, Data-driven computational mechanics, Computer Methods in Applied Mechanics and Engineering 304 (2016) 81-101.
- [184] S. Avril, M. Bonnet, A.-S. Bretelle, M. Grédiac, F. Hild, P. Ienny, F. Latourte, D. Lemosse, S. Pagano, E. Pagnacco, Overview of identification methods of mechanical parameters based on full-field measurements, Experimental Mechanics 48(4) (2008) 381-402.

- [185] F. Zou, P. Liu, Y. Chen, Y. Zhao, Machine learning-based predictions and analyses of the creep rupture life of the Ni-based single crystal superalloy, *Scientific Reports* 14(1) (2024) 20716.
- [186] S. Ouyang, X. Hu, Q. Wu, J.A. Lee, J.H. Lee, C. Zhang, C. Wang, H.S. Kim, G. Yang, W. Jie, Understanding the creep behaviors and mechanisms of Mg-Gd-Zn alloys via machine learning, *Journal of Magnesium and Alloys* 12(8) (2024) 3281-3291.
- [187] S. Biswas, D. Fernandez Castellanos, M. Zaiser, Prediction of creep failure time using machine learning, *Scientific Reports* 10(1) (2020) 16910.
- [188] B. Ma, X. Wang, G. Xu, J. Xu, J. He, Prediction of Creep Curves Based on Back Propagation Neural Networks for Superalloys, *Materials*, 2022.
- [189] A. Shabani, M. Aminaei, M.R. Toroghinejad, Data-driven prediction of ultimate tensile strength in low alloy steel: A machine learning approach, *Computational Materials Science* 258 (2025) 114045.
- [190] M. Kateb, S. Safarian, Machine learning-driven predictive modeling of mechanical properties in diverse steels, *Machine Learning with Applications* 20 (2025) 100634.
- [191] A. Dorbane, F. Harrou, D.-C. Anghel, Y. Sun, Machine Learning Prediction of Aluminum Alloy Stress–Strain Curves at Variable Temperatures with Failure Analysis, *Journal of Failure Analysis and Prevention* 24(1) (2024) 229-244.
- [192] N. Makke, S. Chawla, Interpretable scientific discovery with symbolic regression: a review, *Artificial Intelligence Review* 57(1) (2024).
- [193] Y. Wang, N. Wagner, J.M. Rondinelli, Symbolic regression in materials science, *MRS Communications* 9(3) (2019) 793-805.
- [194] D. Baraldi, S. Holmström, K.-F. Nilsson, M. Bruchhausen, I. Simonovski, 316L(N) Creep Modeling with Phenomenological Approach and Artificial Intelligence Based Methods, *Metals*, 2021.
- [195] W. Li, Y. Chen, X. Gong, J. Wu, W. Hu, Y. Liu, L. Lian, A new creep prediction model in Ni-based superalloys via data-driven symbolic regression, *Materials Genome Engineering Advances* (2025).
- [196] E. Kabliman, A.H. Kolody, M. Kommenda, G. Kronberger, Prediction of stress-strain curves for aluminium alloys using symbolic regression, *AIP Conference Proceedings* 2113(1) (2019) 180009.
- [197] G. Millner, G. Kronberger, M. Mücke, L. Romaner, D. Scheiber, Comparison of semi-empirical models, symbolic regression, and machine learning approaches for prediction of tensile strength in steels, *International Journal of Engineering Science* 212 (2025) 104247.
- [198] B. Dong, T. Gu, Y. Zhang, H. Proudhon, Y.F. Jia, X.J. Pei, X. Long, F.Z. Xuan, Interpretable prediction of sample size-dependent fatigue crack formation lifetime using deep symbolic regression and polycrystalline plasticity models, *International Journal of Fatigue* 199 (2025) 109057.
- [199] W. Subber, P. Pandita, S. Ghosh, G. Khan, L. Wang, R. Ghanem, Data-based discovery of governing equations, *arXiv preprint arXiv:2012.06036* (2020).
- [200] M.C. Kennedy, A. O'Hagan, Bayesian Calibration of Computer Models, *Journal of the Royal Statistical Society Series B: Statistical Methodology* 63(3) (2001) 425-464.
- [201] J. Choi, O. Muránsky, M.C. Messner, J.J. Kruzic, M.D. McMurtrey, Multi-objective calibration of elastic-viscoplastic models to capture the elevated-temperature creep and tensile behaviour of alloy 617, *International Journal of Pressure Vessels and Piping* 218 (2025) 105566.
- [202] J. Choi, O. Muránsky, M.C. Messner, T. Wei, T. Hu, J.J. Kruzic, M.D. McMurtrey, Multi-Objective Surrogate-Assisted Calibration of CPFEM Models Using Macroscopic Response and In Situ EBSD Measurements of Grain Reorientation Trajectories, *Acta Materialia* (2025) 121809.
- [203] J.K. Wright, Next Generation Nuclear Plant Intermediate Heat Exchanger Materials Research and Development Plan (PLN-2804), Office of Scientific and Technical Information (OSTI), 2008.
- [204] M. Sattar, A.R. Othman, S. Kamaruddin, M. Akhtar, R. Khan, Limitations on the computational analysis of creep failure models: A review, *Engineering Failure Analysis* 134 (2022) 105968.

- [205] J.K. Benz, L.J. Carroll, J.K. Wright, R.N. Wright, T.M. Lillo, Threshold Stress Creep Behavior of Alloy 617 at Intermediate Temperatures, *Metallurgical and Materials Transactions A* 45(7) (2014) 3010-3022.
- [206] M.D. McMurtrey, M.P. Heighes, C.J. Gibson, Results of FY 2023 Alloy 617 and Alloy 709 High-Temperature Crack-Growth Testing, United States, 2023.
- [207] W.-G. Kim, S.-N. Yin, G.-G. Lee, Y.-W. Kim, S.-J. Kim, Creep oxidation behaviour and creep strength prediction for Alloy 617, *International Journal of Pressure Vessels and Piping* 87(6) (2010) 289-295.
- [208] O.D. Sherby, Factors affecting the high temperature strength of polycrystalline solids, *Acta Metallurgica* 10(2) (1962) 135-147.
- [209] H. Altenbach, Y. Gorash, K. Naumenko, Steady-state creep of a pressurized thick cylinder in both the linear and the power law ranges, *Acta Mechanica* 195(1) (2008) 263-274.
- [210] P. Barnes, D. Tabor, J. Walker, The friction and creep of polycrystalline ice, *Proceedings of the Royal Society of London. A. Mathematical and Physical Sciences* 324(1557) (1971) 127-155.
- [211] F. Garofalo, D.B. Butrymowicz, Fundamentals of creep and creep-rupture in metals, American Institute of Physics, 1966.
- [212] J. Dorn, L. Shepard, What we need to know about creep, Symposium on effect of cyclic heating and stressing on metals at elevated temperatures, ASTM International, 1954, pp. 3-30.
- [213] R.L. Orr, O.D. Sherby, J.E. Dorn, Correlations of rupture data for metals at elevated temperatures, Institut of Engineering Research, Univ. of Calif., Berkeley, 1953.
- [214] S.S. Manson, G. Succop, Stress-Rupture Properties of Inconel 700 and Correlation on the Basis of Several Time-Temperature Parameters, in: E. Committee (Ed.) *Symposium on Metallic Materials for Service at Temperatures Above 1600 F*, ASTM International, 1956, p. 0.
- [215] L. Xing, J. Zhao, F.-z. Shen, W. Feng, Reliability analysis and life prediction of HK40 steel during high-temperature exposure, *International journal of pressure vessels and piping* 83(10) (2006) 730-735.
- [216] J. Zhao, S.-q. Han, H.-b. Gao, L. Wang, Remaining life assessment of a CrMoV steel using the Z-parameter method, *International Journal of Pressure Vessels and Piping* 81(9) (2004) 757-760.
- [217] X. Wu, R. Liu, F. Khelfaoui, Creep Phenomena, Mechanisms, and Modeling of Complex Engineering Alloys, *Modelling* 5(3) (2024) 819-840.
- [218] F. Dobeš, K. Milička, The relation between minimum creep rate and time to fracture, *Metal Science* 10(11) (1976) 382-384.
- [219] R. Sandström, Basic model for primary and secondary creep in copper, *Acta Materialia* 60(1) (2012) 314-322.
- [220] J. Blank, K. Deb, Pymoo: Multi-Objective Optimization in Python, *IEEE Access* 8 (2020) 89497-89509.
- [221] M. Cranmer, Interpretable Machine Learning for Science with PySR and SymbolicRegression.jl, 2023.
- [222] X.-C. Zhang, J.-G. Gong, F.-H. Gao, F.-Z. Xuan, An Improved Creep-Fatigue Life Model Involving the Cyclic Softening/Hardening and Stress Relaxation Effect, *Journal of Pressure Vessel Technology* 143(4) (2021).
- [223] N.A. Alang, N.A. Razak, Application of ductility exhaustion based damage model to predict creep rupture time of grade 92 steel, *IOP Conference Series: Materials Science and Engineering* 670(1) (2019) 012001.
- [224] H. Li, F. Larsson, M.H. Colliander, M. Ekh, Elastic-viscoplastic self-consistent modeling for finite deformation of polycrystalline materials, *Materials Science and Engineering: A* 799 (2021) 140325.
- [225] H. Zhang, X. Mao, S. Xu, N. Xiao, N. Zhang, Z. Cui, A physically based elasto-viscoplastic constitutive model for modeling the hot deformation and microstructure evolution of a near  $\alpha$  Ti alloy, *Materials Science and Engineering: A* 872 (2023) 144994.
- [226] J.D. Robson, D. Armstrong, J. Cordell, D. Pope, T.F. Flint, Calibration of constitutive models using genetic algorithms, *Mechanics of Materials* 189 (2024) 104881.
- [227] H. Tran, Q. Du, G. Zhang, Convergence analysis for a nonlocal gradient descent method via directional Gaussian smoothing, *ArXiv abs/2302.06404* (2023).

- [228] NEML: the Nuclear Engineering material Model Library, Argonne National Laboratory, 2024.
- [229] R.A. Lebensohn, A.K. Kanjarla, P. Eisenlohr, An elasto-viscoplastic formulation based on fast Fourier transforms for the prediction of micromechanical fields in polycrystalline materials, International Journal of Plasticity 32-33 (2012) 59-69.
- [230] P. Perzyna, Fundamental Problems in Viscoplasticity, in: G.G. Chernyi, H.L. Dryden, P. Germain, L. Howarth, W. Olszak, W. Prager, R.F. Probstein, H. Ziegler (Eds.), Advances in Applied Mechanics, Elsevier1966, pp. 243-377.
- [231] M. Messner, S. Sham, DRAFT PVP2021-61607 A VISCOPLASTIC MODEL FOR ALLOY 617 FOR USE WITH THE ASME SECTION III, DIVISION 5 DESIGN BY INELASTIC ANALYSIS RULES, 2021.
- [232] A.R. Hartloper, A. De Castro E Sousa, D.G. Lignos, Constitutive Modeling of Structural Steels: Nonlinear Isotropic/Kinematic Hardening Material Model and Its Calibration, Journal of Structural Engineering 147(4) (2021) 04021031.
- [233] F.A. Leckie, D.R. Hayhurst, Constitutive equations for creep rupture, Acta Metallurgica 25(9) (1977) 1059-1070.
- [234] V.-T. Phan, M. Messner, S. Sham, A Unified Engineering Inelastic Model for 316H Stainless Steel, 2019.
- [235] M.C. Messner, V.T. Phan, T.L. Sham, Evaluating and modeling rate sensitivity in advanced reactor structural materials: 316H, Gr. 91, and A617, International Journal of Pressure Vessels and Piping 178 (2019) 103997.
- [236] M.C. Messner, T.-L. Sham, Reference constitutive model for Alloy 617 and 316H stainless steel for use with the ASME Division 5 design by inelastic analysis rules, United States, 2021, p. Medium: ED; Size: 68 p.
- [237] F. Riedlspurger, T. Wojcik, R. Buzolin, G. Zuderstorfer, M. Speicher, C. Sommitsch, B. Sonderegger, Microstructural insights into creep of Ni-based alloy 617 at 700 °C provided by electron microscopy and modelling, Materials Characterization 198 (2023) 112720.
- [238] X. Wang, L. Xu, L. Jiao, J. Mei, Y. Zhao, L. Qiao, Microstructure evolution during aging and its effect on mechanical properties of a novel nano-carbide dispersion strengthened steel, Materials Science and Engineering: A 928 (2025) 148064.
- [239] T.-H. Feng, X.-F. Xie, Y. Liu, J.-L. Qu, S.-M. Lyu, J.-H. Du, J.-J. Ruan, L.-L. Zhu, Effects of Solution Treatment on Microstructure Evolution and the Mechanical Properties of GH4780 Superalloy, Materials, 2025.
- [240] S. Zheng, H. Yu, X. Tang, J. Zhou, C. Lu, Y. Li, Y. He, Z. Gao, Effect of phase transformation on the high-temperature tensile behaviors of SA508 Gr. 3 steel: A crystal plasticity finite element investigation, Nuclear Engineering and Design 438 (2025) 114070.
- [241] J.J. Skrzypek, Material Damage Models for Creep Failure Analysis and Design of Structures, Springer Vienna, Vienna, 1999, pp. 97-166.
- [242] C. Gierden, J. Kochmann, J. Waimann, B. Svendsen, S. Reese, A Review of FE-FFT-Based Two-Scale Methods for Computational Modeling of Microstructure Evolution and Macroscopic Material Behavior, Archives of Computational Methods in Engineering 29(6) (2022) 4115-4135.
- [243] L. Minfei, G. Yidong, C. Ze, W. Zhi, S. Erik, Š. Branko, Microstructure-informed deep convolutional neural network for predicting short-term creep modulus of cement paste, Cement and Concrete Research 152 (2022) 106681.
- [244] G. Weber, M. Pinz, S. Ghosh, Machine learning-enabled self-consistent parametrically-upscaled crystal plasticity model for Ni-based superalloys, Computer Methods in Applied Mechanics and Engineering 402 (2022) 115384.
- [245] T. Hu, H.H.J. Choi, M.C. Messner, A mechanistic model for creep and thermal aging in Alloy 709, United States, 2023, p. Medium: ED; Size: 56 p.
- [246] A. Aburakhia, A. Bonakdar, M. Molavi-Zarandi, J. Kelleher, H. Abdolvand, Deformation mechanisms of additively manufactured Hastelloy-X: A neutron diffraction experiment and crystal plasticity finite element modeling, Materials and Design 222 (2022) 111030.

- [247] H. Abdolvand, M.R. Daymond, Internal strain and texture development during twinning: Comparing neutron diffraction measurements with crystal plasticity finite-element approaches, *Acta Materialia* 60(5) (2012) 2240-2248.
- [248] S.R. Agnew, D.W. Brown, C.N. Tomé, Validating a polycrystal model for the elastoplastic response of magnesium alloy AZ31 using in situ neutron diffraction, *Acta Materialia* 54(18) (2006) 4841-4852.
- [249] E. Mengiste, D. Piedmont, M.C. Messner, M. Li, J. Stubbins, J.-S. Park, X. Zhang, M. Kasemer, Effect of irradiation-induced strength anisotropy on the reorientation trajectories and fragmentation behavior of grains in BCC polycrystals under tensile loading, *Acta Materialia* 263 (2024) 119503.
- [250] Y.-c. Shao, T. Tang, D. Li, W. Tang, Y. Peng, Crystal plasticity finite element modelling of the extrusion texture of a magnesium alloy, *Modelling and Simulation in Materials Science and Engineering* 23 (2015).
- [251] F. Lin, M. Giannetta, M. Jugle, S. Couper, B. Dunleavy, L. Miyagi, *Texture Development and Stress–Strain Partitioning in Periclase + Halite Aggregates*, Minerals, 2019.
- [252] O. Ibragimova, A. Brahme, W. Muhammad, J. Lévesque, K. Inal, A new ANN based crystal plasticity model for FCC materials and its application to non-monotonic strain paths, *International Journal of Plasticity* 144 (2021) 103059.
- [253] P. Acar, Crystal Plasticity Model Calibration for Ti-7Al Alloy with a Multi-fidelity Computational Scheme, *Integrating Materials and Manufacturing Innovation* 7(4) (2018) 186-194.
- [254] S. Hwang, S.-K. Choi, Deep learning-based surrogate modeling via physics-informed artificial image (PiAI) for strongly coupled multidisciplinary engineering systems, *Knowledge-Based Systems* 232 (2021) 107446.
- [255] C. Bonatti, B. Berisha, D. Mohr, From CP-FFT to CP-RNN: Recurrent neural network surrogate model of crystal plasticity, *International Journal of Plasticity* 158 (2022) 103430.
- [256] H. Dorward, D.M. Knowles, E. Demir, M. Mostafavi, M.J. Peel, Calibration and surrogate model-based sensitivity analysis of crystal plasticity finite element models, *Materials & Design* 247 (2024) 113409.
- [257] F. Niessen, T. Nyssönen, A.A. Gazder, R. Hielscher, Parent grain reconstruction from partially or fully transformed microstructures in <i>MTEX</i>, *Journal of Applied Crystallography* 55(1) (2022) 180-194.
- [258] Coreform Cubit, Coreform LLC, Orem, UT, 2022.
- [259] A.N. Laboratory, DEER, 2022.
- [260] C. Permann, D. Gaston, D. Andrs, R. Carlsen, F. Kong, A. Lindsay, J. Miller, J. Peterson, A. Slaughter, R. Stogner, R. Martineau, MOOSE: Enabling Massively Parallel Multiphysics Simulation, 2019.
- [261] J. Mandel, Generalisation de la theorie de plasticite de W. T. Koiter, *International Journal of Solids and Structures* 1(3) (1965) 273-295.
- [262] A. Ma, F. Roters, D. Raabe, A dislocation density based constitutive model for crystal plasticity FEM including geometrically necessary dislocations, *Acta Materialia* 54(8) (2006) 2169-2179.
- [263] H. Mecking, U. Kocks, Kinetics of flow and strain-hardening, *Acta metallurgica* 29(11) (1981) 1865-1875.
- [264] A. Alankar, I.N. Mastorakos, D.P. Field, A dislocation-density-based 3D crystal plasticity model for pure aluminum, *Acta Materialia* 57(19) (2009) 5936-5946.
- [265] R.J. Asaro, Micromechanics of Crystals and Polycrystals, in: J.W. Hutchinson, T.Y. Wu (Eds.), *Advances in Applied Mechanics*, Elsevier1983, pp. 1-115.
- [266] G.I. Taylor, The Spectrum of Turbulence, *Proceedings of the Royal Society of London. Series A, Mathematical and Physical Sciences* 164(919) (1938) 476-490.
- [267] H.J. Bunge, Some applications of the Taylor theory of polycrystal plasticity, *Kristall und Technik* 5(1) (1970) 145-175.
- [268] U.F. Kocks, The relation between polycrystal deformation and single-crystal deformation, *Metallurgical and Materials Transactions* 1(5) (1970) 1121-1143.
- [269] S. Alkan, A. Ojha, H. Sehitoglu, Determination of latent hardening response for FeNiCoCrMn for twin-twin interactions, *Acta Materialia* 147 (2018) 149-164.

- [270] M. Zecevic, M. Knezevic, Latent hardening within the elasto-plastic self-consistent polycrystal homogenization to enable the prediction of anisotropy of AA6022-T4 sheets, International Journal of Plasticity 105 (2018) 141-163.
- [271] Y. Wu, M. Bönisch, S. Alkan, W. Abuzaid, H. Sehitoglu, Experimental determination of latent hardening coefficients in FeMnNiCoCr, International Journal of Plasticity 105 (2018) 239-260.
- [272] C. Gérard, B. Bacroix, M. Bornert, G. Cailletaud, J. Crépin, S. Leclercq, Hardening description for FCC materials under complex loading paths, Computational Materials Science 45(3) (2009) 751-755.
- [273] A. Paszke, S. Gross, S. Chintala, G. Chanan, E. Yang, Z. DeVito, Z. Lin, A. Desmaison, L. Antiga, A. Lerer, Automatic differentiation in PyTorch, 2017.
- [274] G. Manache, C. Melching, SENSITIVITY OF LATIN HYPERCUBE SAMPLING TO SAMPLE SIZE AND DISTRIBUTIONAL ASSUMPTIONS, 2007.
- [275] S. Tripoppoom, W. Yu, K. Sepehrnoori, J. Miao, Chapter 2 - Methodology, in: S. Tripoppoom, W. Yu, K. Sepehrnoori, J. Miao (Eds.), Assisted History Matching for Unconventional Reservoirs, Gulf Professional Publishing2021, pp. 17-35.
- [276] M. Vorechovsky, Hierarchical Refinement of Latin Hypercube Samples, Computer-Aided Civil and Infrastructure Engineering (2014) accepted.
- [277] X. Long, Z. Shen, Q. Jia, J. Li, R. Dong, Y. Su, X. Yang, K. Zhou, Determine the unique constitutive properties of elastoplastic materials from their plastic zone evolution under nanoindentation, Mechanics of Materials 175 (2022) 104485.
- [278] H. Abdolvand, M.R. Daymond, C. Mareau, Incorporation of twinning into a crystal plasticity finite element model: Evolution of lattice strains and texture in Zircaloy-2, International Journal of Plasticity 27(11) (2011) 1721-1738.
- [279] E. Barbero, G. Sgambitterra, A. Adumitroaie, X. Martinez, A discrete constitutive model for transverse damage of symmetric laminates with arbitrary stacking sequence, Composite Structures 93 (2011) 1021-1030.
- [280] B. Chen, K. Lutker, J. Lei, J. Yan, S. Yang, H.-k. Mao, Detecting grain rotation at the nanoscale, Proceedings of the National Academy of Sciences of the United States of America 111 (2014).
- [281] C. Qiu, M. Salvalaglio, D.J. Srolovitz, J. Han, Disconnection flow-mediated grain rotation, Proc Natl Acad Sci U S A 121(1) (2024) e2310302121.
- [282] M. Shahmardani, N. Vajragupta, A. Hartmaier, Influence of Crystal Plasticity Parameters on the Strain Hardening Behavior of Polycrystals, Crystals 11(12) (2021) 1473.
- [283] T. Diehl, Modeling of elastic-viscoplastic bahavior and its finite element implementation, 1988.
- [284] X. Wang, F. Cazes, J. Li, A. Hocini, K. Ameyama, G. Dirras, A 3D crystal plasticity model of monotonic and cyclic simple shear deformation for commercial-purity polycrystalline Ti with a harmonic structure, Mechanics of Materials 128 (2019) 117-128.

# Appendix A

## Supplementary materials for Chapter 4

### Appendix A.1. Material parameters of empirical models

Table A.1 summarises the adjustable constitutive material parameters for the selected empirical minimum creep rate, time-to-failure, strain-to-failure, and strain-time response models. The table also contains information about the lower and upper bounds set for each parameter during their optimisations. Note that these bounds were adjusted for normalised stress and temperature values (i.e.,  $\hat{\sigma}$  and  $\hat{T}$ ).

Table A.1. Summary of adjustable constitutive parameters for empirical creep models.

Response	Model	Parameter	Symbol	Units	Lower Bound	Upper Bound
Minimum creep rate	Norton-Arrhenius [208]	Pre-exponential factor	$A_{NA}$	$\text{MPa}^{-n_{NA}} \cdot \text{s}^{-1}$	0	$10^6$
		Stress sensitivity	$n_{NA}$	—	0	10
		Activation energy	$Q_{NA}$	$\text{J} \cdot \text{mol}^{-1}$	0	1000
	Altenbach-Arrhenius [209]	Pre-exponential factor	$A_{AA}$	$\text{MPa}^{-1} \cdot \text{s}^{-1}$	0	$10^6$
		Stress scale factor	$B_{AA}$	$\text{MPa}^{-1}$	0	10
		Stress sensitivity	$n_{AA}$	—	0	10
		Activation energy	$Q_{AA}$	$\text{J} \cdot \text{mol}^{-1}$	0	1000
	Garafalo-Arrhenius [210]	Pre-exponential factor	$A_{GA}$	$\text{s}^{-1}$	0	1000
		Stress scale factor	$\beta_{GA}$	$\text{MPa}^{-1}$	0	10
		Stress sensitivity	$n_{GA}$	—	0	10
		Activation energy	$Q_{GA}$	$\text{J} \cdot \text{mol}^{-1}$	0	1000
Time-to-failure	Monkman-Grant [105]	Material constant	$c_{MG}$	—	0	1000
		Creep rate exponent	$m_{MG}$	—	0	1
	Dorn-Shepherd [212]	Pre-exponential factor	$D_{DS}$	$\text{MPa}^{n_{DS}} \cdot \text{s}$	0	0.1
		Stress sensitivity	$n_{DS}$	—	0	10
		Activation energy	$Q_{DS}$	$\text{J} \cdot \text{mol}^{-1}$	0	1000
	Larson-Miller [100, 215, 216]	Log-stress coefficient	$a_{LM}$	$^{\circ}\text{C}$	0	10
		Linear-stress coefficient	$b_{LM}$	$^{\circ}\text{C} \cdot \text{MPa}^{-1}$	0	10
		Intercept coefficient	$c_{LM}$	$^{\circ}\text{C}$	0	100
		Larson-Miller constant	$C_{LM}$	—	0	10
Strain-to-failure	Dobes [218]	Material constant	$c_{Do}$	—	0	1
		Creep rate exponent	$m_{Do}$	—	0	2
	Evans [102]	Intercept coefficient	$a_{Ev}$	—	-1	1
		Stress coefficient	$b_{Ev}$	$\text{MPa}^{-1}$	-1	1
		Temperature coefficient	$c_{Ev}$	$^{\circ}\text{C}^{-1}$	-1	1

		Stress–temperature coefficient	$d_{Ev}$	$^{\circ}\text{C}^{-1} \cdot \text{MPa}^{-1}$	-1	1
Soares [115]	Intercept coefficient	$a_{So}$	—	—	-1	1
	Temperature coefficient	$b_{So}$	$^{\circ}\text{C}$	—	-1	1
	Stress–temperature coefficient	$c_{So}$	$^{\circ}\text{C} \cdot \text{MPa}^{-1}$	—	-1	1
	Log-temperature coefficient	$d_{So}$	—	—	-1	1
	Stress coefficient	$e_{So}$	$\text{MPa}^{-1}$	—	-1	1
Omega [109]	Primary accelerator	$\Omega_{1,0m}$	$\text{s}^{-1}$	0	1	
	Primary decay	$\Omega_{2,0m}$	—	0	10	
	Tertiary accelerator	$\Omega_{3,0m}$	$\text{s}^{-1}$	0	1	
	Tertiary decay	$\Omega_{4,0m}$	—	0	10	
	Pre-exponential factor	$A_{i,0m}$	$\text{MPa}^{-n_{i,0m}} \cdot \text{s}^{-1} (i = 1,3)$ $\text{MPa}^{-n_{i,0m}} (i = 2,4)$	0	100	
	Stress sensitivity	$n_{i,0m}$	—	0	1	
	Activation energy	$Q_{i,0m}$	$\text{J} \cdot \text{mol}^{-1}$	0	100	
Strain–time	Primary scale	$\phi_{1,Ph}$	$\text{s}^{-1}$	0	1	
	Primary exponent	$\phi_{2,Ph}$	—	0	1	
	Tertiary scale	$\phi_{3,Ph}$	$\text{s}^{-1}$	0	1	
	Tertiary exponent	$\phi_{4,Ph}$	—	0	1	
	Pre-exponential factor	$A_{i,Ph}$	$\text{MPa}^{-n_{i,Ph}} \cdot \text{s}^{-1} (i = 1,3)$ $\text{MPa}^{-n_{i,Ph}} (i = 2,4)$	0	1000	
	Stress sensitivity	$n_{i,Ph}$	—	0	10	
	Activation energy	$Q_{i,Ph}$	$\text{J} \cdot \text{mol}^{-1}$	0	1000	
Theta projection [12, 13, 102]	Primary amplitude	$\theta_{1,TP}$	—	0	1	
	Primary rate sensitivity	$\theta_{2,TP}$	$\text{s}^{-1}$	0	100	
	Tertiary amplitude	$\theta_{3,TP}$	—	0	1	
	Tertiary rate sensitivity	$\theta_{4,TP}$	$\text{s}^{-1}$	0	10	
	Intercept coefficient	$a_{i,TP}$	—	-100	100	
	Stress coefficient	$b_{i,TP}$	$\text{MPa}^{-1}$	-200	200	
	Temperature coefficient	$c_{i,TP}$	$^{\circ}\text{C}^{-1}$	-100	100	
	Stress–temperature coefficient	$d_{i,TP}$	$^{\circ}\text{C}^{-1} \cdot \text{MPa}^{-1}$	-200	200	

## Appendix A.2. Alternate symbolic regression approaches

Symbolic regression (SR) was applied to discover alternative constitutive expressions to predict the minimum creep rate, time-to-failure, and log-transformed strain-to-failure of Alloy 617. The results are presented in Figure

A.1, with the top row comparing the experimental and simulated values, and the bottom row showing the discovered expressions.

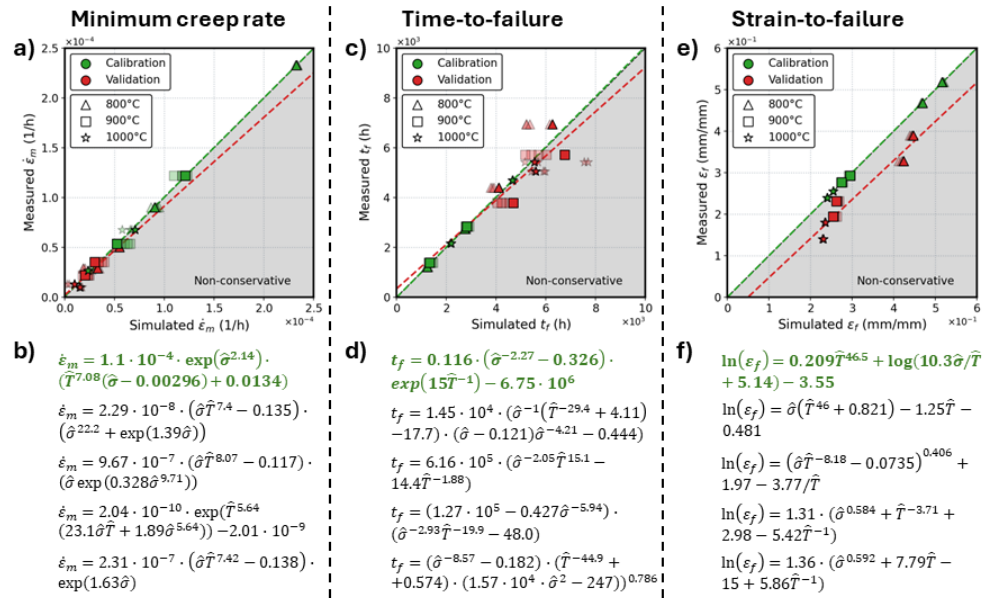


Figure A.1. Supplementary calibration and validation results for the symbolic regression (SR) models in predicting the minimum creep rate, time-to-failure, and log-transformed strain-to-failure across five independent runs. Plots a), c), and e) compare the experimental and simulated values for the calibration (green) and validation (red) datasets, with the dashed lines representing the line of best fit (LOBF) corresponding to the run that achieved the lowest objective value. Panels b), d), and f) show the SR-derived constitutive expressions with the best-performing expression highlighted in green.

### Appendix A.3. Regular strain–time predictions from empirical models

The empirical phi and theta projection models were calibrated using a two-stage calibration approach to capture the regular strain–time response of Alloy 617. The calibration and validation results for the phi and theta projection models are presented in Figure A.2 and Figure A.3, respectively.

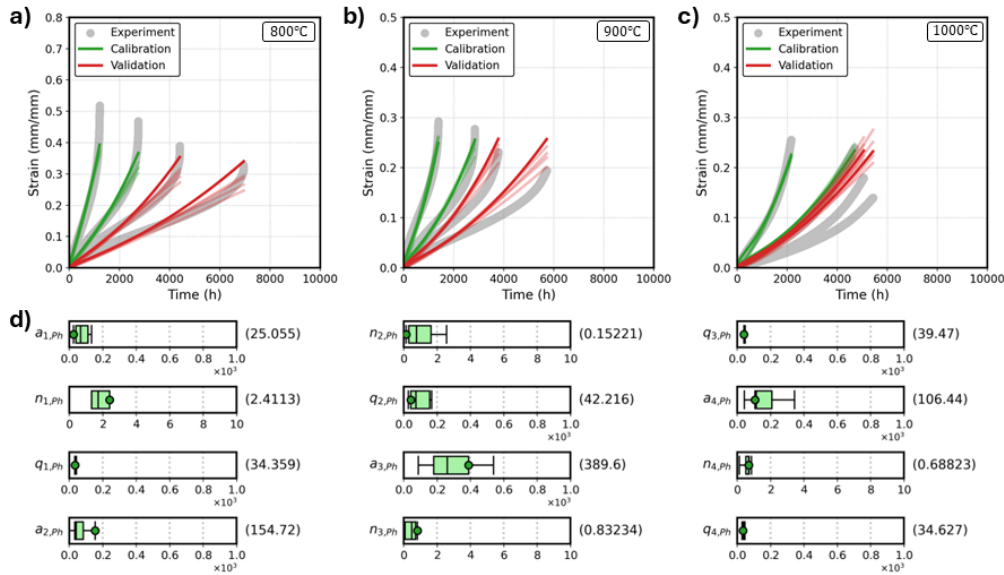


Figure A.2. Calibration and validation results for the phi model in predicting the regular strain–time response across five independent runs. Plots a), b), and c) compare the experimental and simulated strain–time curves at 800°C, 900°C, and 1000°C, respectively, for the calibration (green) and validation (red) datasets. Panels d), e), and f) show the model’s parameter distributions, with the mean (black line), standard deviation (box), range (whiskers), bounds (limits), and best-performing values (green circle and number).

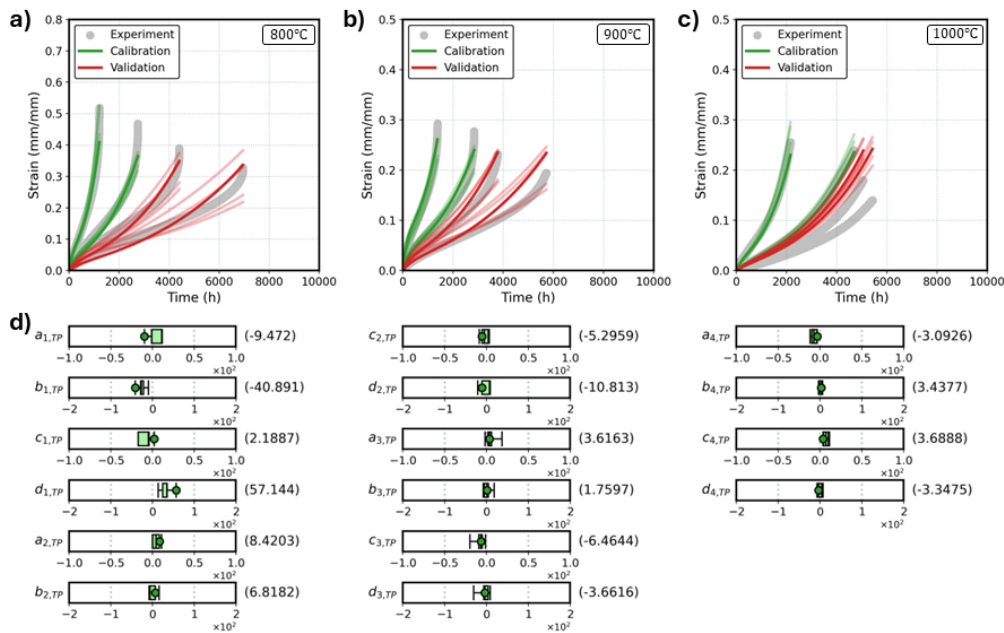


Figure A.3. Calibration and validation results for the theta projection model in predicting the regular strain–time response across five independent runs. Plots a), b), and c) compare the experimental and simulated strain–time curves at 800°C, 900°C, and 1000°C, respectively, for the calibration (green) and validation (red) datasets. Panels d), e), and f) show the model’s parameter distributions, with the mean (black line), standard deviation (box), range (whiskers), bounds (limits), and best-performing values (green circle and number).

#### Appendix A.4. Mechanism-shifted strain–time predictions from empirical models

The empirical phi and theta projection models were also calibrated to capture the mechanism-shifted strain–time response of Alloy 617. The calibration and validation results for the phi and theta projection models are presented in Figure A.4 and Figure A.5, respectively.

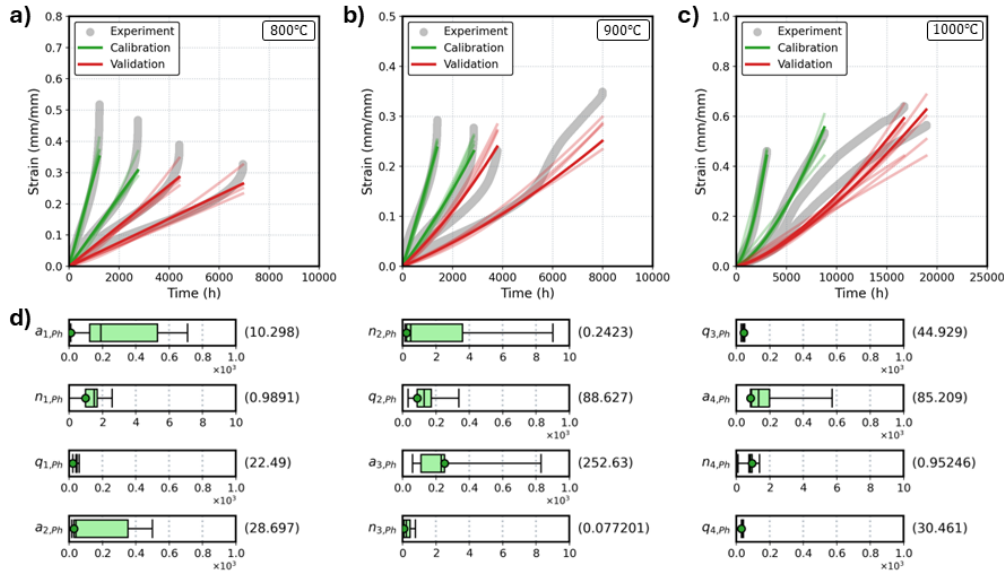


Figure A.4. Calibration and validation results for the phi model in predicting the mechanism-shifted strain–time response across five independent runs. Plots a), b), and c) compare the experimental and simulated strain–time curves at 800°C, 900°C, and 1000°C, respectively, for the calibration (green) and validation (red) datasets. Panels d), e), and f) show the model's parameter distributions, with the mean (black line), standard deviation (box), range (whiskers), bounds (limits), and best-performing values (green circle and number).

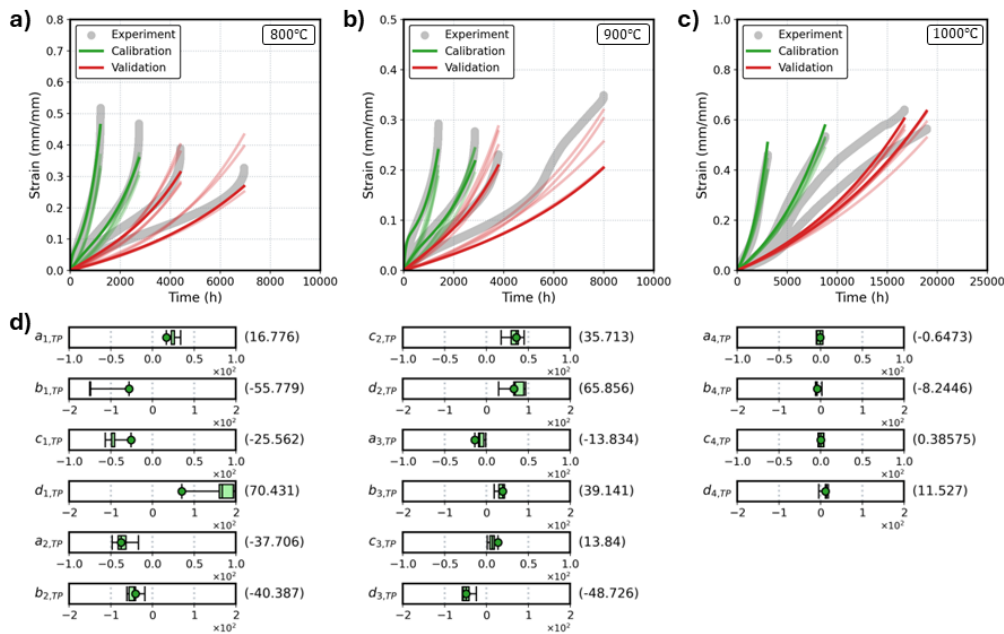


Figure A.5. Calibration and validation results for the theta projection model in predicting the mechanism-shifted strain–time response across five independent runs. Plots a), b), and c) compare the experimental and simulated strain–time curves at 800°C, 900°C, and 1000°C, respectively, for the calibration (green) and validation (red) datasets. Panels d), e), and f) show the model’s parameter distributions, with the mean (black line), standard deviation (box), range (whiskers), bounds (limits), and best-performing values (green circle and number).

# Appendix B

## Supplementary materials for Chapter 5

### Appendix B.1. Material parameter of elastic-viscoplastic models

Table B.1 summarises the material parameters for the semi-empirical elastic-viscoplastic model (EVP), creep damage (CD), and work damage (WD) models. The table also contains information about the lower and upper bounds set for each material parameter during the multi-objective genetic algorithm (MOGA) optimisations.

Table B.1. Summary of material parameters for EVP, EVP-CD, and EVP-WD models.

Material Model	Parameter	Symbol	Lower Bound	Upper Bound	Units
Elastic-viscoplastic (EVP)	Initial yield stress	$\sigma_{y,0}$	0.0	100	MPa
	Isotropic hardening stress	$R_{VIH}$	0.0	1000	MPa
	Isotropic hardening modulus	$d_{VIH}$	0.0	100	—
	Flow surface exponent	$n_{PF}$	0.0	100	—
	Viscoplastic fluidity	$\eta_{PF}$	0.0	10000	MPa
Creep damage (CD)	Stress prefactor	$A_{CD}$	0.0	10000	MPa
	Stress power law exponent	$\xi_{CD}$	0.0	100	—
	Damage power law exponent	$\phi_{CD}$	0.0	100	—
Work damage (WD)	Creep critical work gradient	$A_{WD}$	0.0	1000	s
	Creep critical work intercept	$a_{WD}$	0.0	1000	MPa/s
	Tensile critical work gradient	$B_{WD}$	0.0	1000	s
	Tensile critical work intercept	$b_{WD}$	0.0	1000	MPa/s
	Creep damage exponent	$\alpha_{WD}$	0.0	100	—
	Tensile damage exponent	$\beta_{WD}$	0.0	100	—

### Appendix B.2. Functions for work density and damage exponent

The critical plastic work density ( $W_{crit}$ ) describes the minimum amount of work required to initiate dislocation movement in a material, while the plastic work density rate ( $\dot{W}$ ) is the rate at which energy is expended during plastic deformation. The respective definitions for the critical work density and work density rate are shown in Eqs. (52) and (53), where  $\sigma$  represents stress,  $\varepsilon$  represents strain, and  $\varepsilon_f$  represents the strain-to-failure.

$$W_{crit} = \int_0^{\varepsilon_f} \boldsymbol{\sigma} : d\boldsymbol{\varepsilon}_{vp} \quad (52)$$

$$\dot{W} = \boldsymbol{\sigma} : \dot{\boldsymbol{\varepsilon}}_{vp} \quad (53)$$

The critical work density function is based on the relationship between the critical work density and average work density rate in the INL-provided experimental creep and tensile data of Alloy 617. After removing the effects of oxidation from the affected creep curves (see Section 4.2), the critical work density was plotted against the average work density rate of the experimental data, as shown in Figure B.1. The data points in Figure B.1 suggest independent linear relationships between the critical work density and the logarithmic average work density rate for the creep and tensile data. Notably, the tensile line of best fit is shown to have a higher gradient and higher intercept than the creep line of best fit.

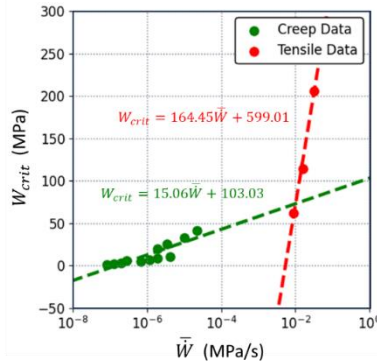


Figure B.1. Critical plastic work density and logarithmic average plastic work density rate of experimental creep and tensile data of Alloy 617; the creep and tensile relationships are represented in green and red, respectively.

To simulate the experimentally observed relationship in Figure B.1, the critical work density is defined as a bilinear function. The definition is shown in Eqs. (54), (55), and (56), where  $A_{WD}$  and  $a_{WD}$  define the linear relationship for creep behaviour and  $B_{WD}$  and  $b_{WD}$  define the linear relationship for tensile behaviour. The  $\lambda_1$  term represents the work density rate threshold where the critical work density begins to asymptotically approach zero, and the  $\lambda_2$  term represents the intersection of the creep line and tensile line. Note that the exponential decay term (when  $\log_{10}(\dot{W}) < \lambda_1$ ) was introduced to ensure that  $W_{crit} \rightarrow 0$  as  $\dot{W} \rightarrow 0$ .

$$W_{crit} = \begin{cases} A_{WD} e^{\log_{10}(\dot{W}) - \lambda_1}, & \log_{10}(\dot{W}) < \lambda_1 \\ A_{WD} \log_{10}(\dot{W}) + a_{WD}, & \lambda_1 \leq \log_{10}(\dot{W}) < \lambda_2 \\ B_{WD} \log_{10}(\dot{W}) + b_{WD}, & \lambda_2 \leq \log_{10}(\dot{W}) \end{cases} \quad (54)$$

$$\lambda_1 = 1.0 - a_{WD}/A_{WD} \quad (55)$$

$$\lambda_2 = \frac{b_{WD} - a_{WD}}{A_{WD} - B_{WD}} \quad (56)$$

The damage exponent ( $n_d$ ) is defined as a step function of the work density rate ( $\dot{W}$ ), such that the value of the damage exponent is dependent on the loading configuration (i.e., creep or tensile). The damage exponent function is defined in Eqs. (57) and (58), where  $\alpha_{WD}$  represents the creep damage exponent,  $\beta_{WD}$  represents the tensile damage exponent, and  $\delta$  represents a sinusoidal function that smoothly transitions between the  $\alpha_{WD}$  and  $\beta_{WD}$  values. Additionally,  $\gamma$  represents some small value that controls the speed of the transition; in this study,  $\gamma$  is set to 0.5.

$$n_d = \begin{cases} \alpha_{WD}, & \log_{10}(\dot{W}) < \lambda_2 - \gamma \\ \delta, & \lambda_2 - \gamma \leq \log_{10}(\dot{W}) < \lambda_2 + \gamma \\ \beta_{WD}, & \lambda_2 + \gamma \leq \log_{10}(\dot{W}) \end{cases} \quad (57)$$

$$\delta = \frac{\beta_{WD} - \alpha_{WD}}{2} \cdot \sin\left(\frac{\pi}{2\gamma} (\log_{10}(\dot{W}) - \lambda_2)\right) + \frac{\alpha_{WD} + \beta_{WD}}{2} \quad (58)$$

Schematics illustrating the critical work density ( $W_{crit}$ ) function and the damage exponent ( $n_d$ ) function are shown in Figure B.2.

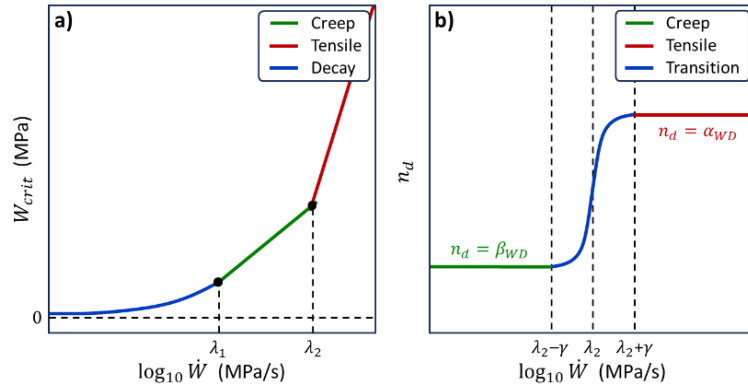


Figure B.2. Schematics of a) critical plastic work density and the b) damage exponent the piecewise functions.

### Appendix B.3. Calibration results at 900°C and 1000°C

Figure B.3 and Figure B.4 show the results of the three-stage calibration process on the EVP-CD model at 900°C and 1000°C, respectively. Similarly, Figure B.5 and Figure B.6 show the results of the calibration process on the EVP-WD model at 900°C and 1000°C, respectively.

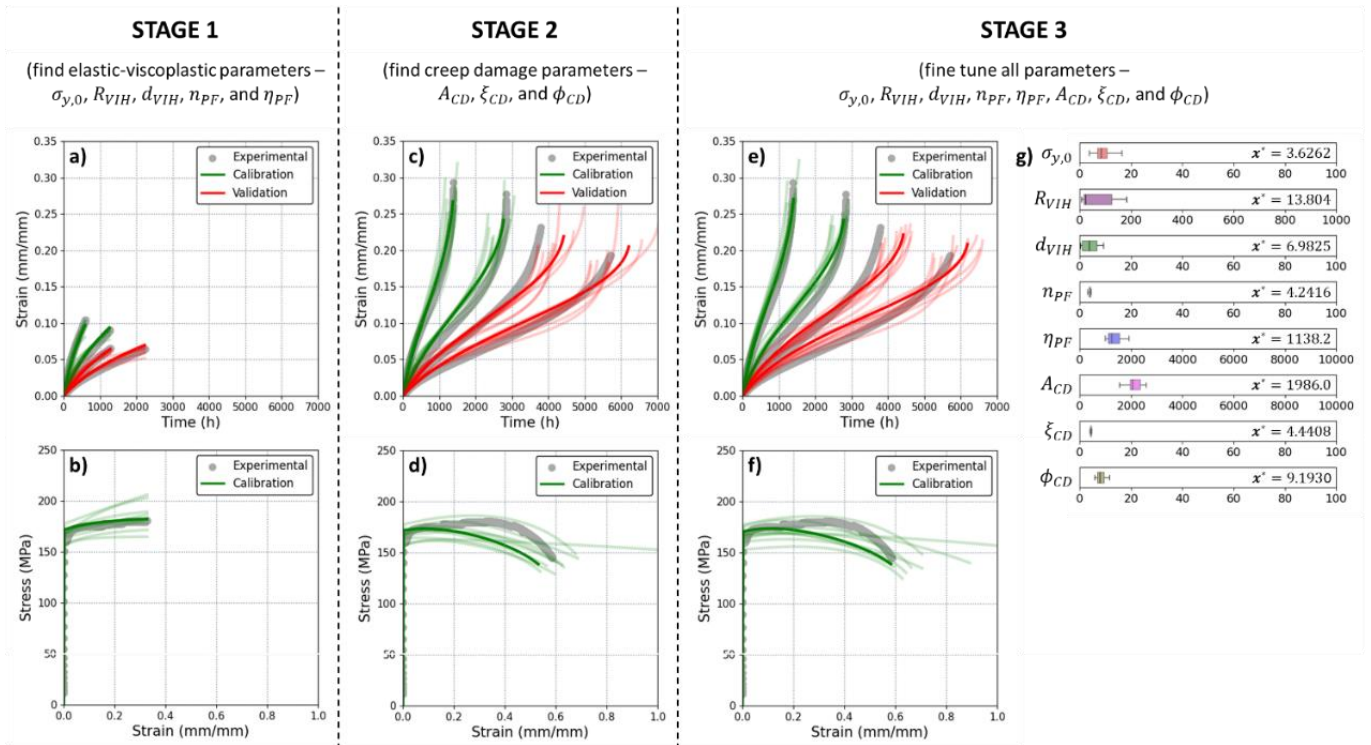


Figure B.3. Calibration results for the EVP-CD model at 900°C, calibrated with short-term creep curves (36MPa and 31MPa) and tensile curve, and validated with longer-term creep curves (28MPa and 26MPa). The top row of plots (a, c, e) shows the creep results while the bottom row of plots (b, d, and f) shows the tensile results after stages 1, 2, and 3. The experimental datasets are in grey, the simulated curves used for calibration are in green, and the simulated curves used for validation are in red. The boxplots (g) show the distribution of the found parameters, where  $x^*$  represents the optimal parameter value, the vertical line represents the mean, the boxes represent the standard deviations, and the whiskers represent the ranges.

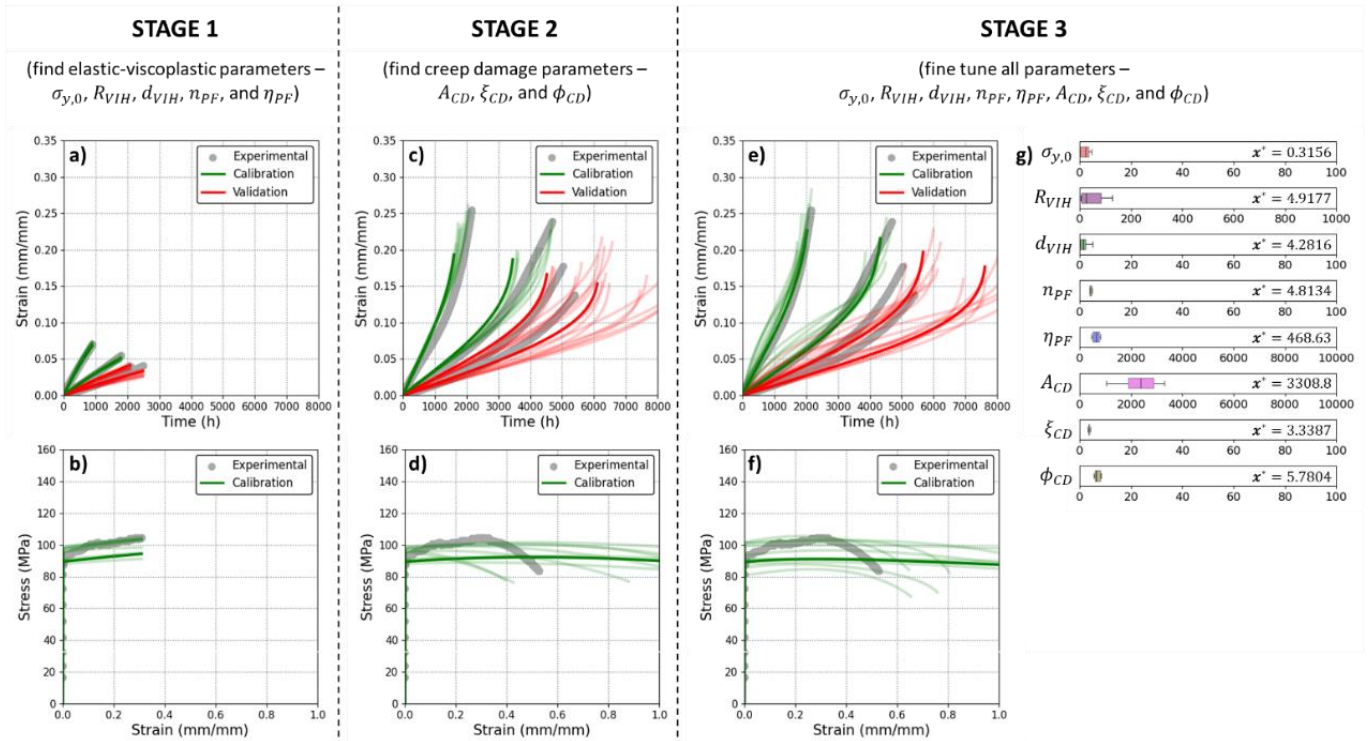


Figure B.4. Calibration results for the EVP-CD model at 1000°C, calibrated with short-term creep curves (16MPa and 13MPa) and tensile curve, and validated with longer-term creep curves (12MPa and 11MPa). The top row of plots (a, c, e) shows the creep results while the bottom row of plots (b, d, and f) shows the tensile results after stages 1, 2, and 3. The experimental datasets are in grey, the simulated curves used for calibration are in green, and the simulated curves used for validation are in red. The boxplots (g) show the distribution of the found parameters, where  $x^*$  represents the optimal parameter value, the vertical line represents the mean, the boxes represent the standard deviations, and the whiskers represent the ranges.

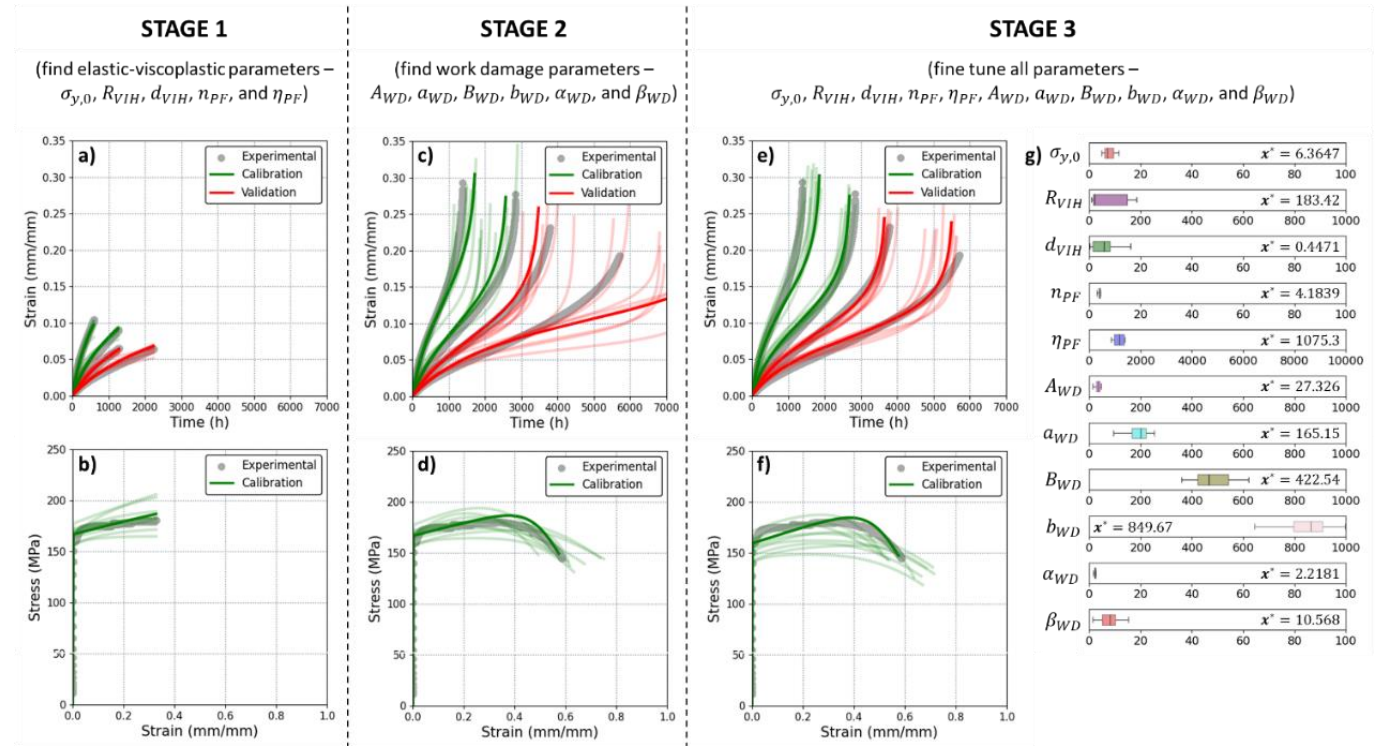


Figure B.5. Calibration results for the EVP-WD model at 900°C, calibrated with short-term creep curves (36MPa and 31MPa) and tensile curve, and validated with longer-term creep curves (28MPa and 26MPa). The top row of plots (a, c, e) shows the creep results while the bottom row of plots (b, d, and f) shows the tensile results after stages 1, 2, and 3. The experimental datasets are in grey, the simulated curves used for calibration are in green, and the simulated curves used for validation are in red. The boxplots (g) show the distribution of the found parameters, where  $x^*$  represents the optimal parameter value, the vertical line represents the mean, the boxes represent the standard deviations, and the whiskers represent the ranges.

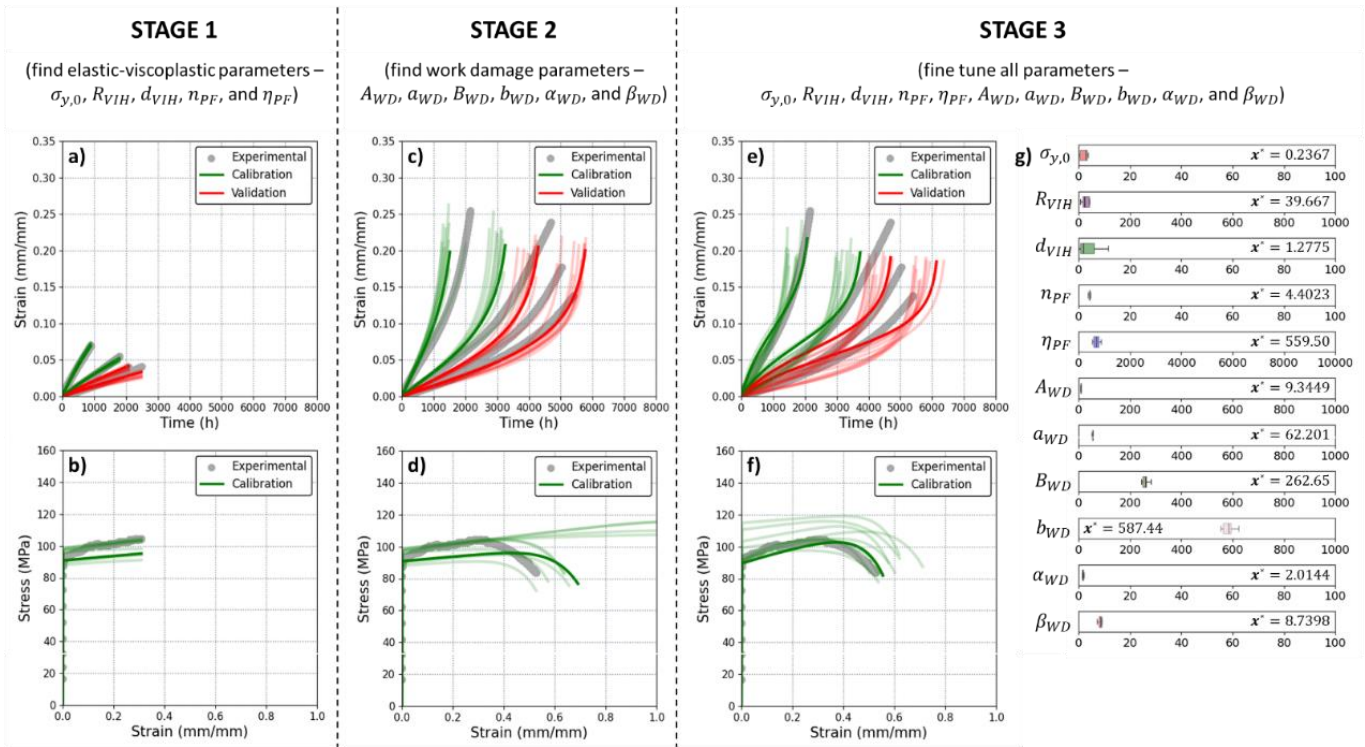


Figure B.6. Calibration results for the EVP-WD model at 1000°C, calibrated with short-term creep curves (16MPa and 13MPa) and tensile curve, and validated with longer-term creep curves (12MPa and 11MPa). The top row of plots (a, c, e) shows the creep results while the bottom row of plots (b, d, and f) shows the tensile results after stages 1, 2, and 3. The experimental datasets are in grey, the simulated curves used for calibration are in green, and the simulated curves used for validation are in red. The boxplots (g) show the distribution of the found parameters, where  $x^*$  represents the optimal parameter value, the vertical line represents the mean, the boxes represent the standard deviations, and the whiskers represent the ranges.

#### Appendix B.4. Optimised material parameter values

Table B.2 and Table B.3 contain the best of the optimised material parameters for the EVP-CD and EVP-WD models after ten independent calibration runs using the three-stage calibration workflow at 800°C, 900°C, and 1000°C. Note that descriptions of the material parameters can be found in Appendix B.1.

Table B.2. Material parameters from the best calibration run for the EVP-CD model at 800°C, 900°C, and 1000°C.

Temperature	$\sigma_{y,0}$	$R_{VIH}$	$d_{VIH}$	$n_{PF}$	$\eta_{PF}$	$A_{CD}$	$\xi_{CD}$	$\phi_{CD}$
800°C	23.304	276.66	0.32123	4.2592	1767.2	2168.5	5.3181	6.7619
900°C	3.6262	13.804	6.9825	4.2416	1138.2	1986.0	4.4408	9.1930
1000°C	0.31556	4.9177	4.2816	4.8134	468.63	3308.8	3.3387	5.7804

Table B.3. Material parameters from the best calibration run for the EVP-WD model at 800°C, 900°C, and 1000°C.

Temperature	$\sigma_{y,0}$	$R_{VIH}$	$d_{VIH}$	$n_{PF}$	$\eta_{PF}$	$A_{WD}$	$a_{WD}$	$B_{WD}$	$b_{WD}$	$\alpha_{WD}$	$\beta_{WD}$
800°C	22.154	462.34	0.17408	4.314	1828.1	40.1	260.65	408.44	853.65	1.9241	7.7562
900°C	6.3647	183.42	0.44712	4.1839	1075.3	27.326	165.15	422.54	849.67	2.2181	10.568
1000°C	0.2367	39.667	1.2775	4.4023	559.5	9.3449	62.201	262.65	587.44	2.0144	8.7398

# Appendix C

## Supplementary materials for Chapter 6

### Appendix C.1. Experimental and simulated deformation of Alloy 617 specimen

Figure C.1 and Figure C.2 visualise the experimentally observed and simulated deformation of the Alloy 617 specimen along 24 irregular strain intervals. Specifically, Figure C.1 shows electron backscatter diffraction (EBSD) maps of the specimen's microstructure, obtained through in situ EBSD. In contrast, Figure C.2 shows the deformation of the high-fidelity finite element mesh of the specimen gauge, simulated using the Voce hardening (VH) model.

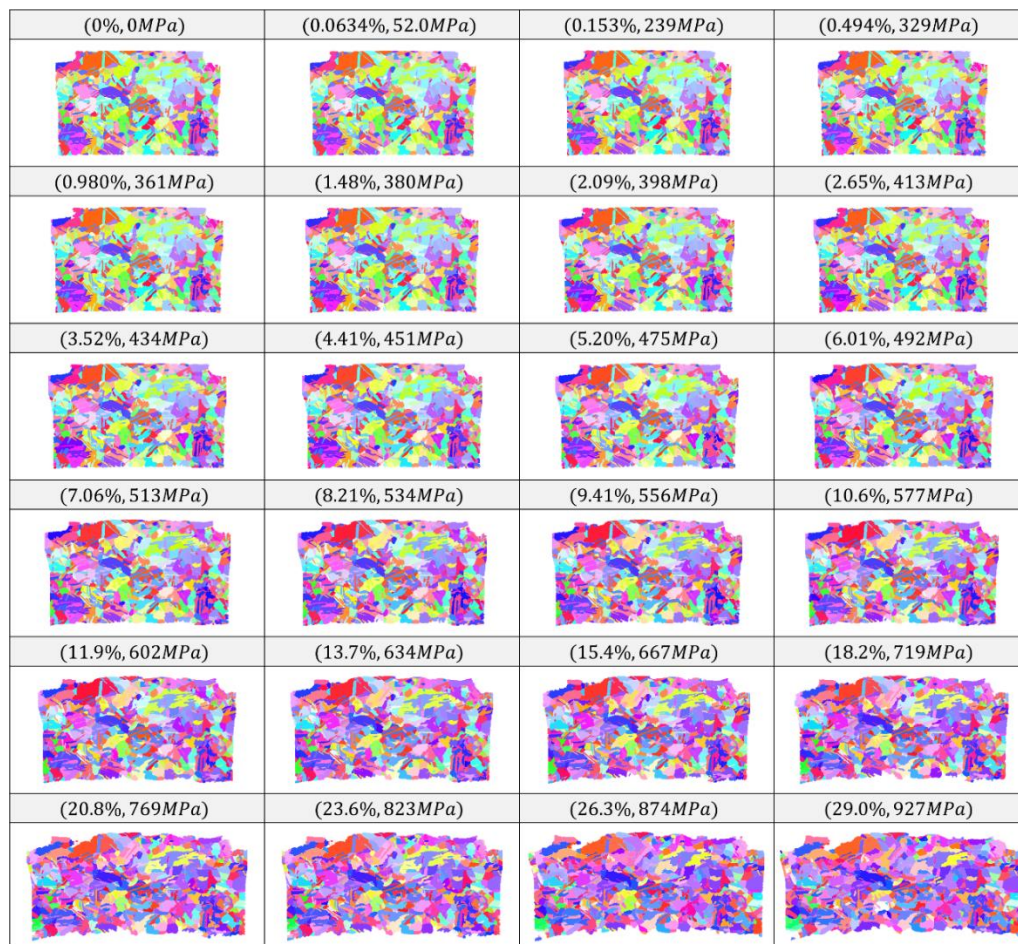


Figure C.1. Electron backscatter diffraction (EBSD) maps of the Alloy 617 specimen shown as IPF- $\bar{x}$  coloured maps.

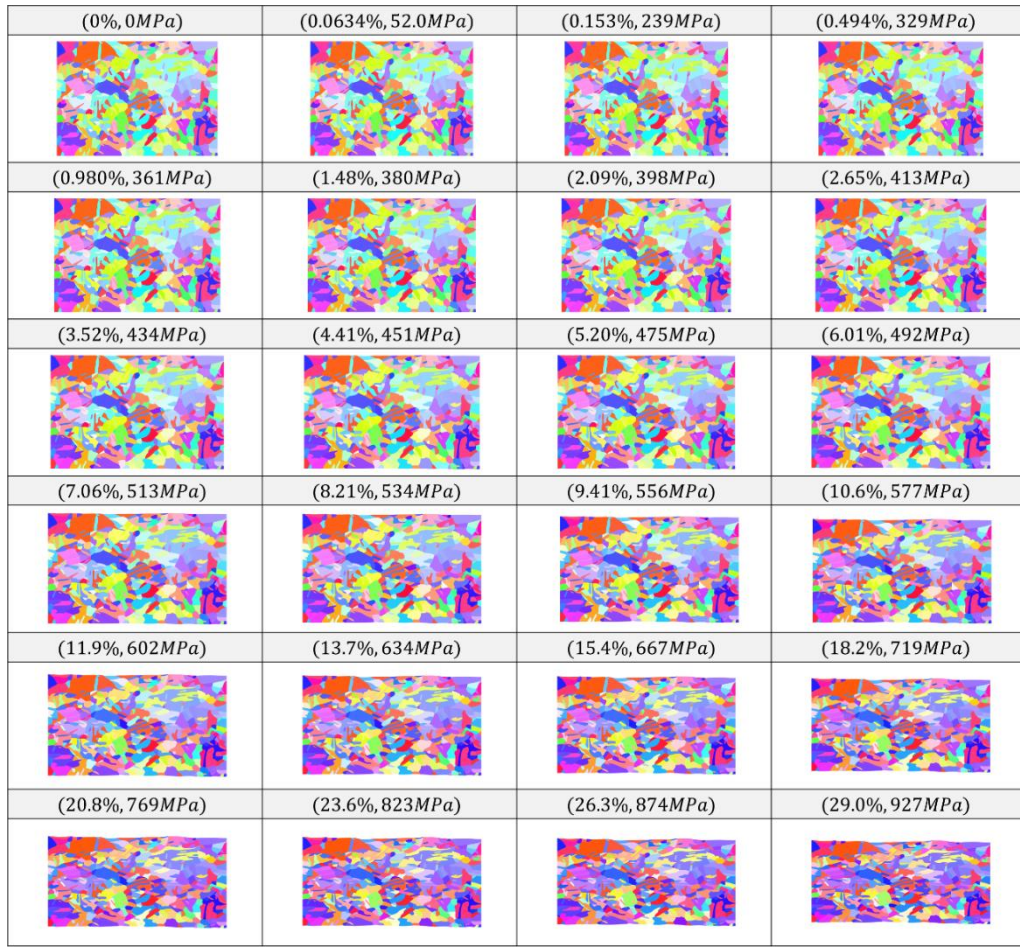


Figure C.2. Simulated deformation of the high-fidelity finite element mesh using the Voce hardening (VH) model shown as IPF- $x$  coloured maps.

### Appendix C.2. Grain tracking across electron backscatter diffraction maps

An algorithm was developed to track the evolution of individual grains in the specimen as it deformed, using a sequence of electron backscatter diffraction (EBSD) maps. This was achieved by repeatedly matching grains between consecutive EBSD maps based on their centroids and crystallographic orientations. A match between two grains from different EBSD maps would thus indicate that those two grains represent the same physical grain in the specimen. The algorithm represented the EBSD maps as separate graphs, where  $G_i$  represents the graph corresponding to the  $i$ -th EBSD map in the sequence. The nodes in  $G_i$  represented the grains in the  $i$ -th EBSD map, with each node containing information about the centroid and orientation of the corresponding grain. Edges between two graphs represented potential grain matches between two EBSD maps.

The algorithm began by matching grains between the first and second EBSD map, which involved creating a list of potential edges between the nodes in  $G_1$  and  $G_2$ . The algorithm created a potential edge between a node in  $G_1$  ( $n_{1,j}$ ) to a node in  $G_2$  ( $n_{2,k}$ ) if the distance between the normalised centroids of the corresponding grains was less than 0.2. The normalised centroid distance ( $D_C$ ) was calculated using Eq. (59), where  $x$  and  $y$  are the centroid coordinates, and  $X$  and  $Y$  are the EBSD map dimensions along the  $x$ - and  $y$ -axes, respectively. This approach eliminated unnecessary comparisons between grains that were too far apart to be potential matches.

$$D_C = \sqrt{\left(\frac{x_{i,j}}{X_i} - \frac{x_{i+1,k}}{X_{i+1}}\right)^2 + \left(\frac{y_{i,j}}{Y_i} - \frac{y_{i+1,k}}{Y_{i+1}}\right)^2} \quad (59)$$

Once all the potential edges were created, each edge was allocated a weight ( $w_{j,k}$ ) based on the sum of the normalised centroid distance ( $D_C$ ) and normalised geodesic distance ( $D_G$ ) of the two grains (i.e.,  $w_{j,k} = D_C + D_G$ ). The normalised geodesic distance was calculated using Eq. (60), where  $q$  represents the orientation of a grain in its quaternion form.

$$D_G = \frac{2}{\pi} \cos^{-1}(q_{i,j} \cdot q_{i+1,k}) \quad (60)$$

After assigning weights to all the potential edges, the algorithm arranged the edges in ascending order of their weights. The algorithm then iteratively selected edges with the lowest weights to establish bijective matching between the nodes in  $G_1$  and  $G_2$ , such that each node in  $G_1$  was matched to at most one node in  $G_2$ , and vice versa. Nodes in  $G_2$  that were not attached to any edges (i.e., unmatched grains) were removed, such that only grains that had been previously matched were retained. This approach excluded grains that had not been part of the initial EBSD map, such as those grains formed due to fragmentation or nucleation. In addition, nodes in  $G_1$  that were not attached to any edges were moved to  $G_2$ . This enabled the algorithm to maintain continuity in the tracking of a grain's evolution, even when the grain temporarily lacked matches. The algorithm repeats the process for subsequent consecutive EBSD maps (i.e.,  $G_i$  and  $G_{i+1}$ ), until the grains from the initial EBSD map have been tracked across the entire sequence of maps. The pseudocode for the algorithm is shown in Figure C.3.

01	Convert all EBSD maps into <code>graph_list</code> .
02	Get <code>graph_pair_list</code> from <code>graph_list</code> .
03	
04	For <code>graph_pair</code> in all <code>graph_pair_list</code> :
05	
06	Get <code>graph_1</code> and <code>graph_2</code> from <code>graph_pair</code> .
07	Create <code>edge_list</code> to contain all potential edges.
08	
09	For <code>node_1</code> in <code>graph_1</code> :
10	For <code>node_2</code> in <code>graph_2</code> :
11	Calculate <code>D_C</code> between <code>node_1</code> and <code>node_2</code> :
12	If <code>D_C</code> < 0.2:
13	Create <code>edge</code> connecting <code>node_1</code> and <code>node_2</code> :
14	Add <code>edge</code> to <code>edge_list</code> .
15	
16	For <code>edge</code> in <code>edge_list</code> :
17	Get <code>node_1</code> and <code>node_2</code> from <code>edge</code> .
18	Calculate <code>D_C</code> between <code>node_1</code> and <code>node_2</code> .
19	Calculate <code>D_G</code> between <code>node_1</code> and <code>node_2</code> .
20	Set <code>edge.weight</code> to <code>D_C + D_G</code> .
21	
22	Sort <code>edge_list</code> based on <code>edge.weight</code> .
23	For <code>edge</code> in <code>edge_list</code> :
24	Get <code>node_1</code> and <code>node_2</code> from <code>edge</code> .
25	If <code>node_1</code> and <code>node_2</code> have not been connected to other added edges:
26	Add <code>edge</code> between <code>node_1</code> and <code>node_2</code> .
27	
28	Remove unlinked nodes in <code>graph_2</code> .
29	Move unlinked nodes from <code>graph_1</code> to <code>graph_2</code> .

Figure C.3. Pseudocode for the grain tracking algorithm.

This algorithm was applied to the 24 EBSD maps of the Alloy 617 specimen described in Section 6.2.1 to track the evolution of individual grains and construct their reorientation trajectories. From the tracked grains, 16 grains were selected to construct reorientation trajectories for use in the calibration ( $g_{1..8}$ ) and validation ( $g_{9..16}$ ) of the CPFEM models. The evolution of the selected grains is shown in Figure C.4. In these figures, the selected grains are shown at five different strains corresponding to five EBSD maps, specifically at 0.0%, 5.2%, 10.6%, 20.8%, and 29.0%. Additionally, the relative size of each grain is preserved within its evolutionary sequence, but not across different grains.

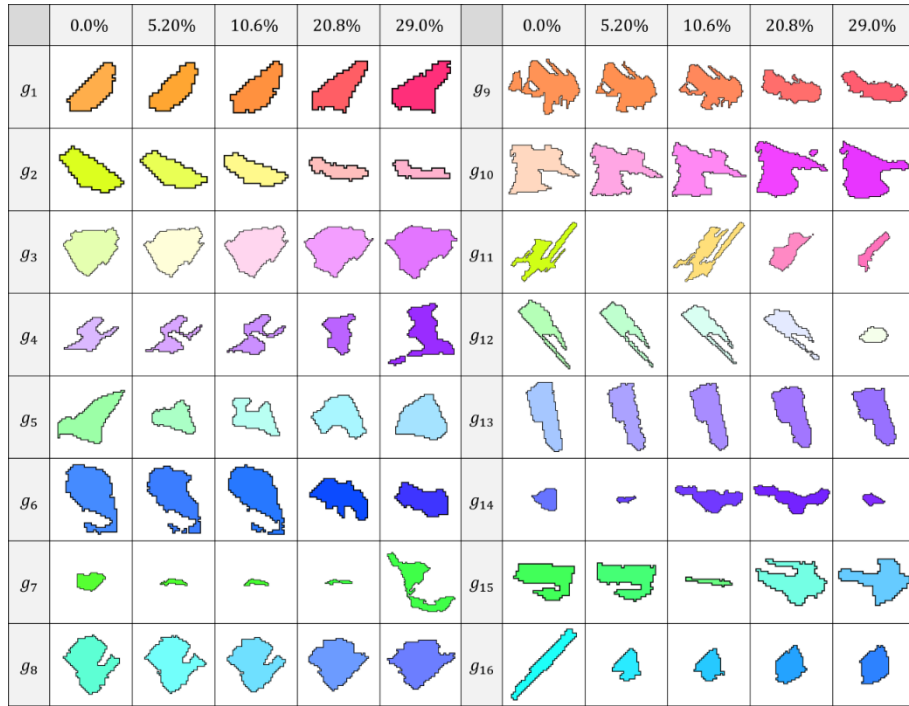


Figure C.4. Evolution of the grains selected for calibration ( $g_{1..8}$ ) and validation ( $g_{9..16}$ ) at  $\varepsilon = 0.0\%, 5.2\%, 10.6\%, 20.8\%$ , and  $29.0\%$ .

The effectiveness of the grain tracking algorithm depends on the accuracy of the grain segmentation procedure. The employed segmentation method could not recognise separated grain segments as being part of the same grain. As a result, the algorithm would temporarily track different segments of the same grain. This can be seen in grains that exhibit merging behaviour (e.g.,  $g_7$  and  $g_{14}$ ) and splitting behaviour (e.g.,  $g_{11}$  and  $g_{12}$ ), as well as grains that contain fully-sectioning twins (e.g.,  $g_{16}$ ). However, as long as the tracked segments retained similar orientations to the actual grains, the reorientation trajectories would remain representative of the grain's overall behaviour. Another issue with the grain tracking algorithm was with unmatched grains, where the algorithm temporarily failed to track the grain across one or more EBSD maps, as seen in  $g_{11}$ . This issue typically occurred when the grain underwent significant deformation, temporary fragmentation, or subtle shifts in centroid position and orientation, preventing the grain from being tracked. To address this issue, the grain tracking algorithm reintegrated previously tracked grains into the tracking sequence, thereby maintaining continuity. Since the EBSD maps were captured at relatively small strain intervals, the algorithm was still able to construct a continuous reorientation trajectory for  $g_{11}$ .

### Appendix C.3. Sensitivity study for mesh resolution

The meshing process involved discretising an electron backscatter diffraction (EBSD) map into a grid of pixels, extruding the grid into a voxellation, and converting the voxellation into a finite element (FE) model. The resolution of this grid affects the accuracy and computational cost of the crystal plasticity finite element method (CPFEM) simulations, with finer grids offering greater microstructural detail at higher computational expense. To determine the most suitable resolution for the discretisation process, a sensitivity study was conducted using nine different FE models with resolutions ranging from 5 $\mu\text{m}$  to 45 $\mu\text{m}$  in increments of 5 $\mu\text{m}$ . Since the EBSD maps were recorded with a spatial resolution of 5 $\mu\text{m}$  (Section 6.2), the 5 $\mu\text{m}$  FE model was taken as the reference (i.e., ground truth).

To analyse the changes in morphology across FE model resolutions, the plots in Figure C.5 compare the number of grains as well as the lognormal distributions of the 2D equivalent radius and circularity of the grains. The plot in Figure C.5a shows the number of grains in the FE model decreasing substantially as the resolution coarsened, largely due to the loss of smaller grains in the discretisation process. Additionally, the plot in Figure C.5b shows that the equivalent radius distributions skewed rightwards as the FE model resolutions coarsened. With coarser resolutions containing fewer grains, the rightwards skew can be attributed to the remaining grains occupying larger areas and subsequently having larger equivalent radii. Finally, the plot in Figure C.5c shows that the circularity increased as the resolution coarsened. This behaviour is expected since grains will consist of fewer elements at coarser resolutions, resulting in more simplified grain geometry that causes the grains to appear rounder.

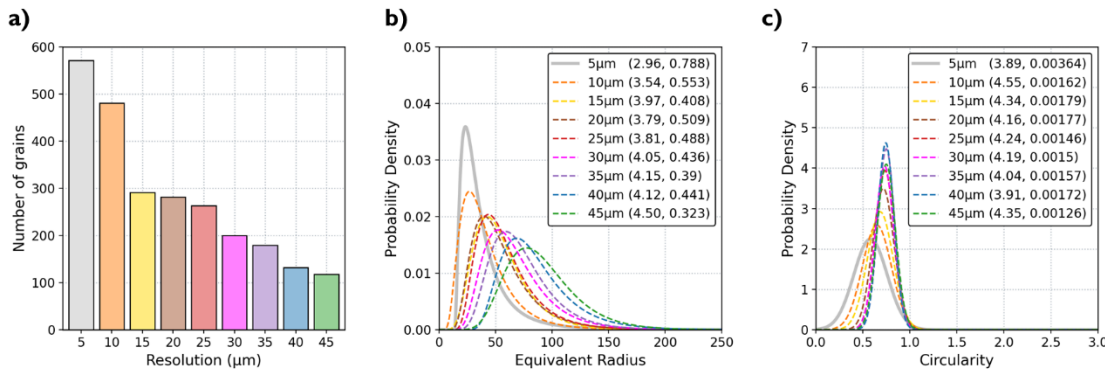


Figure C.5. Plots of the changes in the morphology of the FE models across different resolutions (5 $\mu\text{m}$  to 45 $\mu\text{m}$ ). Plot a) shows the number of grains in FE models, while plots b) and c) show the lognormal distributions of the equivalent radius and circularity of the grains, respectively. The mean and standard deviation of the lognormal distributions are indicated in the legend.

To compare the simulation results across resolutions, the Voce hardening (VH) formulation was evaluated for each FE model using the same 16 sets of constitutive parameters, sampled through the Latin hypercube sampling (LHS) scheme. Each simulation was performed using 192 cores across dual AMD EPYC 96-core processors, and the evaluation times were recorded and averaged. To assess the sensitivity of the VH-simulated responses, the simulated responses using the eight FE models (10 $\mu\text{m}$  to 45 $\mu\text{m}$ ) were compared to the responses using the reference FE model (5 $\mu\text{m}$ ). This comparison involved the stress-strain response and reorientation trajectories of all the trackable grains using the  $E_\sigma$  and  $E_\phi$  objective functions from Eqs. (41) and (51),

respectively. The distributions for the objective values as well as the average evaluation times for the eight FE models are presented in Figure C.6. The plots in Figure C.6a-b show that while both objective values increased with coarser resolutions, they remained unsubstantial. The consistency of the stress-strain responses can be attributed to global properties being less sensitive to local grain morphology when subjected to uniform boundary conditions [279], since the stress and strain fields tend to homogenise across the domain. While grain rotation is typically influenced by the grain's shape and size [280, 281], the results suggest that the morphological variations across resolutions were insufficient to significantly alter the reorientation trajectories. Additionally, the plot in Figure C.6c shows that the evaluation times decreased with coarser resolutions, which is expected since the evaluation times are roughly proportional to the number of elements in the FE model. Following these results, the CPFEM models were calibrated using a low-fidelity FE model ( $40\mu\text{m}$ ) to provide sufficient accuracy and computational efficiency. The optimised CPFEM parameters were then transferred to the high-fidelity FE model ( $10\mu\text{m}$ ) to provide enhanced microstructural fidelity and simulation accuracy.

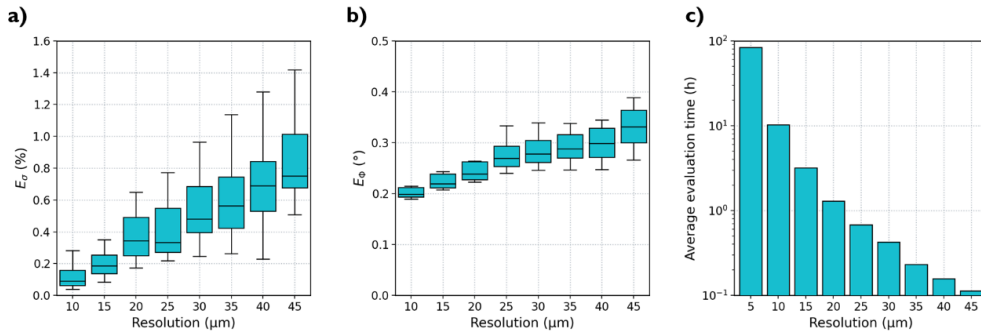


Figure C.6. Plots of the changes in the VH simulation results of the FE models across different resolutions ( $10\mu\text{m}$  to  $45\mu\text{m}$ ). Plot a) shows the  $E_\sigma$  (%) distribution in the stress-strain response while plot b) shows the  $E_\phi$  (°) distribution in the reorientation trajectories compared to the  $5\mu\text{m}$  reference FE model, where the vertical lines represent the means, the boxes represent the standard deviations, and the whiskers represent the ranges. Plot c) shows the average evaluation time at each resolution.

The transferability of the parameters across the low- and high-fidelity FE models was assessed using the 16 VH model evaluations at  $40\mu\text{m}$  and  $10\mu\text{m}$ . This assessment involved plotting the discrepancies between the low- and high-fidelity VH-simulated responses against the discrepancies between the low-fidelity VH-simulated responses and experimental data. The plot in Figure C.7a shows the discrepancies for the stress-strain response calculated using  $E_\sigma$ , while the plot in Figure C.7b shows the discrepancies for the reorientation trajectories using  $E_\phi$ . Both plots show that the discrepancies between fidelities increased somewhat proportionally with the discrepancies between the low-fidelity response and experimental data. These results suggest that parameter sets that accurately reproduce experimental behaviour will remain robust when transferring across resolutions, supporting the use of the low- and high-fidelity FE models.

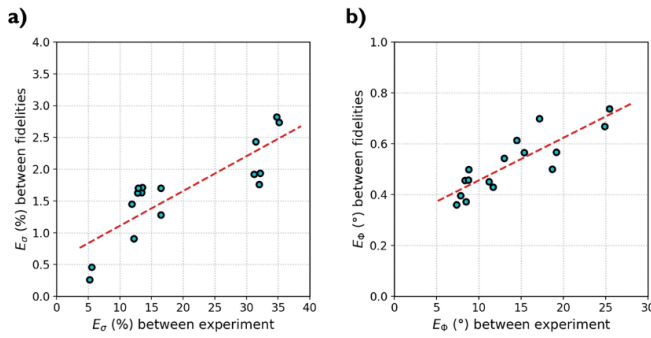


Figure C.7. Plots of the discrepancies between the low- and high-fidelity VH-simulated responses with the discrepancies between the low-fidelity VH-simulated responses and experimental data. The discrepancies were calculated for a) the stress-strain response using  $E_\sigma$  (%) and b) the reorientation trajectories using  $E_\phi$  (°).

#### Appendix C.4. Material parameters of crystal plasticity hardening models

Table C.1 contains a summary of the constitutive parameters for the Voce hardening (VH) formulation, the two-coefficient latent hardening (LH2) formulation, and the six-coefficient latent hardening (LH6) formulation. The table also contains the parameters bounds used in the calibration of those hardening models as well as the referenced literature used to determine those bounds. Note that the parameter bounds were defined to provide a sufficiently large search space to demonstrate the capabilities of the adaptive calibration workflow with the hardening models.

Table C.1. Summary of constitutive parameters for the Voce hardening (VH), two-coefficient latent hardening (LH2), and six-coefficient latent hardening (LH6) formulations.

Model	Parameter	Symbol	Units	Bounds	References
VH, LH2, LH6	Static slip system strength	$\tau_0$	MPa	(0, 500)	[236, 282]
VH, LH2, LH6	Strain rate sensitivity parameter	$n$	—	(1, 20)	[234, 236, 283]
VH	Saturation slip system strength	$\tau_s$	MPa	(0, 4000)	[236, 282, 283]
VH	Saturation rate parameter	$b$	—	(0, 10)	[234, 236]
LH2, LH6	Self-hardening coefficient	$h_{\alpha\alpha}$	MPa	(0, 1000)	[62, 65, 261]
LH2	Latent hardening coefficient	$h_{\alpha\beta}$	MPa		
LH6	Coplanar interaction coefficient	$h_1$	MPa		
LH6	Hirth interaction coefficient	$h_2$	MPa		
LH6	Collinear interaction coefficient	$h_3$	MPa		
LH6	Glissile interaction coefficient	$h_4$	MPa		
LH6	Lomer interaction coefficient	$h_5$	MPa		

#### Appendix C.5. Knee-point identification method

The alignment between the simulated and experimental responses is evaluated using two objective functions –  $E_\sigma$  from Eq. (41) which quantifies the discrepancies between the experimental and simulated stress-strain responses, and  $E_\phi$  from Eq. (51) which quantifies the discrepancies between the experimental and simulated

reorientation trajectories. Among multiple simulated responses, the response that achieves the best agreement with the experimental data is selected as the knee point on the Pareto front. In this study, the knee point is identified by normalising the objective values ( $E_\sigma$  and  $E_\phi$ ) to the range [0,1], and then selecting the solution that minimises the sum of their squares (i.e.,  $\hat{E}_\sigma^2 + \hat{E}_\phi^2$ ). In other words, the knee point corresponds to the minimal Euclidean distance from the origin (0, 0) in the normalised objective value space.

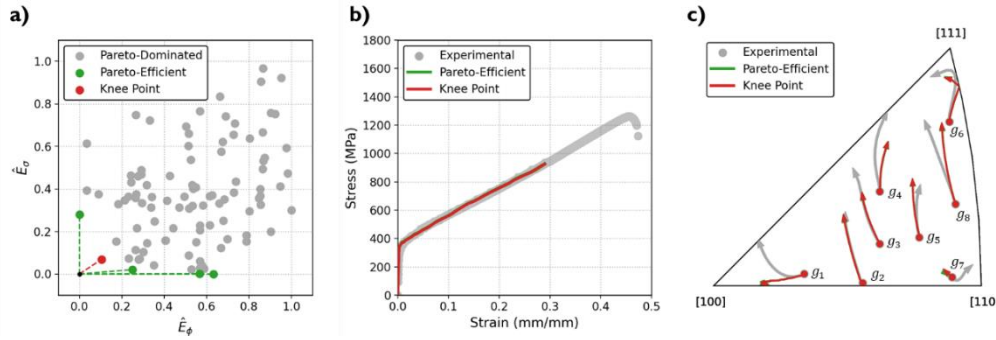


Figure C.8. Results from the Pareto front of the final population of a MOGA optimisation performed on the surrogate model for the VH formulation. Panel a) presents the normalised objective values ( $\hat{E}_\sigma$  and  $\hat{E}_\phi$ ), showing the Pareto-dominated solutions (grey), Pareto-efficient solutions (green), and knee point solution (red). Panels b) and c) present the stress–strain response and reorientation trajectories of  $g_{1..8}$  predicted by the surrogate model, comparing the experimental data (grey), Pareto-efficient solutions (green), and knee point solution (red).

The knee point is used to determine the best solution in the final population of the MOGA optimisations and to select the best calibration run among multiple independent runs. An example of the knee-point identification is presented in Figure C.8, obtained from a MOGA optimisation of the surrogate model for the VH formulation. The normalised objective values ( $\hat{E}_\sigma$  and  $\hat{E}_\phi$ ) of the MOGA’s final population are shown in Figure C.8a, highlighting the Pareto-efficient solutions in green and the knee-point solution in red. The corresponding stress–strain responses and reorientation trajectories of  $g_{1..8}$  predicted by the surrogate model are also presented in Figure C.8b and c, respectively, which show the surrogate model’s responses across the Pareto front achieving comparably close agreement with the experimental data.

#### Appendix C.6. Sensitivity study for initial training dataset size

The adaptive calibration workflow (Section 6.4.3) was designed to efficiently calibrate the CPFEM models. In the first iteration of the workflow, the simulation results from several CPFEM evaluations were used to generate the initial training dataset. In subsequent iterations, the results from an additional CPFEM evaluation were used to update the training dataset. Since CPFEM evaluations account for a substantial portion of the calibration workflow’s computational expense, reducing the number of CPFEM evaluations is crucial.

As such, a sensitivity study was conducted to determine the initial dataset set that minimises the total number of CPFEM evaluations while sufficiently calibrating the CPFEM model. The sensitivity study involved calibrating the Voce Hardening (VH) model across varying initial dataset sizes, ranging from 2 to 16 evaluations in increments of 2. The calibration runs were repeated until termination, five times for each initial dataset size, with the total number of iterations averaged across the runs. The averaged results were then plotted to visualise the influence of the initial dataset size on the number of additional evaluations required, as shown in Figure C.9.

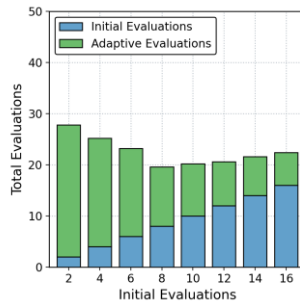


Figure C.9. Plot of the total number of evaluations to calibrate the Voce hardening (VH) model with the adaptive surrogate-assisted calibration workflow using various initial dataset sizes.

When the calibration workflow was performed with an initial dataset size ranging from 2 to 8, the number of additional evaluations decreased as the initial dataset size increased. This was expected, since a larger initial dataset would improve the accuracy of the surrogate model in approximating the VH model's responses, reducing the need for additional evaluations. Importantly, the total number of evaluations also decreased. However, beyond an initial dataset size of 8, no further reduction in additional evaluations was observed, which led to an overall increase in the total number of evaluations. These results suggest that an initial dataset size of 8 minimises the total number of evaluations, and thus the computational cost of the calibration process.

#### *Appendix C.7. Computational costs of crystal plasticity finite element method models*

In addition to predictive performance and transferability, the practical applicability of CPFEM models also depends heavily on their computational cost. To quantify this aspect, each CPFEM model was evaluated using 192 cores across dual AMD EPYC 96-core processors. The average runtime for a single CPFEM evaluation varied significantly across the three hardening models. Specifically, each evaluation of the low-fidelity VH formulation required approximately 0.23 hours of CPU time, while the LH2 and LH6 formulations required roughly 1.46 hours. This increased cost for the latent hardening models reflects the additional internal state variables and non-linear coupling introduced by the latent hardening framework, which increases both the number and stiffness of the equations being solved during each simulation.

As described in Section 6.5.1, the surrogate-assisted calibration workflow required an initial set of CPFEM simulations followed by several additional evaluations as part of the adaptive refinement process. Specifically, the VH and LH2 formulations required 8 initial evaluations, while the LH6 formulation required 16 due to its larger parameter space. On average, an additional 13, 16, and 22 evaluations were needed for the VH, LH2, and LH6 formulations, respectively, to reach convergence in the multi-objective optimisation. The expected computational cost of calibrating each CPFEM model is summarised in Figure C.10. The plot clearly illustrates that the computational demand increases significantly with model complexity. The total CPU time required to calibrate the LH2 and LH6 formulations is approximately 7-12 times greater than that required for the VH formulation. The steep increase in runtime for the LH6 formulation reflects not only the cost per evaluation but also the greater number of evaluations required to sufficiently explore and constrain its higher-dimensional parameter space.

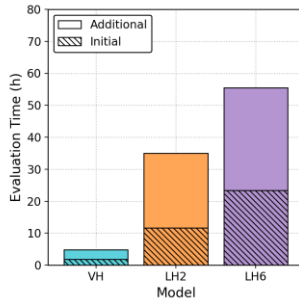


Figure C.10. Comparison of the computational requirements for the calibration of the VH formulation (in cyan), LH2 formulation (in orange), and LH6 formulation (in purple). The average costs for the initial evaluations are represented by single-hashed bars while the costs for the additional evaluations are represented by plain bars.

Taken together with the results presented in previous sections, these findings suggest that the VH formulation provides the most favourable balance between computational efficiency and predictive accuracy. It consistently reproduces the stress–strain response, grain reorientation behaviour, and texture evolution of Alloy 617 under uniaxial tensile loading, while requiring only a fraction of the computational resources consumed by the more complex latent hardening formulations. While the LH2 and LH6 formulations offer greater flexibility and may be better suited for applications involving more complex loading paths or multiaxial stress states, the VH formulation emerges as the most practical choice for routine applications focused on uniaxial deformation with *in situ* validation data.

Notably, the computational cost of the calibration workflow is expected to increase with both microstructural size and loading complexity. Larger microstructures containing more grains will require finer mesh resolutions to accurately represent microstructural heterogeneity, where the cost of each CPFEM evaluation will increase roughly in proportion to the total number of finite elements. Likewise, non-monotonic or multiaxial loading conditions often require smaller time increments and additional solver iterations per increment, further increasing evaluation costs [284]. These factors may also introduce greater variability in the model responses, necessitating more CPFEM evaluations to adequately sample the parameter space and train the surrogate model. That said, an assessment of the workflow’s scalability under such conditions is beyond the scope of the present study.

#### *Appendix C.8. Calibration of Voce hardening formulation with swapped grain trajectories*

To further assess the robustness of the calibration workflow, an additional test was performed on the Voce hardening (VH) formulation by swapping the calibration and validation grain datasets. Using this alternate approach, the VH formulation underwent five additional calibration runs against the experimental stress–strain curve and the reorientation trajectories of  $g_{9..16}$ . After each run, the calibrated model was validated against the  $g_{1..8}$  trajectories and the overall texture evolution. The calibration and validation results are presented in Figure C.11 and can be directly compared to those in Figure 6.9, where the grains  $g_{1..8}$  were used for calibration and  $g_{9..16}$  for validation.

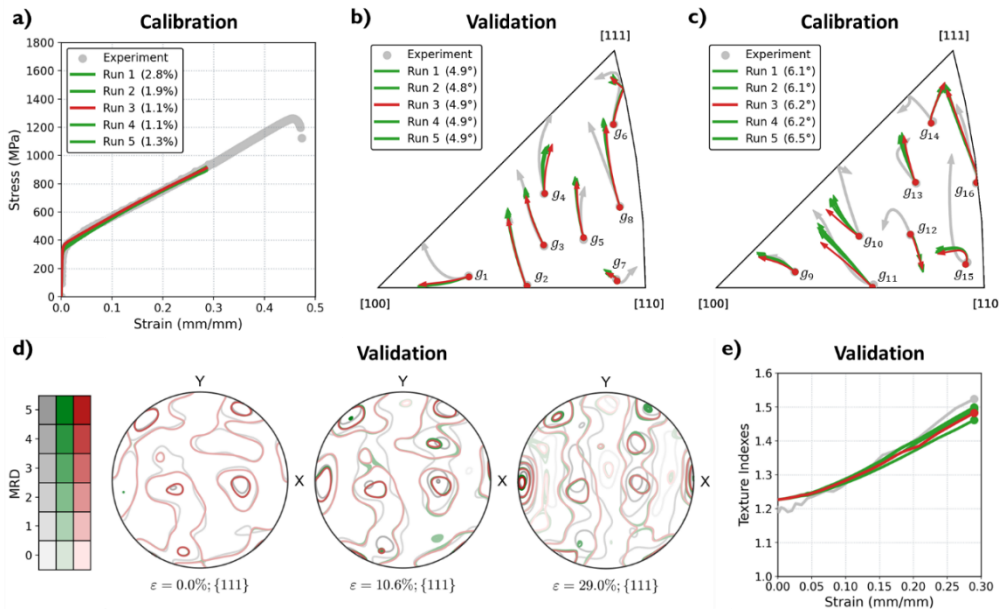


Figure C.11. Supplementary calibration and validation results for the VH formulation after five runs, comparing the experimental data in grey with the simulated responses in green (all runs) and red (best run). The plots in the top row compare the a) stress–strain responses (calibration), b) reorientation trajectories of  $g_{1..8}$  (validation), and c) reorientation trajectories of  $g_{9..16}$  (calibration), including the corresponding objective values ( $E_\sigma$  and  $E_\phi$  from Eqs. (41) and (51)). The plots in the bottom row compare the overall texture evolution (validation) using d) contoured  $\{111\}$  pole figures at  $\varepsilon = 0.0\%$ ,  $10.6\%$ , and  $29.0\%$ , and e) texture indexes over  $0.0\%$  to  $29.0\%$ .

The macroscopic stress–strain predictions maintained excellent agreement with the experimental data in both calibration approaches. At the mesoscale, both sets of reorientation trajectories (i.e.,  $g_{1..8}$  and  $g_{9..16}$ ) showed slight improvements when using this alternate approach, with the average geodesic distance error ( $E_\phi$ ) decreasing from  $4.96^\circ$  to  $4.88^\circ$  for  $g_{1..8}$ , and  $6.4^\circ$  to  $6.22^\circ$  for  $g_{9..16}$ . The overall texture evolution also improved marginally, with the average texture index at  $\varepsilon = 29\%$  increasing from 1.46 to 1.48, which is closer to the experimental value of 1.52. While these improvements could suggest that the complex reorientation paths of  $g_{9..16}$  offer better constraints on grain rotation and texture predictions, they could also be coincidental. Ultimately, the workflow is largely insensitive to the choice of calibration grains, provided that they exhibit representative and trackable rotation behaviour.